ELMINA 2022

SECOND INTERNATIONAL CONFERENCE ON ELECTRON MICROSCOPY OF NANOSTRUCTURES

ДРУГА МЕЂУНАРОДНА КОНФЕРЕНЦИЈА О ЕЛЕКТРОНСКОЈ МИКРОСКОПИЈИ НАНОСТРУКТУРА

August 22nd–26th, 2022, Belgrade, Serbia
22–26. август 2022. Београд, Србија

SECOND INTERNATIONAL CONFERENCE

ELMINA 2022

Serbian Academy of Sciences and Arts, Belgrade, Serbia
August 22nd-26th, 2022
http://elmina.tmf.bg.ac.rs

Program and Book of Abstracts

Organized by:
Serbian Academy of Sciences and Arts
and
Faculty of Technology and Metallurgy, University of Belgrade

Endorsed by:
European Microscopy Society
and
Federation of European Materials Societies

Title: SECOND INTERNATIONAL CONFERENCE
ELMINA 2022
Program and Book of Abstracts

Publisher: Serbian Academy of Sciences and Arts
Knez Mihailova 35, 11000 Belgrade, Serbia
Phone: +381 11 2027200
https://www.sanu.ac.rs/en/

Editors: Velimir R. Radmilović and Vuk V. Radmilović

Technical Editor: Vuk V. Radmilović

Cover page: Raša Hindawi

Printed in: Serbian Academy of Sciences and Arts
Knez Mihailova 35, 11000 Belgrade, Serbia
Phone: +381 11 2027128
stamparija@sanu.ac.rs
Circulation: 55 copies.

At the beginning we wish you all welcome to Belgrade and ELMINA2022 International Conference organized by the Serbian Academy of Sciences and Arts and the Faculty of Technology and Metallurgy, University of Belgrade. We are delighted to have such a distinguished lineup of plenary speakers who have agreed to accept an invitation from the Serbian Academy of Sciences and Arts to come to the second electron microscopy conference: Electron Microscopy of Nanostructures, ELMINA2022. The scope of ELMINA2022 will be focused on electron microscopy, which provides structural, chemical and electronic information at atomic scale, applied to nanoscience and nanotechnology (physics, chemistry, materials science, earth and life sciences), as well as advances in experimental and theoretical approaches, essential for interpretation of experimental data and research guidance. It will highlight recent progress in instrumentation, imaging and data analysis, large data set handling, as well as time and environment dependent processes. The scientific program contains the following topics:

- Instrumentation and New Methods
- Diffraction and Crystallography
- HRTEM and Electron Holography
- Analytical Microscopy (EDS and EELS)
- Nanoscience and Nanotechnology
- Life Sciences

To put this Conference in proper prospective, we would like to remind you that everything related to nanoscience and nanotechnology started 30 to 40 years ago as a long term objective, and even then it was obvious that transmission electron microscopy (TEM) must play an important role, as it was the only method capable of analyzing objects at the nanometer scale. The reason was very simple - at that time, an electron microscope was the only instrument capable of detecting the location of atoms, making it today possible to control synthesis of objects at the nanoscale with atomic precision. Electron microscopy is also one of the most important drivers of development and innovation in the fields of nanoscience and nanotechnology relevant for many areas of research such as biology, medicine, physics, chemistry, etc. We are very proud that a large number of contributions came from young researchers and students which was one of the most important objectives of ELMINA2022, and which indicates the importance of electron microscopy in various research fields. We are happy to present this book, comprising of the Conference program and abstracts, which will be presented at ELMINA2022 International Conference. We wish you all a wonderful and enjoyable stay in Belgrade.

Table of Contents

ORGANIZERS.....5

CONFERENCE PROGRAM 7

PLENARY PRESENTATIONS 21

ORAL PRESENTATIONS 77

POSTER PRESENTATIONS.....127

AUTHOR INDEX 211

ACKNOWLEDGEMENTS 221

ORGANIZERS

SERBIAN ACADEMY OF SCIENCES AND ARTS
Knez Mihailova 35, 11000 Belgrade, Serbia
Phone: +381 11 2027200
https://www.sanu.ac.rs/en/

FACULTY OF TECHNOLOGY AND METALLURGY, UNIVERSITY OF BELGRADE
Karnegijeva 4, 11000 Belgrade, Serbia
Phone: +381 11 3370425
https://www.tmf.bg.ac.rs/en/

Conference Chair

Velimir R. Radmilović

Conference Manager

Vuk V. Radmilović

International Advisory Board

Chair: Robert Sinclair (USA)
Members: Sara Bals (Belgium), Gianluigi Botton (Canada), Fu-Rong Chen (Taiwan), Vladica Cvetković (Serbia), Peter Denes (USA), Rafal Dunin-Borkowski (Germany), Rolf Erni (Switzerland), Hamish Fraser (USA), Randi Holmestad (Norway), Wayne D. Kaplan (Israel), Gerald Kothleitner (Austria), Hannes Lichte (Germany), Laurence Marks (USA), Joachim Mayer (Germany), Paul Midgley (UK), Eva Olsson (Sweden), Stephen Pennycook (Singapore), Quentin Ramasse (UK), Frances Ross (USA), Erdmann Spiecker (Germany), Kazu Suenaga (Japan), Dragan Uskoković (Serbia), Petar Uskoković (Serbia), Maria Varela del Arco (Spain), Johan Verbeeck (Belgium).

Program Committee

Chair: Velimir R. Radmilović (Serbia)
Members: Vladimir Bumbaširević (Serbia), Đorđe Janaćković (Serbia), Aleksandra Korać (Serbia), Irena Nikolić (Montenegro), Zoran Popović (Serbia), Tamara Radetić (Serbia), Vuk Radmilović (Serbia), Miljko Satarić (Serbia), Leposava Šiđanin (Serbia).

Organizing Committee

Chair: Vuk Radmilović (Serbia)
Vice-chair: Ivana Drvenica
Members: Marija Aleksić (Serbia), Vladan Ćosović (Serbia), Aleksandra Hreljac (Serbia), Smilja Marković (Serbia), Nataša Nestorović (Serbia), Nadežda Radmilović (Serbia), Željko Radovanović (Serbia), Zlatko Rakočević (Serbia), Đorđe Veljović (Serbia).

Technical Committee

Chair: Đorđe Veljović
Members: Ivana Dinić, Milena Dojčinović, Jovan Lukić, Tamara Matić, Aleksandra Mašulović, Daniel Mijailović, Marija Milivojević, Željko Mravik, Vladimir Pavkov, Anđela Radisavljević, Vladimir Rajić, Tijana Stamenković, Milica Stefanović, Milena Stevanović, Vukašin Ugrinović.

GENERAL INFORMATION

DATE AND VENUE: The conference will be held August 22nd-26th, 2022 at the Serbian Academy of Sciences and Arts, Knez Mihailova 35, 11000 Belgrade, Serbia with the beginning at 8:30 AM on August 22nd 2022, in the main lecture hall.

REGISTRATION: At the registration desk, located in front of the main lecture hall of the conference venue. Registration desk working hours are: Monday, August 22nd, from 8:00 to 14:00, Tuesday, August 23rd, from 8:15 to 14:00, Wednesday, August 24th, from 8:15 to 14:00 and Thursday August 24th, from 8:15 to 12:00. Registered participants will receive a nametag and a conference bag.

INSTRUCTIONS FOR AUTHORS: The conference will feature plenary sessions, oral sessions and poster sessions as well as vendor presentations during lunch breaks. Presentations during plenary sessions will last 30 minutes each, including discussion while oral presentations will be 15 minutes each, including discussion. Standard and hands-free microphones will be on site. No A-V equipment will be provided for any poster presentations. Poster presenters must remain at their poster on their assigned day during the required poster session. Each poster will be allocated a 1180 mm high and 841 mm wide (A0 format) display area.

CONFERENCE AWARDS: Oral and poster presentations will be reviewed according to the following criteria: (a) relevance to a specific symposium, (b) scientific content, quality and innovative proposals, (c) clarity of the text, and (d) compliance with the format. During the conference, the best three (3) oral and three (3) poster presentations, selected by an award committee, will receive awards.

Second International Conference "Electron Microscopy of Nanostructures"
ELMINA 2022, August 22nd – 26th, Belgrade, SERBIA

Sunday, August 21st, Mama Shelter Rooftop	
18:00-20:00	**Welcome Cocktail**
Monday, August 22nd, Main Lecture Hall	
9:00-9:30	**Opening Ceremony** * Velimir Radmilović, Conference Chair * Vladimir Kostić, President of Serbian Academy of Sciences and Arts * Vladimir Bumbaširević, Former Rector of Belgrade University * Robert Sinclair, Chair of ELMINA2022 International Advisory Board
9:30-11:00	**Plenary Session 1** **Chair:** Xiaoqing Pan
9:30-10:00	**Colin Humphreys** "*Making Optoelectronic Devices from Large-Area Transfer-Free MOCVD Graphene: Magnetic Hall Sensors and OLEDs: Electron Microscope Challenges*"
10:00-10:30	**Vlado Lazarov** *"The Role of Atomic Structure of Interfaces and Defects in Thin Films Heterostructures for Spintronic Applications"*
10:30-11:00	**Quentin Ramasse** *"Monochromated Electron Energy Loss Spectroscopy in the Scanning Transmission Electron Microscope at High Spatial Resolution"*
11:00-11:30	**Coffee Break**
11:30-13:00	**Plenary Session 2** **Chair:** Colin Humphreys
11:30-12:00	**Xiaoqing Pan** "*Emergent Phonon Phenomena at Interfaces probed by Vibrational EELS*"
12:00-12:30	**Kazu Suenaga** "*Electron Microscopy and Spectroscopy of Low-dimensional Hybrid Materials*"
12:30-13:00	**Thomas Kelly** "*Progress Towards Atomic-Scale Analytical Tomography*"
13:00-15:00	**Break / Vendor Presentation Thermofisher Scientific** "*TEM lamella preparation and subsequent atomic resolution imaging from a pure Li metal using Inert Gas transfer workflow from DualBeam to TEM*"
15:00-16:00	**Oral Session 1** **Chair:** Marija Aleksić
15:00-15:15	**Tamara Matić** *"Hydroxyapatite-based Bioceramic Dental Inserts as Dentin Substitutes"*
15:15-15:30	**Darko Ćirić** *"High Fat Diet Increases the Number of Mitophagy-related Structures in Hepatocytes of C57BL/6J Mice"*
15:30-15:45	**Domagoj Belić** *"Imaging of Nanoscale Gold in "Intact" Biological Cells by Environmental Electron Microscopy"*
15:45-16:00	**Igor Golić** *"Investigation of the Action of the Fullerene (C_{60}) Derivatives on*

	Mouse 3T3 Fibroblast Cell Lines"
16:00-17:30	**Poster Session 1**
Tuesday, August 23rd, Main Lecture Hall	
9:00-11:00	**Plenary Session 3** **Chair:** Vlado Lazarov
9:00-9:30	**Robert Sinclair** *"Using STEM-EELS to Optimize Gold Nanoparticles for Early Cancer Detection"*
9:30-10:00	**Rolf Erni** *"Liquid-Phase Atomic-Scale Investigations of Crystal Nucleation, Particle Growth and Core-Shell Formation Using In-Situ Scanning Transmission Electron Microscopy"*
10:00-10:30	**Rafal Dunin-Borkowski** *"In Situ Scanning Transmission Electron Diffraction of Individual Electrically Biased Ag-In-Sb-Te Phase Change Memory Line Cells"*
10:30-11:00	**Laurence Marks** *"Where did That Charge Come From?"*
11:00-11:30	**Coffee Break**
11:30-13:00	**Plenary Session 4** **Chair:** Rolf Erni
11:30-12:00	**Sašo Šturm** *"Nd-Fe-B Permanent Magnets Ecosystem for a Resilient and Sustainable European Electric Mobility and Renewable Energy Future"*
12:00-12:30	**Angus Kirkland** *"From Millions of Images to a Few Numbers: High speed imaging of Defects and Defect Dynamics in Low Dimensional Materials"*
12:30-13:00	**Cécile Hébert** *"Quantitative Chemical Analysis of Complex Samples using Analytical TEM and Machine Learning Tools: from Elemental Maps to Phase Segmentation"*
13:00-15:00	**Break**
15:00-16:15	**Oral Session 2** **Chairs:** Vladan Ćosović and Zoran Šaponjić
15:00-15:15	**Zoran Šaponjić** *"Shaped Eu^{3+}, Co^{2+} or Ru^{3+} doped TiO_2 Nanocrystal from Nanotubular Precursors with Optical, Magnetic and Electrochemical Properties"*
15:15-15:30	**Veljko Djokić** *"Synthesis and Characterization of Highly Active Rutile TiO_2 Nanocrystalline Photocatalysts with Synergistic Exposed Crystal Facets"*
15:30-15:45	**Jelena Lović** *"Morphological and Structural Characterization of Tin Dendritic Nanostructures Produced by Various Electrodeposition Processes"*
15:45-16:00	**Irena Nikolić** *"Alkali activated slag based on steelmaking slag: application and properties"*
16:00-16:15	**Vladan Ćosović** *"Evaluation of Nano-crystalline $NiFe_2O_4$ Obtained via Pressurized Ethanol Synthetic Route"*
Wednesday, August 24th, Main Lecture Hall	
9:00-11:00	**Plenary Session 5**

	Chair: Eva Olsson
9:00-9:30	**Jordi Arbiol** *"2D Nanostructures at Atomic Scale: From Energy an Environmental Applications to Quantum Devices"*
9:30-10:00	**Hamish Fraser** *"Use of Analytical Electron Microscopy to Characterize Microstructure and Develop Transformation Pathways in Compositionally Complex Alloys"*
10:00-10:30	**Gerald Kothleitner** *"Applications and Challenges in STEM Inelastic Imaging"*
10:30-11:00	**Gerhard Dehm** *"Multi-Element Segregation at BCC Iron Grain Boundaries and Their Impact On Mechanical Properties"*
11:00-11:30	**Coffee Break**
11:30-13:00	**Plenary Session 6** **Chair:** Gerhard Dehm
11:30-12:00	**Eva Olsson** *"In Situ Electron Microscopy Revealing Site Specific Strain Induced Changes in Properties and Structure on the Atomic Scale"*
12:00-12:30	**Cristina Scheu** *"A Scale Bridging Approach For Analysis of Extended Defects in Thermoelectric Materials: From Electron Channeling Contrast Imaging, Scanning Transmission Electron Microscopy to Atom Probe Tomography"*
12:30-13:00	**Ivan Lazić** *"Integrated Differential Phase Contrast (iDPC) STEM for Low Dose Imaging of Beam Sensitive Materials and Cryo Nano Particles at Atomic Resolution"*
13:00-13:45	**Oral Session 3** **Chair:** Ivan Lazić
13:00-13:15	**Daniel Stroppa** *"Hybrid-Pixel Detectors for TEM by DECTRIS"*
13:15-13:30	**Viktoria Kovacs Kis** *"Microstructure Investigation of Nanocrystalline Materials Using Electron Diffraction Based Rietveld Analysis – Approximation of Instrumental Broadening"*
13:30-13:45	**Zsolt Czigany** *"Calibration Procedure and Error Analysis to Improve the Accuracy of SAED in Aberration Corrected TEM"*
Thursday, August 25th, Main Lecture Hall	
9:00-11:00	**Plenary Session 7** **Chair:** Velimir Radmilović
9:00-9:30	**Peter Nellist** *"2D and 4D STEM Imaging of Beam Sensitive Materials"*
9:30-10:00	**Joachim Mayer** *"The role of correlative CT and TEM investigations in the development of novel Li-ion battery materials"*
10:00-10:30	**Paulo Ferreira** *"Understanding the Structure of $LiMn_2O_4$ by Aberration-Corrected HAADF STEM and Differential Phase Contrast"*
10:30-11:00	**Erdmann Spiecker** *"Seeing Structural Evolution of Organic Molecular Nano-crystallites Using 4D Scanning Confocal Electron Diffraction (4D-SCED)"*
11:00-11:30	**Coffee Break**
11:30-13:30	**Oral Session 4** **Chairs:** Milivoj Plodinec and Nadežda Radmilović

11:30-11:45	**Duygu Gizem *Senturk*** *"Optimal Experiment Design for Characterising Heterogeneous Nanostructures by Using 4D Scanning Transmission Electron Microscopy"*
11:45-12:00	**Rafael Ferreira** *"Understanding the Influence Of Experimental Parameters On Atomic Electrostatic Configuration Measurements By Segmented-Detector DPC-STEM"*
12:00-12:15	**Zezhong Zhang** *"Fast prediction of ADF-EDX scattering cross-sections for elemental quantification of nanostructures"*
12:15-12:30	**Weixin Song** *"Imaging Structural Defects and Associated Oxygen Positions in 3d Li-rich Metal Oxide"*
12:30-12:45	**Sergej Ražnjević** *"Electron beam induced Brownmillerite – perovskite phase transition in $La_{0.6}Sr_{0.4}CoO_{3-\delta}$ "*
12:45-13:00	**Fatima Zorro** *"In-Situ TEM Study of Flash Sintering in Oxide Materials"*
13:00-13:15	**Milivoj Plodinec** *"Direct insights into dry reforming of methane over Ni nanoparticles by Operando TEM"*
13:15-13:30	***Sorour Semsari*** **Parpari** *"Heterogeneous Electrochemical Dissolution of Au Nanoparticles Observed via In-situ Liquid TEM"*
13:30-15:30	**Break / Vendor Presentation Nanomegas** "Precession Enhanced Electron Diffraction Applications in TEM for nano-scale materials studies"
15:30-17:00	**Poster Session 2**
Friday, August 26th, Main Lecture Hall	
9:00-11:00	**Plenary Session 8** **Chair:** Aleksandra Korać
9:00-9:30	**Jürgen Plitzko** *"Next Generation Sample Preparation for Cryo-Electron Tomography"*
9:30-10:00	**Agnes Kittel** *"Electron Microscopy and the Unsolved Problem Of Extracellular Vesicle Isolation"*
10:00-10:30	**Eric Van Cappellen** *"Electron Beam Damage Mitigation Strategies"*
10:30-11:00	**Coffee Break**
11:00-12:00	**Oral Session 5** **Chair:** Vuk Radmilović
11:00-11:15	**Daniel Mijailović** *"Mesoporous Carbon Nanofibers and Spinel Oxide Nanocomposites for Energy Storage Applications"*
11:15-11:30	**Ruomu Zhang** *"ADF/EDS/EELS Characterization of Spontaneous Cathode/Electrolyte Reaction In Air- and Beam-sensitive Solid-state Li-ion batteries"*
11:30-11:45	**Mila Krstajić-Pajić** *"Characterization of Coated Ni foam Electrodes for Industrial Hydrogen Production"*
11:45-12:00	**Andjelika Bjelajac** *"Carbon Nanotubes Thin Films with Zn, Fe Oxides and Sulphides"*
12:00-13:30	**Awards, Closing Ceremony & Farewell Cocktail**

POSTER SESSION 1

Monday, August 22nd 2022, 16:00-17:30h

• **PO1.1**

The Importance of Transmission Electron Microscopy for the Identification of Ultrastructural Changes in Non-Alcoholic Fatty Liver Disease

Tatjana Radosavljević[1], Milena Vesković[1], Milica Labudović-Borović[2], Jelena Jadžić[3], Dušan Mladenović[1], Danijela Vučević[1]

1 Institute of Pathophysiology, Faculty of Medicine, University of Belgrade, Belgrade, Serbia
2 Institute of Histology and Embriology, Faculty of Medicine, University of Belgrade, Belgrade, Serbia
3 Institute of Anatomy, Faculty of Medicine, University of Belgrade, Belgrade, Serbia

• **PO1.2**

Ultrastructural Analysis of Lymphocyte Nuclei in Type 2 Diabetes Mellitus

Tamara Martinovic[1], Darko Ciric[1], Katarina Lalic[2], Iva Rasulic[2], Danica Djuricic[3], Vladimir Bumbasirevic[1,4], Tamara Kravic-Stevovic[1]

1Institute of Histology and Embryology, School of Medicine, University of Belgrade, Serbia
2 Clinic for Endocrinology, Diabetes and Metabolic Disease, Clinical Center of Serbia, School of Medicine, University of Belgrade, Serbia
3 Health Center “Savski Venac”, Belgrade, Serbia
4 Serbian Academy of Sciences and Arts, Belgrade, Serbia

• **PO1.3**

Euchromatin to heterochromatin ratio in the lymphocyte nuclei of patients with type 2 diabetes and hyperlipidemia

Tamara Kravic-Stevovic[1], Tamara Martinovic[1], Darko Ciric[1], Katarina Lalic[2], Iva Rasulic[2], Danica Djuricic[3], Vladimir Bumbasirevic[1,4]

1Institute of Histology and Embryology, School of Medicine, University of Belgrade, Serbia
2 Clinic for Endocrinology, Diabetes and Metabolic Disease, Clinical Center of Serbia, School of Medicine, University of Belgrade, Serbia
3 Health Center “Savski Venac”, Belgrade, Serbia
4 Serbian Academy of Sciences and Arts, Belgrade, Serbia

• **PO1.4**

Ultrastructural Analysis of Skeletal Muscle Biopsy in the Diagnosis of MELAS Syndrome in Correlation to the Psychiatric Manifestations of the Disease

Maja Lačković[1,2], Maja Ivković[1,2], Vesna Lačković[2,3], Miloš Bajčetić[2,3], Milica Nestorović[2,4], Aleksandra Pavlović[5]

1 Psychiatry Clinic, University Clinical Center of Serbia, Belgrade, Serbia

2 Faculty of Medicine, University of Belgrade, Belgrade, Serbia
3 Institute of Histology and Embryology, Belgrade, Serbia
4 Institute for Human Genetics, Belgrade, Serbia
5 Faculty for Special Education and Rehabilitation, University of Belgrade, Belgrade, Serbia

• **PO1.5**

Cytotoxic and Genotoxic Effects of Polystyrene Nanoparticles and Microplastics *in vitro*

Marina Gazdic Jankovic[1], Sandra Nikolic[1], Marko Zivanovic[2], Nevena Milivojevic[2], Marina Miletic Kovacevic[3], Olivera Milosevic Djordjevic[1,4], Miodrag Stojkovic[5], Biljana Ljujic[1]

1 Department of Genetics, Faculty of Medical Sciences, University of Kragujevac, Kragujevac, Serbia
2 Laboratory for Bioengineering, Institute of Information Technologies Kragujevac, University of Kragujevac, Kragujevac, Serbia
3 Department of Histology and Embryology, University of Kragujevac, Faculty of Medical Sciences, Kragujevac, Serbia
4 Department of Biology and Ecology, Faculty of Science, University of Kragujevac, Kragujevac, Serbia
5 SPEBO Medical, Fertility Clinic Leskovac, Serbia

• **PO1.6**

Morphology of Waterborne Polyurethanes Based on Poly(dimethylsiloxane)

Ivan S. Stefanović[1], Jasna V. Džunuzović[1,2], Enis S. Džunuzović[3], Andrea Basagni[4] and Carla Marega[4]

1 Institute of Chemistry, Technology and Metallurgy, Center of Chemistry, University of Belgrade, Belgrade, Serbia
2 Institute of Chemistry, Technology and Metallurgy, Center of Excellence in Environmental Chemistry and Engineering, University of Belgrade, Belgrade, Serbia
3 Faculty of Technology and Metallurgy, University of Belgrade, Belgrade, Serbia
4 Department of Chemical Sciences, University of Padova, Padova, Italy

• **PO1.7**

The effect of poly(dimethylsiloxane) segment content on the morphology of polyurethane composite materials

Marija V. Pergal[1], Igor Kodranov[2], Dana Vasiljević-Radović[1], Milos Steinhart[3], Gordana Gojgić-Cijović[1], Dragan Manojlović[2], and Milena Špírková [3]

1 Institute of Chemistry, Technology and Metallurgy, University of Belgrade, Department of Microelectronic Technologies, Belgrade, Serbia
2 Faculty of Chemistry, University of Belgrade, Belgrade, Serbia
3 Institute of Macromolecular Chemistry AS CR, v.v.i. (IMC), Prague, Czech Republic

• **PO1.8**

Establishing of 3D Scaffolds Based on Human Adipose Tissue Extracellular Matrix for *in vitro* Breast Cancer Research

Drenka Trivanović[1], Ivana Drvenica[2], Djordje Veljović[3], Branko Bugarski[3], Diana Bugarski[1] and Aleksandra Jauković[1]

1 Group for Hematology and Stem Cells, Institute for Medical Research, National Institute of Republic of Serbia, University of Belgrade, Serbia
2 Group for Immunology, Institute for Medical Research, National Institute of Republic of Serbia, University of Belgrade, Serbia
3 Faculty of Technology and Metallurgy, University of Belgrade, Belgrade, Serbia

• **PO1.9**

Application of Scanning Electron Microscopy in the Analysis of Tissue Response to Implanted Collagen-based Biomaterials

Sanja Stojanović[1,2], Milena Radenković[2] and Stevo Najman[1,2]

1 Department of Biology and Human Genetics, Faculty of Medicine, University of Niš, Niš, Serbia
2 Department for Cell and Tissue Engineering, Scientific Research Center for Biomedicine, Faculty of Medicine, University of Niš, Niš, Serbia

• **PO1.10**

Influence of Post-Synthesis Treatments on the Properties of Brushite/Monetite Powders

Željko Radovanović[1], Lidija Radovanović[1], Aleksandar Kremenović[2], Đorđe Janaćković[3] and Rada Petrović[3]

1 Innovation Center of Faculty of Technology and Metallurgy, Belgrade, Serbia
2 University of Belgrade, Faculty of Mining and Geology, Belgrade, Serbia
3 University of Belgrade, Faculty of Technology and Metallurgy, Belgrade, Serbia

• **PO1.11**

Hydroxyapatite Reinforced Poly(methacrylic acid)/Gelatin Interpenetrating Network Hydrogels for Drug Delivery Applications

Vukasin Ugrinovic[1], Vesna Panic[1], Milica Milutinovic[2], Bojan Bozic[3], Rada Petrovic[4], Djordje Janackovic[4] and Djordje Veljovic[4]

1 Innovation Center of Faculty of Technology and Metallurgy, University of Belgrade, Belgrade, Serbia
2 Department of Biochemical Engineering and Biotechnology, Faculty of Technology and Metallurgy, University of Belgrade, Belgrade, Serbia
3 Institute of Physiology and Biochemistry „Ivan Đaja“, University of Belgrade, Belgrade, Serbia
4 Department of Inorganic Chemical Technology, Faculty of Technology and Metallurgy, University of Belgrade, Belgrade, Serbia

• **PO1.12**

Hydroxyapatite-based Bioceramic Dental Inserts as Dentin Substitutes

Tamara Matić[1], Maja L. Zebić[2], Vesna Miletić[3], Rada Petrović[4], Djordje Janaćković[4], Djordje Veljović[4]

1 Innovation Center of the Faculty of Technology and Metallurgy Ltd, Belgrade, Serbia
2 University of Belgrade, School of Dental Medicine, Belgrade, Serbia
3 The University of Sydney, Faculty of Medicine and Health, Sydney Dental School, Surry Hills NSW, Australia
4 University of Belgrade, Faculty of Technology and Metallurgy, Belgrade, Serbia

• **PO1.13**

Synthesis and Characterization of ZnO Deposited on Hydroxyapatite for Dental Application

Marija Stevanović[1], Marija Milivojević[1], Rada Petrović[2], Đorđe Veljović[2], Suzana Dimitirijević[2], Đorđe Janaćković[2]

1 Innovation Center of the Faculty of Technology and Metallurgy, Belgrade, Serbia
2 University of Belgrade, Faculty of Technology and Metallurgy, Belgrade, Serbia

• **PO1.14**

TEM Study on the Nanostructure Change of Primary Dental Enamel Subjected to Mechanical and Chemical Surface Modifications

Viktória K. Kis[1], Attila Sulyok[1], Máté Hegedűs[2], Noémi Rózsa[3] and Zsolt Kovács[2]

1 Centre for Energy Research, Budapest, Hungary
2 Department of Materials Physics, Eötvös Loránd University, Budapest, Hungary
3 Department for Pedodontics and Orthodontics, Semmelweis University, Budapest, Hungary

• **PO1.15**

Synthesis of Silica Fibers from Natural Asbestos by Acid Leaching Procedure

Branko Matović[1], Jelena Maletaškić[1], Nadežda Radmilović[1], Nina Daneu[2], Biljana Babić[1], Jelena Ercić[1], Milovan Stoiljković[1]

1 Vinča Institute of Nuclear Sciences, National Institute of Republic of Serbia, University of Belgrade, Belgrade, Serbia
2 Department for Nanostructured Materials, Jozef Stefan Institute, Ljubljana, Slovenia

• **PO1.16**

Effect of concentration pigment particles on microstructure of the metal matrix copper composite coatings

Ivana Mladenović[1], Nebojša D. Nikolić[1], Jelena Lamovec[2], Dana Vasiljević Radović[1] and Vesna Radojević[3]

1 University of Belgrade, Institute of Chemistry, Technology and Metallurgy, Belgrade, Serbia
2 University of Criminal Investigation and Police Studies, Belgrade, Serbia
3 Faculty of Technology and Metallurgy, University of Belgrade, Belgrade, Serbia

• **PO1.17**

The Microstructure Evolution of AA6026 Al-Mg-Si alloy during Homogenization

Tamara Radetić and Miljana Popović

University of Belgrade, Faculty of Technology and Metallurgy, Belgrade, Serbia

• **PO1.18**

Microstructural study of hematite formation during extraction of valuable metals from Jarosite PbAg sludge

Nataša Gajić[1], Željko Kamberović [2], Marija Korać[2], Milisav Ranitović[1], Vaso Manojlović[2]

1 Innovation Center of the Faculty of Technology and Metallurgy University of Belgrade, Belgrade, Serbia
2 Faculty of Technology and Metallurgy, University of Belgrade, 11120 Belgrade, Serbia

• **PO1.19**

Detecting the Changes on Fibers' Surfaces after Different Chemical Treatments using Scanning Electron Microscopy

Aleksandra Ivanovska[1], Mirjana Kostić[2]

1 University of Belgrade, Innovation Center of the Faculty of Technology and Metallurgy, Department for Textile Engineering, Belgrade, Serbia
2 University of Belgrade, Faculty of Technology and Metallurgy, Department for Textile Engineering, Belgrade, Serbia

• **PO1.20**

Gain the maximum throughput with artifact-free surfaces for sample characterization by using high current plasma FIB-SEM

Martin Suchanek

TESCAN ORSAY HOLDING, a.s.

POSTER SESSION 2

Thursday, August 25th 2022, 15:30-17:00h

• PO2.1

Mesoporous Carbon Nanofibers and Spinel Oxide Nanocomposites for Energy Storage Applications

Daniel M. Mijailović[1], Vuk V. Radmilović[2], Uros Č. Lačnjevac[3], Dusica B. Stojanović[2], Vladimir D. Jović[3], Velimir R. Radmilović[2,4] and Petar S. Uskoković[2]

1 University of Belgrade, Innovation Center, Faculty of Technology and Metallurgy, Belgrade, Serbia
2 University of Belgrade, Faculty of Technology and Metallurgy, Belgrade, Serbia
3 University of Belgrade, Institute for Multidisciplinary Research, Belgrade, Serbia
4 Serbian Academy of Sciences and Arts, Belgrade, Serbia

• PO2.2

Nickel manganite-carbonized alginate composite for use as energy storage electrodes

Milena Dojcinovic[1], Zorka Vasiljevic[1], Nenad Tadic[2], Matjaz Spreitzer[3], Lazar Rakocevic[4], Maria Vesna Nikolic[1]

1 University of Belgrade, Institute for Multidisciplinary Research, Department for Materials Science, Belgrade, Serbia
2 University of Belgrade, Faculty of Physics, Belgrade, Serbia
3 Jozef Stefan Institute, Ljubljana, Slovenia
4 University of Belgrade, Institute of Nuclear Sciences Vinca, Belgrade, Serbia

• PO2.3

Sodium-pillared vanadium oxide decorated with carbon particles as electrode material for more sustainable energy storage of the future

Milica Vujković[1], Tamara Petrović[1], Dušan Mladenović[1], Miloš Milović[2], Danica Bajuk-Bogdanović[1], Biljana Šljukić-Paunković[1], Slavko Mentus[1,3]

1 University of Belgrade, Faculty of Physical Chemistry, Belgrade and Serbia
2 Institute of Technical Sciences of Serbian Academy of Sciences and Arts, 11000 Belgrade, Serbia
3 Serbian Academy of Sciences and Arts, Belgrade, Serbia

• PO2.4

Sol-gel Synthesis of $MgMn_2O_4$ and $MgCr_{0.15}Mn_{1.85}O_4$

Nikolina Jokić[1], Dragana Jugović[2], Srečo Škapin[3], Ivana Stojković Simatović[4]

1 Institute Mol, Stara Pazova, Serbia
2 SASA Institute of Technical Sciences, Belgrade, Serbia
3 Institute Jožef Stefan, Ljubljana, Slovenia

4 Faculty of Physical Chemistry, Belgrade, Serbia

• **PO2.5**

Characterizing Graphene Supported PtAu and PdAu Nanoparticles with SEM, TEM and XPS for use as Catalysts for Hydrogen Evolution Reaction

Lazar Rakočević[1], Irina Srejić[1], Aleksandar Maksić[1], Vladimir Rajić[1], Mirjana Novaković[1], Svetlana Štrbac[2]

1 INS Vinča, Department of Atomic Physics, University of Belgrade, Belgrade, Serbia
2 Institute of Chemistry, Technology and Metallurgy, Department of Electrochemistry, University of Belgrade, Belgrade, Serbia

• **PO2.6**

Electrodeposited Platinum Group Metals Catalysts on Max Phases Based Support for Hydrogen Energy Related Applications

Nevenka R. Elezovic[1], Uros Lacnjevac[1], Mila Krstajic Pajic[2], Piotr Zabinski[3], Vladimir Jovic[1]

1 University of Belgrade Institute for Multidisciplinary Research, Belgrade, Serbia
2 University of Belgrade Faculty of Technology and Metallurgy, Belgrade Serbia
3 AGH University of Science and Technology, Faculty of Non-Ferrous Metals, Krakow, Poland

• **PO2.7**

Characterization of Coated Ni foam Electrodes for Industrial Hydrogen Production

Jelena Gojgić[1], Aleksandar Petričević[1], Thomas Rauscher[2], Christian Bernaecker[2], Mila Krstajić Pajić[1], and Vladimir Jović[3]

1 University of Belgrade, Faculty of Technology and Metallurgy, Belgrade, Serbia
2 Fraunhofer Institute for Manufacturing Technology and Advanced Materials IFAM, Branch Lab Dresden, Germany
3 University of Belgrade, Institute of Multidisciplnary Research, Belgrade, Serbia.

• **PO2.8**

Cu_{upd}@Pd/C and Pd-Cu/C Nanocatalysts for Electrochemical Ethanol Oxidation in Alkaline Solution

Maja D. Obradović[1], Jelena R. Rogan[2], Uroš Č. Lačnjevac[3], Aleksandra Gavrilović-Wohlmuther[4], Vuk V. Radmilović[2], Velimir R. Radmilović[2,5], Snežana Lj. Gojković[2]

1 University of Belgrade, Institute of Chemistry, Technology and Metallurgy, Belgrade, Serbia
2 University of Belgrade, Faculty of Technology and Metallurgy, Belgrade, Serbia
3 University of Belgrade, Institute for Multidisciplinary Research, Belgrade, Serbia
4 Schoeller-Bleckmann Nitec GmbH, Ternitz, Austria
5 Serbian Academy of Sciences and Arts, Belgrade, Serbia

• **PO2.9**

Development of the Low-cost Carbon-based Mid-IR Transparent Electrode

Sara Joksović[1], Jovana Stanojev[1], Branimir Bajac[1], Vladimir V. Srdić[2]

1 BioSense Institute, University of Novi Sad, Novi Sad, Serbia
2 Faculty of Tecnology Novi Sad, University of Novi Sad, Novi Sad, Serbia

• **PO2.10**

Thin Film Polyaniline/Silver Nanowires Nanocomposites for Optoelectronic Applications

Jovan Lukic and Vuk V. Radmilovic

Faculty of Technology and Metallurgy, University of Belgrade, Belgrade, Serbia

• **PO2.11**

Improving the contact surface between TiO_2 nanotubes and $MAPbBr_3$ to make perovskite solar cells

Milica Stefanović[1], Ivana Lukić[2], Jelena Vujančević[3], Rada Petrović[2] and Đorđe Janaćković[2]

1 Innovation Center of Faculty of Technology and Metallurgy, Belgrade, Serbia
2 University of Belgrade, Faculty of Technology and Metallurgy, Belgrade, Serbia
3 Institute of Technical Sciences of SASA, Belgrade, Serbia

• **PO2.12**

Synthesis of Up-converting β-$NaYF_4$:Yb/Er Nanoparticles by Low-temperature Sonochemical Method

Ivana Dinić[1], Marina Vuković[2], Paula Jardim[3] and Lidija Mančić[1]

1 Institute of Technical Sciences of SASA, Belgrade, Serbia
2 Innovative Centre, Faculty of Chemistry, University of Belgrade, Serbia
3 Department of Metallurgical and Materials Engineering, Federal University of Rio de Janeiro, Rio de Janeiro, Brazil

• **PO2.13**

Scanning and Transmission Electron Microscopy Investigation of $SrGd_2O_4$: Yb,Tm Up-conversion Luminescent Material

Tijana Stamenković[1], Ivana Dinić[2], Marina Vuković[2], Vladimir Rajić[1], Nadežda Radmilović[1], Lidija Mančić[2], Vesna Lojpur[1]

1 Vinča Institute of Nuclear Sciences, National Institute of the Republic of Serbia, University of Belgrade, Belgrade, Serbia.
2 Institute of Technical Science of SASA, Belgrade, Serbia.

• **PO2.14**

Different Up-conversion Oxides Co-doped with Er^{3+}/Yb^{3+} Synthesized at High Temperatures

Nadežda Radmilović[1], Tijana Stamenković[1], Vesna Lojpur[1], Ivana Dinić[2], Lidija Mančić[2]

1 Vinča Institute of Nuclear Sciences, National Institute of the Republic of Serbia, University of Belgrade, Department for atomic physics, Belgrade, Serbia
2 Institute of Technical Science of SASA, Belgrade, Serbia

• **PO2.15**

Carbon quantum dots-assisted CdS/TiO_2 heterojunction for photocatalytic reduction of hexavalent chromium under visible light

Jana Petrović[1], Slavica Lazarević[1], Nemanja Barać[2], Vukašin Ugrinović[2], Đorđe Janaćković[1] and Rada Petrović[1]

1 University of Belgrade, Faculty of Technology and Metallurgy, Belgrade, Serbia
2 Innovation Center of Faculty of Technology and Metallurgy, Belgrade, Serbia

• **PO2.16**

Structural Properties of $CaCu_3Ti_3RuO_{12}$

Smilja Marković[1], Ljiljana Veselinović[1], Lidija Mančić[1] and Paula M. Jardim[2]

1 Institute of Technical Sciences of SASA, Belgrade, Serbia
2 Department of Metallurgical and Materials Engineering, Federal University of Rio de Janeiro, Rio de Janeiro, Brazil

• **PO2.17**

Multilayer and Epitaxial Multiferroic Thin Films Prepared by Solution Deposition Technique

Danica Piper[1], Jelena Vukmirović[1], Branimir Bajac[2], Sara Joksović[2], Miloš Bokorov[3], Andrea Nesterović[1], Ivan Stijepović[1], Marija Milanović[1], Elvira Toth[4], Željka Cvejić[4], Vladimir V. Srdić[1]

1 Faculty of Technology, Department of Materials Engineering, University of Novi Sad, Serbia
2 BioSense Institute, University of Novi Sad, Serbia
3 Faculty of Sciences, Department of Biology and Ecology, University of Novi Sad, Serbia
4 Faculty of Sciences, Department of Physics, University of Novi Sad, Serbia

• **PO2.18**

Nanodomain Structure and Charged Domain Walls in Single Crystal $BiFeO_3$

Wanbing Ge[1], Quentin Ramasse[2], Richard Beanland[1], Marin Alexe[1], Ana Sanchez[1]

1 Department of Physics, University of Warwick, Coventry, United Kingdom
2 SuperSTEM Laboratory, SciTech Daresbury, Warrington, United Kingdom

• **PO2.19**

Cobalt Ferrite Nanospheres for Removal of Cr^{6+} Ions from Waste Water

Sonja Jovanović, Željko Mravik, Jelena Rmuš, Marija Grujičić, Marko Jelić, Milica Pejčić, Zoran Jovanović

Laboratory of Physics, Vinča Institute of Nuclear Sciences, National Institute of the Republic of Serbia, University of Belgrade, Belgrade, Serbia

• **PO2.20**

Influence of Plasmon-excitation Electrons on Ptychography Phase Imaging

Zhiyuan Ding[1], Angus I. Kirkland[1,2,3], and Peter D. Nellist[1]

1 Department of Materials, University of Oxford, Oxford, UK
2 Electron Physical Sciences Imaging Centre, Diamond Light Source Ltd., Harwell Science and Innovation Campus, Didcot, UK
3 The Rosalind Franklin Institute, Harwell Campus, Didcot, UK

• **PO1.21**

Atomic Scale Observations and Analysis of the Island Grain Shrinkage in <110> Au Thin Films

Tamara Radetić[1] and Ulrich Dahmen[2]

1 University of Belgrade, Faculty of Technology and Metallurgy, Belgrade, Serbia
2 Molecular Foundry - NCEM, LBNL, Berkeley, USA

PLENARY PRESENTATIONS

Making Optoelectronic Devices from Large-Area Transfer-Free MOCVD Graphene: Magnetic Hall Sensors and OLEDs: Electron Microscope Challenges

Colin Humphreys[1,2], Hugh Glass[2] and Zhichao Weng[1,2]

1 School of Engineering and Materials Science, Queen Mary University of London, Mile End Road, London E1 4NS, UK.

2 Paragraf Ltd, Somersham, 7-8 West Newlands, Cambs PE28 3EB, UK

Many impressive graphene electronic devices have been made in laboratories worldwide, using small flakes of exfoliated graphene and assembling the devices by hand. However, it has been difficult to scale up to manufacturing graphene electronic devices. Hence these impressive graphene devices largely remain at the laboratory level. We have scaled-up to produce graphene and graphene devices using a new growth method, metal organic chemical vapour deposition (MOCVD). This method is large-area, catalyst-free and transfer-free. It is promising for the manufacture of graphene devices and in this talk we will show some recent results for graphene Hall-effect sensors and graphene OLEDs.

Hall sensors are extremely widely used for measuring magnetic fields, electric currents, the speed of motors, etc. For example, a typical car contains from 20 to 50 Hall sensors. Silicon is the most widely used Hall sensor. It has a room-temperature sensitivity of typically 70 V/AT. The best Hall sensor, using a semiconductor quantum well, has a room-temperature sensitivity of about 1000 V/AT. The most sensitive graphene Hall sensor has a room-temperature sensitivity of 2000 V/AT and is one of a range of graphene Hall sensors being manufactured by Paragraf. In addition, Paragraf makes a graphene Hall sensor that operates at cryogenic temperatures down to less than 1 K, making it useful for dilution refrigerators and quantum computers.

Paragraf has produced a graphene Hall sensor that operates at very high magnetic fields, up to 30 T, making it suitable for use in next-generation fusion reactors. Semiconductor Hall sensors fail at fields above a few Tesla. Because the active element of our Hall sensor is the thinnest material in the world, a single layer of carbon atoms, it has a negligibly small planar Hall effect, making it insensitive to stray fields. It has an extremely low power consumption of pW, one hundred times less than the power consumption of a silicon Hall sensor. In addition, its resolution is in parts per billion.

Organic light emitting diodes (OLEDs) are widely used as the displays in smartphones, TVs, etc. They usually have indium tin oxide (ITO) as the transparent conducting electrode. However, indium is one of the nine rarest elements in the earth's crust. Indium is on the EU list of Critical Materials, and more than 50% comes from one country. Indium is widely used, and the EU states: "Indium has an irreplaceable role in industry and society." Most homes have many items that contain indium, for example, LED lights, where the light emission is from InGaN quantum wells.

QMUL and Paragraf have fabricated an OLED with graphene replacing the ITO electrode. Our graphene-OLED has an identical performance (in fact, slightly better) than our ITO-OLED, fabricated under the same conditions, demonstrating the potential for graphene to replace the unsustainable ITO [1].

The successful MOCVD-grown graphene devices raise the expectation that a wide range of graphene optoelectronic devices may be manufacturable and transformative, thus helping to fulfil the original expectations that graphene would hugely benefit society. A detailed understanding of the structure

and electronic properties of atomic-level defects in MOCVD graphene and other 2D materials is now required to manufacture optimised graphene/2D devices, including biosensors and solid-state devices such as transistors. Electron microscopy will play an essential role in this, and initial results will be presented at the conference [2].

References:

[1] Z Weng *et al,* Adv. Optical Mater. **10** (2022), 2101675
[2] The authors acknowledge funding from the Engineering and Physical Sciences Research Council UK and from Innovate UK.

The role of atomic structure of interfaces and defects in thin films heterostructures for spintronic applications

Vlado Lazarov[1], Barat Achinuq[2], Arsham Ghasemi[1], Zlatko Nedelkovski, Pedro Galindo, Leonardo Lari[1], Thorsten Hesjedal[2], Demie Kepaptsoglou[1,4], Lian Li[5], Kohei Hamaya[6] and Mike Weinert[5]

1 Department of Physics, University of York, York YO10 5DD, UK
2 Department of Physics, Clarendon Laboratory, University of Oxford, Oxford OX1 3PU, UK 3 Department of Computer Science and Engineering, Universidad de Cádiz, 11510 Puerto Real, Spain
4 SuperSTEM Laboratory, SciTech Daresbury Campus, Daresbury WA4 4AD, United Kingdom
5Department of Physics, University of Wisconsin, Milwaukee, WI 53211, USA

Spintronics is burgeoning field in the nanoscience that has attracted a lot of attention in the last decade due to its potential to revolutionize CMOS based logic and data devices, by utilising the electron spin. Spin manipulation via spin currents generation, propagation, as well as spin injection and detection are key steps for realization of fast, non-volatile and increasingly important low power computational devices. The successful realization of these goals are rather challenging since it requires atomic level control of interfaces and thin film structures in multilayered heterostructures that can consist of both ferromagnetic and antiferromagnetic alloys and oxides, semiconductor layers, halfmetals, as well as topological insulators, for example.

In this work, by utilising advanced electron microscopy techniques such as Scanning Transmission Electron Microscopy (STEM), Electron Energy Loss Spectroscopy (EELS), Energy Dispersive X-Ray, as well as Scanning Tunneling Microscopy and Spectroscopy (STM and STS), we will present an overview of correlation between atomic structure and functionality of thin films and heterostructures, with focus on the role of various inhomogeneities such as interfaces, grain boundaries, point defects, and strain. Firstly we will discuss how to optimize atomic chemical ordering in full Co based Heusler alloys (i.e. $Co_2FeAlSi$-CFAS), in order to achieve close to 100% spin polarization in thin films, and how to control the interfaces with Si and Ge to achieve maximum spin injection (Figure 1 and 2). We will show that spin polarization is critically dependent on the chemical ordering of each of sublattices of CFAS, and that the spin injection is inherently not possible even in atomically abrupt $Co_2FeAlsSi$/Si(111) systems, while $Co_2FeAlSi$/Ge(111) heterostructures are distinctively better and less sensitive to both structural and chemical abruptness at the interfaces [1, 2]. Second part will focus on the role of the strain in controlling the topological states in the prototype Bi_2Se_3 3D topological insulator, where tensile strain leads to opening the band gap at the topologically protected surface states [3]. Furthermore on example of Bi_2eTe_3/Ge(111) we will show that Van der Waals type of heterointerfaces can accommodate large amount of stress without developing misfit dislocations, and that Heusler alloys both via atomically abrupt and crystalline interface (i.e. CFAS/$BaTiO_3$) as well as amorphous (CFAS/PMN-PT) can magneto elastically couple, hence magnetisation control by strain can be achieved [4,5].

References:
[1] B Kuerbanjiang, Y Fujita, M Yamada, S Yamada *et al*, Phys. Rev. B, **98** (2018), 115304
[2] Z Nedelkoski, B Kuerbanjiang, SE Glover, AM Sanchez, Scientific reports **6**, (2016), p.1
[3] Y Liu, YY Li, S Rajput, D Gilks, L Lari, *et al*, Nature Physics, **10** (4), (2014), p. 294
[4] K Nawa, D Kepaptsoglou, A Ghasemi, P Hasnip *et al*, Phys. Rev. Materials **5** , (2021) 024203
[5] S Fujii, T Usami, Y Shiratsuchi, AM Kerrigan, *et al*, NPG Asia Materials **14** (2021), p.1

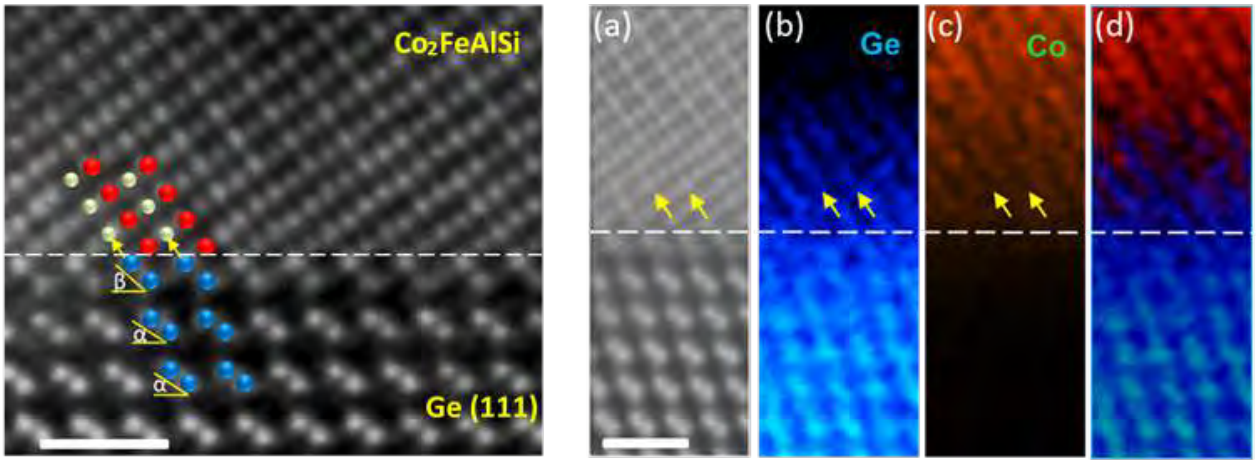

Figure 1. Left: Atomic resolution HAADF STEM image of the interface showing that the CFAS film terminates on a Co(111) atomic plane. The colour coding is as follows: Ge –blue; Co –red; Fe-Si/Al –grey. The white scale-bar corresponds to 0.7 nm. The tilt angle of the Ge dumbbells from $\alpha = 37°$ in the bulk-like region increases to $\beta = 51°$ for the interfacial Ge bilayer. **Right:** EDXS chemical mapping across the interface. (a) HAADF STEM image acquired simultaneously with the EDXS maps which serves as a reference image. The white scale-bar corresponds to 0.7 nm. (b) Ge Kα edge map showing the selective outdifussion of Ge across the reference interface plane (white dashed line). Yellow arrows are inserted as a guide to the eye. (c) Co Kα edge map showing the abrupt decrease of the Co signal across the interface. (d) Ge and Co overlaid map clearly showing the out-diffused Ge atoms in the Fe-Si/Al atomic planes which are in-between the Co(001) planes.

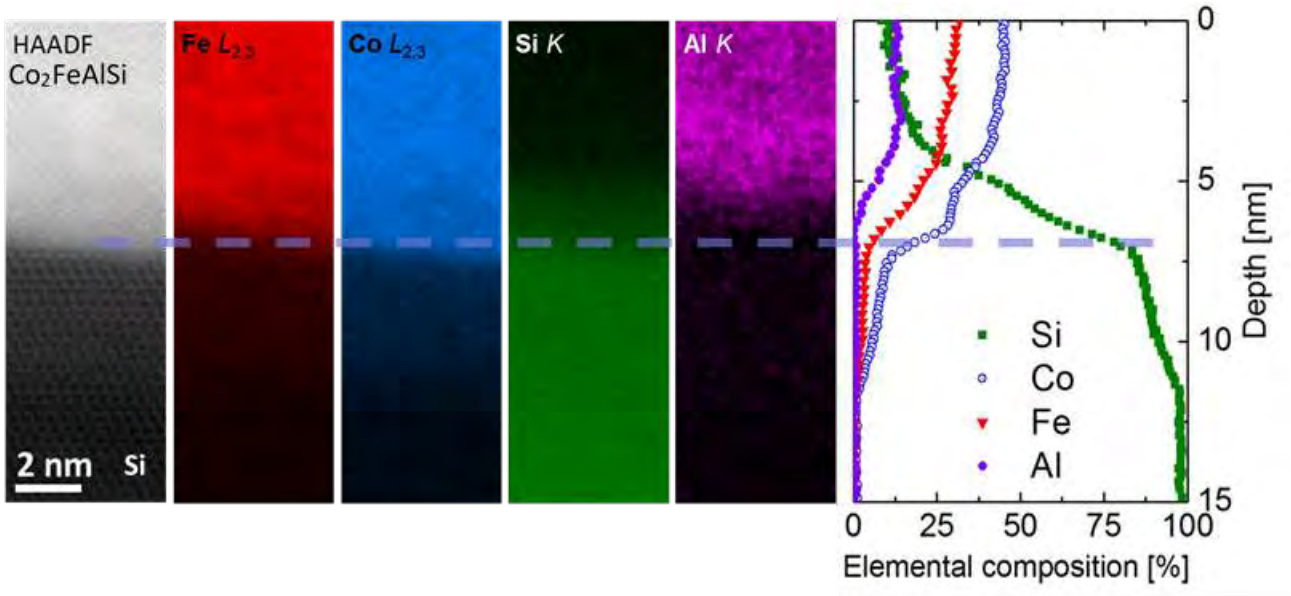

Figure 2. Atomic resolution HAADF from $Co_2FeAlSi$/Si (111) interface region outlining the region for which chemical map of all elements by EELS is presented. Outdiffusion between the film elements and substrates is present even though the films were grown at room temperature.

Monochromated Electron Energy Loss Spectroscopy in the Scanning Transmission Electron Microscope at High Spatial Resolution

Quentin M. Ramasse[1,2], Fredrik S. Hage[1,3], Matthieu Bugnet[1,4], Demie M. Kepaptsoglou[1,5]

1 SuperSTEM Laboratory, SciTech Daresbury, Keckwick Lane, Daresbury WA4 4AD, UK
2 School of Physics and Astronomy & School of Chemical and Process Engineering, University of Leeds, Leeds LS2 9JT, UK
3 Department of Physics, University of Oslo, Oslo, Norway
4 Univ Lyon, CNRS, INSA Lyon, UCBL, MATEIS, UMR 5510, 69621 Villeurbanne, France
5 York NanoCentre & Department of Physics, University of York, York YO10 5DD, UK

Instrumentation advances have pushed the energy resolution of electron energy loss spectroscopy (EELS) in monochromated scanning transmission electron microscopes (STEMs) into the meV range, all the while retaining atomic-sized probes and thus truly realizing the promise of placing a 'synchrotron in a microscope' [1]. This now allows for probing the chemical and electronic structure of a wide range of materials systems with unprecedented detail, from the core-loss to the vibrational spectroscopy regimes. This contribution will review a number of recent developments achieved using a monochromated Nion UltraSTEM100 MC across the energy loss scale.

The energy loss near-edge structure (ELNES) arising from core-level excitation provides a wealth of information on chemical bonding between atoms, and can be interpreted by first-principles calculations in favourable cases. Here, the increased sensitivity and resolution of instruments equipped with new-generation monochromators were used to obtain real-space maps of π^* and σ^* states in epitaxial graphene multilayers observed in side view. ELNES interpretation at the atomic scale relies crucially on understanding how the beam propagation through the sample affects the observed fine structure, using combined multi-slice and density functional theory calculations, and pave the way towards using ELNES to map electronic orbitals in real space: figure 1. [2]

In the low loss regime, a dark field (DF) EELS detection geometry can be used to map atomic scale variations in acoustic and optical phonon excitations in materials, down to atomically thin single-layer graphene. Individual point defects such as a single-atom-dopants substituted in the graphene host lattice (figure 2) can also be shown to have a characteristic vibrational response [3]. Optimising signal levels thanks to highly-sensitive direct electron detectors and to custom-developed annular collection apertures for EELS reveals the emergence of locally resolved fine structure in the phonon spectra. In addition to a direct interrogation of the chemical bonds in a system consisting of Bi_2Se_3 films grown by chemical vapor deposition on epitaxial graphene, it is thought these observations could also be linked to the interplay between the various phonon modes and the Dirac plasmons in the topological insulator Bi_2Se_3.

Finally, the prospects for observing the spectral signature of spin waves, or magnons, arising from the collective excitation of the electrons' spin in a lattice and which qualitatively occupy the same energy range as phonons, are explored through preliminary experiments and the development of a theoretical framework based on the diffuse scattering of electrons due to magnons. [4,5]

References:

[1] Q.M. Ramasse, **180** (2017), pp. 41-51
[2] M. Bugnet et al., Phys. Rev. Lett. **128** (2022), 116401
[3] F. S. Hage et al., Science **367** (2020), aba1136
[4] K. Lyon et al., Phys. Rev. B **104** (2021), 214418
[5] SuperSTEM is the UK National Research Facility for Advanced Electron Microscopy, supported by the Engineering and Physical Sciences Research Council (EPSRC)

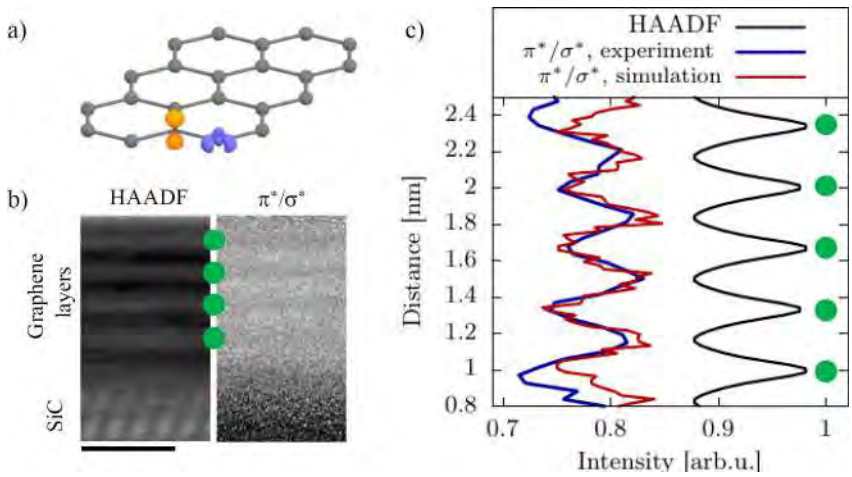

Figure 1. a) Schematic representation of the π* (orange) and σ* (blue) electron densities obtained from density functional theory superimposed on the structural model of a graphene layer. (b) High-resolution STEM-HAADF image of a graphene multilayer grown on SiC acquired simultaneously with a spectrum image. The corresponding π*/ σ* map shows maxima between the carbon layers. Scale bar: 1 nm. (c) Experimental and calculated (inelastic channeling) π*/ σ* profiles extracted from STEM-EELS maps, and corresponding calculated HAADF signal, for a specimen with 25.6 nm projected thickness. The position of the graphene layers is indicated by green circles. Probe size and shot noise corresponding to the experiments were added to the calculated profile.

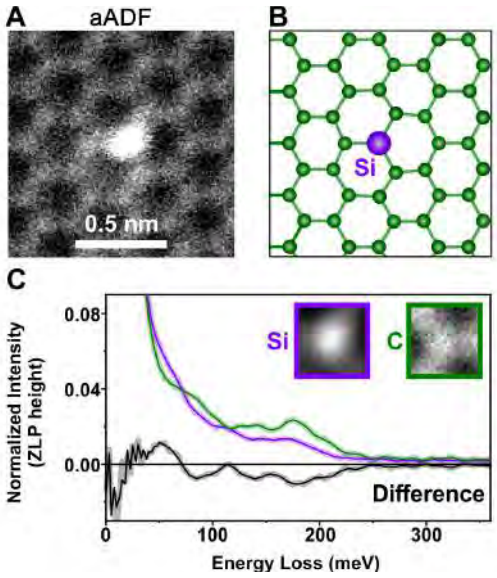

Figure 2. (A) aADF image (thus named due to the off-axis geometry) and (B) model of a single substitutional Si dopant in graphene. (C) Vibrational spectrum of the Si atom ("Si") and of a defect-free part of the graphene a few atoms away from the Si atom ("C"). The difference spectrum is calculated by subtracting the C spectrum from the Si spectrum. [3].

Emergent Phonon Phenomena at Interfaces probed by Vibrational EELS

Chaitanya A. Gadre[1], Xingxu Yan[2] and Xiaoqing Pan[1,2,3]

1 Department of Physics and Astronomy, University of California-Irvine, Irvine, CA 92697
2 Department of Materials Science and Engineering, University of California-Irvine, Irvine, CA 92697
3 Irvine Materials Research Institute, University of California-Irvine, Irvine, CA 92697

Uncovering phonon transport mechanisms is crucial in determining thermal conductivity in materials. Phonon transport can be greatly modulated by nanostructures, interfaces, and defects. Interfaces between two differing materials can scatter phonons efficiently. In addition, interface modes are known to increase thermal conductivity by providing an intermediate mode to facilitate transport of phonons between different materials [1]. However, this requires detailed study of the nanoscale physics and has hardly been explored by experimental means. The phonon resistance provided by these structures are often a result of a mismatch between the local phonon density of states (LDOS) [1], studies of which have eluded optical measurement techniques due to their insufficient spatial resolution and cannot aid in the physical understanding of nanoscale thermal transport. However, recent developments in electron microscopy have enable the acquisition of vibrational spectra with few-meV energy resolution and down to sub-ångström spatial resolution [2,3]. In this work, we demonstrate a mapping of phonons revealing an interface mode at the Si-Ge interface and phonon dynamics of SiGe quantum dots (QDs).

Fig. 1A shows an atomic resolution HAADF image of an atomically sharp Si-Ge interface acquired using a 33-mrad convergence semi-angle probe. Representative electron energy-loss spectra (EELS) in Fig. 1B show distinct spectral features of Ge, Si-Ge interface, and Si vibrational modes including the optical phonon modes of Si and Ge at 60 meV and 34 meV, respectively, as well as low-energy acoustic phonon modes. The contour plot in Fig. 1C reveals an abrupt transition between the vibrational structures of Ge and Si and reveals an interfacial mode at the interface at around 48 meV which cannot be ascribed to the bulk phonon modes of either Si or Ge or be fitted by their linear combination [4]. This is more clearly demonstrated by the line profile in Fig. 1D and reveals that the 48-meV interface mode is confined to within a 1.3 nm of the interface.

The abruptness of the interface between Si-Ge correlates to the spatial extent of the interface modes as well as affect phonon transmission and reflection properties. The growth mechanism of SiGe quantum dots (QDs) produces two types of interfaces that form the boundary of the QDs: a gradual interface at the top and an abrupt one at the bottom [5]. To see the effect of various interfaces on phonon transport, we employ a 3 mrad convergence semi-angle probe to enable the investigation of phonon modes at specific points in momentum space within the first Brillouin zone (FBZ). Additionally, post-specimen lenses are utilized to collect the scattered, off-axis beam at different locations in momentum space. By taking the difference of forward and backward propagating modes, net momentum information i.e., direction of propagation, is obtained. Utilizing this novel technique, the differential momentum mapping reveals that there is indeed a strong reflection from the abrupt interface while the gradual interface provides a weaker directionality. The abrupt change in LDOS creates an environment where propagating Si optical modes experience a shortage of corresponding modes on the other side of the interface, leading to a reflection. By utilizing averaged and resolved momentum conditions, phonon momenta can be imaged to obtain information about phonon propagation at the nanometer scale [5].

Our work unveils the non-equilibrium phonon dynamics at nanoscale interfaces and can be used to study actual nanodevices and aid in the understanding of heat dissipation near nanoscale hotspots, which is crucial for future high-performance nanoelectronics [6].

References:

[1] E. T. Swartz, and R. O. Pohl. *Reviews of modern physics* 61.3 (1989): 605.
[2] O. L. Krivanek, et al. Nature 514.7521 (2014): 209.
[3] F. S. Hage, et al. *Physical review letters* 122.1 (2019): 016103.
[4] Z. Cheng, R. Y. Li, and X. Yan et al., Nat. Commun. 12 (2021), p. 6901
[5] C. A. Gadre et al. *Nature* (2022). DOI: 10.1038/s41586-022-04736-8.
[6] This work was supported primarily by the Department of Energy (DOE), Office of Basic Energy Sciences, Division of Materials Sciences and Engineering under grant no. DE-SC0014430, and by the National Science Foundation Materials Research Science and Engineering Center program through the UC Irvine Center for Complex and Active Materials (DMR-2011967).

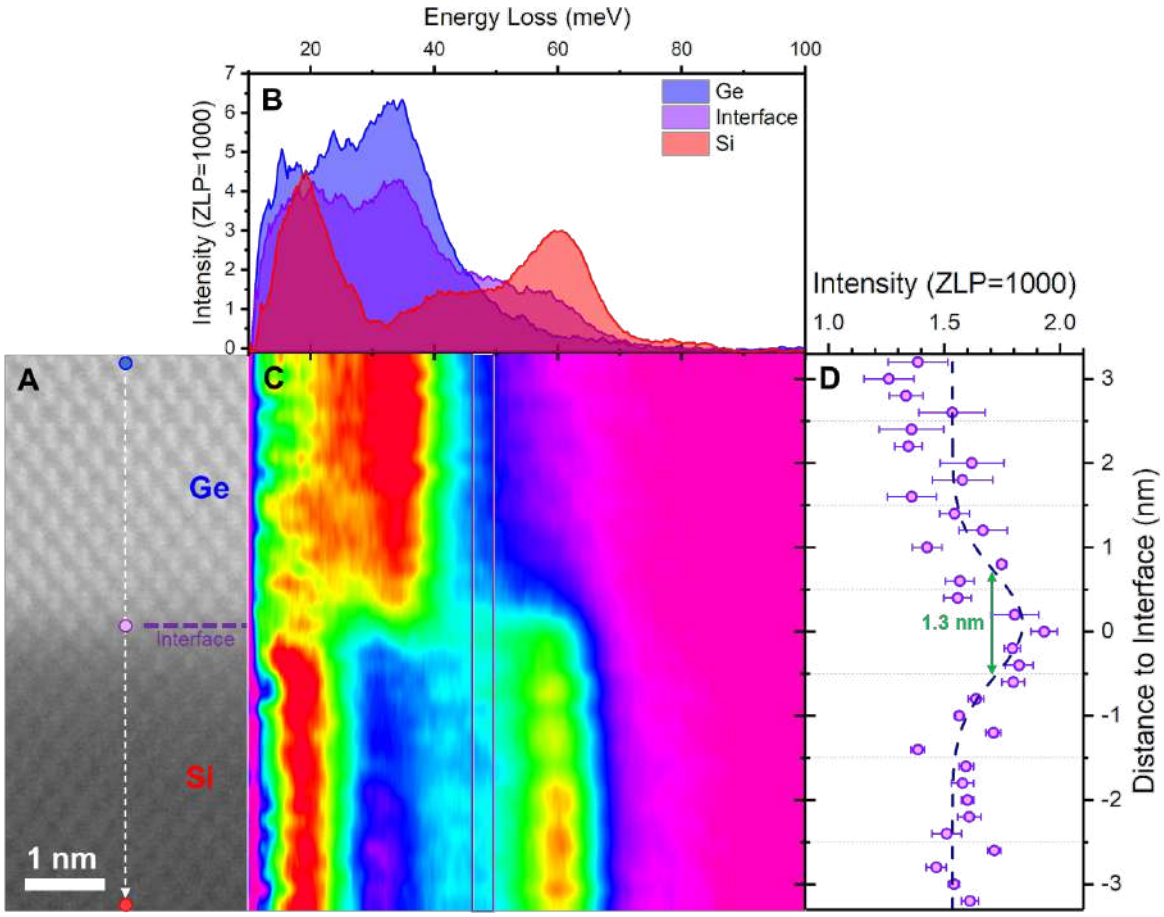

Figure 1. Vibrational spectra across a Si-Ge interface under a 33mrad, on-axis beam-detector geometry**. A**. [110]-zone-axis HAADF STEM image of the Si-Ge interface. Scale bar: 1 nm. **B**. Representative vibrational spectra of Ge, Si-Ge interface, and Si at locations marked in **A** by the blue, purple, and red circles, respectively. **C**. Spectral contour plot of spatially resolved vibrational spectra along the direction denoted by the white arrow in **A**. **D**. Line profile of spectral intensity at 48 meV in **C**, overlaid with a Gaussian fit.

Electron microscopy and spectroscopy of low-dimensional hybrid materials

Kazu Suenaga

ISIR-SANKEN, Osaka University, 567-0047, Osaka, Japan

Electron microscopy and spectroscopy are widely used to characterize various low-dimensional materials. Identifying the atomic structures and/or measurements of local optical properties are of great importance in designing nanoscale devices based on hybrid nanostructures. Electron energy-loss spectroscopy (EELS) has been widely used for elemental identification in transmission electron microscopes (TEM) by using core-level excitations. Recent developments of monochromators after the e-beam guns have enabled us to access optical and vibrational information from the valence EELS ranges of nanometric materials. Here we show our latest studies to develop the possibilities of EELS applied for low-dimensional hybrid materials. Examples for atomic defects in in-plane hybrid TMDCs[1], monolayer structures of metal chlorides intercalated in bi-layer graphene[2, 3], surface adatoms for catalysis[4], two-dimensional iodine-monofluoride epitaxy[5], isotopically heterogeneous graphene[6], and the other new forms of 2D materials [7] will be shown.

References:

[1] Y.-C. Lin et al., Adv. Mater., (2021) 2007819
[2] Y.-C. Lin et al., Adv. Mater. (2021) 2105898
[3] Y.-C. Lin et al., Nano Lett., (2021) 21, 10386-10391
[4] S. Wu et al., J. Am. Chem. Soc., (2021) 143, 9105-9112
[5] Y.-C. Lin et al., njp 2D Mater. Appl., (2021) 18
[6] R. Senga et al. Nature 603 (2022) 68-73
[7] J. Zhou et al. (2022) in press
[8] The works presented here are supported by JST-CREST and ERC MORE-TEM projects.

Progress Towards Atomic-Scale Analytical Tomography

Thomas F. Kelly[1], and Brian P. Gorman[2]

1 Steam Instruments, Inc., Madison, WI USA
2 Colorado School of Mines, Department of Metallurgical and Materials Engineering, Golden, CO USA

Atomic-Scale Analytical Tomography (ASAT) has been defined [1] as the determination of the correct (isotopic) identification of every atom and its precise three-dimensional (3-D) location in a structure for large volumes (>10^6 nm^3) of material, Figure 1. Taking this a step further, ASAT should also be able to determine the local electronic structure of these atoms which makes true 3-D atomic-structure / electronic-property relationships possible. Thus, analytical information is also an important essential ingredient of ASAT [2].

Over the past decade or so, there have been projects aimed at achieving ASAT. The ATOM Project was developed in the USA during 2010-2012 [3] but was not funded. Project Tomo was developed in Germany beginning in 2014 and was funded in 2019. It is led by Rafal Dunin-Borkowski and Joachim Mayer of Forschungszentrum Jülich. Two of the authors (TFK and BPG) recently completed a book with S.P. Ringer on the topic [4].

The essential premise is that no single technique that exists today has achieved or can achieve ASAT. However, combining transmission electron microscopy (TEM) and atom probe tomography with improved (100% quantum detection efficiency) detector technology has been identified as a path toward ASAT [1]. Atom Probe Tomography (APT) provides mass spectral identification for each individual atom and atom positions; however, 3-D image reconstruction methods lack information about the specimen that limits the spatial resolution. Originally, the notion for ASAT was that the TEM would provide information about the shape and distribution of electric fields at the specimen apex in an atom probe sufficient to improve the spatial resolution of the reconstructions [1]. This was termed APT-centric atom positioning [4]. Gorman et al. [4,5] have pursued atom positioning by determining real space coordinates of atoms in the specimen before field evaporation in a method they term STEM-centric atom positioning. Using 4D-STEM of the specimen [6], the positions of atoms in three-dimensions are determined with very high precision (~5 pm) [7]. It is fortunate that there exist two fundamentally different approaches to the same key task. They should both give the same answer and time will tell which is more effective in practice.

As an illustration of ASAT's promise, ASAT images of semiconductor nanostructures will reveal the 3-D position of individual dopant atoms with pm spatial resolution, the 3-D position of nuclear spin isotopes, nanometer-scale changes in strain due to structural defects and lattice mismatch, the 3-D position of point defects such as vacancies, and any electronic band structure changes at all these atomic-scale features.

Within the next five years, it is expected that ASAT will be achieved through integration of 100% efficiency ion detectors, improved data handling algorithms, and integration of TEM and APT into a single instrument, Figure 2 [6].

References:

[1] T.F. Kelly, M.K. Miller, K. Rajan, S.P. Ringer, Microsc. Microanal. **19** (2013) 652–664.
[2] T.F. Kelly, Microsc. Microanal. **23** (2017) 34–45.

[3] T.F. Kelly, *et al.*, Microsc Microanal. 17 (Suppl 2) (2011) 708–709.
[4] T.F. Kelly, B.P. Gorman, S.P. Ringer in "Atomic-Scale Analytical Tomography," (Cambridge University Press, Cambridge, England) 2022.
[5] A.V. Ceguerra, A.J. Breen, J.M. Cairney, *et al.*, Microsc. Microanal. **27** (2021) 140–148.
[6] B. Gorman, M. Holtz, C.J.K. Richardson, C. Gaspe, E. Supple, R. Butera, Microsc. Microanal. **27** (2021) 184–186.
[7] E. Padgett, M.E. Holtz, P. Cueva, Y.-T. Shao, E. Langenberg, D.G. Schlom, D.A. Muller, Ultramicroscopy. 214 (2020) 112994.
[8] The authors acknowledge fruitful discussions with I.V. Veryovkin, J.A. Hunt, M.E. Holtz, N. Salmon, S.P. Ringer, D.B. Williams, and H. Fraser.

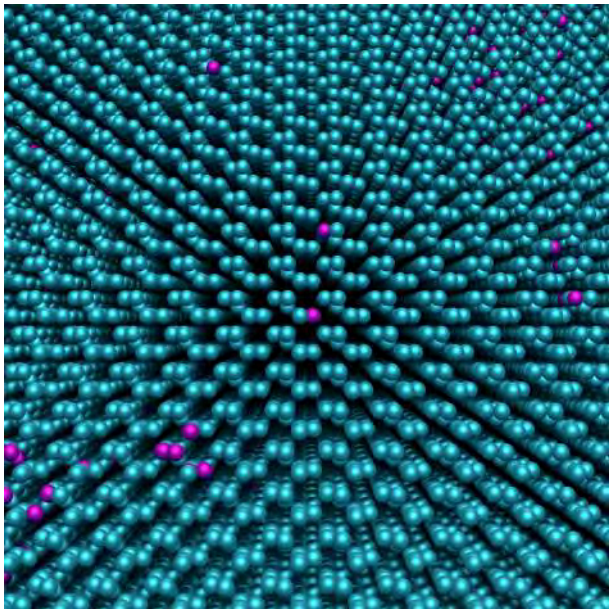

Figure 1. Simulated ASAT image of silicon with dopant atoms located in the three-dimensional structure.

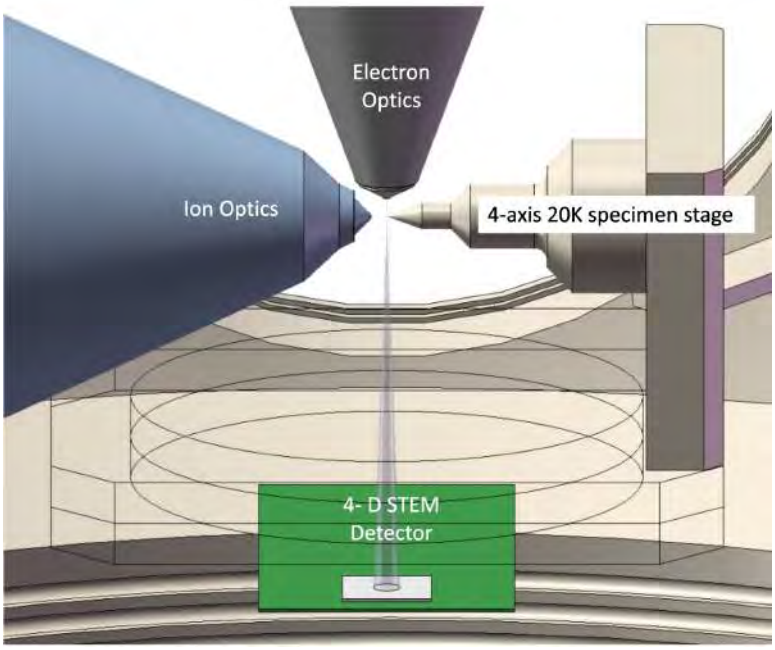

Figure 2. Nominal configuration of an ASAT instrument based on 4-D STEM with APT.

Using STEM-EELS to Optimize Gold Nanoparticles for Early Cancer Detection

Robert Sinclair, Yitian Zeng, Steven J. Madsen and Victor Warlop Piers de Raveschoot

Department of Materials Science and Engineering, Stanford University, Stanford, CA 94305, United States

There are various ways in which nanotechnology can assist in early cancer detection, oftentimes utilizing sensitive physical properties of nanomaterials to detect them attached to tumors or circulating cancer cells [1]. The group with whom we collaborate has successfully employed gold nano-spheres contained within a silica shell as a triple modality detection agent [2]. One of the properties utilized is surface-enhanced Raman spectroscopy (SERS) whereby the gold nano-spheres significantly enhance the Raman signal from an organic dye when exposed to an illuminating laser beam, which has been incorporated into a working endoscopic system [3]. While this works well, to our knowledge there has never been any systematic study as to the influence of nanomaterial structure parameters such as size, shape, seperation, coating etc. on the strength of the Raman signal, and hence its utility in detecting small tumors. It is recognized that surface plasmons in noble metal nanoparticles directly contribute to the Raman signal [4], and that the surface plasmon energy is in turn determined by the nanomaterial parameters mentioned above [5]. In this paper, we describe an approach to study the effect of these parameters in order to establish the optimum conditions to generate the highest possible Raman signal.

Arrays of gold nanoparticles of various sizes, shape and separation are fabricated from a vapor-deposited gold thin film utilizing standard electron lithographic processes [6]. When a Raman dye is spread over the array, Raman imaging shows the variations of signal and hence the parameters giving rise to maximum signal [7]. Nanoparticle size is seen to be a critical feature. The plasmon resonances and energies are then determined across the array using electron energy loss spectroscopy (EELS) in a scanning TEM (STEM) [6,7] and the individual spectra are then correlated with the Raman signal from the exact same nanoparticle structures. By this procedure we can establish the critical parameters which yield the highest Raman signal, which leads to the systematic design of the most effective SERS nanoparticles. We have further been exploring the influence of shapes more complex than discs or triangles and have found an interesting correlation between surface plasmon energies and particle isoperimetric ratios. These results will be discussed in terms of the usefulness of STEM-EELS in providing a scientific understanding of the physical phenomena involved [8].

References:

[1] H. Arami *et al*, ACS Nano, **13** (2019), p. 2858-2869.
[2] M. F. Kircher *et al*, Nature Medicine, **18** (2012), p. 829-834.
[3] A. S. Thakor *et al*, **3** (2011), 79ra33.
[4] K. Kneipp *et al*, J. Phys. Condens. Matter **14** (2002), R597-R624.
[5] M. Bosman *et al*, Nanotechnology **18** (2007), p. 165505.
[6] Y. Zeng *et al*, Nanoscale, **12** (2020), p. 23768-23779.
[7] R. Sinclair *et al*, J. Mater. Res., **36**, (2021), p. 3383-3397.
[8] This work was supported by the Center for Cancer Nanotechnology Excellence for Translational Diagnostics (CCNE-TD) at Stanford University through an award (grant No: U54 CA199075) from the National Cancer Institute (NCI) of the National Institutes of Health (NIH). The inspirational contributions and advice from our principal investigators Drs. Sam Gambhir and Shan Wang are most appreciated.

Liquid-Phase Atomic-Scale Investigations of Crystal Nucleation, Particle Growth and Core-Shell Formation Using In-Situ Scanning Transmission Electron Microscopy

Rolf Erni, Walid Dachraoui, Debora Keller and Trond R. Henninen

Electron Microscopy Center, Empa – Swiss Federal Laboratories for Materials Science and Technology, Dübendorf, Switzerland.

There are, of course, thermodynamic reasons why solids are solid and why they can be crystalline. How this happens, however, is less evident. Classical nucleation theory extrapolates thermodynamic properties of bulk materials to systems that merely consist of dozens of atoms or even less. We are interested in studying how solids become solid and how they adopt crystallinity. We try to trigger the formation of nanocrystals in small systems that we can observe by high-resolution scanning transmission electron microscopy and aim at monitoring the atomic mechanisms that lead to the formation of crystalline matter. In a first approach, we study Pt atoms, deposited on support films, in the vacuum environment of the microscope and activate them by temperature as well as by the electron beam to eventually form metallic clusters and nanoparticles. These studies clearly show that for Pt the bulk crystalline structure already dominates the configuration of tiny clusters. Using the total electron dose a structure survives, before it undergoes a structural transition, the electron irradiation is taken as a measure to assess the relative stability of a cluster configuration. Analyzing in this way a variety of different Pt clusters, clearly shows that the face centered cubic structure with cuboidal morphology dominates, even for clusters that merely consist of a dozen of atoms.

The analysis of clusters in vacuum under electron irradiation provides fundamental information about their structure, their stability and their interaction with the support film. Yet, in order to mimic realistic scenarios of particle formation more complex environments, particularly liquid phase studies, are needed. A metallic precursor dissolved in a liquid can be reduced by the electron beam and by the reactive environment of the liquid when exposed to the electron beam. The reduced metallic species then undergo nucleation reactions and are supposed to finally form crystalline nanoparticles. Despite the fact that valuable nano-scale information of such processes can be gathered when working with commercial liquid cells [1], owing to the thickness of the SiN windows and the rather thick liquid phase (typically >100 nm), atomic scale information is not accessible. As we are interested in exploring atomic mechanisms, we thus implemented two experimental approaches that allow us for studying nucleation reactions and particle growth with single atom sensitivity in liquids.

The first strategy is based on employing graphene-based liquid cells, where tiny, liquid nanoreactors are encapsulated between two graphene membranes. Using this approach, we studied the nucleation of Au and Pt nanoparticles in aqueous solutions [2,3]. The first step in the nucleation of Au consists of the formation of diffuse clouds of Au atoms, which abruptly undergo condensation to form partially crystalline nanoparticles. These defective nanoparticles remain surrounded by a diffuse cluster cloud, which is critical for the further development of the Au particle. Namely, the defective nanoparticle, consisting of differently oriented crystalline and amorphous parts, exchanges matter with the surrounding cluster cloud. Reattachment of the matter expelled to the cluster cloud eventually leads to mature, crystalline Au nanoparticles that show very little defective areas. Reattachment of the matter dissolved in the cluster cloud occurs by single atom attachment and by the oriented attachment of crystalline clusters formed in the diffuse cloud [2]. In the case of Pt, the formation of crystalline nanoparticles follows a more direct pathway. In a first step, Pt atoms agglomerate to form amorphous clusters. These clusters continue growing by attachment of

individual atoms. After reaching a certain size (1-2 nm), the amorphous clusters undergo a crystallization step, forming 1-2 nm sized crystalline, facetted Pt particles. These particles continue growing, by single atom attachment, but also by oriented attachment of particles of similar size [3]. The same approach based on graphene-based liquid cells also revealed the dependence of the shell morphology of catalytic Pd-Pt core-shell nanoparticles as a function of Pt precursor concentration [4].

The second strategy that we explore for atomic scale observations in liquids is based on vacuum compatible ionic liquids. Nanodroplets of ionic liquid with dissolved metal precursors are deposited on heating chips compatible with an in-situ heating and electrical biasing holder. These nanoreactors can be heated up moderately in the microscope in order to adjust the viscosity of the liquid phase. We use this system to study the atomic mechanisms of the growth of 1-2 nm sized Au nanoparticles. We observe a variety of different growth mechanisms, i.e. Ostwald ripening, oriented attachment, slow and fast coalescence processes, sometimes via neck formation. What we find is that different growth mechanisms are simultaneously active, and most importantly, that the local environment of a particular particle is decisive for the pathway the particle follows in its growth process. Similarly sized particles tend to coalescence while, e.g., differently sized particles more frequently undergo Ostwald ripening on expense of the smaller particle.

In conclusion; both approaches, the one based on graphene liquid cells and the one involving nanodroplets of ionic liquids, allow us to monitor in-situ and with single atom sensitivity the nucleation and growth processes of metallic nanoparticles in simplified systems that mimic realistic synthesis conditions. We find that these nucleation processes are more complex that what classical nucleation theory predicts and often involve several steps. Our observations of particle growth processes show that often multiple pathways are active simultaneously and that the local environment of a particular particle is critical for the mechanism that dominates its growth.

References:

[1] Y. Zhang et al., Chem. Mater. **29** (2017) 10518.
[2] W. Dachraoui et al., Nano Lett. **21** (2021) 2861.
[3] W. Dachraoui et al., Sci. Rep. **11** (2021) 23965.
[4] W. Dachraoui et al., Appl. Phys. Rev. **8** (2021) 041407.
[5] D. Keller, T. R. Henninen and R. Erni, Micron **117** (2019) 16.
[6] D. Keller, T. R. Henninen and R. Erni, Nanoscale **12** (2020) 22511.

In Situ Scanning Transmission Electron Diffraction of Individual Electrically Biased Ag-In-Sb-Te Phase Change Memory Line Cells

Vadim Migunov[1], Karina Ruzaeva[1], Dieter Weber[1], Alexander Clausen[1], Xuan Thang Vu[2], Sebastian Walfort[2], Benedikt Kersting[2], Martin Salinga[2] and Rafal E. Dunin-Borkowski[1]

1 Ernst Ruska-Centre for Microscopy and Spectroscopy with Electrons and Peter Grünberg Institute, Forschungszentrum Jülich, 52425 Jülich, Germany

2 RWTH Aachen University, 52074 Aachen, Germany

Resistive-switching-based phase change memory (PCM) devices are of interest for high performance computing with reduced cost and power, non-volatililty, byte addressability and fast response times, as well as for applications in neuromorphic computing [1]. However, key questions remain about the evolution of individual crystallites during switching, about the microscopic origin of "threshold switching" in amorphous PCMs and about the details of resistance drift. Here, we study switching processes in individual Ag-In-Sb-Te (AIST) PCM devices *in situ* in the TEM. We use dedicated chips, in which free-standing (electron-transparent) SiN_x membranes are used to support nanostructured line cells. Switching of the devices requires the use of very short (< 50 ns) current pulses with sharp trailing edges (of a few ns). A dedicated TEM specimen holder and a specific device geometry were developed to allow such pulses to be used to observe switching processes reproducibly. The fact that the switching layer is thin (40 nm) compared to the total thickness of the device (300 nm, including 150 nm of SiN_x and additional protective capping layers) also complicates imaging, as contrast differences between the crystalline and amorphous phases are strongly reduced. Nanobeam scanning TEM (STEM) imaging with a probe convergence semi-angle of a few mrad and a high camera length was found to be optimal for providing a low-angle annular dark-field imaging setup, resulting in an enhancement in contrast from crystalline regions of the PCM device.

Figure 1 illustrates the cycling of an AIST cell between a low resistance state (LRS) and a high resistance state (HRS). A square voltage pulse of duration 50 ns and 2.1 V height was initially used to RESET the cell to the HRS (Figs 1 b, c, e). 100 ns triangular pulses sweeping to voltages between 1.1 and 1.5 V were then used to SET the cell to the LRS (Figs 1d, f). In the pristine LRS (Fig. 1a), the cell shows grainy contrast that is typical of crystalline material. Depending on their orientations, individual grains appear dark or bright. Upon switching to the HRS (Fig. 1b), the region on the right changes contrast to mid-grey as a result of the formation of an amorphous region, whose presence was confirmed using STEM diffraction. Figure 1c corresponds to a HRS with reduced resistance after one "sweep" pulse. The size of the amorphous region has decreased, with some crystallites growing into it. Figure 1d corresponds to a LRS recorded after a second SET pulse. The resistance is higher than that of the pristine state. A continuous crystalline conducting channel is present at the lower side of the bridge, while the amorphous region is not fully crystallized. Figure 1e shows a HRS after another RESET pulse. The amorphous region has increased in size and blocks the conduction channel. Figure 1f shows the bridge in an almost fully crystallized state, with only one small amorphous region left. The resistance is slightly higher than in the pristine state. Two approaches based on STEM diffraction were used to better identify amorphous and crystalline regions in the device. In the first approach, the deviation of each diffraction pattern from a reference amorphous pattern was calculated to reveal amorphous and crystalline regions. In the second approach, bandpass filtering was applied to the patterns to filter out both low frequency variations and noise. The total intensities in the filtered patterns were assumed to be proportional to the intensities of the diffracted beams and used to identify amorphous regions. Representative results recorded from a line cell using scanning transmission electron diffraction are shown in Fig. 2. Plans for future experiments will be

discussed [2].

References:

[1] M Wuttig and N Yamada, Nature Materials **6** (2007), 824–832.
[2] Funding from the DFG (German Science Foundation) within the collaborative research centre SFB 917 "Nanoswitches" is gratefully acknowledged.

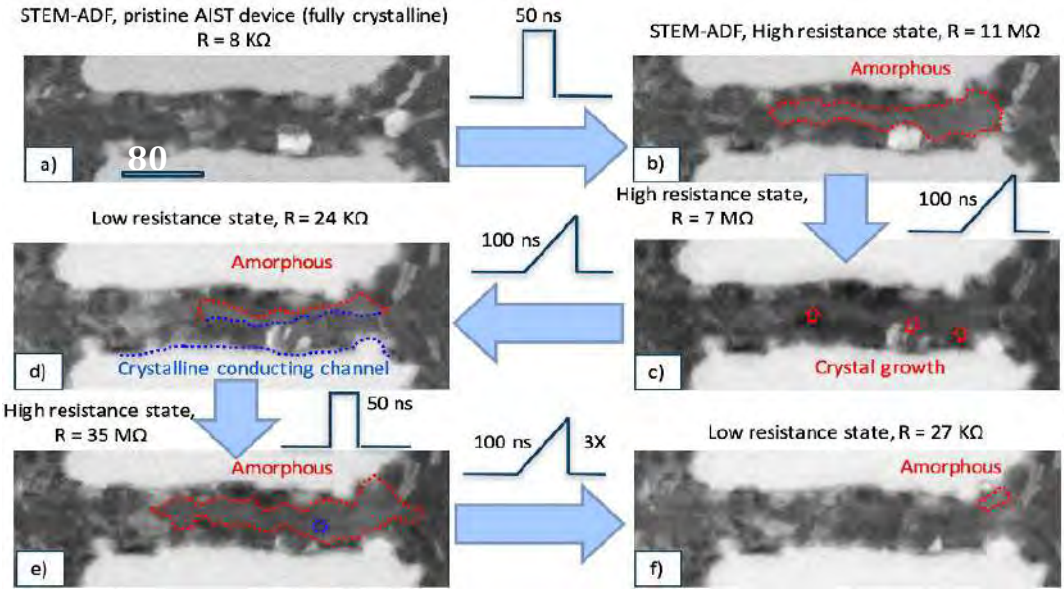

Figure 1. STEM ADF images recorded during switching of an AIST phase change memory line cell. a) Pristine crystalline low resistance state (LRS) with a resistance of 8 kΩ switched inside the TEM using a square pulse of duration 50 ns to b) a high resistance state (HRS). An amorphous region is outlined by a red dashed line. Images recorded after first and second "sweep" pulses (of duration 100 ns) are shown in c) and d) for the HRS and LRS, respectively. A crystalline conducting channel is marked with a blue dashed line. e, f) Subsequent switching from the HRS to the LRS.

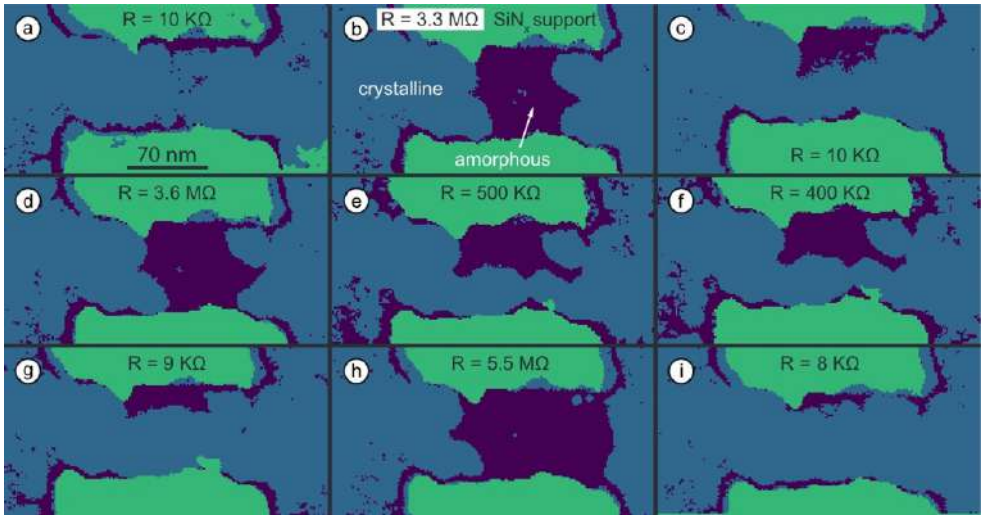

Figure 2. Results obtained by using scanning transmission electron diffraction to follow the local evolution of crystalline and amorphous regions (marked in light blue and dark blue, respectively) during switching of an individual AIST device. The SiN_x support is marked in green.

Where did That Charge Come From?

Karl Olson, Christopher Mizzi, Alex Lin and Laurence Marks

Department of Materials Science, Northwestern University, Chicago IL, USA

Almost as old as tribology, triboelectricity dates back to the work of Thales of Miletus in the sixth century BCE, and has been known for at least twenty-five centuries [1]. It can be a boon or a bane in industries ranging from xerography [2] to packing of pharmaceutical powders [3], and plays a critical role in many processes such as dust storms [4] and planetary formation [5].

Triboelectricity and tribology shares the same grammatical root "tribo" for friction, and it has been known empirically for centuries that there is a connection. As shown by Bowden and Tabor [6], friction and wear are due to adhesion between as well as elastic deformation of nanoscale asperities – something amenable to in-situ analysis in electron microscopes [7]. The macroscopic friction one observes is due to the variations in the statistical number of nanoscale contacts with load, not a fundamental materials property. Similar to friction, macroscopic charging will be a statistical average over local charge mosaics [8].

Despite decades of effort, some of which included full incorporation of established tribological processes such as asperity contacts, why charge transfer should occur has baffled scientists. The problem has been that none of the conventional approaches such as differences in work functions or piezoelectricity can explain experiments. There are many less rigorous, somewhat ad-hoc models without basis in other known physics – but these only work in a few cases, and in general fail.

What are we missing?

We have recently pointed out [9] that there is one electromechanical term which had been missed in the analysis: flexoelectricity. This is the coupling of strain gradients with polarization, different from piezoelectricity which is strain and polarization. Because it is a gradient term, it becomes very important at the nanoscale and there is now extensive experimental and theoretical evidence that it often dominates. It can also play a significant role in the charging and bending of samples in electron microscopes [10]. While charging is often something electron microscopists want to run away from, charging and polarization can be interesting physics worth more study [11].

Asperities are often at the nanoscale, and deform during contact. It turns out that the polarization, and consequently the potential differences that the asperity deformations lead to can be several volts or more, large enough to drive charge transfer. Proper analysis requires including not just elastic strain terms, but also what is called "surface flexoelectric" terms – but is really the strain dependence of the mean-inner potential [12]. The various electromechanical terms lead to band bending coupling polarization with strain [13], see Figure 1.

This talk will discuss some of the analysis for a range of materials and geometries, plus more recent work [14] on the flexoelectric band-bending of sliding Schottky contacts based upon both experimental and theoretical data. In particular, the talk will mention some of the known unknowns, as well as the unknown unknowns, and the potential for advanced electron microscopy techniques such as 4D STEM to shed new light on a shocking problem.

References:

[1] W.R. Harper, Contact and Frictional Electrification, Oxford University Press, Oxford, 1967.
[2] C.B. Duke, J. Noolandi, T. Thieret, The surface science of xerography, Surface Science, 500 (2002) 1005-1023.
[3] H. Watanabe, M. Ghadiri, T. Matsuyama, Y.L. Ding, K.G. Pitt, H. Maruyama, S. Matsusaka, H. Masuda, Triboelectrification of pharmaceutical powders by particle impact, International Journal of Pharmaceutics 334 (2007) 149-155.
[4] J.F. Kok, N.O. Renno, Electrostatics in Wind-Blown Sand, Physical Review Letters, 100 (2008) 014501.
[5] J. Blum, G. Wurm, The Growth Mechanisms of Macroscopic Bodies in Protoplanetary Disks, Annual Review of Astronomy and Astrophysics, 46 (2008) 21–56.
[6] F.P. Bowden, D. Tabor, The friction and lubrication of solids, Oxford University Press, New York, 1950.
[7] Y. Liao, L.D. Marks, In situ single asperity wear at the nanometre scale, International Materials Reviews, 62 (2017) 99-115.
[8] H.T. Baytekin, A.Z. Patashinski, M. Branicki, B. Baytekin, S. Soh, B.A. Gryzbowski, The Mosaic of Surface Charge in Contact Electrification, Science, 333 (2011) 308-312.
[9] C.A. Mizzi, A.Y.W. Lin, L.D. Marks, Does Flexoelectricity Drive Triboelectricity?, Phys Rev Lett, 123 (2019) 116103.
[10] P. Koirala, C.A. Mizzi, L.D. Marks, Direct Observation of Large Flexoelectric Bending at the Nanoscale in Lanthanide Scandates, Nano Lett, 18 (2018) 3850-3856.
[11] C.A. Mizzi, P. Koirala, A. Gulec, L.D. Marks, Charging ain't all bad: Complex physics in DyScO3, Ultramicroscopy, 203 (2019) 119-124.
[12] C.A. Mizzi, L.D. Marks, The role of surfaces in flexoelectricity, J. Appl. Phys., 129 (2021) 224102.
[13] C.A. Mizzi, L.D. Marks, How Does Flexoelectricity Drive Triboelectricity?, ArXiv preprint arXiv:2010.12963, (2021).
[14] K.P. Olson, C.A. Mizzi, L.D. Marks, Band Bending and Ratcheting Explain Triboelectricity in a Flexoelectric Contact Diode, Nano Lett, (2022).

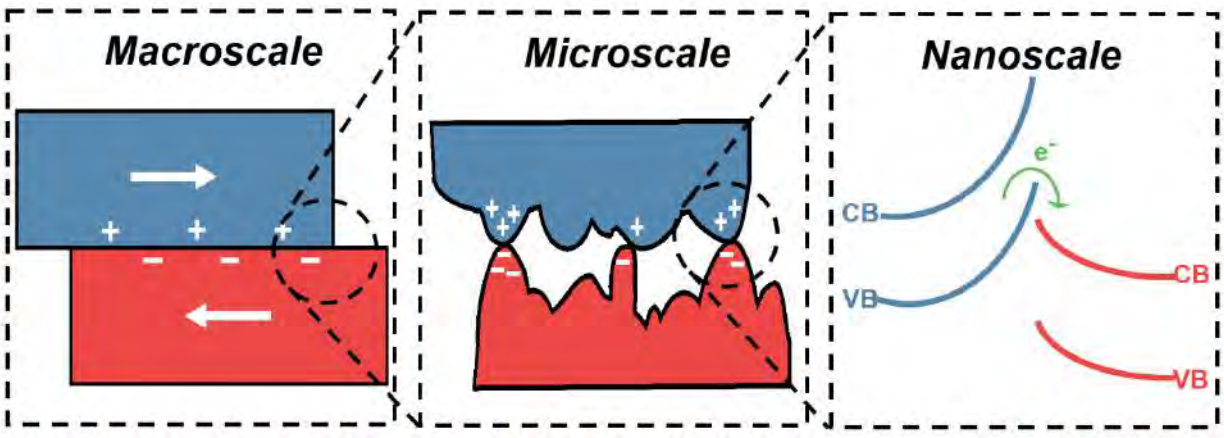

Figure 1. Charge created by macroscopic sliding, as illustrated on the right, is really due to nanoscale asperities in contact as illustrated in the middle, in turn due to local band-bending as illustrated on the right.

Nd-Fe-B Permanent Magnets Ecosystem for a Resilient and Sustainable European Electric Mobility and Renewable Energy Future

Kristina Žužek[1], Spomenka Kobe[1], Kristina Žagar Soderžnik[1], Matej Komelj[1], Mateja Podlogar[1], Benjamin Podmiljšak[1], Sorour Samsari Parapari[1], Tomaž Tomše[1], Boštjan Markoli[2], Xu Xuan[3], Awais Ikram[4], Rafal E. Dunin-Borkowski[5], András Kovács[5] and Sašo Šturm[1]

1 Jožef Stefan Institute, Department for Nanostructured Materials, Ljubljana, Slovenia
2 University of Ljubljana, Faculty of Natural Sciences and Engineering, Department of Materials and Metallurgy, Ljubljana, Slovenia
3 Inner Mongolia University, School of Chemistry and Chemical Engineering, Inner Mongolia Engineering and Technology Research Center for Catalytic Conversion and Utilization of Carbon Resource Molecules & Inner Mongolia Key Lab of Nanoscience and Nanotechnology, Hohhot, People's Republic of China
4 Faculty of Mechanical Engineering, University of Ljubljana, Ljubljana, Slovenia
5 Ernst Ruska-Centre for Microscopy and Spectroscopy with Electrons and Peter Grünberg Institute, Forschungszentrum Jülich, Jülich, Germany

European strategies for transition to a low-carbon and energy-efficient society, as planned in the European Green Deal, will require radical solutions to reduce greenhouse gas emissions by 80% until 2050. The major contributing sectors to achieve this goal are intimately related to the development of the electric-mobility and eco-power generation, which will need highly efficient but still economically and ecologically sustainable electric power conversion systems to meet the target. This can only be achieved by using high-performance rare-earth-element (REE) based permanent magnets (PMs) i.e., Nd–Fe–B system, which holds the highest maximum energy product $(BH)_{max}$ of more than 400 kJ/m^3. For this reason, they are in very high demand and are an essential subject of further research aiming at even improved properties and performances. Controversially, REEs are also on the EU's list of most critical raw materials (CRMs), which necessitates the measures encompassing their recycling that will be, in the future, embedded in the PMs initial development. In this talk, we will present our efforts to turn this vicious circle into an opportunity for the European electric-mobility and renewable energy sectors by radical innovation of PMs processing combined with the efficient recycling and reprocessing routes in a holistic circular manner, thus placing the Nd-Fe-B PMs ecosystem into a domain of a resilient and sustainable circular economy. So far, the vast majority of Nd-Fe-B PMs development efforts have been devoted to overcoming the so-called Brown paradox, stating that only a part of the base-material properties can be exploited in a bulk magnet due to material-processing artifacts. The potential remains huge, as in these magnets we currently exploit only 20% of the theoretical coercivity - the ability of a magnet to resist against external magnetic fields. The most recent activities towards this goal are commonly referred to as grain-boundary engineering, focused on manipulating the non-magnetic two-dimensional-like regions between the particular three-dimensional-like magnetic manifolds to avoid undesired effects. On the other hand, the reuse of end-of-life Nd-Fe-B PMs is often associated with various recycling and reprocessing strategies, like hydrogenation disproportionation desorption recombination (HDDR) processing, remelting, spark plasma sintering (SPS), electrochemical leaching and deposition, that turn magnet waste into new functional magnets with only a little or negligible loss of overall magnetic performance.

Detecting and understanding the underlying chemical and physical mechanisms is thus the key to optimization of the overall magnetic performance and associated recycling routes. For example, chemical and structural peculiarities at interfaces can be directly linked to the coercivity of the bulk sintered Nd-Fe-B system, facilitating further optimization of the magnet. Advanced Transmission

Electron Microscopy with various specialized analytical techniques, including Electron Holography for quantitative magnetic characterization with nm spatial resolution, was employed to assess the most pressing research challenges encountered during the development of various processing and recycling routes in the Nd-Fe-B PMs system. From a plethora of our scientific exploration, we will, among other things, show how grain-boundary structural refinement (Figure 1 a,b) or small amounts of the REEs (Dy, Tb) that partially replace the Nd in the grain-boundary diffusion process have a large, positive influence on the coercivity of the whole Nd–Fe–B bulk magnets [1]. We report on the prospects for direct reuse of end-of-life PMs by applying the HDDR process combined with spark plasma sintering (SPS) to fabricate dense reprocessed magnets [2]. Lastly, we propose new concepts of electrochemical separations for the sintered Nd-Fe-B PMs by either direct recovering of the matrix phase or metal winning (Figure 1 c,d), the methods still under-exploited but already proven to be feasible by our group [3,4].

References:

[1] K. Ž. Soderžnik, K. Žužek, S. Šturm, *et al*, Journal of Alloys and Compounds 864 (2021), 58915.
[2] A. Ikram, K. Žužek, S. Šturm, *et al*, Journal of Rare Earths 38.1 (2020), 90-99.
[3] X. Xu, K. Žužek, S. Šturm, *et al*, Green Chemistry 22.4 (2020), 1105-1112.
[4] X. Xu, K. Žužek, S. Šturm, *et al*, ChemSusChem 12.21 (2019), 4754-4758.
[5] Several authors acknowledge funding from the Slovenian Research Agency ARRS (P2-0084)

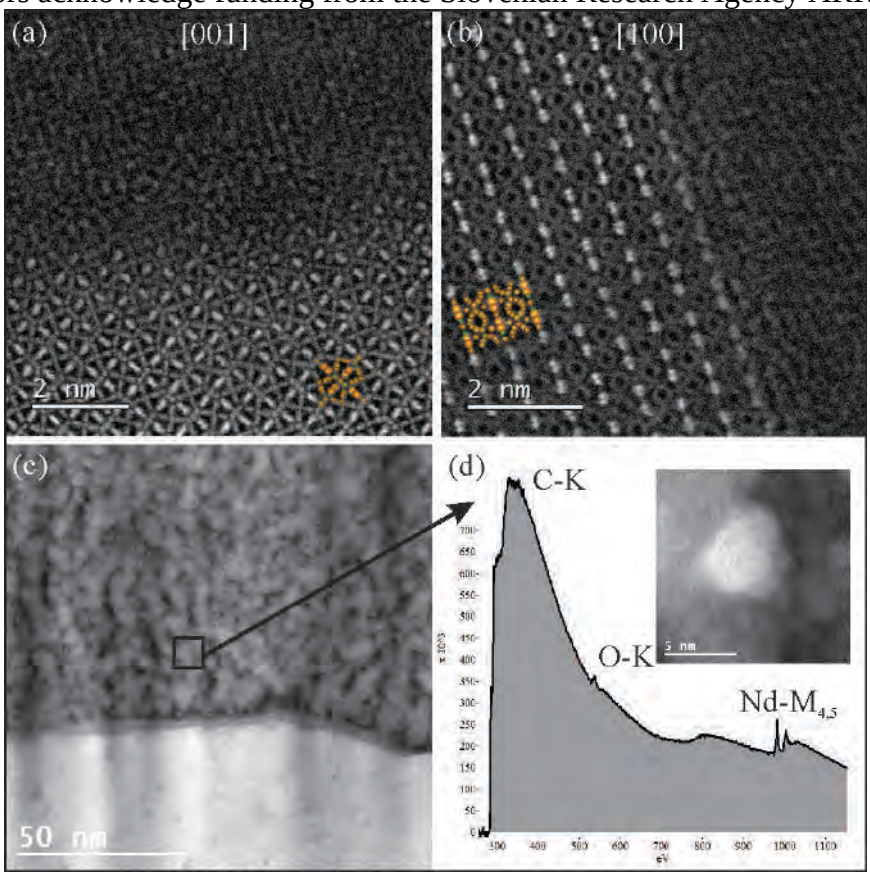

Figure 1. HAADF-STEM image of differently processed SPSed HDDR Nd-Fe-B PMs showing (a) rough disordered and (b) smooth, highly faceted grain boundary structure. The coercivity of the latter was improved by 45%. The underlying projected crystal structure is superimposed (Nd-orange, Fe-brown, B-green). (c) Induced electro-co-deposition film of Nd and Fe from an ionic-liquid electrolyte annealed at 350°C. (d) Background subtracted EELS spectrum acquired from the single nanoparticle indicates the formation of the NdC_2 phase suggesting initial electrodeposition of metallic Nd^0.

From Millions of Images to a Few Numbers: High speed imaging of Defects and Defect Dynamics in Low Dimensional Materials

Angus I. Kirkland[1,2,3], Chen Huang[3]

1 Department of Materials, Parks Road, Oxford, UK.

2 Electron Physical Sciences Imaging Centre (ePSIC), Diamond Light Source, Oxford, UK.

3 The Rosalind Franklin Institute, Harwell Campus, Didcot, OX11 0FA, UK.

This lecture will describe firstly recent developments in the use of Scanning Transmission and Transmission Electron Microscopy applied to studies of dynamics in low dimensional materials. I will describe recent work using high speed direct electron detectors and artificial intelligence / machine learning to automatically map defect and adatom migrations in graphene from large data sets. I will then show how this approach can be extended to probe the local kinetics of defect transitions. Finally, I will discuss the use of similar detectors in electron ptychography, under extremely low dose conditions using binary counting.

The development and commercialization of direct electron detectors suitable for use at intermediate electron energies as typically employed in the transmission electron microscope has led to significant progress in imaging, diffraction and spectroscopy [1]. In the life sciences improved detection efficiency has made electron microscopy the most rapidly growing structural method used in studies of biological structures [2]. In the physical sciences improved detector resolution due to a lack of scattering in a coupled scintillator and increased frame rates have enabled high resolution imaging of dynamic processes and have supported new experimental geometries including 4D STEM [3].

To usefully deploy Graphene and related materials in electronic applications [4-6] it is essential to understand the behavior of defects, which have been the subject of extensive research in silicon devices for decades. Moreover, instrumental advances make it possible to image these defects at primary energies below those that cause significant specimen damage whilst retaining sufficient spatial resolution to resolve the local atomic configurations around the defect site [7]. Combining these electron-optical developments with new high-speed detectors has further advanced this field and defect motions and rearrangements can now be tracked with ms timings.

However, the extremely large datasets (typically 10^6 images or greater) that can be routinely acquired makes conventional manual image processing, with human intervention intractable. Theses also put a hard restriction on the scalability of data processing in some important areas, in particular where the collection of large image series is routine. I will describe how this can be overcome using a deep learning neural network [8] which performs atomic model abstraction from low dose high framerate experimental graphene images (Fig. 1). Although the training of such neural networks requires significantly more effort than classical image processing, this method is more general can autonomously process large datasets and can readily be extended to studies of other two-dimensional materials. Using this approach, it is possible to identify many instances of specific defect transitions and to map the lifetimes of defect states. In turn these can be used as input to density functional theory to model the potential energy landscape for the transitions.

Finally, I will highlight the use of fast detectors for electron Ptychography at low dose. Acquisition of a ptychographic dataset requires the collection of a series of far field diffraction patters as a function of probe position at the specimen plane. This dataset can then be used to recover the

complex specimen object function using either an iterative or non-iterative algorithm. Importantly, ptychography is a dose efficient technique, enabling effective phase reconstruction of radiation sensitive samples. At low dose the sampling of the diffraction pattern in the far field is sparse and a counting direct electron detector can be operated in a binary mode to provide an effective speed increase. I will illustrate this method using examples of radiation sensitive mesoporous materials

References:

[1] J. A. Mir*et al*, Ultramicroscopy **182** (2017), 44.
[2] E. Callaway, Nature **525** (2015), 172.
[3] S. Gao *et al*, Nature Comm. **8** (2017), 163.
[4] K. S. Novoselov *et al*, Nature **490** (2012), 192.
[5] F. Schwierz, Nature Nanotech. **5** (2010), 487.
[6] L. Britnell *et al*, Science **335** (2012), 947.
[7] A. W. Robertson *et al*, Nature Comm. **3** (2012), 1144.
[8] Y. LeCun, *et al*, Nature **521** (2015), 436.

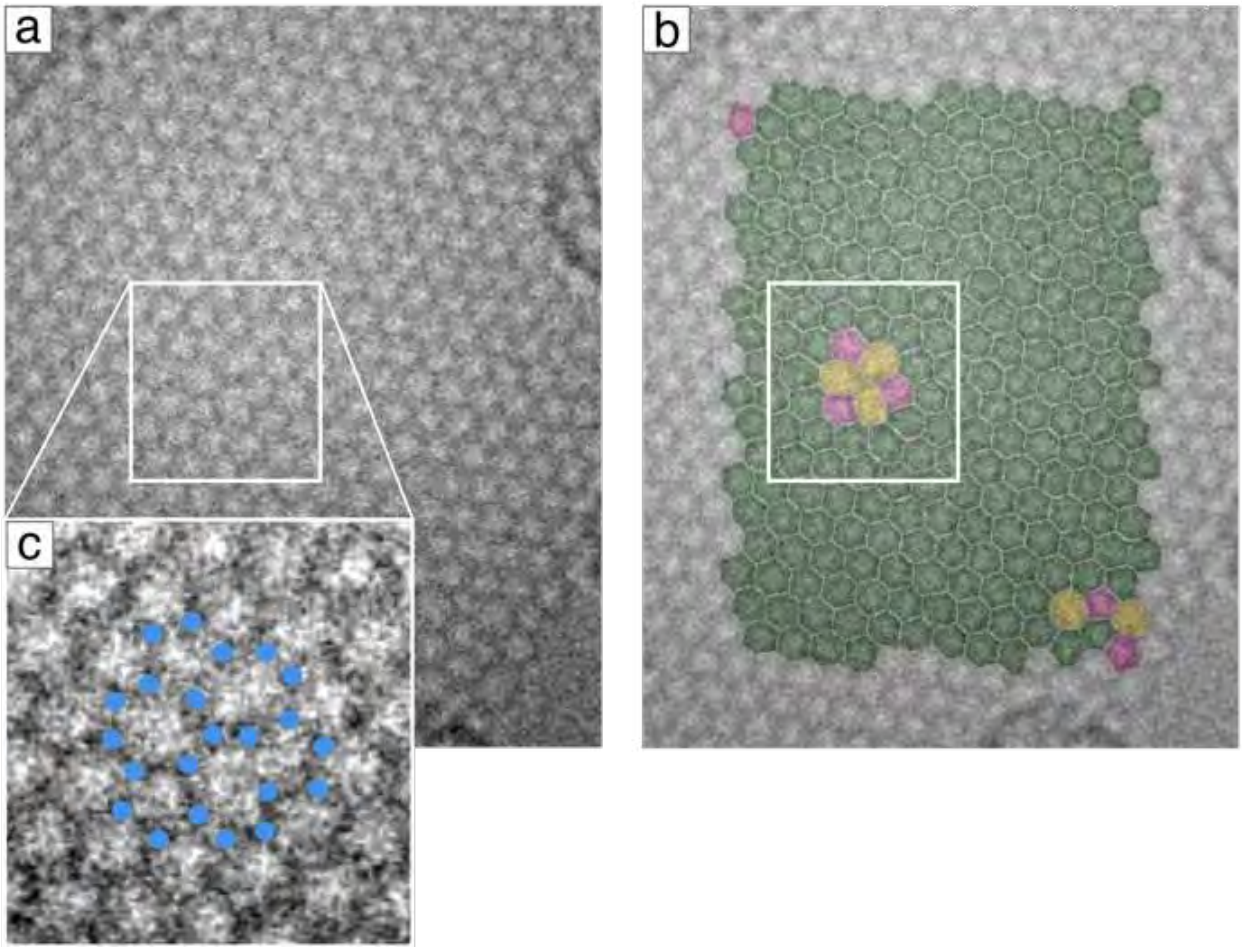

Figure 1. (a) Low-dose image of a graphene sheet recorded with a 1ms exposure at 80KV containing defects; (b) Automatically generated annotation with 5-membered rings (pink), 6-membered rings (green), and 7-membered rings (yellow) overlaid on top of the experimental image; (c) enlarged defect area with carbon atom positions marked by blue circles.

Quantitative Chemical Analysis of Complex Samples using Analytical TEM and Machine Learning Tools: from Elemental Maps to Phase Segmentation

Cécile Hébert[1,2], Hui Chen[1] and Adrien Teurtrie[1,3]

1 LSME - IPHYS Ecole Polytechnique Fédérale de Lausanne, Lausanne, Switzerland

2 Institut de Matériaux, Ecole Polytechnique Fédérale de Lausanne, Lausanne, Switzerland

3 Unité Matériaux et Transformations, Université de Lille, France

Modern Transmission Electron Microscopes allow capturing huge hyperspectral datasets in relatively short period of time. In such a typical dataset, spatial information is complemented by pixel-by-pixel chemical information in the form of energy dispersive x-ray spectra or electron energy loss spectra (or both). The ultimate goal is to be able to separate the different domains of the sample by their chemical composition and/or physical properties such as oxidation state, and on one hand to quantify those properties domain-by-domain, and on the other hand to assess the relative proportion and distribution of each domain.

Statistical analysis tool such as Principal Component Analysis, Non Negative Matrix Factorization (NMF), etc. are in principle well suited to deal with such large datasets, which have a strong noise component, and only few relevant spectral components, mixed spatially. Those tools are very efficient for denoising, provided artifacts from the detection system do not dominate the structure of the noise, as well as for recognizing the number of relevant components. In general, the spatial distribution of domains is correctly highlighted in the resulting decomposition. However, fundamentally, the resulting spectral components are not representative of the actual spectral components of the domains really present in the specimen. The main reason is that the data is decomposed into a linear combination of individual components. However, the number of mathematically valid decomposition is infinite, while only one represents the physics of the specimen. Some constraints can be applied to ensure that the result has a chance to be physically relevant. The most common one is to sate that both spectral and spatial components cannot have negative values (NMF). While this will help constrain the result, this is not sufficient to ensure that the correct spectral components are retrieved.

In this presentation, we will review some of the main routes that have been envisaged so far for data decomposition of hyperspectral datasets acquired in TEM. In a second part, we will discuss the route that we have chosen: on one hand, a-priori knowledge that we have on the sample is used. For example the fact that some spatial areas are pure phase, or that some chemical elements must be present or absent in some phases; on the other hand we aimed at modeling the spectrum as much as possible using the knowledge we have about its shape. By combining those approach, we show that we a) can obtain a very good decomposition even in the case of complex specimen with many spatially overlapping phases, and b) obtain good results even if the data are extremely noisy.

2D Nanostructures at Atomic Scale: From Energy an Environmental Applications to Quantum Devices.

Jordi Arbiol[1,2]

1 Catalan Institute of Nanoscience and Nanotechnology (ICN2), CSIC and BIST, Campus UAB, Bellaterra, 08193 Barcelona, Catalonia, Spain
2 ICREA, Pg. Lluís Companys 23, 08010 Barcelona, Catalonia, Spain

Technology at the nanoscale has become one of the main challenges in science as new physical effects appear and can be modulated at will. As developments in materials science are pushing to the size limits of physics and chemistry, there is a critical need for understanding the origin of these unique properties and relate them to the changes originated at the atomic scale, e.g.: linked to structural changes of the material, many times related to the presence of crystal defects or crystal surface terminations. Especially on 2D materials designed for electrocatalysis in energy and environmental applications, crystallography and distribution of the atomic species are of outmost importance in order to determine the active sites that will improve the reaction performance, including efficiency and selectivity towards certain reactions. In 2D nanomaterials the distribution and coordination of metal species at the surface are determining their final electrocatalytic behavior as the reactions of interest mainly occur at the surface. The presentation will show how pristine and perfect crystalline surfaces may tend to be inert versus particular reactions, while creation of certain types of defects or even a predetermined surface amorphization may highly improve the catalytic activity of these 2D nanomaterials [1-4].

In the present work, a combination of advanced electron microscopy imaging with electron spectroscopy, in an aberration corrected STEM will allow us to probe the elemental composition and structure in a high spatial detail, while determining the growth mechanisms and correlating the structural properties to their electrocatalytic performance.

The first electrocatalyst system to study is based on 2D MoS_2 nanoflakes. MoS_2 basal plane is not pretty catalytically active, in this sense, we need to find other ways to improve the activity of this material for example for the electrocatalytic hydrogen evolution reaction (HER). The hypothesis of the work considers that the grain boundaries (GBs) created at the interface between nanoflake domains, can be considered as a highly defective perimeter which can certainly improve the density of active sites. Taking this idea in mind, we engineered MoS_2 connected nanoflakes at 5nm diameter range, which create a, ultra-high density of GBs (up to ~10^{12} cm^{-2}). The obtained GBs present a complex bonding coordination that could be studied by atomic resolution aberration corrected (AC) high angle annular dark field (HAADF) scanning transmission electron microscopy (STEM). Using the 2D atomic models obtained from our AC HAADF STEM observations we could study the different hydrogen adsorption preferential sites on the different atomic arrangements in MoS_2 (including different GBs and Edges). Theoretical DFT calculations of the H_2 absorption free energy in these preferential sites in comparison to the MoS_2 Basal Plane (BP) were performed, showing that some GB structures show better electrocatalytic activity than edges, and much better than the MoS_2 BP [1].

In a second part, we study the way to obtain the maximum utilization of noble metal atoms in our 2D catalysts. We demonstrate the fabrication of a wafer-size amorphous $PtSe_x$ films on a SiO_2 substate via a low-temperature amorphization strategy, which offers single-atom-layer Pt catalysts with high atom-utilization efficiency (~26 wt%). This amorphous $PtSe_x$ behaves as a fully activated surface, accessible to catalytic reactions, and features a nearly 100% current density relative to a pure Pt

surface and reliable production of sustained high-flux hydrogen. Such an amorphization strategy is potentially extendable to other noble metals, including the Pd, Ir, Os, Rh and Ru elements, demonstrating the universality of single-atom-layer catalysts. The study is performed by combining AC HAADF STEM with DFT calculations and precise electrochemical tests [2].

References:

[1] Y He *et al*, Nature Communications **11** (2020), p. 57.
[2] Y He *et al*, Nature Catalysis **5** (2022), p. 212.
[3] T Zhang *et al*, Energy & Environmental Science **14** (2021), p. 4847.
[4] Z Liang *et al*, Advanced Energy Materials **11** (2021), 2003507.

[5] ICN2 acknowledges funding from Generalitat de Catalunya 2017 SGR 327. This study was supported by MCIN with funding from European Union NextGenerationEU (PRTR-C17.I1) and Generalitat de Catalunya. The authors thank support from the project NANOGEN (PID2020-116093RB-C43), funded by MCIN/ AEI/10.13039/501100011033/ and by "ERDF A way of making Europe", by the "European Union". ICN2 is supported by the Severo Ochoa program from Spanish MINECO (Grant No. SEV-2017-0706) and is funded by the CERCA Programme / Generalitat de Catalunya.

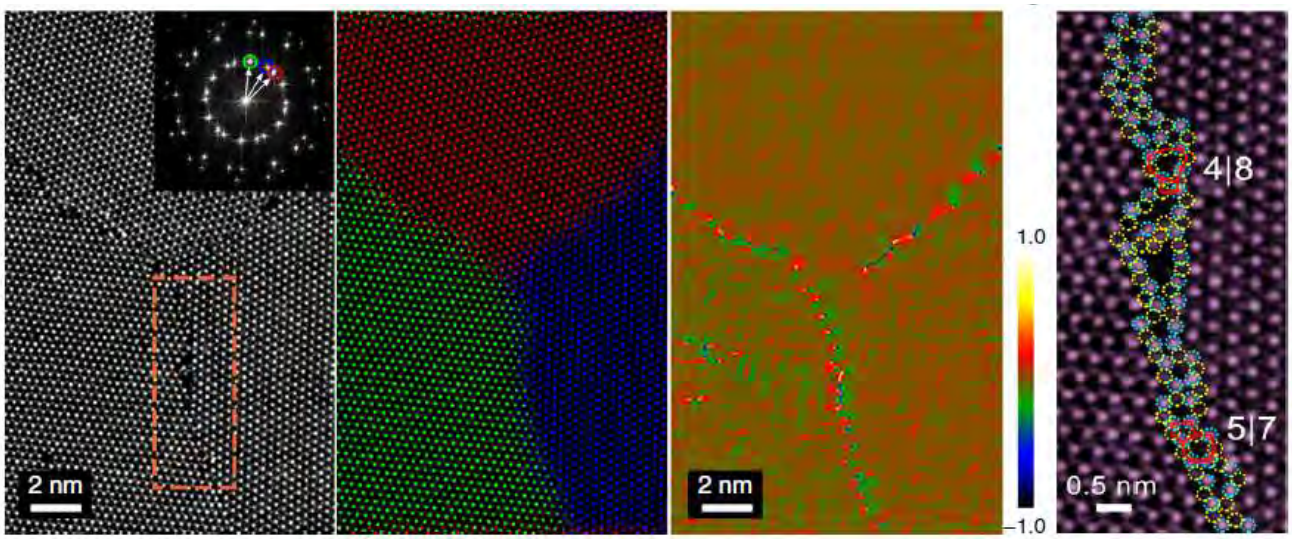

Figure 1. AC HAADF STEM magnified example of a triple grain boundary and a detail of the complex bonding coordination [1].

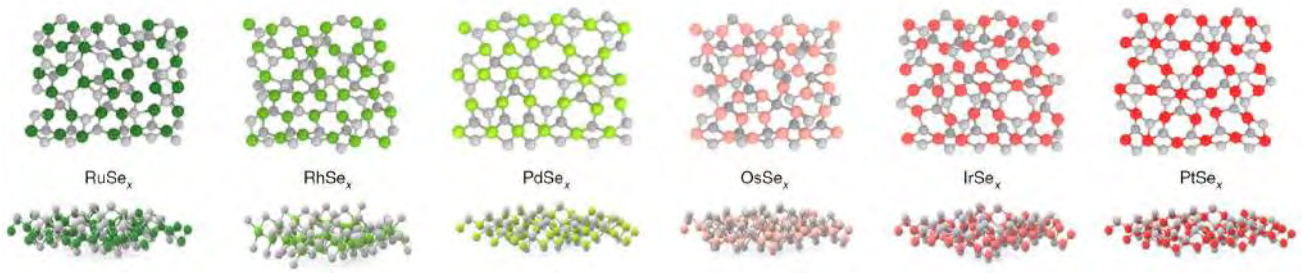

Figure 2. Design of a family of noble metal single-atom-layer catalysts from their amorphous selenides, such as $RuSe_x$, $RhSe_x$, $PdSe_x$, $OsSe_x$, $IrSe_x$ and $PtSe_x$, boosting the potential for various electrocatalytic applications [2].

Use of Analytical Electron Microscopy to Characterize Microstructure and Develop Transformation Pathways in Compositionally Complex Alloys

Zachary Kloenne[1], Kamalnath Kadirvel[1], Jean-Philippe Couzinié[2], Jake Jensen, William Clark[1], Gopal Viswanathan[1], Yunzhi Wang[1], and Hamish L. Fraser[1]

1 Center for the Accelerated Maturation of Materials, Department of Materials Science and Engineering, The Ohio State University, Columbus, OH USA

2 Univ. Paris Est Creteil, CNRS, ICMPE, UMR 7182, 2 rue Henri Dunant, 94320, Thiais, France

Compositionally complex alloys (CCA) have been the subject of considerable study in the recent past. They are a variety of High Entropy Alloys (HEA) which are alloys consisting of a number of alloying elements approaching equiatomic compositions. CCAs also contain such a large number of alloying elements but unlike HEAs, which are generally single phase, CCAs tend to consist of two or more phases such that refractory versions of the alloys would be expected to exhibit useful creep performance. In the present study, the alloy $AlMo_{0.5}NbTa_{0.5}TiZr$ has been the subject of study, chosen on the basis of early work indicating the retention of compressive strength at very high temperatures [1].

The microstructure of this alloy ($AlMo_{0.5}NbTa_{0.5}TiZr$) following an anneal at 1400°C for 24 hours followed by furnace cooling to room temperature is shown in Fig. 1. As may be noted, the vast majority of the microstructure consists of a mixture of two phases, one being a *bcc* solid solution and the other a B2 intermetallic compound. It has been shown by STEM-HAADF tomography that the B2 compound is the continuous phase, and the bcc solid solution is the discontinuous phase, i.e., precipitated within the B2 compound. The microstructure resembles somewhat that of a Ni-base superalloy but "inverted" such that the ordered phase is continuous, and the disordered phase is discontinuous, opposite to that in a superalloy. There appears to be lattice correspondence between the two phases and the orientation relationship is $\{100\}_{B2}//\{100\}_{bcc}$ and $<100>_{B2}//<100>_{bcc}$. Annealing samples possessing this microstructure at 1000°C for 2 hours followed by quenching to room temperature leads to a small degree of coarsening of the two phases and a loss of coherency between them. Much of the characterization has been reported in [2 & 3].

The interfaces between the B2 and *bcc* precipitates in both the two types of microstructure (i.e., that evolved following annealing at 1400°C followed by furnace cooling to room temperature and that further annealed at 1000°C and quenched to room temperature) have been characterized using aberration-corrected STEM, dichromatic analysis, and diffraction contrast TEM. It has been shown that aging at 1000°C leads to a loss of coherency such that an array of misfit dislocations with **b**=1/2<111> are present to accommodate the misfit between the two phases.

The presence of a B2 phase in this CCA is of interest. Thus, it is important to determine the degree of ordering, and hence it is necessary to determine the distribution of the various elements over the two sub-lattices. This has been attempted by use of spatially resolved XEDS in an aberration-corrected STEM, coupled with the use of the ordering-tie line approach [4]. There are problems with the effect of phonon scattering producing "cross-talk" between the spatially-resolved XEDS data, and also sample drift, however, an estimate of the degree of ordering indicates that the B2 compound is fully ordered.

Using the detailed characterization described above, a phase field model of the phase transformation pathway has been developed. It is shown that the pathway involves a conditional spinodal of the

ordered phase in which the dilute phase formed congruently transforms to a *bcc* phase. The details of this phase field model may be found in [5].

References:

[1] O. Senkov, C. Woodward, D. Miracle, JOM, Vol 66, No. 10,(2014), p. 2030.
[2] J.K.Jensen, B.A. Welk, R.E.A. Williams, J.M. Sosa, D.E. Huber, O.N. Senkov, G.B. Viswanathan, and H.L. Fraser, Scripta Materialia, 121, (2016), 1-4.
[3] J. M. Sosa, J. K. Jensen, D. E. Huber, M. A. Gibson, and H.L. Fraser, Materials Science and Technology **31**, 1250-1258, (2015).
[4] D.H. Hou, I.P.Jones, and H.L.Fraser, Phil. Mag., A74, (1996), p. 741.
[5] K. Kadirvel, Z. Kloenne, J. Jensen, H. Fraser, R. Banerjee, and Y. Wang, Appl. Phys. Lett. 119, 171905 (2021); doi: 10.1063/5.0065522

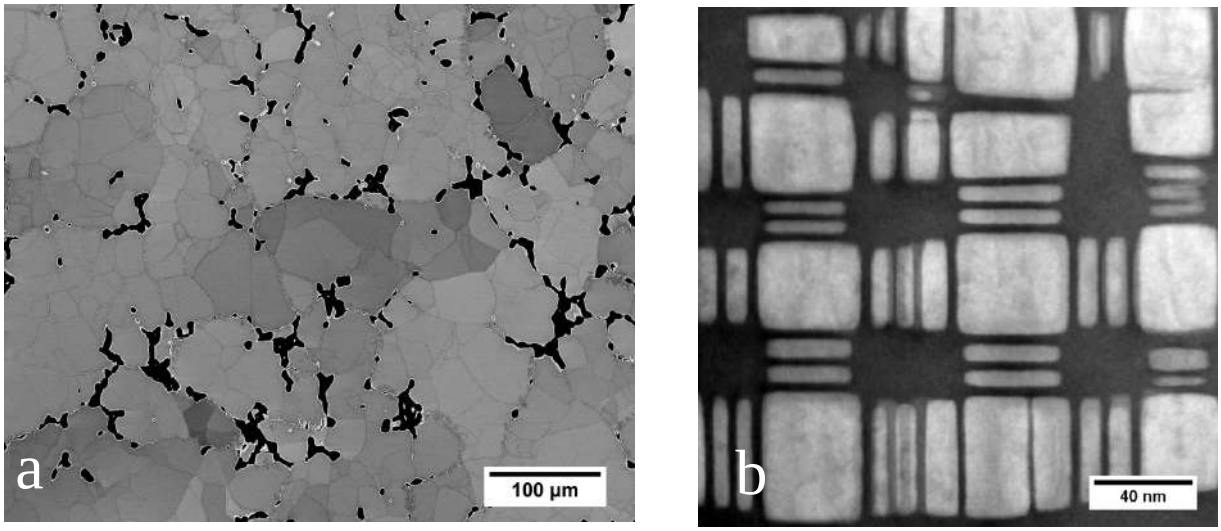

Figure 1. a) Backscattered electron image of the microstructure of the alloy $AlMo_{0.5}NbTa_{0.5}TiZr$ following aging at 1400°C for 24 hours and furnace cooling to room temperature. The microstructure of the light gray phase is shown in the HAADF image in (b). In this latter image, the dark phase is a B2 compound and the light phase is a *bcc* solid solution.

Applications and Challenges in STEM Inelastic Imaging

Gerald Kothleitner[1], Mihaela Albu[2], Evelin Fisslthaler[2], Georg Haberfehlner[1], Robert Krisper[1,2], Judith Lammer[1,2] and Werner Grogger[1]

1 Institute of Electron Microscopy and Nanoanalysis (FELMI), Graz University of Technology, Steyrergasse 17, 8010 Graz, Austria
2 Centre for Electron Microscopy (ZFE), Steyrergasse 17, 8010 Graz, Austria

STEM inelastic imaging based on signals with X-rays (and energy-loss electrons) has made tremendous progress in the past. Large area elemental maps, as well as atomic resolution images, have become routine due to innovations both in the electron column and analytical equipment. High-brightness guns, fast scan engines, as well as increased collection efficiency, high read-out rates, artifact correction (drift), and processing capabilities (quantification) now allow for efficient studies of a variety of material systems and have also paved the way for enhanced 3D tomographic investigations.

The opening part of the paper intends to highlight some exciting findings related to defects. The first example shall demonstrate the intricacies of defect formation on precipitation in aluminium alloys, which contain zirconium and scandium constituents [1]. The 3D presence of Al atoms, detectable by electron tomography only, at the Zr/Sc positions in the minority sublattice enables solute diffusion inside the precipitates. This becomes possible through the formation of Al channels that then accelerate precipitate homogenization. In another study of a eutectic Al-Si alloy twinning mechanisms have been studied [2], showing that twin nucleation at Sr columns is energetically favorable and twins may nucleate in Si precipitates after solidification, providing a different perspective to the currently accepted mechanisms. Finally, in the class of oxide ceramics with high oxygen, proton, and electronic conductivities, local variations in the column occupancies can lead to altered mass and charge transport properties. By treating the underlying X-ray signal generation in a quantitative manner, the correct intensities from neighboring atomic columns can be obtained from technologically rather promising Ruddlesden-Popper phases. Despite the convenient applicability of X-ray analysis, the technique still suffers from quite some issues that need to be better understood. The second part of the submission, therefore, concentrates on more fundamental technical aspects, ultimately related to quantitative investigations and more faithful 3D tomographic reconstructions. In tomography, complementary signals with potentially differing intrinsic sampling and resolution (e.g. HAADF vs. EDX) ought to be correlated and linked in reconstructions to gain extra information and prevent artifacts. By implementing different variational norms and penalty terms into a novel total generalized variation (TGV) based reconstruction scheme, 3D chemical phase gradients and unsharp interfaces are put out correctly [3,4,5]. Another complication is added when in-situ heating experiments are performed, while recording X-ray spectra, possibly under oriented sample conditions. Holder-induced detector shadowing, IR radiation, peak resolution losses, etc. are encountered and need to be tackled, requiring also thorough modeling of the collection geometries.

References:

[1] A Orthacker et al, Nature Materials 17 (2018) p. 1101.
[2] M Albu et al, Scientific Reports 6 (2016) p. 31635.
[3] R. Huber et al, Nanoscale 11 (2019) p. 5617.
[4] A number of collaborators not mentioned in the authors list shall be thanked for their contributions to this work: The substantial help of R.C. Picu (Rensselaer Polytechnic Institute, US), B. Sonderegger (IMAT TU Graz, Austria), K. Bredies (IMSC KFU Graz, Austria), B.

Mendis (Durham University, UK) M. Dienstleder (ZFE Graz, Austria) and L.J. Allen (Monash Univ., Melbourne Australia) is acknowledged.

[5] Much of the presented work has received funding within a project from the European Union's Horizon 2020 research and innovation program under Grant Agreement No. 823717, titled ESTEEM3.

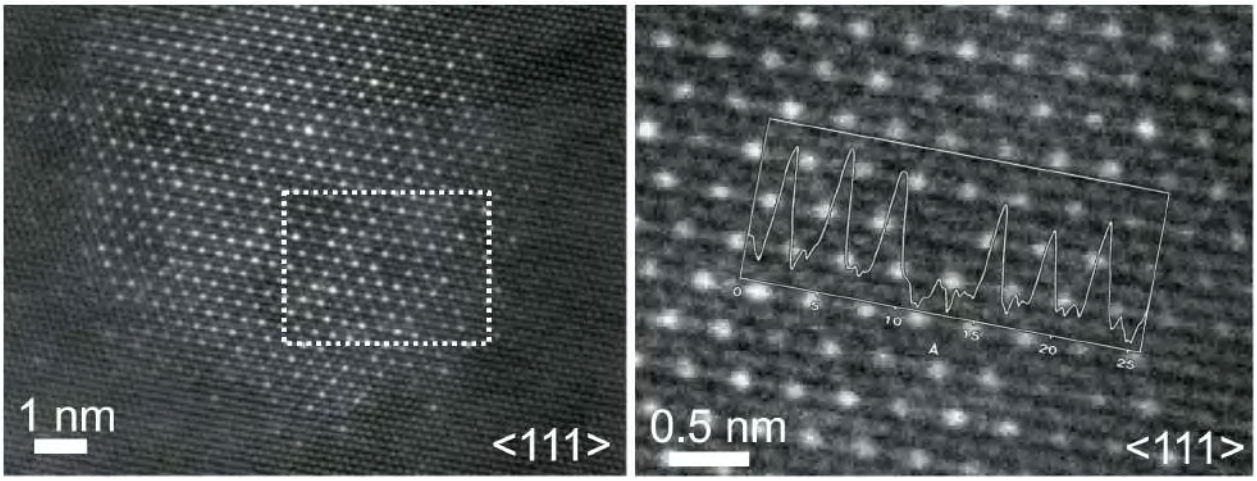

Figure 1. Al (Sc, Zr) alloy showing coherently embedded, heterogeneous core-shell $Al_3Zr_xSc_{1-x}$ precipitates with $L1_2$ structure (left). Column defects therein (right).

Multi-Element Segregation at Bcc Iron Grain Boundaries and Their Impact On Mechanical Properties

Ali Ahmadian[1], Daniel Scheiber[2], Xuyang Zhou[1], Baptiste Gault[1,3], Christian H. Liebscher[1], Lorenz Romaner[2,4] and Gerhard Dehm[1]

1 Max-Planck-Institut für Eisenforschung GmbH, Düsseldorf, Germany

2 Materials Center Leoben GmbH, Leoben, Austria

3 Department of Materials, Royal School of Mines, Imperial College London, London, UK

4 Montanuniversität Leoben, Leoben, Austria

The chemical composition and structure of grain boundaries in steels is known to have a significant impact on the resulting mechanical properties. It is well established that for example B promotes grain boundary cohesion, while Zn decreases it [1]. However, the multitude of elements present in steels and their interactions at the grain boundary make predictions of arising co-segregation behavior difficult and thus prevent a detailed understanding of the resulting mechanical properties.
Nowadays the lack of experimental insights elucidating the atomic structure and local chemical composition of a grain boundary can be mitigated by combining atomic resolved scanning transmission electron microscopy (STEM) with the unprecedented chemical sensitivity of atom probe tomography. In this overview we report our recent findings on co-segregation of Al, B, C [2] and Zn, Al, B, C at a Σ5 (3 1 0)[0 0 1] tilt grain boundary in Fe. Fig. 1 presents an atomic resolved Z contrast image of the grain boundary structure without Zn. Note in the red boxed region deviations from the perfect kite structure indicating already different site occupation. Upon Zn segregation substantial differences are observed and an inhomogeneous Zn decoration occured. The experiments are complemented by first-principles calculation explaining enrichment or depletion of certain elements due to their attractive or repulsive interactions. These insights provide information on the cohesive strength of the grain boundary.

References:

[1] P. Lejček, Grain Boundary Segregation in Metals. No. 136 in Springer Series in Materials Science (Springer-Verlag, Berlin, 2010).
[2] A. Ahmadian, D. Scheiber, X. Zhou, B. Gault, C. H. Liebscher, L. Romaner and G. Dehm, Nature Communications **12** (2021), 6008. doi.org/10.1038/s41467-021-26197-9

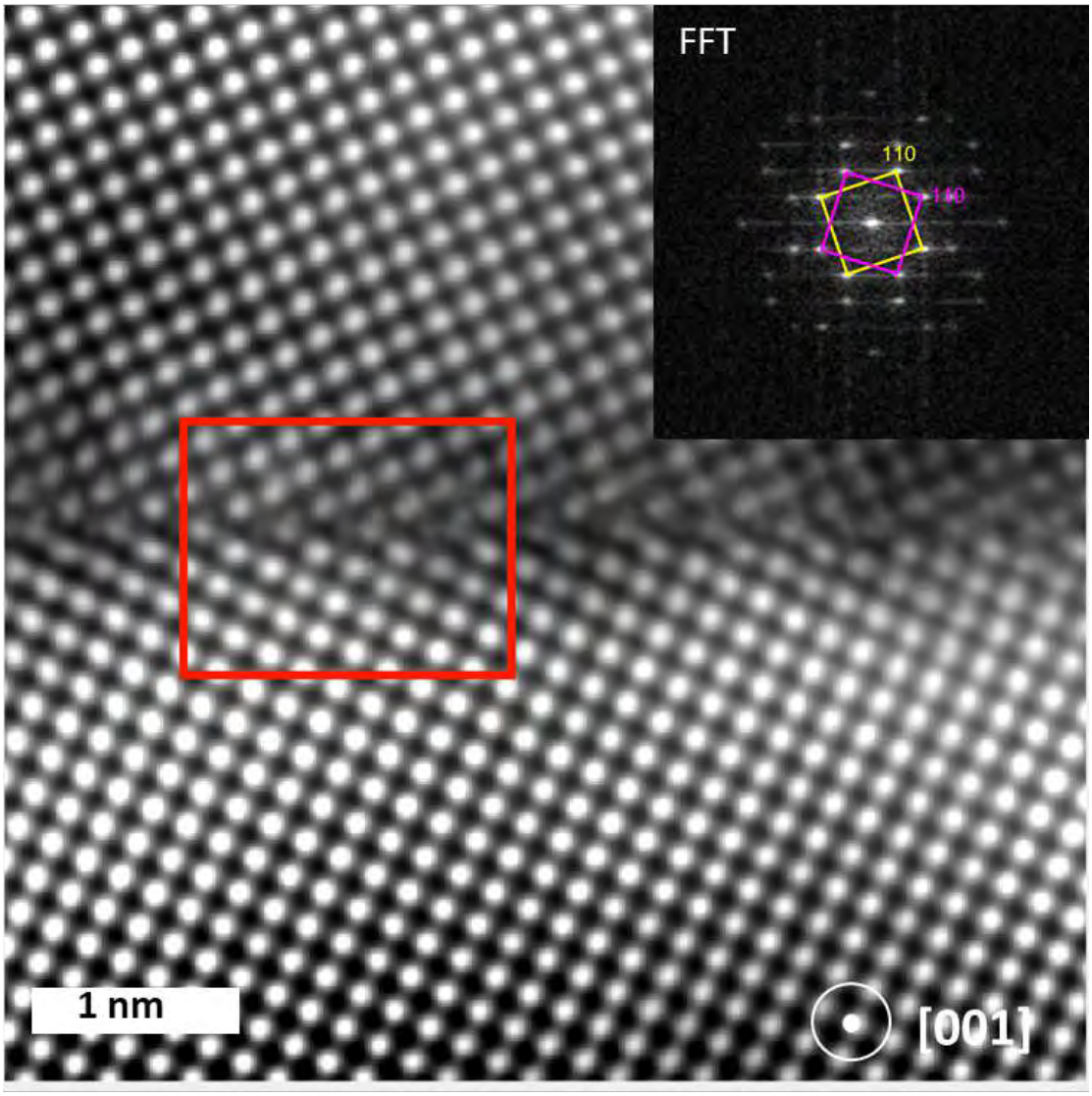

Figure 1. High angle annular STEM image and corresponding Fast Fourier Transformation (FFT) of Σ5 (3 1 0)[0 0 1] tilt grain boundary in Fe (Al,C,B). Note in the red box deviations of atomic column positions from the perfect kite structure due to segregation effects. Taken in modified form from [2].

In Situ Electron Microscopy Revealing Site Specific Strain Induced Changes in Properties and Structure on the Atomic Scale

Eva Olsson

Department of Physics, Chalmers University of Technology, Gothenburg, Sweden.

Electron microscopy enables direct site specific determination of structure and properties on the atomic scale using the imaging, diffraction and spectroscopy modes of the instrument. High resolution annular dark field (ADF) scanning transmission electron microscopy (STEM) imaging can, for example, provide high spatial resolution (better than 1 Å) and high precision (better than 1 pm) information about the local atomic structure [1]. Crucial information about the effects of atomic structure and site specific strain can be obtained by correlating *ex situ* measurements of properties and modelling of, for example, catalytic activity. Additional important information about site specific properties can be obtained by in situ microscopy where the material structure is exposed to different types of stimuli. Examples of stimuli are gas, liquid, temperature, electric field, mechanical strain and light. This talk will focus on *in situ* microscopy enabled by sample holders with piezo driven in situ manipulation to study effects of electric field, light, mechanical strain and temperature on properties and structure. Important aspects, that need to be considered to ensure that the *in situ* studies are representative of the true behaviour of the material structures, will also be discussed.

The material surface is the initial point of contact with gases, liquids and solids in applications of catalysis, sensing, biomolecular interactions and nano- and molecular electronics. An ability to switch the atomic structure of a surface would also switch the characteristics of the device. During *in situ* electron microscopy studies of cold field emission of electrons from gold nano-cones it was shown, that at a critical electric field, that a few-atomic-surface-layer was transformed from a perfect crystalline structure to a disordered structure [2]. The transition was reversible where the structure reverted to the crystalline structure when the electric field was reduced to below the critical value. The structural changes were directly observed in real time by imaging using high resolution transmission electron microscopy. The critical electric field was 25 V/nm and was controlled and achieved by the combination of precise control of the distance between the tip of the gold nano-cone and the counter electrode and also to the conical geometrical shape that enhanced the field at the tip.

The electric field switching of the atomic structure of the gold surface is one example of how *in situ* manipulation in the electron microscopy enables the direct correlating between material structure and properties at high spatial resolution. The effect of electric fields, light, mechanical strain and temperature on both structure and properties can be quantitatively studied using imaging, diffraction and spectroscopy. The obtained knowledge is used to tune the properties of advanced materials and devices. Catalytic activity of metal nanoparticles [1] and electrical properties of semiconducting nanowires [3-7] are examples where strain has a strong influence on the properties and performances. The heat dissipation [8] and the thermal handling capabilities can be changed by the presence of a one atomic layer thin surface film [9]. New aspects of material properties and mechanisms, not obvious from measurements on the macro scale, can be revealed using *in situ* electron microscopy. The knowledge is crucial for not only the understanding of the mechanisms that are involved but also for the design or materials and devices with tailored properties.

References:

[1] T. Nilsson Pingel *et al*, “Influence of atomic site-specific strain on catalytic activity of supported nanoparticles”, *Nature Comm.* **9** (2018) 2722.
[2] L. de Knoop *et al*, Electric field controlled reversible order-disorder switching of a metal tip surface”, *Phys. Rev. Mat.* **2 (**2018) 085006.
[3] L. J. Zeng *et al*, ”Correlation between electrical transport and nanoscale strain in InAs/In0.6Ga0.4As core-shell nanowires, *Nano Letters* **18** (2018) 4949.
[4] L. Zeng *et al*, “The effect of bending deformation on charge transport and electron effective mass of p-doped GaAs nanowires”, *Phys. Status Solidi RRL* **13** (2019) 1900134.
[5] J. Holmér *et al*, ”An STM-SEM setup for characterizing photon and electron induced effects in single photovoltaic nanowires”, *Nano Energy* **53** (2018) 175.
[6] J. Holmér *et al*, ”Enhancing the NIR photocurrent in single GaAs nanowires with radial p-i-n junctions by uniaxial strain”, *Nano Letters* **21** (2021) 9038.
[7] L. Zeng, J. Holmér, R. Dhall, C. Gammer, A.M. Minor, E. Olsson, ”Tuning hole mobility of individual p-doped GaAs nanowires by uniaxial tensile stress”, *Nano Letters* **21** (2021) 3894.
[8] N. Voskanian, E. Olsson, J. Cumings, “Field-dependent heat dissipation of carbon nanotube electric currents”, *Scientific reports* **9** (2019) 10785.
[9] H.M. Nilsson, L. de Knoop, J. Cumings, E. Olsson, “Localized resistance measurements of wrinkled reduced graphene oxide using in situ transmission electron microscopy”, *Carbon* **113** (2017) 340.

A Scale Bridging Approach For Analysis of Extended Defects in Thermoelectric Materials: From Electron Channeling Contrast Imaging, Scanning Transmission Electron Microscopy to Atom Probe Tomography

Christina Scheu[1], Lamya Abdellaoui[1], Ruben Bueno Villoro[1], Oana Cojocaru-Mirédin[2], Baptiste Gault[1,3], Ting Luo[1], Chanwon Jung[1], Yuan Yu[2], Stefan Zaefferer[1] and Siyuan Zhang[1]

1 Max-Planck-Institut für Eisenforschung GmbH, Düsseldorf, Germany
2 Institute of Physics (IA), RWTH Aachen University, Aachen, Germany
3 Department of Materials, Royal School of Mines, Imperial College London, London, UK

Thermoelectric materials can contribute to environmentally friendly energy generation by converting waste heat into electricity. Their conversion efficiency is described by the figure of merit *ZT*, which is defined as $ZT = S^2\sigma T/\kappa$. Here S is the Seebeck coefficient, T the temperature, σ the electrical conductivity and κ is the thermal conductivity. Several approaches exist to reduce the thermal conductivity such as reducing grain size, insertion of point defects or precipitates and adding planar defects or dislocation. All of these defects can scatter phonons efficiently, thus reducing the thermal conductivity. At the same time, they often reduce the electrical conductivity, which is unwanted. However, a few cases are reported, where defects can also show an enhanced electrical conductivity due to the formation of conductive pathways. In order to booster the efficiency further, it is of great importance to characterize the defects on different length scales – starting from the millimeter/micrometer level down to the atomic scale. The defect density has to be evaluated in a statistically relevant manner while at the same time the atomic arrangement and chemical composition need to be determined with high spatial resolution.

In order to fulfill this task, we deployed a scale-bridging approach. Defects are characterized from the millimeter/micrometer level down to the atomic scale using a combined approach of various imaging and spectroscopic techniques. Electron channeling contrast imaging (ECCI) in conjunction with electron back-scatter diffraction (EBSD) mapping in a scanning electron microscope (SEM) are used to determine the distribution and densities of extended defects. (Scanning) transmission electron microscopy (STEM) imaging, energy-dispersive X-ray spectroscopy (EDX) and electron energy-loss spectroscopy (EELS) in STEM mode are often combined with atom probe tomography (APT) to unravel the atomic structure and composition of the defects.

This approach was applied to analyze the δ-phase of an $Ag_{16.7}Sb_{30}Te_{53.3}$ thermoelectric material [1]. EBSD measurements revealed that the as-quenched material possesses a mosaic structure with low angle grain boundaries with misorientation angles up to 3°. These grain boundaries consist of planar faults as determined by ECCI in conjunction with STEM investigation. Target sample preparation by focused ion beam milling allowed to study identical areas with different techniques. The density of the planar faults was estimated on a larger scale using the ECCI data and found to be around 10^8 m^{-1}, in close agreement to the STEM data [1]. According to the Callaway-Klemens models, the planar faults enhance the phonon scattering rate which leads to a lower thermal conductivity [1].

In another study, we investigated the dislocation network of an $Eu_{0.03}Na_{0.025}Pb_{0.945}Te$ alloy [2]. A kernel average misorientation map obtained through EBSD mapping and ECCI revealed that the grains possess small misorientations of less than 1° and an array of parallel edge dislocations was observed (Figure 1a and 1b). The Burgers vector of the edge dislocation is 1/2[110] as determined by TEM. A similar dislocation density of about 10^{10} cm^{-2} was estimated from the TEM images (Figure 1c), in accordance to the ECCI results [2]. However, the dislocations density alone cannot explain the low thermal conductivity of the alloy. We found that another important factor is the chemical

composition of the dislocation. APT revealed Na enrichment at the dislocation core of 7 at.% while the content in the matrix was only 0.6 at.% (Figure 1d). The strain field and Cottrell atmosphere associated with the Na decoration at the dislocations lead to an increased phonon scattering and a reduction in the thermal conductivity [2]. Similar effects were found in an $(PbTe)_{0.97}(Ag_2Te)_{0.03}$ alloy, also studied by our developed methodology. In that case, the amount of Ag at dislocations was 10-times higher in comparison to the matrix [3].

References:

[1] L Abdellaoui, S Zhang, S Zaefferer, R Bueno-Villoro, A Baranovskiy, O Cojocaru-Mirédin, Y Yu, Y Amouyal, D Raabe, GJ Snyder and C Scheu, Acta Materialia, **178** (2019), 135.

[2] L Abdellaoui, Z Chen, Y Yu, T Luo, R Hanus, T Schwarz, R Bueno, O Cojocaru-Mirédin, GJ Snyder, D Raabe, Y Pei, C Scheu and S Zhang, Advanced Functional Materials, **31** (2021), 2101214.

[3] Y Yu, S Zhang, AM Mio, B Gault, A Sheskin, C Scheu, D Raabe, F Zu, M Wuttig, Y Amouyal, O Cojocaru-Mirédin, ACS Applied Materials Interfaces, **10** (2018), 3609.

[4] The authors would like to acknowledge the fruitful collaboration, discussion with Y Amouyal (Technion, Israel), G.J. Snyder (Northwestern University, USA) and Y. Pei (Tongji University, China) and for providing the materials.

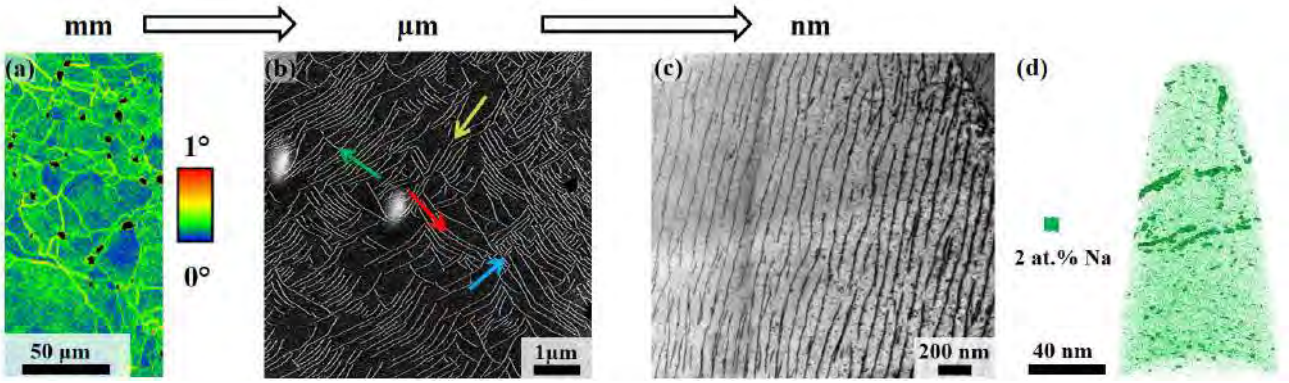

Figure 1. a) Kernel misorientation map obtained from EBSD data set, b) ECCI image, c) bright field TEM image and d) APT reconstruction showing dislocation networks and Na enrichment at the dislocations. Figures and data taken from [2].

Integrated Differential Phase Contrast (iDPC) STEM for Low Dose Imaging of Beam Sensitive Materials and Cryo Nano Particles at Atomic Resolution

Ivan Lazić[1], Maarten Wirix[1], Max Leo Leidl[2,3,4,5], Daniel Mann[2,5], Maximilian Beckers[2,6], Evgeniya V. Pechnikova[1], Knut Müller-Caspary[3,4,5], Anna Carlsson[1], Arno Meingast[1], Felix de Haas[1], Carsten Sachse[2, 5, 7]

1 Materials and Structural Analysis Division, Thermo Fisher Scientific, Eindhoven, The Netherlands.
2 Ernst Ruska-Centre for Microscopy and Spectroscopy with Electrons (ER-C-3): Structural Biology, Jülich, Germany.
3 Department of Chemistry and Centre for NanoScience, Ludwig-Maximilians-University, Munich, Germany
4 Ernst Ruska-Centre for Microscopy and Spectroscopy (ER-C-1): Physics of Nanoscale Systems, Jülich, Germany.
5 Institute for Biological Information Processing (IBI-6): Cellular Structural Biology, Jülich, Germany.
6 Structural and Computational Biology Unit, European Molecular Biology Laboratory (EMBL), Heidelberg, Germany
7 Department of Biology, Heinrich Heine University, Universitätsstr. 1, Düsseldorf, Germany.

Historically, light elements and beam sensitive materials have been imaged using conventional transmission electron microscopy (TEM) exploiting parallel electron beam illumination. Through single particle analysis (SPA) and cryo TEM technology electron microscopy has also found its way towards life science (LS) and biological applications. In these directions, scanning TEM (STEM) has played only a modest role, particularly low in revealing biological nano particle structures at near atomic resolution. Recently, a new modality called integrated differential phase contrast (iDPC) STEM [1, 2] revealed a strong capacity to image light next to heavy elements at atomic resolution [3, 4, 5] also within structures that are highly beam sensitive to electron radiation [6, 7].

iDPC-STEM is utilized as the integration of the DPC vector field to resolve the iDPC scalar field [1]. For a thin sample the DPC vector field represents the projected electric field, which, when integrated into iDPC, yields the projected electrostatic potential field of the sample [1, 2]. Consequently, iDPC-STEM is directly interpretable since the potential field has maxima at the atomic core positions. Classically, annular dark field (ADF)-STEM, also offers a direct interpretation albeit *the square* of the electrostatic potential field of the sample [1, 8], favorizing heavy elements. On the other hand, iDPC-STEM visualizes the entire periodic table, down to hydrogen [9]. *In addition, the benefits listed above remain* true at all high tensions down to 30 kV so that the accelerating voltage can be freely chosen, to reduce beam damage [10] or to suit sample thickness [11].

These desirable properties do not come at the expense of low-dose performance. Experimentally, capability to image metal organic frameworks (MOF-s) [6] and zeolites including single molecules [7] with unprecedented resolution has been proven. An iDPC-STEM image of a MOF structures as used in [6] is shown in Fig. 2, with resolutions of 1.4 Å using total electron dose of *54* $e^-/Å^2$ and 2 Å using total electron dose of *42* $e^-/Å^2$. This strongly encourages STEM investigation in biological applications [12], including imaging of biological cryo nano particles at near-atomic resolution [13].

Here, STEM imaging of various beam sensitive materials and cryo-EM specimens will be presented. For LS, cryo SPA micrographs have been acquired using iDPC-STEM, e.g. of Keyhole Limpet Hemocyanin (KLH) protein and Tobacco Mosaic Virus (TMV) and have been successfully used for near atomic resolution 3D reconstructions (Fig. 2).

Tobacco mosaic virus (TMV) is a well-known and in-depth studied specimen [14], used to show capabilities of the new approach. The micrographs show complete signal transfer to high resolution. This enables cryo-STEM 3D structure reconstruction routinely at 3.5 Å resolution using standard helical reconstruction. The associated map B-factors from iDPC-STEM match those obtained by CTEM recordings using 2nd generation cameras.

References:

[1] I. Lazić, E.G.T. Bosch and Sorin Lazar, Ultramicroscopy **160** (2016), 265.
[2] I. Lazić and E.G.T. Bosch, Advances in Imaging and Electron Physics **199** (2017), 75.
[3] E. Yücelen, I. Lazić and E.G.T. Bosch, Scientific Reports **8** (2018), 2676.
[4] H. Nahor *et al.*, Acta Materialia **154** (2018), 71.
[5] D. Song *et al.*, Advanced Functional Materials **29** (2019), 1903843.
[6] B. Shen *et al.*, Nature Communications **11** (2020), 2692.
[7] B. Shen *et al.*, Nature **592** (2021), 541.
[8] E.G.T. Bosch and I. Lazić, Ultramicroscopy **156** (2015), 59.
[9] S. de Graaf *et al.*, Science Advances **6** (2020), eaay4312.
[10] S. de Graaf *et al.*, Nanoscale **13** (2021), 20683.
[11] E.G.T. Bosch and I. Lazić, Ultramicroscopy **207** (2019), 112831.
[12] X. Li, *et al.*, Journal of Structural Biology **214** (2022), 107837.
[13] I. Lazić, *et. al.*, Nature Methods, accepted, (2022), preprint bioRxiv: https://doi.org/10.1101/2021.10.12.464113
[14] S.A. Fromm *et.al.*, Journal of Structural Biology, **189** (2015) 87.
[15] C Gatsogiannis and J. Markl, Journal of Molecular Biology **385**, (2009) 963.

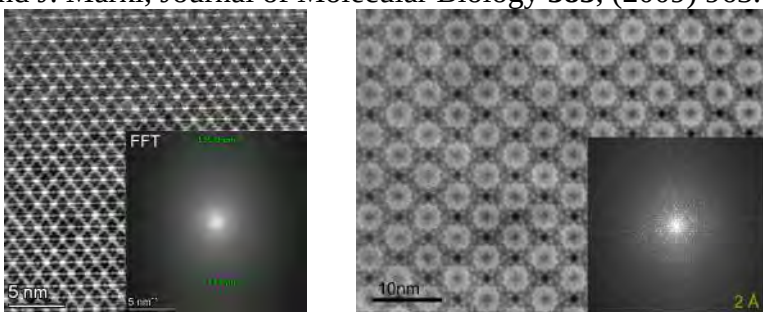

Figure 1. 200kV STEM imaging (Sample courtesy: Prof. Y. Han, KAUST Catalysis Center; Images: Arno Meingast and Anna Carlsson) **left)** iDPC-STEM image of metal organic framework (MOF), UiO-66 acquired with total electron dose of 54 $e^-/Å^2$, showing resolution of 1.41 Å (FFT insert) and **right)** *iDPC-STEM image of* MOF, MIL-101 acquired with total electron dose of 42 e^-/A^2, showing resolution of 2 Å

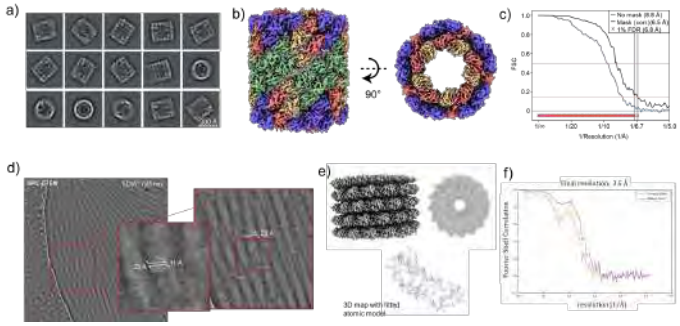

Figure 2. 300kV iDPC-STEM cryo SPA examples. **Top:** KLH at 3.5 mrad convergence semi-angle (CSA). **a)** 2D projections **b)** 3D volume reconstruction, side and top view **c)** FSC resolution determined at 6.5 Å (earlier reported 9 Å [15]) **Bottom:** TMV at 3.5 mrad CSA beam **d)** Example of iDPC-STEM micrograph **e)** Reconstructed 3D volume (side and top view) and molecular model fit **f)** FSC resolution determined at 3.5 Å.

2D and 4D STEM Imaging of Beam Sensitive Materials

Peter D. Nellist[1], Mathias Uller Rothmann[2], Michael B. Johnson[2], Laura M. Herz[2], Weixin Song[1], Peter G. Bruce[1], Hui Luo[1], Botao Hao[1], Hazel E. Assender[1] and Colum M. O'Leary[1,3]

1 Department of Materials, University of Oxford, Oxford, UK

2 Department of Physics, University of Oxford, Oxford, UK

3 Now at University of California Los Angeles and NCEM Berkeley, USA

The development and widespread application of aberration-corrected electron microscopy over the past 25 years has made atomic resolution imaging and spectroscopy of materials routine. Many candidate materials for important applications in energy conversion and energy storage are highly susceptible to damage under the irradiating electron beam and so an important current challenge is to develop methods that can allow the high-spatial resolution advantages of aberration correction to be applied to these materials.

Here the use of the aberration-corrected scanning transmission electron microscope (AC-STEM) for such applications will be described. It will be shown that the dose fractionation in both space and time enable by AC-STEM enables atomic resolution images to be formed for materials that hitherto have eluded such imaging.

Rapidly scanned annular dark-field (ADF) will be used to analyse defects in the organic-inorganic hybrid perovskite material, formamidinium lead iodide (FAPbI). It is shown that the remnant lead iodide precursor material is stabilized in an uncommonly observed trigonal structure that forms highly coherent interfaces with the cubic perovskite [1]. The initial effect of beam damage is found to be the formation of vacancies on the formamidinium sub-lattice which are seen to order into a superlattice (Figure 1), which explains why degraded material can be regenerated by exposure to a formamidinium-containing vapour.

Combining ADF imaging and ptychography provides a method that makes use of a very large fraction of the transmitted electrons. Simultaneous ADF STEM and ptychography is a powerful combination for the examination of Li-ion battery materials. In the case of a Li-rich cathode candidate material, the ADF image provides a reference for the transition metals in the layered monoclinic structure and the ptychography image reveals the location of the oxygen and lithium atoms (Figure 2). The distortion of the oxygen sublattice can be observed through the first charge-discharge cycle. Distortions of the O octahedra seen during the first charge are found to persist during discharge [2].

Careful choice of imaging conditions is required to enable the most dose-efficient imaging [3]. This approach will be demonstrated by application the structure of crystalline domains in polymer materials. [4]

References:

[1] M.U. Rothmann, et al., Science, **370**, eabb5940 (2020).
[2] W. Song et al., Joule **6** (2022) 1049–1065
[3] C.M. O'Leary, et al., Ultramicroscopy **221**, 113189 (2021).
[4] The author acknowledges support from JEOL UK, PNDetector, and funding from the EPSRC (EP/K040375/1, EP/M010708/1, EP/P033229/1), The Henry Royce Institute (Grant reference EP/R010145/1), EU 823717 ESTEEM3.

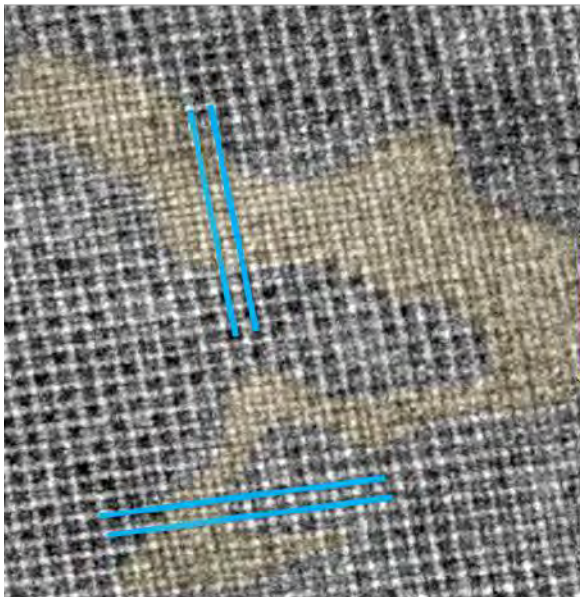

Figure 1. STEM LAADF image of FAPbI showing the coherent interface with PbI_2 precursor material and ordering of vacancies on the formamidinium sub-lattice. The unit cell size is 0.64 nm.

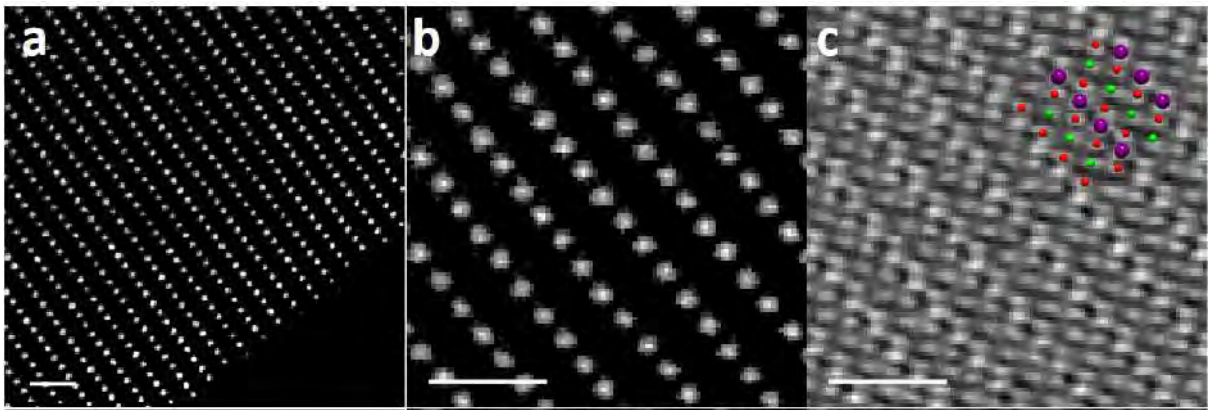

Figure 2. STEM imaging of $Li_{1.2}[Ni_{0.13}Mn_{0.54}Co_{0.13}]O_2$: (a) and (b) ADF images showing the transition metal layers. (c) Ptychography phase image recorded simultaneously with (b) showing the Li and O positions. Scale bar 1 nm.

The role of correlative CT and TEM investigations in the development of novel Li-ion battery materials

Joachim Mayer[1,2], Lara Ahrens[1,2], Helen Valencia-Naranjo[1,2], Shibabrata Basak[2,3]

1 Central Facility for Electron Microscopy, RWTH Aachen University, Aachen, Germany

2 Ernst Ruska-Centre, Forschungszentrum Jülich, Jülich, Germany

3 Institute for Energy and Climate Research, Forschungszentrum Jülich, Jülich, Germany

Here we report on investigations aiming at a scale-bridging and three-dimensional understanding of Li-ion battery electrodes and their functionalities, which requires information typically not fully accessible with electron microscopy techniques. Therefore, we employ microCT and nanoCT investigations, which provide very valuable insight in battery structures and ageing mechanisms, in a complementary and correlative way to gain information which can be combined with EM experiments. These investigations are then followed by higher resolution SEM, TEM and HRTEM characterization of the electrode microstructures, the anode and cathode materials and the surfaces and interfaces of a broad range on battery materials. The scale bridging results on materials and functionalities can be employed to design novel battery materials with improved storage capacities and to optimize the properties of the resulting concepts (Fig. 1).

MicroCT and NanoCT were used to determine the three-dimensional microstructure of the electrode samples. The MicroCT images were collected on a ZEISS Xradia 520 Versa 3D X-ray Microscope and NanoCT was performed on a ZEISS Xradia 810 Ultra 3D X-ray Microscope. The main difference of these two microscopes is the resolution, which is determined by the resolution on the detector of 0.35 µm/voxel for the 520 Versa and 32 nm/voxel for the 810 Ultra. The actual resolution on the sample can be estimated to be about twice the voxel size. The increased resolution of the 810 Ultra provides a very detailed picture of the active material, with microstructural details clearly resolved. Because of the lower x-ray energy used in the 810 Ultra, however, the sample geometries have to be limited to several ten micrometers in diameter. The CT images of the new and the aged cell can be visually and analytically compared and offer valuable insights in the structural changes during the ageing process.

For our HR-TEM investigations of Cathode materials, one specific example is the study of the Li-Co antisite exchange in Fe-substituted $LiCoPO_4$ (LCP) cathodes for high-voltage lithium ion batteries [1-3]. To improve the cycling performance of $LiCoPO_4$, the key approaches are to stabilize the structure of $LiCoPO_4$ and minimize or even prevent the antisite exchange between Li^+ and Co^{2+} ions. In principle, a stable structure indicates a good cycling performance. To stabilize the structure of $LiCoPO_4$ and suppress the Li-Co antisite exchange, doping Fe ions into $LiCoPO_4$ (LCFP) has been reported as an efficient approach. However, direct experimental evidences are still needed to prove the suppression effect on the Li-Co antisite exchange by Fe substitution.

Based on the above results, a schematic model of the antisite exchange process and the effect of Fe substitution could be developed. During the delithiation process, some Co atoms migrate to the Li^+ sites after the extraction of Li^+ ions. In the following lithiation process, the increased degree of cation disorder impedes the reinsertion of Li^+ ions into their original sites, which are now being occupied by Co^{2+} ions. As a consequence, the degree of Li-Co antisite exchange in LCP/C increases with each cycle, and it can form locally a new cation-ordered structure after cycling. With respect to LCFP/C, the substituted Fe^{2+} ions distribute uniformly in the Co sites. The preferential occupation of Co sites

by substituted Fe^{2+} effectively suppresses the exchange of Li ions and transition metal ions, mitigating the irreversible modification of the structure and in particular preserves the Li^{+} ion transport capabilities of LCFP/C.

References:

[1] Xiaochao Wua, Maria Meledina, Juri Barthel, Zigeng Liu, Hermann Tempel, Hans Kungl, Joachim Mayer, Rüdiger-A. Eichel, Energy Storage Materials 22 (2019) 138–146

[2] Wu, Maria Meledina, Hermann Tempel, Hans Kungl, Joachim Mayer, Rüdiger-A. Eichel, Journal of Power Sources 450 (2020) 227726

[3] Shibabrata Basak, Vadim Migunov, Amir H. Tavabi, Chandramohan George, Qing Lee, Paolo Rosi, Violetta Arszelewska, Swapna Ganapathy, Ashwin Vijay, Frans Ooms, Roland Schierholz,Hermann Tempel, Hans Kungl, Joachim Mayer, Rafal E. Dunin-Borkowski, Rüdiger-A. Eichel,Marnix Wagemaker, and Erik M. Kelder. ACS Applied Energy Materials 2020 3 (6), 5101-5106

[4] The authors gratefully acknowledge support by the BMBF in the framework of the Clusters AQUA and MEET HiEnd.

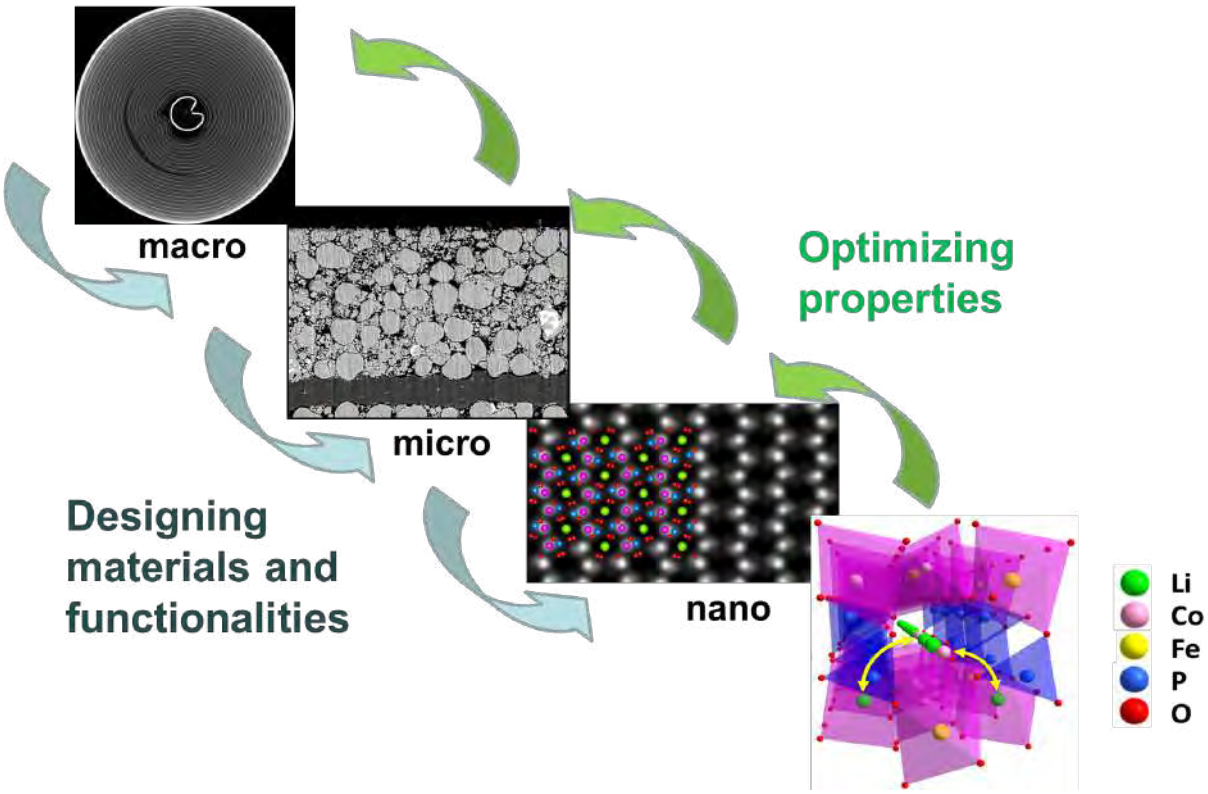

Figure 1. Schematic representation of the complementary and correlative workflow to gain information by combining CT, SEM and TEM characterization of the electrode microstructures, the anode and cathode materials of Li-ion battery systems.

Understanding the Structure of $LiMn_2O_4$ by Aberration-Corrected HAADF STEM and Differential Phase Contrast

Paulo J. Ferreira[1,2,3]

1 INL – International Iberian Nanotechnology Laboratory, Braga, Portugal

2 Mechanical Engineering Department and IDMEC, Instituto Superior Técnico, University of Lisbon, Lisboa, Portugal

3 Materials Science and Engineering Program, The University of Texas at Austin, Austin, Texas, USA

The rising need for portable energy storage has led to the creation of a formidable Li-ion battery industry, which is poised to grow strongly in the near future. Of the many cathode chemistries for Li-ion batteries, $Li[Mn_2]O_4$ (LMO) stands out as a particularly appealing cathode due to its moderate capacity, use of environmentally-friendly and cost-effective Mn, and high rate capabilities associated with its cubic spinel framework, which allows three dimensional Li^+ diffusion. Yet, this material has shown capacity loss, attributed to the dissolution of Mn to the electrolyte [1,2]. In this work we show by HAADF STEM that a restructured surface is formed in this material (Figure 1), where a stable surface layer of Mn_3O_4, followed by $Li_{1+x}Mn_2O_4$ subsurface with retention of bulk $LiMn_2O_4$ is formed [3]. In addition, recent advances in STEM allow us to observe not only the structure of the materials at atomic level, but also to obtain images proportional to the projected potential, the projected electric field and the projected charge distribution, by using differential phase contrast technique (DPC). Thus, in this work we also use DPC to determine the Li, Mn and O atomic positions, thus providing a novel insight into the structure of $LiMn_2O_4$. Our results clearly show local regions depleted in Li and the existence of manganese atoms in tetrahedral sites occupying a typical Li atom position, or occupying a free octahedral site in the same column (Figure 2), in agreement with the Mn disproportionation reaction reported for such compound [4] These findings contribute to a better understanding of the mechanisms of lithium and manganese exchange in $LiMn_2O_4$ spinel structures.

References:

[1] Hunter, J. J. Solid State Chem. 1981, 39, 142−147.
[2] Thackeray, M.; Johnson, P.; de Picciotto, L.; Bruce, P.; Goodenough, J. Mater. Res. Bull. 1984, 19, 179−187.
[3] Charles Amos, Manuel Roldan, Maria Varela, John Goodenough, Paulo Ferreira, Nanoletters, Vol. 16, pp 2899–2906 (2016).
[4] S. Calderon, R. Ribeiro. P.J. Ferreira, Ultramicroscopy, Vol. 225, pp. 113285 (2021)
[5] This work was supported by a NASA Office of the Chief Technologist's Space Technology Research Fellowship and the EU Framework Program for Research and Innovation H2020, scheme COFUND – Co-funding of Regional, National and International Programs, under Grant Agreement 713640. This work was supported by FCT, through IDMEC, under LAETA, project UIDB/50022/2020.

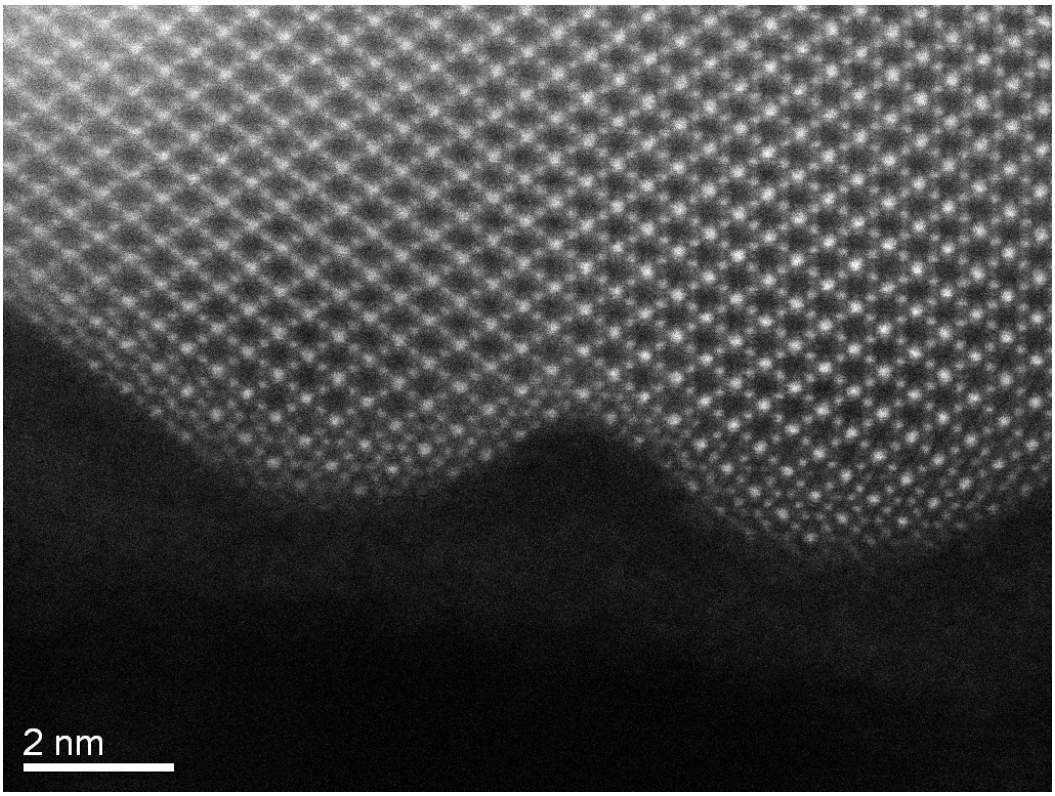

Figure 1. HAADF STEM image of LMO viewed along the [110] zone axis, showing the reconstructed surface [3].

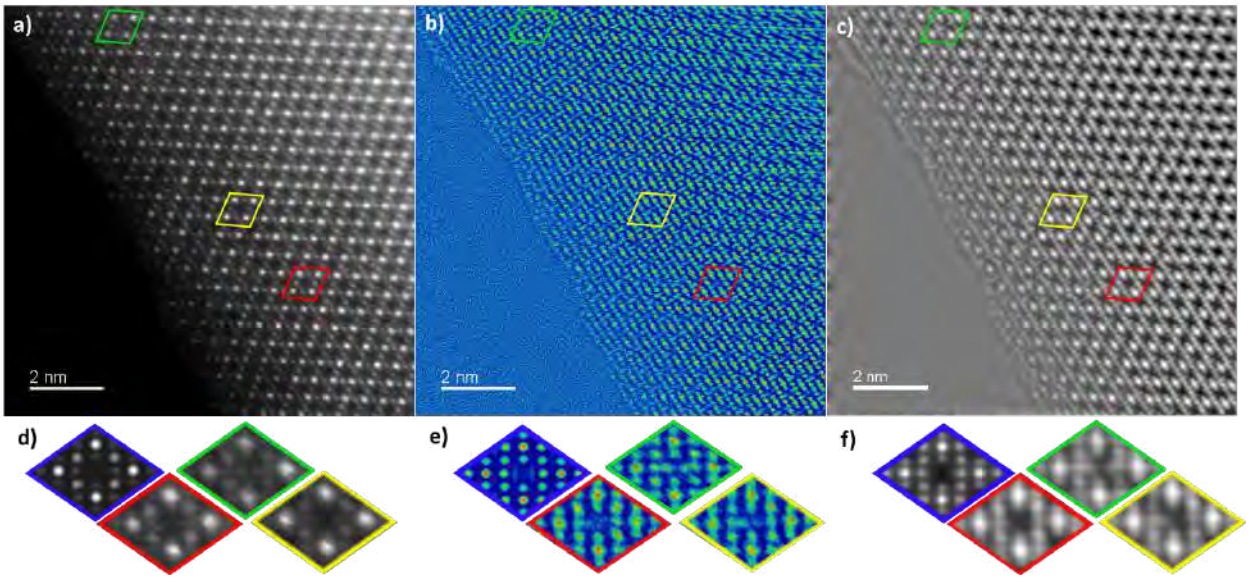

Figure 2. ADF-STEM experimental image of the surface of $Li_{1-x}Mn_2O_4$ along the [011] direction, (b) dDPC image (c) iDPC image. The inset diamonds highlight three different regions; (green) where Mn is observed by ADF and DPC in tetrahedral positions, (yellow) where no Mn is observed by ADF but it is shown by DPC and (red) where Mn is inexistent. (d-f) [4].

Seeing Structural Evolution of Organic Molecular Nano-crystallites Using 4D Scanning Confocal Electron Diffraction (4D-SCED)

Mingjian Wu[1], Christina Harreiß[1], Colin Ophus[2], Manuel Johnson[3], Rainer H. Fink[3] and Erdmann Spiecker[1]

1 Institute of Micro- and Nanostructure Research & Center for Nanoanalysis and Electron Microscopy (CENEM), Department of Materials Science, Universität Erlangen-Nürnberg, Erlangen, Germany.

2 National Center for Electron Microscopy, Molecular Foundry, Lawrence Berkeley National Laboratory, Berkeley, CA, USA, 94720

3 Department of Chemistry und Pharmacy, FAU, Erlangen, Germany

Direct observation of organic molecular nanocrystals and their evolution using electron microscopy is extremely challenging, due to their radiation sensitivity and complex structure. Diffraction imaging, or 4D-STEM, using small convergence angle α (i.e., nano-beam diffraction, NBD) has recently demonstrated its power to reveal the rich structural information in soft materials [1]. For crystallography-related studies, spot-like diffraction signals are preferred, not only due to the large unit cells (thus small diffraction angles) of typical molecular crystals, but also to increase the elastic diffraction signal to noise ratio (SNR) as well as signal to (inelastically scattered) background ratio (SBR). In standard NBD, the angular size of diffraction disks is coupled to the illumination convergence, resulting in conditions which are not optimized for SNR and SBR. Here, we introduce 4D-scanning confocal electron diffraction (4D-SCED) as a 4D-STEM modality which combines high dose-efficiency and high angular resolution. With 4D-SCED the complex (crystalline) structure of soft materials can be studied in detail and we demonstrate that the technique even enables direct *in situ* observation of nanocrystal growth and coarsening in bulk heterojunction (BHJ) thin films [2].

4D-SCED applies defocused pencil beam illumination (Fig. 1b) on the sample and combines confocal electron optic setup with a pixelated detector to record focused spot-like diffraction patterns (Fig. 1c). The defocused illumination reduces the dose and generates a more homogenous electron beam sample interaction compared to 4D-NBD, even if the latter is performed with extremely small customized condenser apertures. Moreover, the confocal optics generates spot-like diffraction signals, boosting SNR and SBR. The spatial and angular resolution can be estimated using geometric considerations (Fig. 1d), which is largely decoupled from illumination convergence. To balance spatial and angular resolution, small convergence (α~1 mrad) and large defocus ($z>>t$) is typically applied [2].

We first show the figure of merit of 4D-SCED compared to 4D-NBD (using standard apertures) with a single crystal thin film of organic semiconductor α,ω-DH6T bilayer [3], and compare 4D-NBD and 4D-SCED datasets subsequently acquired from identical region (Fig. 1e-h) (see Ref. [2] for details). We then apply 4D-SCED to study an active layer in DRCN5T:$PC_{71}BM$ bulk heterojunction (BHJ) solar cell thin films after solvent vapor annealing (Fig. 2a-c). With its high angular resolution, the patterns acquired via SCED enables mapping of the orientation of nano-crystallites not only in edge-on (large diffraction angles) but also in face-on orientation (small diffraction angles). Furthermore, the sharp diffraction spots in SCED can be used to locally analyze the crystallographic structure of individual nano-crystallites. Finally, we even use 4D-SCED to study the structural evolution of DRCN5T:$PC_{71}BM$ during thermal annealing by *in situ* heating the sample thin film in the vacuum of TEM (Fig. 2d). This allows us to directly reveal the evolution of crystallite size (coarsening) and

texture, as well as the progressive enrichment of $PC_{71}BM$ at interfaces.

The unique combination of high dose-efficiency and high angular resolution makes 4D-SCED an ideal technique for studying beam sensitive soft materials with large unit cells. The new possibilities of the technique are currently employed for the investigation of further soft materials.

References:
[1] Bustillo, K., Zeltmann, S., Chen, M., et. al., Accounts of Chemical Research 11 (2021) 2543.
[2] Wu, M., Harreiß, C., Ophus, C., et. al., Nat. Comm. 13 (2022) 2911.
[3] Johnson, M., Hawly, T., Wu, M., et. al., Soft Mater, 17 (2021) 9765.
[4] The authors acknowledge financial support from DFG via projects GRK1896 and SFB953. Work at the Molecular Foundry has been supported by U.S. DoE under contract No. DE-AC02-05CH11231.

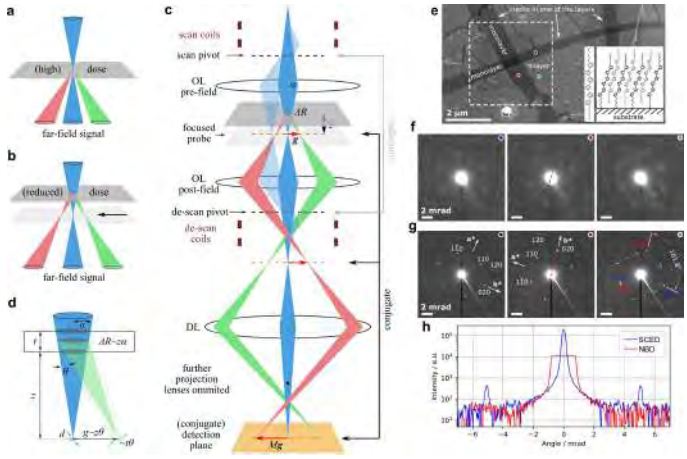

Figure 1. (a) Typical STEM setup where detectors are located at far field. (b) Defocusing the probe mitigates limited dose budget for beam-sensitive samples. (c) A simplified optical path of scanning confocal electron diffraction. OL: objective lens, DL: diffraction lens. (d) A geometric scheme for considering spatial and angular resolution. (e-h) Comparison of NBD and SCED applied to a molecular 2D single crystal film (α,ω-DH6T bilayer). (e) STEM-ADF image of the area of interest. Insets show the molecular structure and scheme of the assembled monolayer on the substrate. 4D-NBD and 4D-SCED data were acquired subsequently at the white box region. Representative raw patterns extracted from the positions marked with color dots are shown in (f) for NBD and in (g) for SCED. (h) Intensity profiles of the raw pattern comparing SNR/SBR of NBD and SCED.

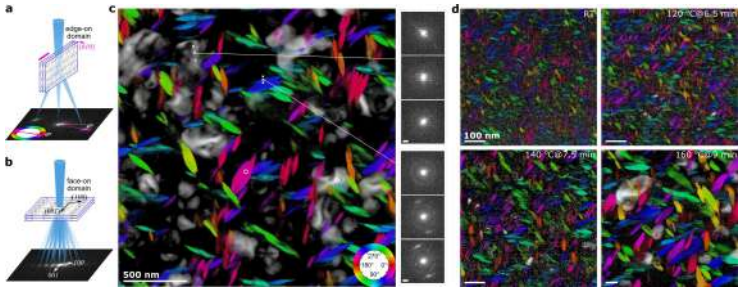

Figure 2. Orientation of donor nano-crystallites in DRCN5T:PCBM blends. (a) scheme illustrating color wheel method to encode the edge-on domain orientation at a probed location; (b) demonstrates our ability to determine the grain orientation of the face-on domains. Only gray scale pixels are superimposed in the maps to indicate the location of the face-on domains. (c) Nano-crystallites structure of the donor after solvent vapor annealing in CS_2 for 840 s. Insets on the right (scale bars: 2 mrad) are raw diffraction patterns extracted from the white dots. (d) The structural evolution of donor nano-crystallites during an in situ annealing experiment in the TEM.

Next Generation Sample Preparation for Cryo-Electron Tomography

Juergen M. Plitzko[1], Sven Klumpe[1], Oda Schioetz[1], Sagar Khavnekar[1], Christoph Kaiser[1], Alexander Rigort[2]

1 CryoEM Technology, Max Planck Institute of Biochemistry, Martinsried, Germany

2 Thermo Fisher Scientific, FEI Deutschland GmbH, Planegg, Germany

The recent technological breakthrough in cryo-electron tomography (cryo-ET) opens the possibility of imaging macromolecular complexes in their native cellular context at sub-5Å resolution [1,2]. This technology is the foundation for an emerging field in the life sciences, often termed structural cell biology, capable of revealing how different conformational states of protein complexes are linked to biological functions. However, imaging is highly dependent on sample preparation. This is especially true for transmission electron microscopy (TEM), where samples must be thin enough to provide high-resolution information, homogeneous in thickness for consistent high-quality data, and in their original state, as in cryo-TEM, to preserve the structural features of macromolecules. Sample preparation, while largely underappreciated, is thus a vital part of imaging.

Since its beginnings as a sample-thinning technique for cryoET, cryogenic focused ion beam milling (cryoFIB) using gallium ions has evolved into a procedure that encompasses several different methods. Methods like on-the-grid lamella-preparation of plunge frozen samples, iterative FIB ablation and scanning electron microscopy (SEM) imaging, and most recently lift-out for high-pressure frozen (HPF) multicellular samples [3,4]. The latter is an established method in materials science, but since its introduction for cryo-ET, it has been used rather rarely [5]. The reasons why the lift-out method falls short compared to lamellar preparation on the grid are quite obvious: First, it is very time consuming to mill high-pressure frozen (HPF) samples that are up to 200 microns thick, and for gallium ions it is almost pointless to go beyond 30 microns; second, the whole process is often disappointingly inefficient, mainly because of its complexity; third, there is no way to assess ice quality before or during preparation, only after the first TEM image does one know whether the ice is "good" or "bad"; and finally, the "survival rate" of lift-out lamellae is low, either they are lost during manual transfer or they are contaminated beyond recognition.

Yet, there must be ways to streamline this process and make multicellular specimens and small organisms amenable to routine access in a reasonable time frame. PlasmaFIB technology promises to do just that: Higher beam currents and higher ablation rates to make bulky samples easily accessible, hardware automation that frees the user from any manual operation and increases survival rates, and finally integrated solutions for targeting (correlative fluorescence microscopy, CLEM) and ice quality assessment. Moreover, one could even consider transferring on-the-grid milling approach directly to high-pressure frozen samples, that would even bypass the tedious lift-out process (i.e., going ‘lift-less’).

Here we present the latest developments towards full automation for plunge-frozen and especially for high pressure frozen samples, as well as initial results and experiences with a novel plasma cryo-FIB system specifically designed for large scale cryo-FIB milling.

References:

[1] D. Tegunov et al., Nature Methods **18**, 186–193 (2021).
[2] S. Khavnekar et al. bioRxiv; DOI: 10.1101/2022.06.16.496417 (2022).
[3] S. Klumpe et al., eLife 2021;10:e70506 (2021).
[4] S. Klumpe et al., Microscopy Today **30**(1), 42-47 (2022).
[5] M. Schaffer et al., Nature Methods **16**, 757-762 (2019).

Electron Microscopy and the Unsolved Problem Of Extracellular Vesicle Isolation

Agnes Kittel

ELNR, Institute of Experimental Medicine, Budapest, Hungary

Extracellular vesicles (EV) are sub-micron, single membrane surrounded structures that can be released from any cell into the extracellular space. They could be promising biomarkers or drug carriers and have importance in a wide spectrum of biological functions in health and disease.
However, the lack of standardized methods for isolating and analyzing EVs has prevented their potential from being exploited and makes the comparison of the results from different sources difficult, and in some cases even impossible [1]. In the interest of solving this serious problem, new protocols are published regularly in prestigious journals [2, 3].

EVs derived from cancer cells have been shown to contribute to horizontal cellular transformation, cellular reprogramming, functional alterations, and even metastasis. Identification of the tumor-derived material carried by EVs isolated from different body fluids can help the early detection of different cancers, the more accurate diagnosis, and prognosis. These small vesicles might become an efficient therapeutic tool in the future.
My main goal is to convince you about the importance of EVs, to give an insight into the difficulties of their isolation and identification, and to prove the usefulness of electron microscopy in this field, too.
Because we cannot forget that there are several techniques to measure the size of the particles collected by a given technique, nothing has been proved to be more reliable to demonstrate the nature of a vesicle-like particle than electron microscopy.

Although there is a growing availability of cryo-EM techniques and in several cases, their application means lots of advantages in EV research, however, there are still questions that we can answer by traditional TEM, too [4].

References:

[1] B Gyorgy *et al*. Blood **117** (2011) p.39.
[2] Z Onodi *et al*. Front Physiol **9** (2018) p.1479.
[3] R Crescitelli, C Lässer and J Lötvall, Nat Protoc **16,** (2021) p.1548.
[4] Professor Edit Buzás, Dr. Zoltán Giricz, Dr. Gábor Valcz and Dr.Imre Sallai are thanked for their many useful discussions and contributions to this work.

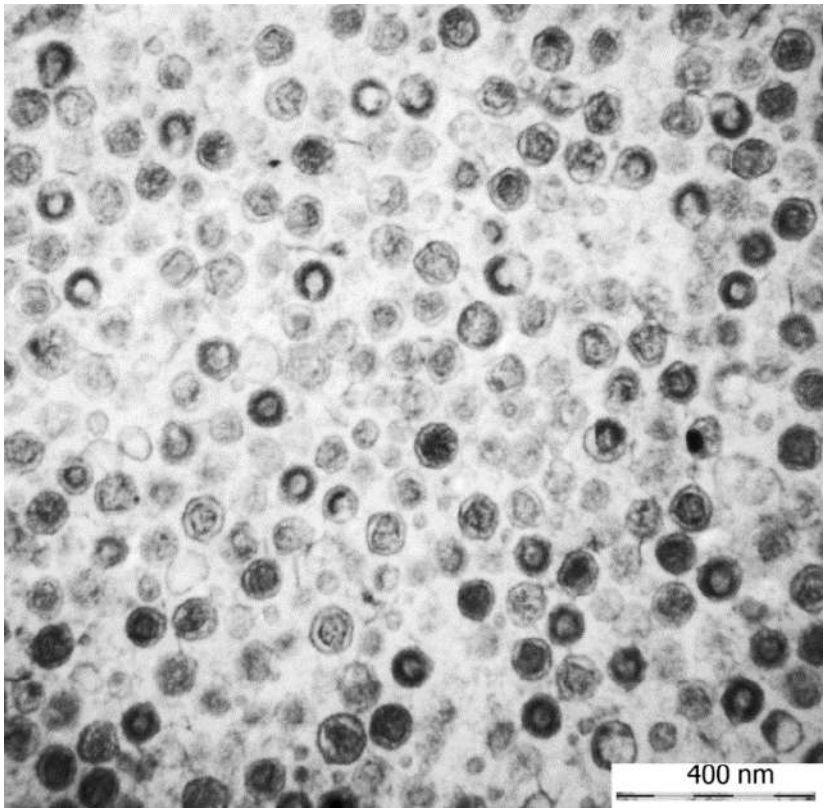

Figure 1. Exosome fraction separated from the supernatant of 5/4 T cell hybridoma line.

Electron Beam Damage Mitigation Strategies

Eric Van Cappellen[1], Paolo Longo[1], Mauro Porcu[2], Maarten Wirix[2], Christian Maunders[2], David Foord[1], Lin Jiang[1], Cigdem Ozsoy-Keskinbora[2], Bert Freitag[2], Anna Carlsson[2], Arno Meingast[2], Eric G.T. Bosch[2] and Ivan Lazić[2]

1 Thermo Fisher Scientific, Hillsboro, OR 97124, USA

2 Thermo Fisher Scientific, 5651 GG Eindhoven, The Netherlands

Since the invention of the electron microscope scientists have been arguing about how the electrons affect or even damage the sample. Life scientists have always looked at ways to increase contrast, and reduce beam damage, for improving productivity (throughput) and performance (resolution) when studying biological structures. Now materials science is commanding similar tactics. Many materials classes such as polymers, 2D materials, zeolites, MOF's (metal organic frameworks) and others require a frugal use of the electrons that have transited through the sample in order to minimize the damage they can cause. Here we will discuss recent developments but also mention ongoing research and development projects at Thermo Fisher Scientific in the field of low-dose imaging and analysis.

Electron beam damage mitigation strategies consist of both hardware and software solutions requiring fewer primary electrons without sacrificing the signal-to-noise of generated data. Generally speaking, detectors must be made more sensitive and software-based imaging and analysis techniques must yield a higher contrast for a given dose.

On the hardware side we will discuss Panther the new Spectra STEM engine with single electron sensitivity, Ultra-X the new super-sized EDX detector enabling EDX analysis of materials otherwise too beam sensitive and the Falcon 4i the new direct electron detector with an industry leading DQE. The software story will be about EDC (Electron Dose Control), detecting fluorine dopants with EDX in lithium-ion battery cathode material and iDPC (integrated Differential Phase Contrast) for extreme low-dose STEM imaging.

In the last decade Bright Field-STEM imaging techniques (ABF, e-ABF and OBF) have enjoyed a renaissance because contrary to Dark Field (DF) techniques they allow for many more transmitted electrons to participate in the imaging process. Unfortunately, none of the BF techniques are linear and retrieving the object from the image is all but trivial. iDPC-STEM is another imaging technique that uses close to all the transmitted electrons but without the inconveniences of non-linear BF imaging. iDPC-STEM was first utilized as the actual integration of the DPC vector field to resolve the iDPC scalar field by Ivan Lazić, et al. [1, 2]. For a thin sample, the DPC vector field represents the projected electric field, which when integrated yields the projected electrostatic potential field (φ) of the sample [1, 2]. iDPC-STEM is a one-to-one representation of the atomic model one is trying to resolve. (HA)ADF-STEM (φ^2) also offers a direct representation of the atomic model, albeit for heavy elements only whereas iDPC visualizes the entire periodic table, down to hydrogen [3]. In short, iDPC yields a HAADF-like contrast, praised all over the world, but with the added benefit that light elements are also imaged. iDPC-STEM has successfully been utilized to image MOF's [4] and zeolites [5,6] with unprecedented resolution under very low-dose conditions. Figure 2 is an example of a MOF (UiO-66) imaged with a total dose of 22 $e^-/Å^2$.

References:

[1] I. Lazić, E. Bosch and S. Lazar, Ultramicroscopy **160** (2016), 265.
[2] I. Lazić and E. Bosch, Advances in Imaging and Electron Physics **199** (2017), 75.
[3] S. de Graaf et al., Sci. Adv. **6** (2020), eaay4312.
[4] B. Shen et al., Nature Communications **11** (2020), 2692.
[5] I. Lazić et al., Microsc. Microanal. **22**, (2016), 36
[6] B. Shen et al., Nature **592** (2021), 541.

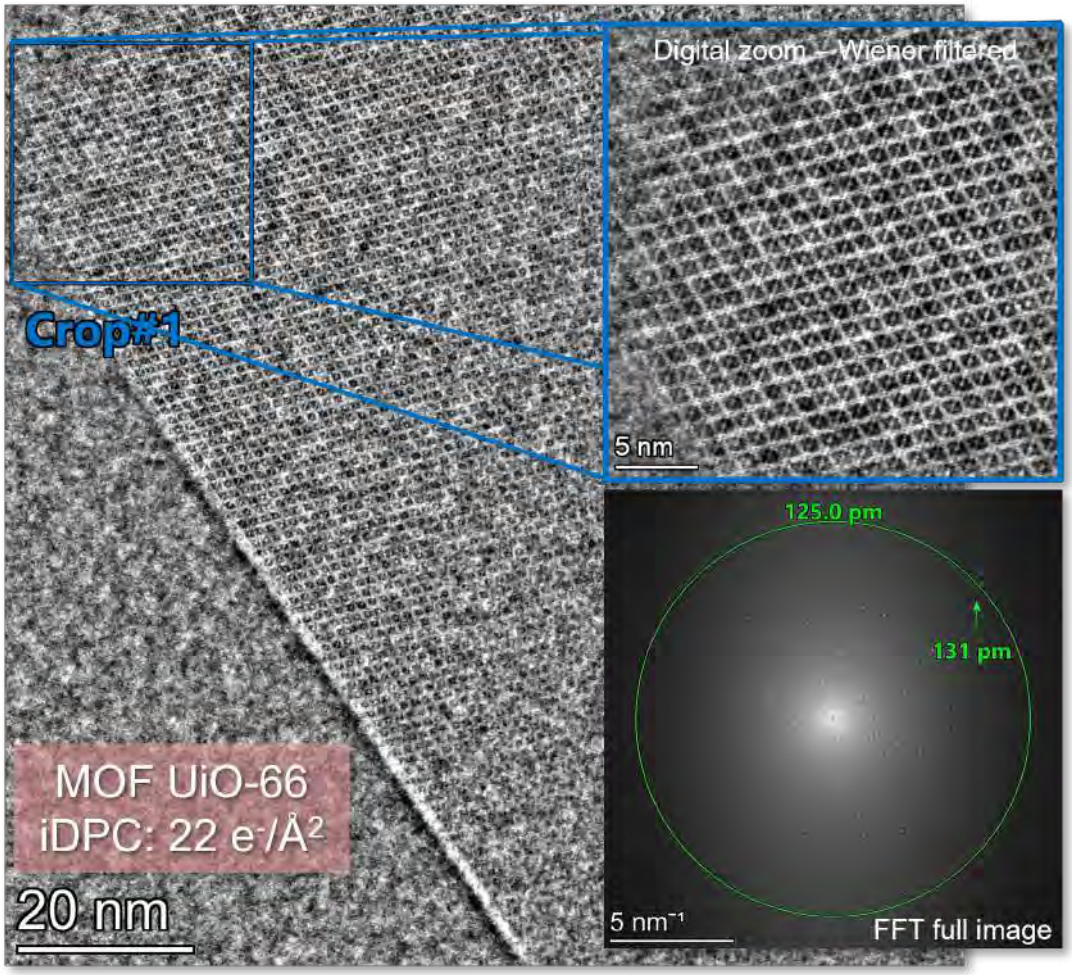

Figure 1. A 200kV iDPC-STEM example of a MOF (UiO-66) imaged with 22 $e^-/Å^2$. The probe current was 0.5pA, the frame time 10s and the convergence angle 10mrad.

ORAL PRESENTATIONS

Hydroxyapatite-based Bioceramic Dental Inserts as Dentin Substitutes

Tamara Matić[1], Maja L. Zebić[2], Vesna Miletić[3], Rada Petrović[4], Djordje Janaćković[4], Djordje Veljović[4]

1 Innovation Center of the Faculty of Technology and Metallurgy Ltd, Belgrade, Serbia

2 University of Belgrade, School of Dental Medicine, Belgrade, Serbia

3 The University of Sydney, Faculty of Medicine and Health, Sydney Dental School, Surry Hills NSW, Australia

4 University of Belgrade, Faculty of Technology and Metallurgy, Belgrade, Serbia

Tooth caries presents one of the most common diseases worldwide, and its treatment involves removal of the decayed tooth structure, and the cavity restoration using restorative dental materials. Resin based composites (RBCs) are the most commonly used restorative material in practice owing to their great aesthetic appearance allowing the clinicians to adapt the nuance of the restoration to the patient's tooth color. However, the RBCs harden by the polymerization of monomers that leads to the polymerization shrinkage of the restoration, leaving the micro-gaps at the teeth-restorations interface which allows the secondary caries formation.

In order to overcome this problem inorganic dental inserts based on feldspar, glass, porcelain etc. were introduced as cavity megafillers [1]. Nevertheless, these materials were very distinct from the human dentin tissue, leading to inadequate properties. Recently, the bioactive, biomimetic materials gained more attention for application in biomedicine. The goal of this study was to develop a dentin substitute based on hydroxyapatite, the main inorganic component of the bones and teeth, processed in the form of dense compacts with satisfactory mechanical properties, in order to mimic the removed dentin tissue. The dental inserts are intended to be placed in the central area of the removed dentin, while a thin layer of RBCs would be used as a top coat in the area of enamel for great aesthetic, wear and sealing purposes [2]. Therefore, a great bonding ability of the dental inserts with commercially available restorative materials needs to be achieved as well.

Hydroxyapatite nanosized powders doped with 5 mol. % magnesium and binary doped with 3 mol. % magnesium and 3 mol. % strontium ions were synthesized hydrothermally at 150 °C, pressed into compacts by applying cold isostatic pressing and sintered at 1200 °C for 2 h in order to obtain bioceramic dental inserts. Microstructure, average pore and grain size, phase composition and mechanical properties of the obtained dental inserts were determined. The bonding ability of the inserts with commercially available dental composites, adhesives and cements applied by *total-etch* and *self-etch* clinical protocols were tested by the shear bond strength test. The *total-etch* protocol implied acidic surface pre-treatment of the inserts with 37 % phosphoric acid. A Field Emission Scanning electron microscope (FE-SEM Tescan Mira 3 XMU) was engaged to determine the particles morphology, inserts' microstructure, as well as the intimate bonding of the dental inserts with the restorative materials, applied by the *self-etch* and *total-etch* protocols. A cross-section of a molar restored by the proposed protocol involving a hydroxyapatite-based dental insert was also examined by using the FE-SEM.

The results showed that dopants have a significant effect on the microstructure and phase composition of the hydroxyapatite-based dental inserts, distinct solubility and mechanical properties. Smaller average grain and pore size, as well as greater hardness by Vickers were obtained in the case

of magnesium doped hydroxyapatite. The bonding strength values of both dental insert types with the Filtek Z_250 dental composite applied by Single Bond Universal adhesive system by both *self-etch* and *total-etch* protocols were in the range of the bonding strength values previously reported for human dentin [3].
In conclusion, the obtained hydroxyapatite-based dental inserts present dentin substitutes that are chemically and structurally similar to the mineral component of the human dentin, with adequate mechanical properties, as well as great bonding ability to restorative materials commonly used in dental practice, which makes them promising materials for application in restorative dentistry [4].

References:

[1] M Federlin, B Thonemann and G Schmalz, Clinical Oral Investigations **4** (2000), p. 1.
[2] M Lezaja et al., Dental Materials **31** (2015), p. 171.
[3] L Bracher and M Özcan, Journal of Adhesion Science and Technology, **32** (2018) p. 258.
[4] The authors wish to acknowledge funding from the Ministry of Education, Science and Technological Development of the Republic of Serbia (Contract No. 451-03-68/2022-14/200135, 451-03-68/2022-14/200287, and 451-03-9/2021-14/200129).

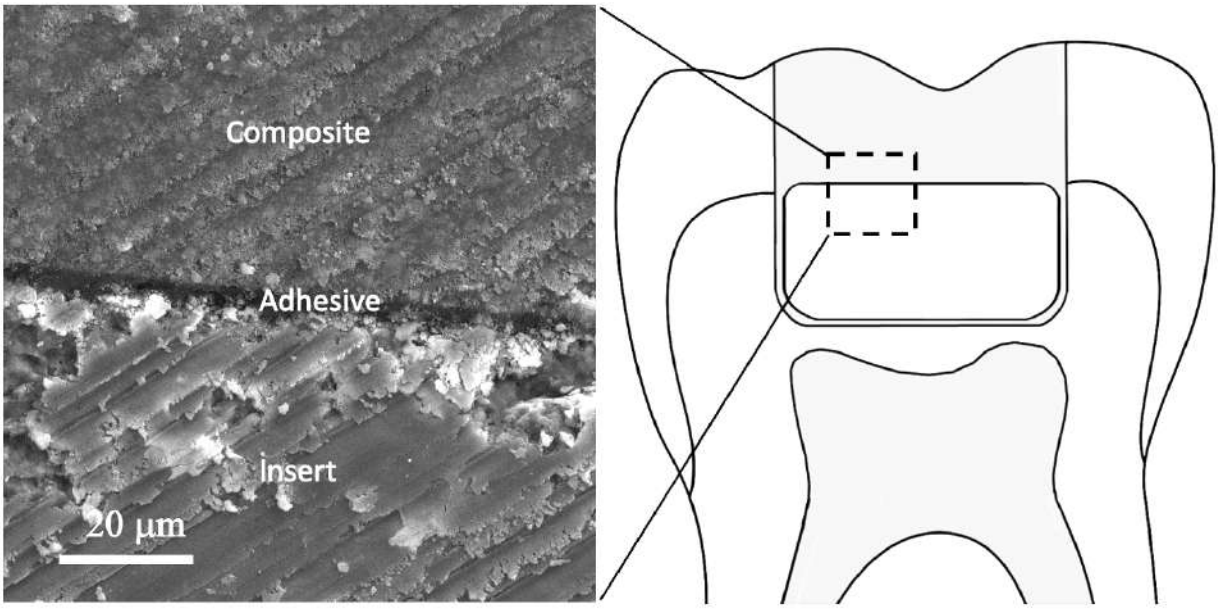

Figure 1. Schematic representation of cross-section of a molar restored by the newly proposed protocol involving hydroxyapatite-based dental insert, and FE-SEM micrograph of the composite-adhesive-insert interface. The dental insert based on hydroxyapatite doped with magnesium is bonded with Filtek Z_250 dental composite by Single Bond Universal adhesive applied by *total-etch* protocol.

High Fat Diet Increases the Number of Mitophagy-related Structures in Hepatocytes of C57BL/6J Mice

Darko Ciric[1], Tamara Martinovic[1], Sasa Petricević[2], Vladimir Bumbasirevic[1,3], Tamara Kravic-Stevovic[1]

1 Institute of Histology and Embryology, Faculty of Medicine, University of Belgrade, Belgrade, Serbia

2 Institute of Medical and Clinical Biochemistry, Faculty of Medicine, University of Belgrade, Belgrade, Serbia

3 Serbian Academy of Sciences and Arts, Belgrade, Serbia

High fat diet (HFD) fed C57BL/6J mice are frequently used as an experimental model for metabolic syndrome and diabetes mellitus type 2 [1]. Suspected causative event that leads to the development of these conditions is mitochondrial dysfunction [2]. Dysfunctional or otherwise damaged mitochondria are being removed by autophagy [3]. Autophagy is a well conserved cellular catabolic process which cells deploy to remove damaged or otherwise unwanted parts of their cytoplasm, including organelles [3]. This begins with a formation of isolation membrane (phagophore) which closes around a selected part of the cytoplasm [3]. Closure of free phagophore end leads to the formation of the autophagosome, double membrane cytoplasmic vacuole [3]. Autophagosomes fuse with a cell lysosomes leading to the formation of autolysosomes [3]. The content of autolysosomes is then being degraded by lysosomal enzymes [3]. While nonselective autophagy is typically activated when there is a scarcity of nutrients, selective forms of autophagy specifically target certain structures in the cytoplasm, such as organelles, protein aggregates or foreign pathogens [3]. Selective autophagy that specifically targets mitochondria is termed mitophagy [3].

Mice were fed with a HFD containing 60% calories derived from fat (mostly lard) in the period of 6 months, or with a standard chow (control group). At the end of the feeding period, mice were subjected to the OGTT (oral glucose tolerance test) to assess glucose handling to verify that mice were indeed developed glucose intolerance, hallmark of metabolic syndrome and type 2 diabetes. Liver samples were taken and immersed into 4% formaldehyde for confocal microscopy, or 3% glutaraldehyde for transmission electron microscopy (TEM). After 72h, formaldehyde fixed samples were dehydrated in graded alcohols, cleared in Xylol solution and embedded in paraffin wax. Specimens for TEM were postfixed in osmium tetroxide, dehydrated in graded alcohols and embedded in polycomponent epoxy resins. For confocal microscopy, specimens were stained with anti-LC3 and anti-TOM20 antibodies in order to detect autophagic vacuoles that contained mitochondria. For electron microscopy, epoxy embedded specimens were cut on the ultramicrotome, after which ultrathin sections (50-70 nm thickness) were mounted on cooper grids. Grids with samples where then contrasted with lead-citrate and uranile-acetate contrasting solutions. Specimens were further analyzed on Leica SP2 confocal microscope and on Morgagni 268D transmission electron microscope.

The numbers of mitophagy-related structures (autophagic vacuoles containing mitochondria) were significantly elevated in HFD fed versus control group of mice.

We conclude that HFD increases the amount of observable cellular structures related to mitophagy in C57BL/6J mice hepatocytes.

References:

[1] Surwit RS et al, Diabetes, **37** (1988), p. 1163-1167.
[2] Rovira-Llopis S et al, Redox Biol, **11** (2017), p. 637-645.
[3] Youle RJ and Narendra DP, Nat Rev Mol Cell Biol, **12** (2011), p. 9-14.
[4] The authors acknowledge funding from the Ministry of Education, Science, and Technological Development of the Republic of Serbia (Grant No. 41025) and SASA (grant No F-35).

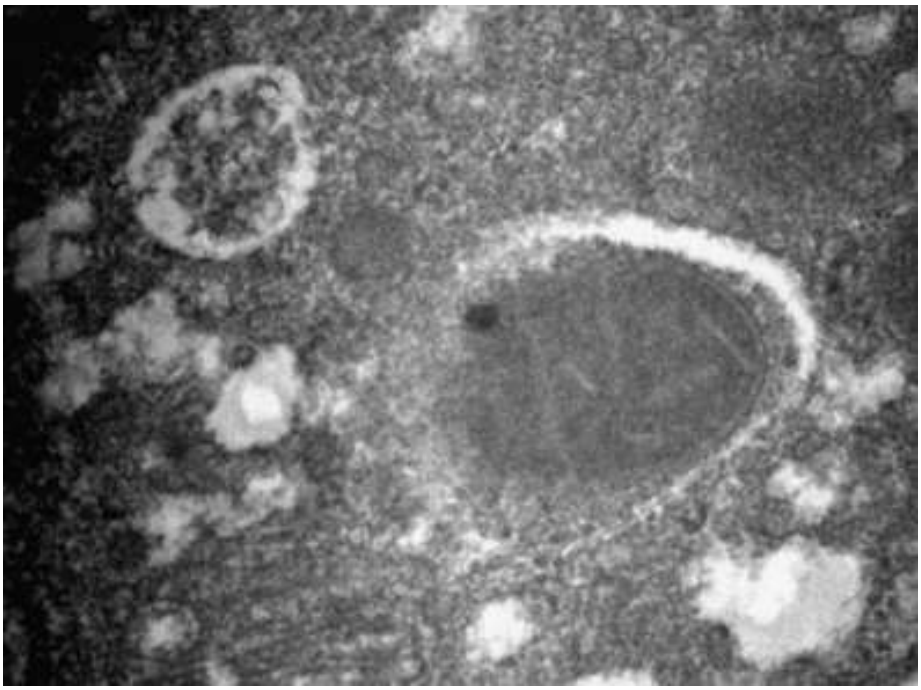

Figure 1. Isolation membrane in the process of engulfing a mitochondrion (TEM, x44000).

Imaging of Nanoscale Gold in "Intact" Biological Cells by Environmental Electron Microscopy

Domagoj Belić[1,2], Oihane Fragueiro[1], Dina Salah[1,3], Alison Beckett[4], Martin Volk[5], Mathias Brust[1]

1 Department of Chemistry, University of Liverpool, Liverpool, UK

2 Department of Physics, Josip Juraj Strossmayer University of Osijek, Osijek, Croatia

3 Department of Physics, Ain Shams University, Cairo 11566, Egypt

4 Biomedical Electron Microscopy Facility, University of Liverpool, Liverpool, UK

5 Surface Science Research Centre, Department of Chemistry, University of Liverpool, Liverpool, UK

The ability to monitor the cellular uptake and distribution of engineered nanomaterials is a basic requirement in nanomedicine and nanotoxicology [1-3]. This is commonly achieved by using optical and electron microscopies. Optical microscopy allows for easy sample preparation and live cell imaging but is inherently limited in resolution to typically tens to hundreds of nanometers [4], making it unsuitable for detailed investigation of nanoscale objects. On the other hand, electron microscopy allows for imaging with subnanometer resolution but requires a dedicated sample preparation that is usually cumbersome and costly [5-9].

Here we demonstrate direct imaging of engineered nanomaterials in biological cells under preservation of cellular ultrastructure by means of environmental scanning electron microscopy (ESEM) and wet scanning transmission electron microscopy (wet-STEM) [10,11]. Specifically, we outline protocols for imaging fully hydrated cells on glass slides or standard TEM grids, requiring no prior processing steps [12]. This enables high-throughput analysis of structurally uncompromised biological samples with nanometer resolution by using a minimal electron dose (<1 e$^-$/Å^2) at low electron energy ($\leq$30 keV). Here we refer to these cells as "intact", which should not be interpreted as "alive", although the cells are alive before being exposed to the electron beam.

To corroborate the accuracy of our ESEM and wet-STEM observations, we have also imaged equivalent samples prepared by conventional biological electron microscopy techniques, *i.e.* fixation-staining-embedding-sectioning-TEM, or cryo-TEM of whole vitrified cells. All the results are compared, highlighting the innovative aspects of ESEM and wet-STEM with respect to common electron microscopy methods when dealing with the analysis of engineered nanomaterials present inside biological cells. Our approach can thus be a viable alternative to the established electron microscopy methods for cellular imaging.

References:

[1] W Zhou *et al*, Chemical Reviews **115** (2015), p. 10575
[2] LA Dykman, NG Khlebtsov, Chemical Reviews **114** (2013), p. 1258.
[3] EC Dreaden *et al*, Chemical Society Reviews **41** (2012), p. 2740.
[4] YM Sigal, R. Zhou, X. Zhuang, Science **361** (2018), p. 880.
[5] AM Schrand *et al*, Nature Protocols **5** (2010**)**, p. 744.
[6] H Wu *et al*, Advanced Materials **32** (2020), p. 2001582.
[7] "Liquid Cell Electron Microscopy", ed. FM Ross, (Cambridge University Press, Cambridge)
[8] J Park *et al*, ACS Nano **15** (2021), p. 288.
[9] M Textor, N de Jonge, Nano Letters **18** (2018), p. 3313.

[10] “Principles and Practice of Variable Pressure/Environmental Scanning Electron Microscopy (VP-ESEM)”, DJ Stokes, (D. J. John Wiley & Sons, Ltd, Chichester)
[11] A Bogner *et al*, Micron 38 (2007), p. 390.
[12] D Belić *et al*, The Journal of Physical Chemistry C **125** (2021), p. 27865.

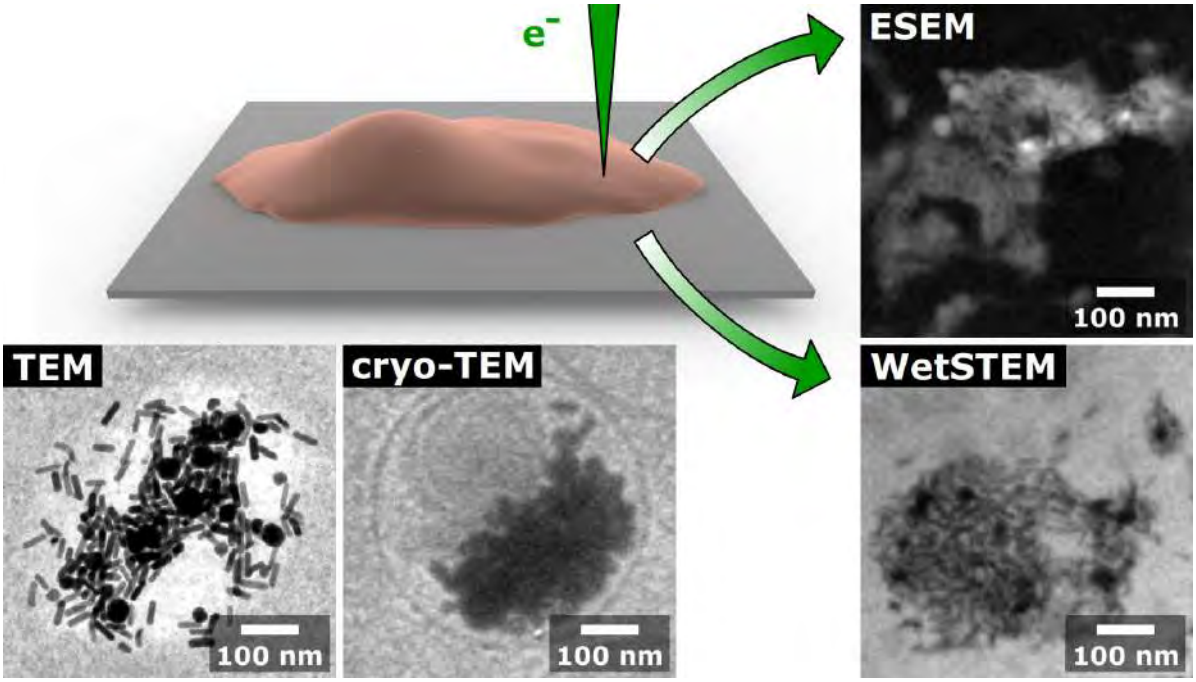

Figure 1. ESEM and wet-STEM imaging of engineered nanomaterials in “intact” biological cells at the resolution of ~ 3nm. These straightforward approaches may represent a viable alternative to complex and costly fixation-staining-embedding-sectioning-TEM, cryo-TEM, or liquid-cell-TEM.

Investigation of the Action of the Fullerene (C_{60}) Derivatives on Mouse 3T3 Fibroblast Cell Lines

Igor Golić[1], Tamara Krajnović[2], Sanja Jelača[2], Sanja Mijatović[2], Danijela Maksimović-Ivanić[2], Djuro Koruga[3]

1 Center for Electron Microscopy, Faculty of Biology, University of Belgrade, 11000 Belgrade, Serbia

2 Institute for Biological Research "Siniša Stankovic", National Institute of Republic of Serbia, University of Belgrade, 11060 Belgrade, Serbia

3 TFT Nano Center, 11050 Belgrade, Serbia

Fullerene C_{60} is the third allotropic modification of carbon in nature. Exceptional physical and structural features of C_{60} molecule make it attractive for biomedical research in a wide spectrum of applications from imaging, drug delivery, to therapy of different disorders. However, its low solubility in water or polar solvents, and genotoxic potential represent serious barriers for its usage. To overcome mentioned limits the second derivative of fullerene C_{60} (Hyper harmonized hydroxylated fullerene water complex - 3HFWC) is created through functionalization of the first fullerene C_{60} derivative (fullerol - $C_{60}(OH)x$) by the addition of paired OH groups in water layers surrounding the solid phase of substance. The solid phase consists of the C_{60} molecule, covalent OH groups and 3-6 water layers with strong hydrogen bonds. The liquid phase consists of additional water layers bonded by moderate to weak hydrogen bonds. In addition, the third derivative of fullerene is made when 3HFWC was integrated with nano-gold particles (nAu@3HFWC). The aim of this study was to evaluate fullerene C_{60} derivatives uptake and their intracellular distribution in mouse 3T3 fibroblasts. Cells were exposed to 30 µg/ml $C_{60}(OH)x$, or 30 µg/ml 3HFWC, or 5µg/ml nAu@3HFWC during 30 min, 1h or 2h and analysis was done by Philips FEI CM12 transmission electron microscope. Ultrastructural analysis showed mainly cytoplasmic localization of $C_{60}(OH)_x$ and its derivatives, and also a sporadic presence in mitochondria and nuclei. The concentration of fullerene derivatives in these cells was time-dependent, i.e., more concentration was observed in cells with longer exposition to these fullerenes. Furthermore, $C_{60}(OH)_x$ is also localized in lysosomes in higher concentrations. These results suggest that novel C_{60} fullerene derivatives show better biocompatibility in mouse 3T3 fibroblasts compared to $C_{60}(OH)_x$, which mainly ends in lysosomes, the waste disposal system of the cell.

References:

[1] M Markelić *et al*. Nanomaterials (Basel) **12** (2022) p 1331.
[2] S Miljkovic *et al*. J Cosmet Dermatol **19** (2020) p 3018.
[3] D Koruga. U.S. Patent 8.058.483 B2 (2011)
[4] D Koruga. International Patent WO 2021/110234 A1 (2021)

Shaped Eu^{3+}, Co^{2+} or Ru^{3+} doped TiO_2 Nanocrystal from Nanotubular Precursors with Optical, Magnetic and Electrochemical Properties

Mila Vranješ[1], Vladimir Nikolić[2], Milica Marčeta Kaninski[2], Dubravka Milovanović[2] and Zoran Šaponjić[2]

1 Quant Labs, Belgrade, Serbia

2 Institute of General and Physical Chemistry, Belgrade, Serbia

Numerous synthetic procedures based on wet chemical methods have been reported for the preparation of transition metal ions and rear earth ions doped TiO_2 nanocrystals of various sizes and shapes. Applying these methods the generally different mechanisms of dopant incorporation in bulk materials and nanocrystals should be taken into account [1]. Using molecular precursors for the synthesis of doped nanocrystals by wet chemical methods the dopant ions could be expelled from the core of nanoparticle during the crystal growth [2]. In order to escape such 'self-purification' phenomena we exploited dispersion of titania nanotubes, **Fig. 1**, in the presence of selected dopant ions (Eu^{3+}, Co^{2+} or Ru^{3+}) as a precursor during hydrothermal process for the synthesis of doped TiO_2 faceted nanocrystals and prolate nanospheroids.

Eu^{3+} doped TiO_2 nanocrystals are synthesized by a two-step hydrothermal method. The shape and sizes of precursor nanotubes, Eu^{3+} doped TiO_2 nanocrystals and prolate nanospheroids, **Fig. 1**, were characterized structurally, morphologically and optically. The obtained Eu^{3+} doped anatase TiO_2 nanocrystals independently of its shape exhibited red photoluminescence followed by four characteristic $^5D_0$ emissions of Eu^{3+} ($^5D_0 \rightarrow {}^7F_1$; $^5D_0 \rightarrow {}^7F_2$; $^5D_0 \rightarrow {}^7F_3$; $^5D_0 \rightarrow {}^7F_4$ transitions) [3].

In order to examine the influence of shape of doped TiO_2 nanoparticles on their magnetic properties Co^{2+} doped TiO_2 polygonal and prolate spheroid-like nanocrystals applying hydrothermal treatment were synthesized. Anatase crystal phase in Co^{2+} doped TiO_2 nanocrystals was confirmed independently of Co^{2+} concentrations. TEM analysis revealed the presence of mixture of nanocrystal shapes. These samples exhibited weak ferromagnetic ordering at room temperature that was accompanied with paramagnetic behavior [4]. Comparing disproportionate values of observed magnetic moment and concentrations of incorporated dopant in TiO_2 crystalline structure indicated the lower total number of surface defects/oxygen vacancies.

The same synthetic approach which implies the use of dispersion of titania nanotubes and dopant ions as precursor was applied for the synthesis of Ru^{3+} doped TiO_2 nanocrystals. The structure and morphology of Ru^{3+} doped TiO_2 nanocrystals as interactive Pt catalyst support applicable for direct alcohol fuel cells were examined by XRPD and TEM. XRPD pattern proved anatase TiO_2 crystalline structure of Ru^{3+}doped TiO_2 nanocrystals. Rietveld full profile refinement method was applied for obtaining cell parameters of Ru^{3+} doped TiO_2 anatase crystalline phase. Shifts of lattice parameters *a* and *c*, as well as cell volume in comparison to bare TiO_2 nanocrystals synthesized under the same conditions indicated successful incorporation of Ru^{3+} ions in TiO_2 crystalline structure. The electrochemical behavior of the Pt/Ru^{3+} doped TiO_2 catalysts was studied by performing cyclic voltammetry measurements in alkaline electrolytes and compared with commercial Pt/C catalysts. The electrochemical stability, after 1000 cycles and corrosion stability indicated interactive property of the Ru^{3+} doped TiO_2 catalyst support.

This study demonstrated the possible route for the preparation of doped titania nanocrystals with different functions using scrolled nanotubes as a precursor.

References:

[1] S.C. Erwin, L. Zu, M.I. Hafter*et al,* Nature **436**(2005) p. 91.
[2] J.D. Bryan, D. R. Gamelin, ProgInorgChem**54** (2005) p. 47.
[3] M. Vranješ *et al,* Ceramics International **38**(2012) p. 5629.
[4] M. Vranješ *et al,* Journal of Advance Ceramics **6(3)** (2017) p. 220.

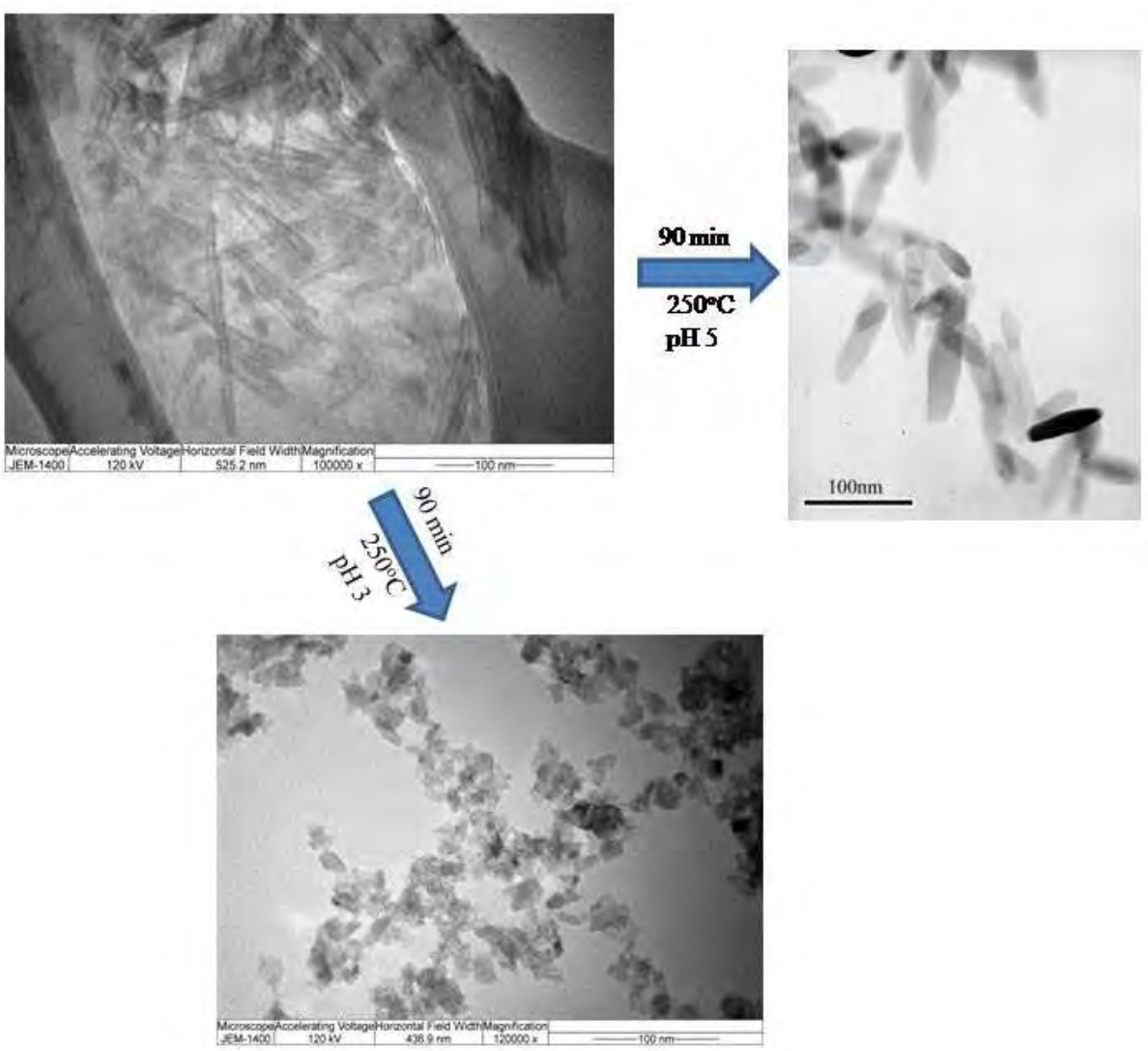

Figure 1. Bright field TEM image of nanotubular precursor, 0.041% Eu^{3+} doped TiO_2 prolate nanospheroids and Ru^{3+} doped TiO_2 nanoparticles.

Synthesis and Characterization of Highly Active Rutile TiO_2 Nanocrystalline Photocatalysts with Synergistic Exposed Crystal Facets

Veljko R. Djokić[1], Aleksandar D. Marinković[1], Rada D. Petrović[1], Ovidiu Ersen[2], Spyridon Zafeiratos[3], Miodrag Mitrić[4], Colin Ophus[5], Velimir R. Radmilović[1,6], and Djordje T. Janaćković[1]

1 Faculty of Technology and Metallurgy, University of Belgrade, Karnegijeva 4, 11120 Belgrade, Serbia

2 Institut de Physique et Chimie des Matériaux de Strasbourg (IPCMS), UMR CNRS – Université de Strasbourg 7504, 23, rue du Loess, BP 43, F-67034 Strasbourg Cedex 2, France

3 Institut de Chimie et Procédés pour l'Energie, l'Environnement et la Sante (ICPEES), ECPM, UMR 7515 du CNRS, Strasbourg University, 25 rue Becquerel, 67087 Strasbourg Cedex 02, France

4 Condensed Matter Physics Laboratory, Vinča Institute, University of Belgrade, P. O. Box 522, 11001 Belgrade, Serbia

5 NCEM, Molecular Foundry, Lawrence Berkeley National Laboratory, Berkeley, CA, USA 94720

6 Serbian Academy of Sciences and Arts, Knez Mihailova 35, 11000 Belgrade, Serbia

Titanium dioxide (TiO_2) is one of the most widely studied semiconductors (*n*-type) due to its low cost, abundant resource, high photocatalytic activity, resistance to chemical corrosion and photo-corrosion and non-toxicity.[1] Since the discovery of the photo-induced decomposition of water on TiO_2 electrodes,[2] interest in TiO_2 as a strategic material for environmental protection and photo-electrochemical solar energy conversion has continuously increased. However, the controllable synthesis of rutile TiO_2 single crystal particles with the preferential orientation of {111} facets still remain a scientific and technological challenge.

The aim of this research was to study the effect of the Ti/H_2O_2 molar ratio and the decomposition time of the peroxo-titanium complex (PTC) on the crystal structure, crystallite size and nanoscale morphology evolution of rutile TiO_2 nanorod crystals **(**$RTiO_2NRs$**)**, as well as to elucidate the effect of self-aggregation of $RTiO_2NRs$ on their photocatalytic activity. Here, we developed a facile route to fabrication of rutile TiO_2 nanorod crystals ($RTiO_2NRs$) having high ratios of oxidative {111} to reductive {110} surfaces. The thus obtained $RTiO_2NRs$ revealed a high tendency to agglomerate through orientation-dependent attachment along the {110} facets (Fig. 1). This resulted in an increased {111}/{110} surface ratio and lead to a markedly improved photocatalytic activity of $RTiO_2NRs$ aggregates (Fig. 2).[3]

High photocatalytic activities of the obtained catalysts indicated that synergistic effects of the exposed crystal facets facilitate electron excitation and electron/hole separation. In addition, the photocatalytic degradation process of a common textile dye, Reactive Orange 16, was completed 2.6 times faster in the presence of the herein synthetized PTA 1/100 than for the reference photocatalyst, P25 (Fig. 2). The presented methodology offers an alternative for the production of rutile titania with a favorable ratio of oxidative/reductive facets to obtain high photocatalytic activity and selectivity. Furthermore, our approach excludes the use of toxic capping agents and avoids the high-pressure and high-temperature treatments, thus facilitating green- and energy-efficient synthesis of nanostructured rutile TiO_2-based photocatalysts, as well as ensuring simple upscaling of the proposed technology.[3.4]

References:

[1] Fujishima, A.; Zhang, X.; Tryk, D. A. Surf. Sci. Rep. **63** (2008), p. 515–582.
[2] Fujishima, A.; Honda, K. Nature **238** (1972), p. 37-38.
[3] Djokić, V. R. *et al*, ACS Applied Materials and Interfaces **12** (2020), p. 33058−33068.
[4] Financial support through the Ministry of Education, Science and Technological Development of the Republic of Serbia, Contract No. 451-03-68/2020-14/200135, is acknowledged. V.R. Radmilović acknowledges support from the Serbian Academy of Sciences and Arts under project No. F-141. Work at the Molecular Foundry was supported by the Office of Science, Office of Basic Energy Sciences, of the U.S. Department of Energy under Contract No. DE-AC02-05CH11231.

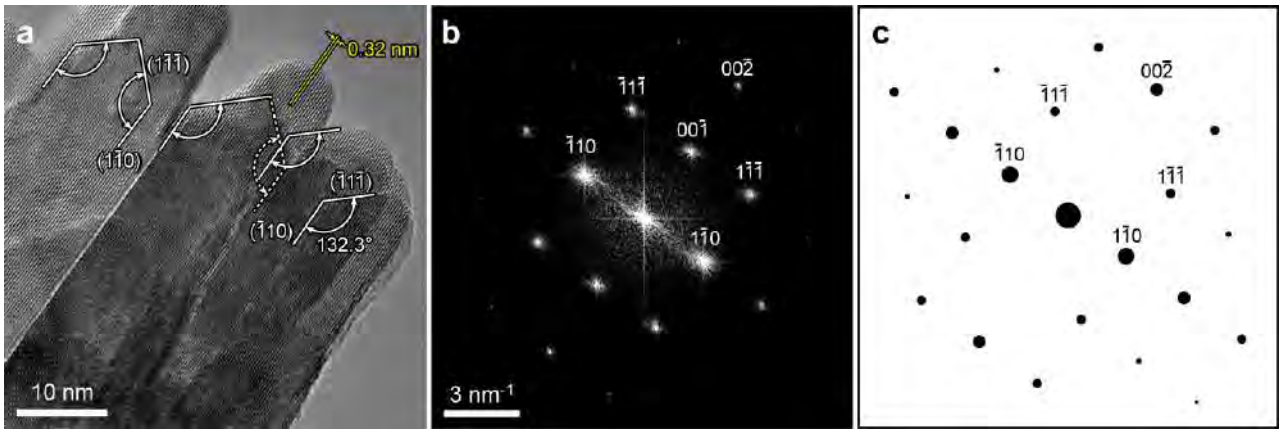

Figure 1. a) HRTEM micrograph of self-assembled PTA 1/100 nanorod clusters demonstrating orientation-dependent attachment, imaged close to the 110 zone axis (exposed {111} facets marked by arrows); b) FFT of the image in a), indicating the identical orientation of all nanorods; c) simulated diffraction pattern of rutile in 110 zone axis.

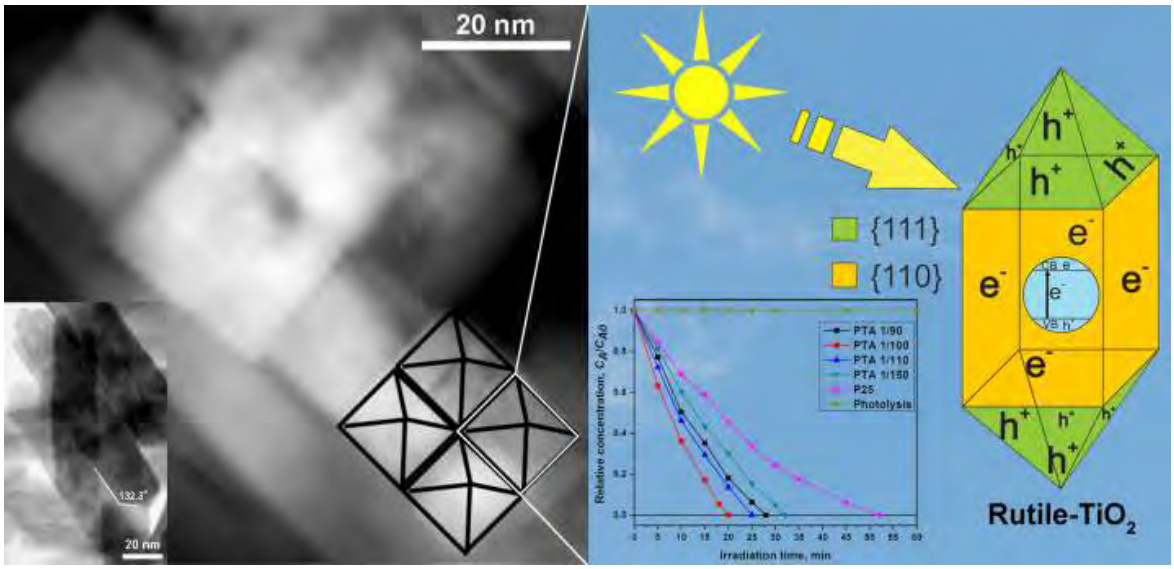

Figure 2. STEM–HAADF image of self-assembled PTA 1/100 nanorod clusters; the bright-field STEM image in the inset shows the triangular tips at both ends of the TiO_2 nanorods. Proposed mechanism for the enhanced photocatalytic activity of the $RTiO_2NRs$ with the relative concentration change of the C.I. Reactive Orange 16 dye *vs*. time in the presence of the photocatalysts.

Morphological and Structural Characterization of Tin Dendritic Nanostructures Produced by Various Electrodeposition Processes

Jelena D. Lović[1], Nebojša D. Nikolić[1], Vesna M. Maksimović[2] and Predrag M. Živković[3]

1 University of Belgrade, Institute of Chemistry, Technology and Metallurgy, Department of Electrochemistry, Belgrade, Serbia

2 University of Belgrade, Vinča Institute of Nuclear Science – National Institute of the Republic of Serbia Belgrade, Serbia

3 University of Belgrade, Faculty of Technology and Metallurgy, Karnegijeva 4, Belgrade, Serbia

Tin powders found wide application in many branches of the industry, such as powder metallurgy, lithium-ion battery production, electronic industry and manufacture of tin solder paste [1]. Application of Sn is based on specific features of this metal like high electrical conductivity, low electrochemical migration behavior, excellent solderability and low material cost [2]. The main methods used for synthesis of Sn in the powder forms are: gas atomization process, cementation process, chemical reduction process, and electrodeposition [1,2]. Electrodeposition is widely used method for a synthesis of metals in the powder form, since the shape and the size of particles can be easily regulated by choice of parameters and regimes of the electrodeposition [3].

In this study, Sn powders were electrodeposited from an alkaline electrolyte containing 20 g/l $SnCl_2 \times 2H_2O$ in 250 g/l NaOH at the room temperature by application of both potentiostatic and galvanostatic regimes of the electrolysis. Electrodeposition was performed at various cathodic potentials (−1185, – 1200, −1270, – 1400, – 1600 and – 1800 mV vs. Ag/AgCl), and at a current density outside the plateau of the limiting diffusion current density (−3.0 mA cm^{-2}). Morphology of Sn particles is characterized by scanning electron microscope (SEM) and crystal structure by X-ray diffraction (XRD).

The dendritic particles of various shapes and size were produced by the electrolysis processes. With increasing the applied cathodic potential, the shape of dendrites changed from the spear-like and the needle-like (Figure 1a) to the fern-like (Figure 1b) and the stem-like dendrites (Figure 1c). The various dendritic forms, including those with prismatic branches were formed by the galvanostatic regime of the electrolysis (Figure 2). Formation of various dendritic forms has been explained by correlation of the morphology of produced dendritic particles with the polarization characteristics for this Sn electrodeposition system. Irrespective of parameters and regimes of electrolysis, the XRD analysis showed that all types of dendritic particles had nanostructural features, with the average crystallite size in the range (63.1–90.3) nm [4].

References:

[1] Z Wang *et al*, J Solid State Electrochem **25** (2021), p. 1111.
[2] https://nanografi.com/blog/tin-sn-powder/.
[3] K.I. Popov, S.S. Djokić, N.D. Nikolić, V.D. Jović, *Morphology of Electrochemically and* Chemically Deposited Metals, Springer International Publishing, 2016.
[4] This work was supported by MPNTR of Republic of Serbia (RS) (Grant No. 451-03-68/2022-14/200026) and Science Fund of RS (Grant No. AdCatFC: 7739802).

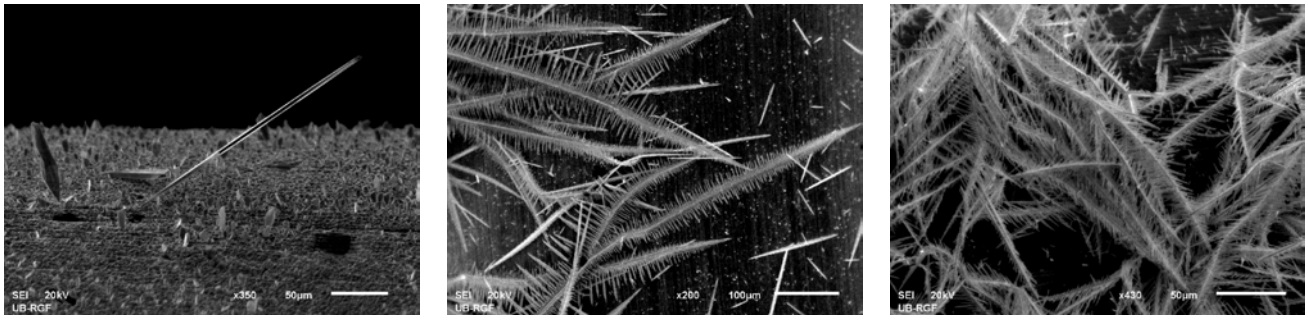

a) b) c)

Figure 1. Morphologies of Sn dendritic particles obtained by electrodeposition at cathodic potentials of: a) −1185 mV (the spear-like and the needle-like dendrites), b) −1270 mV (the fern-like dendrites), and c) −1800 mV vs. Ag/AgCl (the stem-like dendrites).

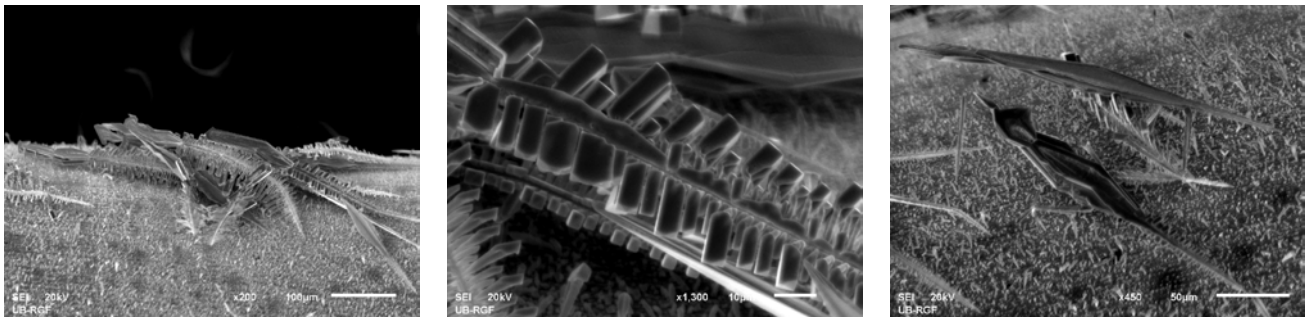

a) b) c)

Figure 2. Morphologies of Sn dendritic particles obtained by a galvanostatic regime of the electrodeposition at a current density of −3.0 mA cm^{-2}: a) and b) very branchy dendrite with branches of prismatic shape, and c) the spear-like dendrites.

Alkali activated slag based on steelmaking slag: application and properties

Irena Nikolić[1], Vuk Radmilović[2], Smilja Marković[3], Ljiljana Veselinović[3], Ivona Janković-Častvan[2] and Velimir Radmilović[4]

1 Faculty of Metallurgy and Technology, University of Montenegro, Podgorica, Montenegro

2 Faculty of Technology and Metallurgy, University of Belgrade, Belgrade, Serbia

3 Institute of Technical Sciences of SASA, Belgrade, Serbia

4 Serbian Academy of Sciences and Arts, Belgrade, Serbia

Alkali activated slag (AAS) is an environmentally friendly material which were extensively investigated in a pass two decade. Currently, these materials are considering as an effective alternative for cement binder. Process of slag alkali activation involves a chemical reaction between solid calcium aluminosilicate materials and a highly alkaline activator. The alkali activation mechanism of slag consists of the slag dissolution in a highly alkaline which is followed by the condensation and hardening processes yielding formation of calcium (alumina) silicate hydrate C–(A)–S–H gel as a reaction product of slag alkali activation [1]. Properties of these materials primarily depends on the choice of solid row materials. Primarily, granulated blast furnace slag, by product of iron production) is considering as a precursor for AAS synthesis. However, an important shift towards the use of steelmaking slag is also observed [2].

Although electric arc furnace slag has already found its application mainly in civil engineering, this investigation has aimed to investigate properties of AAS prepared using the electric arc furnace slag (EAFS) with an emphasize with different possibilities of its application. Characterization of AAS involved XRDP, SEM/EDS and pore size analysis with the aim to build up a detailed illustration of AAS from the stand point of different application.

AAS prepared using EAFS and Na_2SiO_3 solution at solid to liquid ratio of 4 and cured at 65 ^oC for a period of 48 h, reached the compressive strength of 38.8 MPa which enables its application in civil engineering. Sintering of such prepared AAS at temperature up to 1000 ^OC additionally increased the strength of AAS up to 51 MPa. Strengthening of AAS structure upon sintering is attributed to the mineralogical transformation of wüstite into magnetite and pore size reduction (Fig 1). Strengthening of AAS upon heating enables its application in a high temperature conditions.

Powdered AAS can be used as an effective adsorbent for Cu^{2+} removal from sulphate aquatic solution. The ions of copper are adsorbed on the surface of AAS slag in the form of postnjakite (Fig. 2. The achieved removal efficiency of Cu^{2+} ions at 20 ^oC was 63.93%. The adsorption of Cu^{2+} onto AAS proceeds via pseudo second adsorption mechanism and Langmuir isotherm model fits well the experimental data. Adsorption process is fast, spontaneous and endothermic in nature.

AAS can also be used as an effective agent for stabilization/solidification of toxic electric arc furnace dust (EAFD) which is also the byproduct of steel production in electric arc furnaces. Slag replacement with dust in the order of 5% enables potential use of product in construction applications while the product with higher amounts of dust met the criteria for landfill purposes. Fixation of dust into the AAS matrix occurred by chemical (A area in Fig 3) and physical immobilization (B area in Fig. 3)

References:

[1] W Chen and HJH Brouwers, Journal of Material Science **42** (2007) p.428.
[2] I Nikolić, et. al , Materials Letters **133** (2014) p.251.
[3] The authors acknowledge the support of the Centre for Nanoanalysis and Electron Microscopy (CENEM), Friedrich-Alexander University Erlangen-Nürnberg, Erlangen, Germany and the National Center for Electron Microscopy the Molecular Foundry, Lawrence Berkeley National Laboratory, which is supported by the U.S. Department of Energy under Contract # DE-AC02-05CH11231.

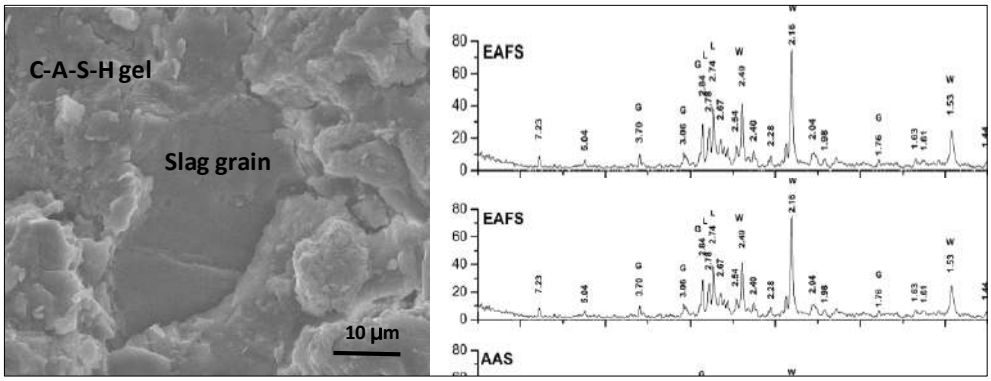

Figure 1. SEM and XRD of alkali activated slag before and after sintering

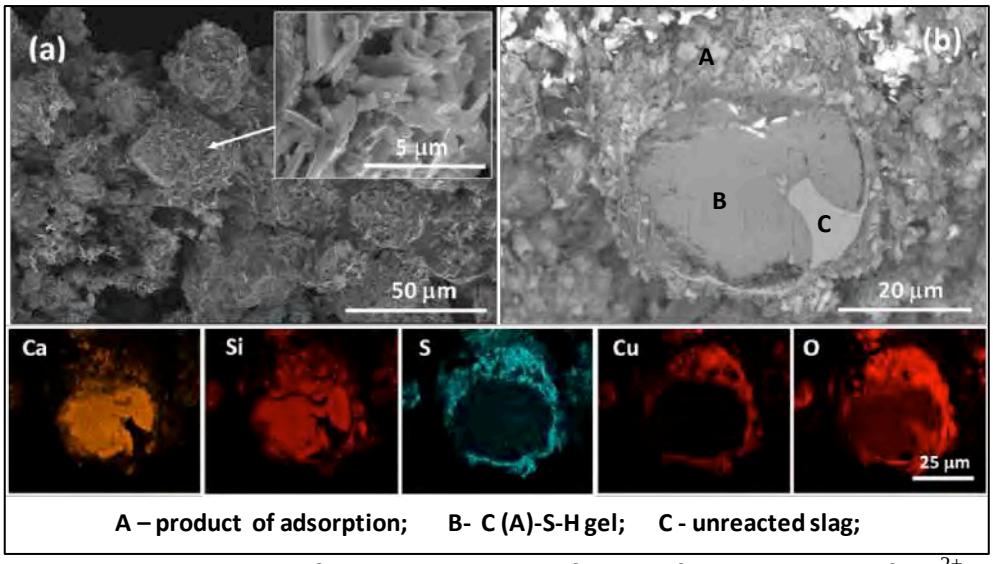

Figure 2. SEM micrographs of the cross-section of AAS after adsorption of Cu^{2+} ions and appropriate EDS composite maps of elemental distribution.

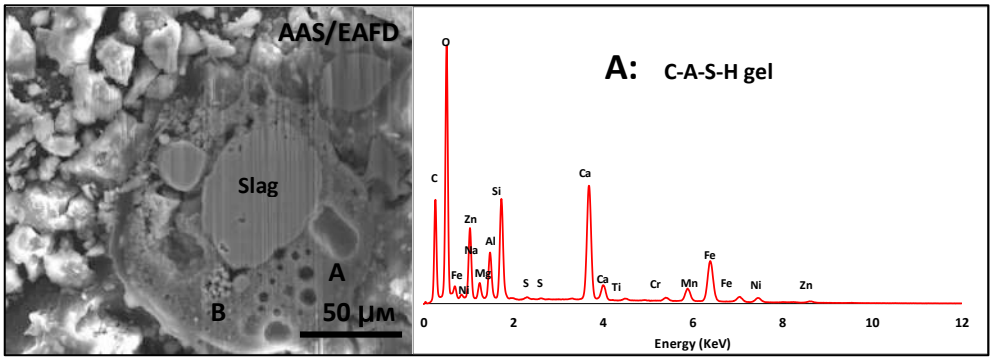

Figure 3. SEM/EDS of AAS sample doped with 5% EAFD.

Evaluation of Nano-crystalline $NiFe_2O_4$ Obtained via Pressurized Ethanol Synthetic Route

Aleksandar Ćosović[1], Vladan Ćosović[2], Tomáš Zák[3], Nadežda Talijan[4], Sandra Glišić[1], Aleksandar Orlović[1]

1 Faculty of Technology and Metallurgy, University of Belgrade, Belgrade, Serbia

2 University of Belgrade - Institute of Chemistry, Technology and Metallurgy, Belgrade, Serbia

3 CEITEC IPM, Institute of Physics of Materials ASCR, Brno, Czech Republic

4 AESS, Department of Technology, Metallurgy and Materials Science, Belgrade, Serbia

Nano-crystalline nickel ferrite is well-established soft magnetic material. Throughout the years it has been tried and tested for broad range of applications [1]. As the conditions during synthesis process have significant influence on its properties and in many cases the desired properties are favored by conflicting conditions [1], performance of the final material is usually a result of a reasonable choice and a compromise. This creates an ongoing challenge to explore and develop innovative synthesis routes. It is known that unique and adjustable nature of supercritical fluids' properties provide good conditions for crystallization and that the reaction kinetics in supercritical fluids can be controlled to a certain degree through regulation of only temperature and pressure [2,3]. Solvo-thermal method (STM) is one of several developed techniques, which utilizes supercritical conditions for nanoparticles synthesis [2,3]. Due to low values of critical temperature and pressure, supercritical alcohols are fairly commonly used as solvents. In addition, they promote high nucleation rates and thus enable formation of smaller particles, offer an adjustment of degree of H-bonding and in a way improve sinterability [4].

The aim of this study was to investigate synthesis of $NiFe_2O_4$ via novel synthesis route under subcritical and supercritical conditions of ethanol using only p.a. grade inorganic salts $Ni(NO_3)_2 \cdot 6H_2O$, $Fe(NO_3)_3 \cdot 9H_2O$ as precursors and concentrated C_2H_5OH as solvent. In addition, a control sample was prepared via conventional atmospheric co-precipitation method. The ethanol solution with necessary quantities of salts to achieve molar ratio of 1:2 of Ni:Fe was placed in the pressure vessel (autoclave) where in the first case it was kept below critical point of ethanol at 200 ^oC for 2h at 33.7 bar. In the second case supercritical region of ethanol was utilized and the precursor solution was kept for 2 h at 260 ^oC and 72.7 bar. The all three obtained powders were then annealed at 650 ^oC for 4 h and for 8 h, and at 900 ^oC for 4 h. Crystalline structure of the prepared powders was analyzed by X-Ray diffraction method (XRD) using X-ray diffractometer with CoKα radiation at ambient temperature. Composition was also analyzed by Fourier Transform Infrared spectroscopy (FTIR) in the range of 370–4000 cm^{-1}. Powder morphology and particle sizes were analyzed by Scanning Electron Microscope (SEM) and by Transmission Electron Microscope (TEM). Porosity was measured by means of Brunauer–Emmett–Teller (BET) method by nitrogen adsorption desorption measurements at 77K. Room temperature magnetic measurements were carried out on Vibrating Sample Magnetometer (VSM), with magnetic field strength of 10 kOe.

The results of FTIR analysis for the "as prepared" powders show that apart from characteristic $NiFe_2O_4$ bands traces of precursor salts, intermediates, and alkoxyde moieties are present. It was found that the highest conversion was achieved under supercritical conditions. FTIR spectrums of the annealed powders clearly show that $NiFe_2O_4$ was formed in each of the applied synthesis routes and indicate that initially present reactant residues have been removed. The results of XRD support these

findings as presence of $NiFe_2O_4$ and α-Fe_2O_3 phases was confirmed in all of the prepared samples. Content of $NiFe_2O_4$ phase in the supercritical samples is somewhat higher (97–98%) compared to the both subcritical and control samples. The determined crystallite sizes of $NiFe_2O_4$ phase for subcritical samples ranges from 37 to 80 nm, for supercritical 47–107 nm, and for the control one from 70–187 nm, indicating strong influence of temperature and duration of the annealing process. TEM images of the "as prepared" powders (Figure 1) show that both STM samples contain nano-sized loosely aggregated particles with visible pores. Slightly finer structure of subcritical sample was ascribed to the higher density of ethanol during synthesis. The third conventionally prepared sample exhibits significantly larger primary particles compared to the other two. The obtained SEM micrographs of the samples annealed at 900^{o}C for 4h depict extensive agglomeration upon annealing and reveal similar morphology of both of the STM powders consisting of fairly large rounded particles (cca. 100 nm) that is finer in comparison to the control one, and with subcritical sample having the finest structure of them all. BET analysis also confirms this, as in the structure of the STM powders in "as prepared" state mesopores are prevailing as opposed to the control sample, in which much of the porosity is present in micropores. Their overall porosities are also about 2–4 times higher than that of the control one, which in contrast has significantly larger surface area. Annealing seems to have quite different impact on the powders, and while the STM samples almost completely lose mesoporosity and convert into compact structures, the control sample seems to undergo fracturing leading to the increased surface area and microporosity. All of the samples displayed characteristic soft magnetic behavior at room temperature. The saturation magnetization (Ms= M(10,000 Oe)) of the STM samples is comparable to the conventionally obtained sample, but their coercivity (Hc) and remanence are significantly higher, resulting in more square shaped hysteresis loops. It can be concluded that studied novel STM route provides higher conversion, but also a material with larger average crystallite size upon annealing and yet with potentially advantageous magnetic properties for magnetic recording, electrical, optical or similar applications.

References:

[1] D.S. Mathew and R.S. Juang, Chem. Eng. J. 129 (2007) p. 51.
[2] F. Cansella, C. Aymonie, J. Supercrit. Fluids 47(3) (2009) p. 508.
[3] A. Orlović, Đ. Janaćković, D. Skala, Catal. Commun. 3(3) (2002) p. 119.
[4] J.A. Darr, M. Poliakof, Chem. Rev. 99 (1999) p. 495.
[5] The authors acknowledge funding from the Ministry of Education, Science and Technological Development of the Republic of Serbia, Contract No. 451-03-68/2022-14/200026.

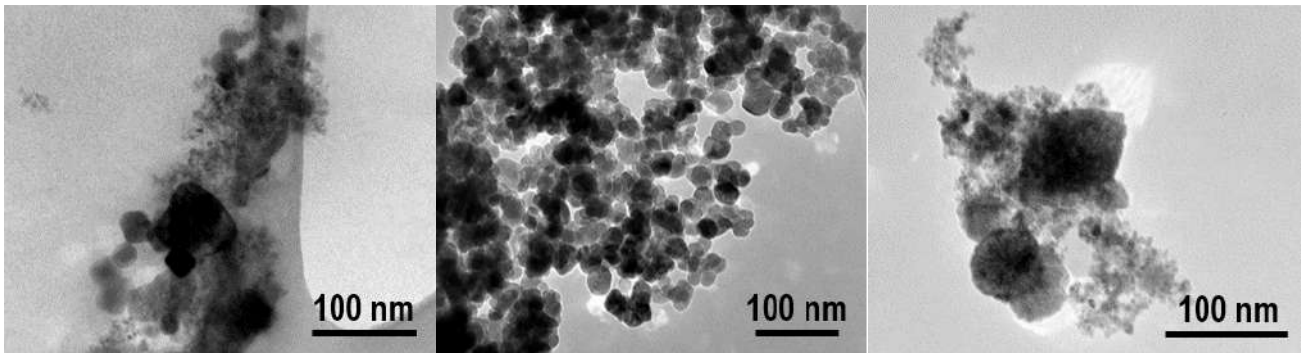

a) b) c)

Figure 1. TEM images of the "as prepared" powders: a) STM subcritical conditions, b) STM supercritical conditions and c) conventional co-precipitation.

Hybrid-Pixel Detectors for TEM by DECTRIS

Daniel Stroppa, Matthias Meffert, Luca Piazza

DECTRIS Ltd., Taefernweg 1, 5405 Baden-Daettwil, Switzerland

25 years of advances in aberration correction have clearly shifted the TEM characterization limits from the electron optics to other factors, among them the electron detectors. Recent improvements on electron detection technology clearly influence the TEM characterization on both Materials Sciences and Life Sciences, particularly when beam-sensitive samples are involved [1].

Hybrid-pixel detector (HPD) [2] is one of the approaches to directly detect and count electrons, with the distinctive advantage of flexible design with respect to the sensor material and electronics for optimization to different applications.

Building from its successful HPD technology for X-rays detectors, recently DECTRIS optimized its design to enable the precise detection of electrons. Among the required adaptations were the determination of optimal threshold values for counting electrons with zero read-out noise within a wide energy range and the retrigger technology fine-tuning to allow counting from 1 to 10^7 counts/pixel/second [3].

These characteristics already indicate that HPDs are fit to variety of TEM applications, including low-dose imaging with single-electron sensitivity, and 4D-STEM and EELS experiments with simultaneous high dynamic range and frame rate up to 18 kHz.

An application example is the flexible EELS collection from zero-loss peak (ZLP) to zero-noise core-loss (CL) region in the same acquisition range (Figures 1 adapted from reference [3]). Ongoing developments hint that improved frame rates and dynamic range can be expected with the next HPD generation.

References:

[1] A. R. Faruqi *et al*., Nucl. Inst. Methods Phys. Res., A **878** (2018), 180-190.
[2] N. Bochenek *et al*., IEEE Trans Nucl Sci **65 (6)** (2018), 1285-1291.
[3] B. Plotkin-Swing *et al*., Ultramicroscopy **217** (2020), 23-30.

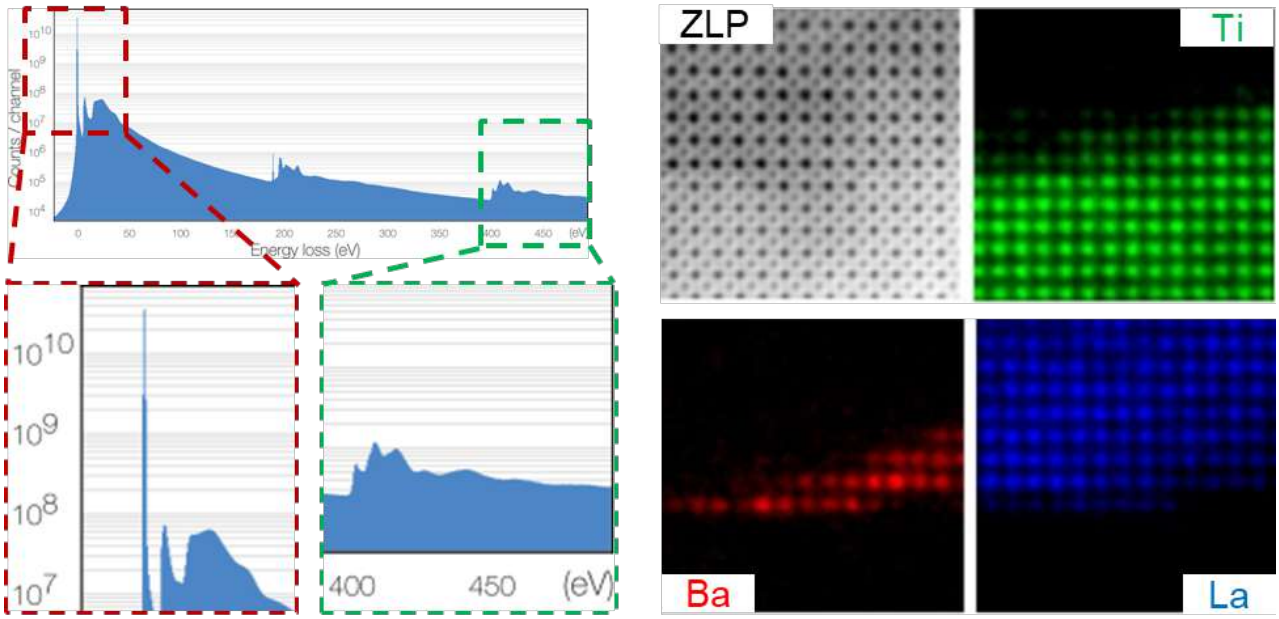

Figure 1. (left) EELS spectrum of h-BN at 60kV. Simultaneous ZLP and CL collection without saturation across 6 orders of magnitude. (right) Spectrum imaging of STO/BTO/LSMO. Flexible elemental mapping with multipass EELS allowed by zero-readout noise.

Microstructure Investigation of Nanocrystalline Materials Using Electron Diffraction Based Rietveld Analysis – Approximation of Instrumental Broadening

Viktoria Kovács Kis[1], Zsolt Czigány[1], Zsolt Kovács[2]

1 Thin Film Physics Laboratory, Centre for Energy Research, Budapest, Hungary

2 Department of Materials Physics, Eötvös Loránd University, Budapest, Hungary

Rietveld analysis [1] is commonly used for the evaluation of XRD and neutron powder diffraction patterns providing quantitative data on phase composition, crystal structure and microstructure parameters, such as crystallite size, anisotropic shape, preferred orientation, microstrain. However, this full pattern fitting method is less used for electron powder diffraction (EPD) patterns, mostly because the contribution of dynamical scattering of electrons to the detected intensity distribution hampers direct interpretation of diffraction pattern. Another difficulty is concerning the large variability of electron optics, which requires standardized measurements to control e.g. instrumental broadening in electron diffraction. So far, the number of papers presenting results based on Rietveld analysis of EDP does not exceed 25, however, this method has a great potential in nanoparticle and thin film analysis, as yields quantitative and statistically representative information on nanostructures materials.

Indeed, to achieve accuracy and reproducibility of EPD similar to that of the other diffraction methods, and to obtain as small instrumental broadening of diffraction peaks as possible, strict control on lens currents of the electron microscope is needed.

To measure and reproduce the instrumental broadening parameters for EPD Rietveld analysis, a three-step procedure was proposed [2], which comprises subsequent XRD and EPD measurements of two different calibration samples.

In this contribution, we present a single step procedure to determine the instrumental broadening parameters of the TEM using a few layer graphene sample (Ted Pella). Graphene is considered as an infinite, perfect 2D crystal (crystallite size is limited only by the aperture, i.e. 3 μm), which EPD is free of dynamical scattering, and influence of crystallite size and strain to peak broadening is negligible. Thus, the peak shape represents the instrumental broadening caused by a given combination of microscope lens currents. Therefore, diffraction peaks of the few layer graphene sample were used to measure broadening quantitatively and obtain analytical parameters of the Cagliotti function [3] which is implemented to model instrumental broadening during Rietveld analysis in e.g. the Maud software [4].

These instrumental broadening parameters obtained experimentally were further used in Rietveld analysis of various samples including nanoparticles, thin films (Figure 1) and bioapatites. Experience, limitations and possible further steps towards more reliable EPD Rietveld analysis are discussed herein [5].

References:

[1] Rietveld, H. M. Acta Cryst. **22** (1967), p. 151.
[2] Boullay, P., Lutterotti, L., Chateigner, D. and Sicard, L. Acta Cryst A. **70** (2014), p. 448.
[3] Caglioti, G., Paoletti, A. and Ricci, F. P. Nuclear Instruments. **3** (1958), p. 223.
[4] Lutterotti, L., Matthies, S., Wenk, H.-R., Schultz, A. S. and Richardson, J. W. Journal of Applied Physics **81** (1997), 594.
[5] The author are grateful to Levente Illés for his help during FIB milling of the dental enamel sample. Financial support was provided by the National Research, Development and Innovation Fund Office, Hungary, grant number K-125000. Electron microscopy and FIB facility at Centre for Energy Research was granted by the European Structural and Investment Funds, grant no.s VEKOP-2.3.3-15-2016-00002 and VEKOP-2.3.2-16-2016-00011, respectively.

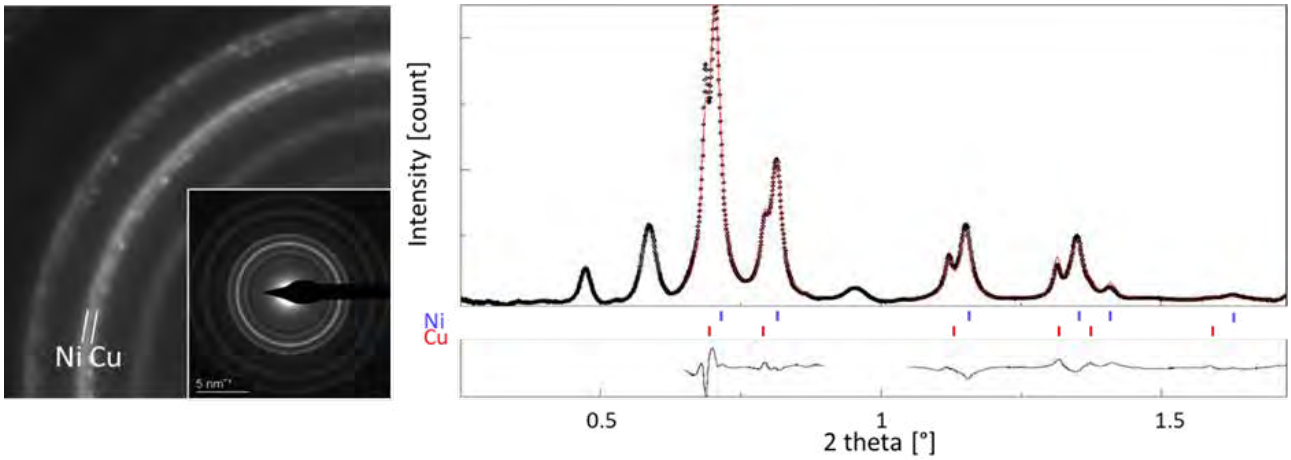

Figure 1. SAED of a Cu-Ni thin film deposited at 150 °C using DC magnetron sputtering (left) and corresponding integrated intensity profile (right). Black dots are measurement data and red line is fitted curve. Bragg positions of Cu and Ni, and difference curve of the fitted regions are also plotted.

Calibration Procedure and Error Analysis to Improve the Accuracy of SAED in Aberration Corrected TEM

Zsolt Czigány and Viktória Kovács Kis

Thin Film Physics Laboratory, Centre for Energy Research, Budapest, Hungary

The aim of this work is to improve the accuracy and reproducibility of selected area electron diffraction (SAED) by fine tuning of experimental and evaluation parameters to create the basis of reliable structure analysis of multicomponent nanocomposites or textured materials and/or having close diffraction rings. Among diffraction techniques used for structure investigation electron diffraction provides very local information, however, its accuracy and reproducibility are generally considered to be lower than that of X-ray diffraction (XRD). A conservative estimate, according to the famous handbook by Williams and Carter [1], for the accuracy and reproducibility of interplanar (d) spacing determination from electron diffraction is 1-3% without internal standard. The primary reason for this degree of uncertainty is that a focussed diffraction pattern can be achieved by different combination of specimen height, illumination conditions and diffraction focus giving rise to different camera length (CL) values and widths of diffraction rings. This can be improved by application of standard acquisition parameters to achieve of reproducible TEM settings. At our department Lábár et al. [2] elaborated a calibration procedure and achieved 0.3% accuracy. Higher accuracy (~0.1%) can only achieved by application of internal standard. Since systematic study of the effect of these parameters on the data is missing, similar estimates apply for the error of camera length in a recent aberration corrected transmission electron microscopes. State-of-the-art aberration corrected microscopes have an order of magnitude better acceleration voltage and lens current stability compared to conventional TEMs, which implies an order of magnitude better reproducibility and accuracy in electron diffraction. Besides the stability of acceleration voltage and lens currents, field emission gun (FEG) electron sources provide a coherent electron beam with narrow energy spread which also decrease the instrumental broadening. For standard SAED acquisition we applied a C_S corrected Themis (Thermo Fisher) TEM with operated at 200kV and equipped with Schottky field emission gun (FEG) having an energy spread of ~0.7eV. SAED patterns were recorded by a 4kx4k Ceta camera using Velox software (Thermo Fischer). The diffraction patterns were exported in 16 bit tiff format and 1D diffraction profiles, containing intensity distribution as function of scattering angle, were obtained using Process diffraction software [2]. The software allows visual fit and refinement of centre of the pattern (X, Y), eccentricity (ε) and its angle (α) together with calibration of camera length. By reproducing lens currents through careful control of specimen height and illumination conditions we reached a session to session reproducibility better than $3x10^{-4}$ for camera length. Refinements of the centre of the diffraction pattern and corrections for lens distortions (ellipticity of rings) allowed for determining the ring diameters with an accuracy of 10^{-3}. For determination of the ellipticity parameters by visualization of the intensity distribution an ideal calibration specimen is composed of nanocrystalline grains free of texture and produce narrow diffraction rings. For this purpose we deposited a polycrystalline Cu layer on TEM grid coated with nanocrystalline graphene. The achieved accuracy of 10^{-3} for lattice spacing measurement without internal standard is compatible with that of XRD, and reduction of instrumental broadening due to the elaborated evaluation procedure allows for separation of close reflections (Figure 1). Furthermore, we analyse the effect of different error sources and reason the achieved absolute accuracy of the measurement.

References:

[1] D.B. Williams & C.B. Carter (2009) *Transmission Electron Microscopy; A Textbook for Materials Science*, p. 285. New York, London: Plenum Press.
[2] J. Lábár et al. Microscopy and Microanalysis **8** (2012) 406
[3] The authors acknowledge the support of projects OTKA K-125100; VEKOP-2.3.3-15-2016-00002 and thank György Zoltán Radnóczi for preparation of FIB lamellae of tooth enamel.

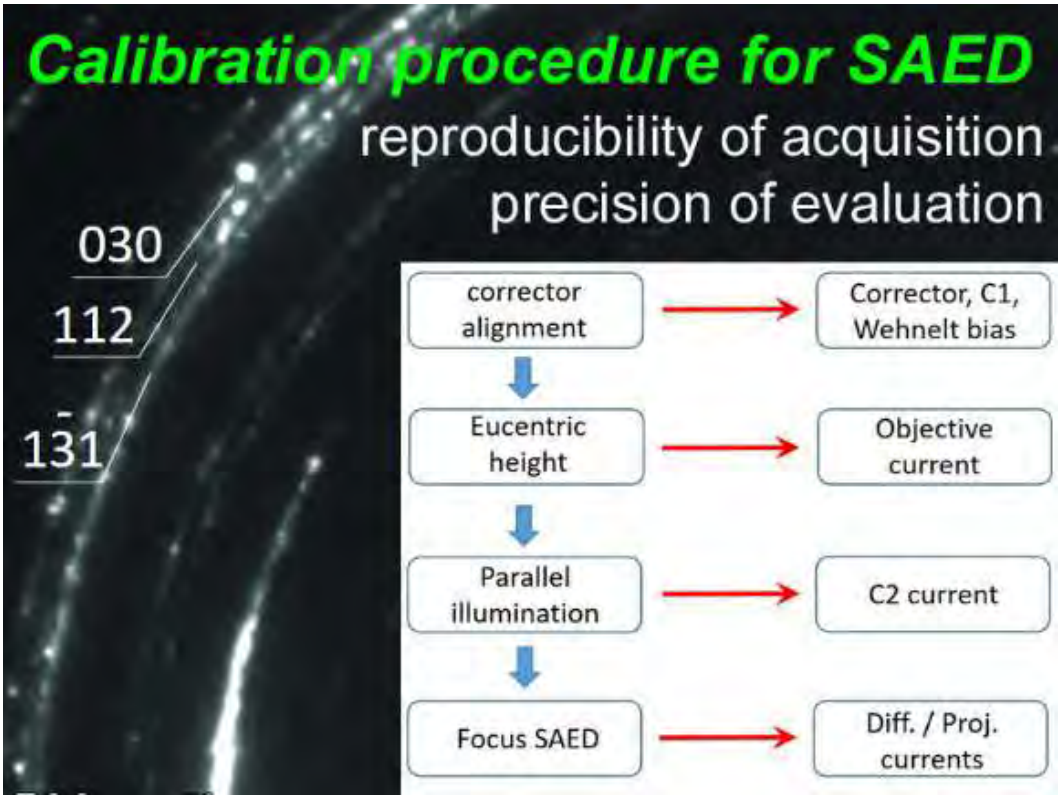

Figure 1. Electron diffraction of dental enamel bioapatite. Very close indexed rings could be distinguished which made possible a texture analysis. The inset shows the main steps of the procedure and their influence on the lens currents.

Optimal Experiment Design for Characterising Heterogeneous Nanostructures by Using 4D Scanning Transmission Electron Microscopy

Duygu Gizem Sentürk[1,2], Annick De Backer[1,2], Thomas Friedrich[1,2], Sandra Van Aert[1,2]

1 EMAT, University of Antwerp, Antwerp, Belgium

2 NANOlab Center of Excellence, University of Antwerp, Antwerp, Belgium

Quantitative analysis such as atom-counting from aberration-corrected STEM plays an important role to understand the structure-property relationship of nanomaterials. To obtain reliable atom-counting results, one can predict the optimal collection angles of the annular detector. For this purpose, the probability of error (Pe) was introduced [1,2] using statistical detection theory for monotype nanostructures. When extending the atom-counting problem to complex hetero nanostructures, the use of pixelated detectors offers important advantages by providing conventional STEM images with any number of virtual detectors without the need for pre-configured fixed detector angles [3] or ultimately to use the full 4D STEM dataset.

Here, we extended the concept of the Pe to investigate the possible benefits of analysing multiple 2D STEM images when counting atoms of different chemical nature. The atom-counting problem is then formulated as a statistical hypothesis test, where each hypothesis corresponds to a specific number and type of atoms in an atomic column. The Pe corresponds to the probability to choose the wrong hypothesis. To compute the Pe, realistic 4D STEM simulations were performed from which multiple 2D STEM images were generated with varying inner and outer detector angles. From these 2D images, so-called scattering cross-sections (SCS) can be computed corresponding to the total scattered intensity for each atomic column which performs as an optimal criterion for atom-counting [2]. Moreover, the presence of electron counting noise is taken into account when computing the Pe.

In a first case study, the Pe has been calculated to distinguish the different types of elements for binary mixed columns corresponding to a Au@Pt core-shell nanoparticle. In Figure 1a, the yellow curve represents the slightly lowered Pe as a function of varying detector settings when a combination of two independent 2D STEM images is used under an incident electron dose of 10^5 $e^-/Å^2$. In Figure 1b, the Pe is evaluated as a function of the electron dose under the optimal detector settings and for the full dark field region of the 4D STEM dataset. The dashed horizontal line shows that to distinguish the mixed atomic columns with a Pe of 5%, the electron dose can be reduced by a factor of 50 when using two optimal non-overlapping detectors. The required incident electron dose can be further reduced with a factor of 10^3 when exploring the full dark field region of the 4D dataset. Subsequently, the potential advantage of three independent optimal detector settings is further explored for a trimetallic nanostructure, consisting of a varying number of Au, Ag and Al atoms. Figure 2a, under an incident electron dose of 10^4 $e^-/Å^2$, shows that the Pe can be even further reduced when the combination of three 2D STEM images is analysed instead of two independent 2D STEM images reconstructed from a 4D STEM dataset. Figure 2b, illustrates that the required electron dose to identify the type and number of atoms can be considerably lowered with the use of multiple non-overlapping detectors. In summary, we have shown that the concept of the Pe can be used to find optimal strategies to count atoms from 4D STEM datasets. In particular, the method is generalised to create a set of multiple 2D STEM images providing independent information concerning thickness, composition, and ordering of the atoms along the viewing direction [4].

References:

[1] J. Gonnissen *et al*, Appl. Phys. Lett. 105 (2014) 063116
[2] A. De Backer *et al*, Ultramicroscopy 151 (2015) 46
[3] N. Shibata *et al*, J. Electron Microsc. 59 (2010) 473
[4] This work was supported by the European Research Council (Grant 770887 PICOMETRICS to SVA and Grant 823717 ESTEEM3). The authors acknowledge financial support from the Research Foundation Flanders (FWO Belgium) through project fundings and a postdoctoral grant to ADB.

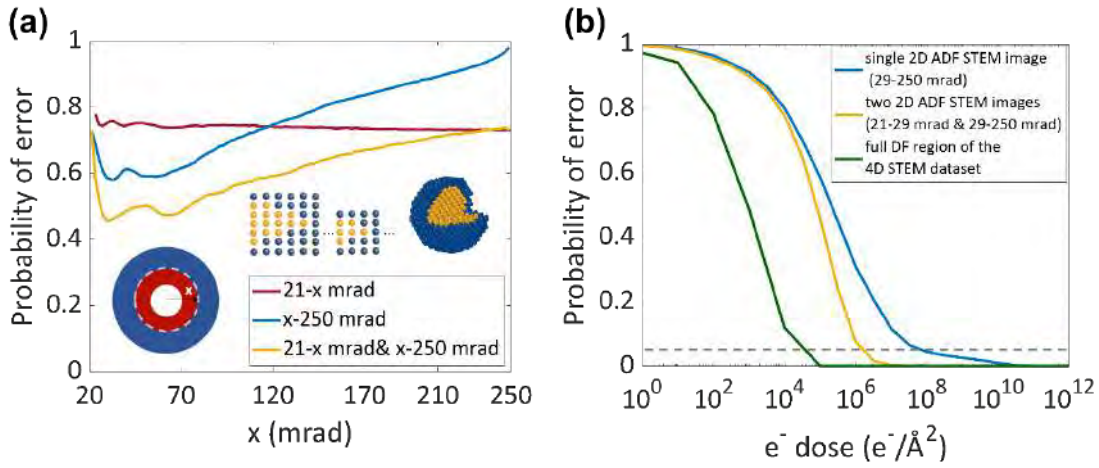

Figure 1: Pe for Au@Pt core-shell nanoparticle to distinguish between the total number of atoms and type of atoms in a binary mixed atomic column varying from 1 up to 20 atoms **(a)** as a function of the outer angle of a single ADF detector with fixed inner angle (red), the inner angle of a single ADF detector with fixed outer angle (blue), and the common angle x for two independent detectors (yellow) for an incident electron dose of 10^5 $e^-/Å^2$ **(b)** Pe as a function of the incident electron dose calculated for a single ADF detector (blue), two independent ADF detectors (yellow) and dark field region of full 4D STEM dataset (green).

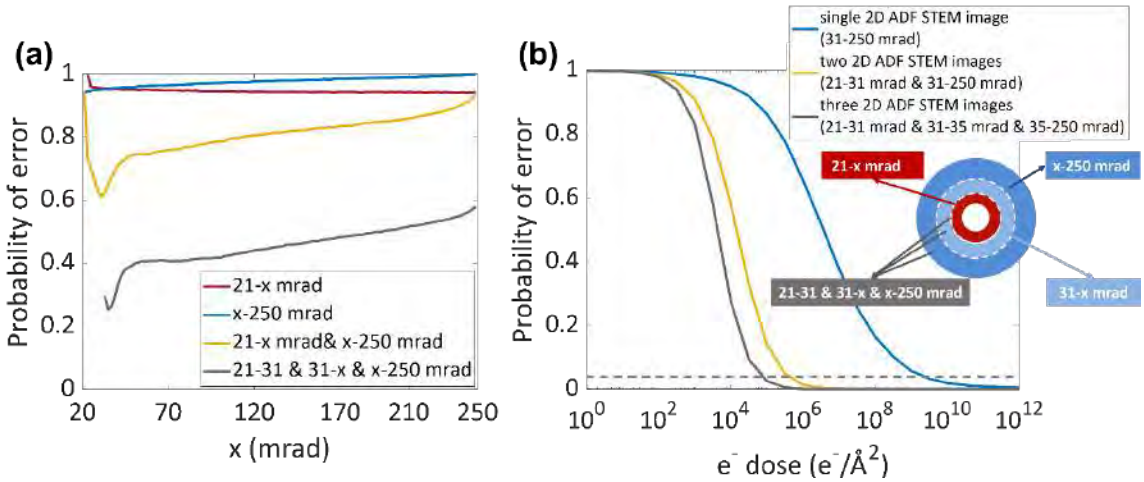

Figure 2: Pe for characterising Al@Au@Ag mixed nanostructure **(a)** as a function of the outer angle of a single ADF detector with fixed inner angle (red), the inner angle of a single ADF detector with fixed outer angle (blue), the common angle x for two independent detectors (yellow) and the common angle x for two independent detectors while third detector has fixed settings (grey) under an incident electron dose of 10^4 $e^-/Å^2$ **(b)** as a function of the incident electron dose calculated for a single ADF detector (blue), two independent ADF detectors (yellow), three independent ADF detectors (grey).

Understanding the Influence Of Experimental Parameters On Atomic Electrostatic Configuration Measurements By Segmented-Detector DPC-STEM

Rafael V. Ferreira[1,2], Sebastian Calderon[3], Deepyanti Taneja[4], Jayanth Raghavendrarao[4], Langyan Zhou[4], Ricardo M. Ribeiro[1,5], Deji Akinwande[3,6] and Paulo J. Ferreira[1,2,6]

1 INL – International Iberian Nanotechnology Laboratory, Braga, Portugal

2 Mechanical Engineering Department and IDMEC, Instituto Superior Técnico, University of Lisbon, Lisboa, Portugal

3 Department of Materials Science and Engineering, Carnegie Mellon University, Pittsburgh, Pennsylvania, USA

4 Microelectronics Research Center, Department of Electrical and Computer Engineering, The University of Texas at Austin, Austin, Texas, USA

5 Department and Centre of Physics, University of Minho, Braga, Portugal

6 Materials Science and Engineering Program, The University of Texas at Austin, Austin, Texas, USA

The study of prevalent defects and their impact on functional properties is currently a critical aspect in the development of two-dimensional (2D) materials, which are held as promising candidates for implementation in next-generation devices. However, the direct characterization of the structural and functional properties of a specific defect, especially at atomic scales, is a challenging task, both in terms of spatial resolution and nature of the measurements, which must be in some way sensitive to the electronic structure of the material. In this regard, the use of differential-phase contrast (DPC) in scanning transmission electron microscopy (STEM) stands out as a method well suited for this purpose, making use of the natural coupling between the fine electron probe and the electromagnetic fields within a sample. This interaction induces a redistribution of intensity at the diffraction plane, which allows the mapping of electrostatic forces at the atomic level. This capability has been demonstrated in the study of dopants and defects in graphene [1], stacking-type dependence of the charge distribution in bilayer MoS_2 [2], and negative charge channels induced by line defects in MoS_2 and WS_2 [3].

DPC-STEM measurements can be conducted either with pixelated detectors capable of recording the entire diffraction disk, or with segmented detectors, which are typically annular detectors that integrate the intensity of the disk over four independent quadrants. Pixelated detectors offer accurate measurements of the center of mass of the diffraction disk and, therefore, of the electrostatic fields acting on the electron probe, but do so at the cost of slow readout speeds and large datasets. On the other hand, segmented detectors cannot match pixelated detectors in terms of resolution, making them unsuitable for quantitative analyses, but they present important advantages: image acquisitions are significantly faster (an important factor for sensitive materials) and DPC images can be generated in real time, making it easier to identify interesting electrostatic features and to correct lens aberrations. Thus, the benefits afforded by segmented detectors justify their relevance, especially for the observation of sensitive structures such as 2D materials, so that it becomes essential to understand the effect of experimental parameters on DPC-STEM observations.

In this work, the influence of key experimental parameters on atomic-resolution segmented-detector

DPC-STEM measurements is evaluated on two of the most promising 2D transition metal dichalcogenides (TMDs), MoS_2 and $MoSe_2$, including some of their most prevalent defects. Since TMDs are more complex 2D material systems due to their two-element compositions arranged in a structure of three atomic planes, they present a larger variety of structural and chemical features, which is advantageous for the purposes of this investigation. Additionally, MoS_2 and $MoSe_2$ are similar enough to allow for testing the sensitivity of DPC-STEM in discerning between the electrostatic features of the two materials. This study is primarily carried out using extensive multislice simulations to understand the influence of defocus, probe convergence angle and source intensity distribution profile on atomic-resolution DPC-STEM images of the two 2D TMDs and associated defects. Corresponding experimental images are then analyzed in view of the conclusions drawn from the simulation-based studies. [4]

References:

[1] R. Ishikawa *et al*, Nat. Commun. **9** (2018), p. 3878.
[2] K. Müller-Caspary *et al*, Phys. Rev. B **98** (2018), p. 121408.
[3] S. Fang *et al*, Nat. Commun. **10** (2019), p. 1127.

[4] R.V.F. acknowledges funding from the FCT Ph.D. studentship SFRH/BD/149390/2019. R.M.R. acknowledges the FCT grant UIDB/FIS/04650/2020-2023. D.A. acknowledges the Presidential Early Career Award for Scientists and Engineers (PECASE) through the Army Research Office (W911NF-16-1-0277), and a National Science Foundation grant (ECCS-1809017).

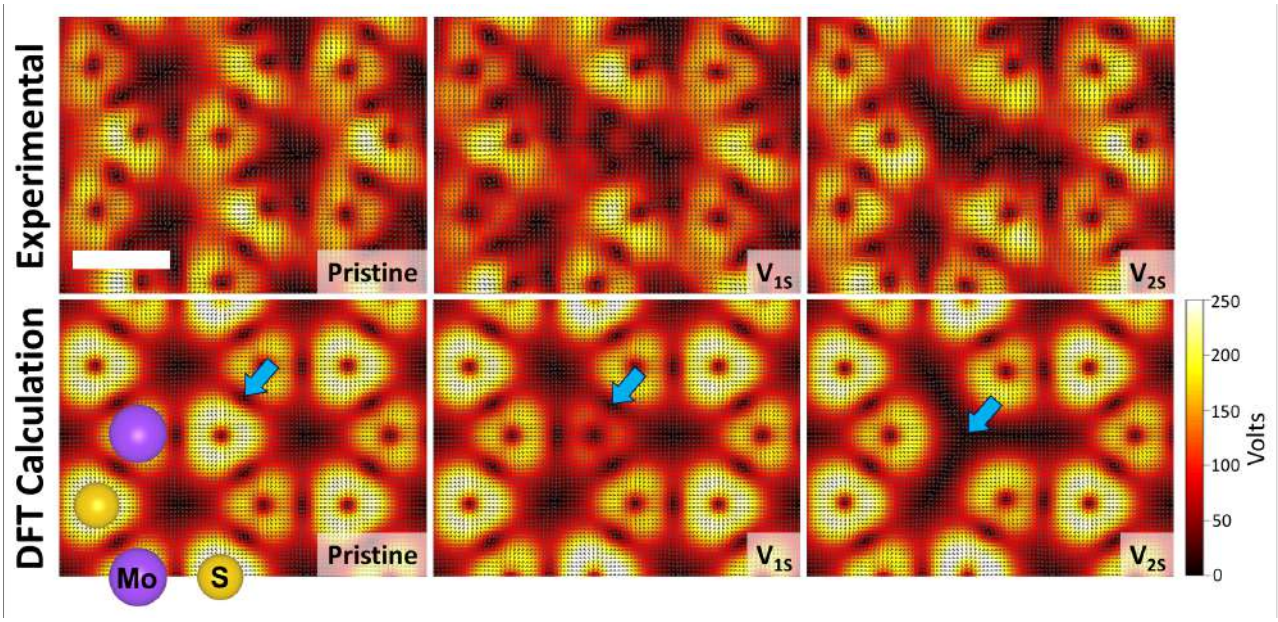

Figure 1. Projected probe-convolved atomic electric field maps for pristine MoS_2, and for regions containing sulfur mono- and divacancies, indicating the magnitude (color) and direction (arrows) for each pixel of the field calculated from experimental images taken at 200 kV and DFT calculations. The blue arrows in the DFT calculated maps point to the location of the electric field minima. The scale bar corresponds to 2 Å and the color bar corresponds to the DFT calculated maps.

Fast prediction of ADF-EDX scattering cross-sections for elemental quantification of nanostructures

Zezhong Zhang[1,2,3], Annick De Backer[1,2], Ivan Lobato[1,2], Sandra Van Aert[1,2], Peter Nellist[3]

1 EMAT, University of Antwerp, Antwerp, Belgium

2 NANOlab Center of Excellence, University of Antwerp, Antwerp, Belgium

3 Department of Materials, University of Oxford, 16 Parks Road, Oxford OX1 3PH, United Kingdom

To understand the structure-property relationship in nanostructured materials, we need to probe their crystal structures and compositions at the atomic scale. From a single ADF-STEM image, it has been demonstrated that one can determine the atomic column positions and count the number of atoms for homogenous materials with high precision and accuracy [1-2]. Advanced materials usually consist of multiple elements in a complicated structure. Significant difficulties remain to disentangle the contributions of composition and thickness in STEM due to dynamic scattering, which needs to be taken into account by detailed simulations. However, the combination of the computationally intensive nature of the multislice calculation and the enormous amount of possible configurations for a given composition makes the quantification of mixed columns almost impossible. To address these challenges, we here report the development of an incoherent non-linear method for the fast prediction of ADF-EDX scattering cross-sections of mixed columns under channelling conditions.

Due to the dynamic nature of electron scattering, ADF and EDX have a non-linear relationship against thickness and composition, particularly at the atomic scale in zone axis orientation. However, preliminary experiments indicate a linear dependence between EDX and ADF scattering cross-sections, which are defined as the integration of signal intensities for each atomic column. We performed frozen phonon multislice calculations for a pure Au crystal and investigated the linear dependence of the ADF-EDX scattering cross-sections using the coefficient of determinantion R^2 for different ADF inner and outer collection angles. Since EDX can be considered as a perfect incoherent reference, an R^2 value equal to 1 suggests perfect longitudinal incoherence of the ADF. As shown in Fig. 1, this is the case for ADF at high collection angles.

Because of the incoherent signal mode, we can treat dynamical scattering as a superposition of individual atoms focussing the incident electrons. Here we expanded the so-called atomic lensing model [3] (developed previously for ADF) to spectroscopy. For a mixed column, the ordering possibilities grow exponentially with the thickness and types of elements thus quickly exceeding the capability of multislice calculations due to computational cost. In contrast, the atomic lensing model allows fast generation of EDX scattering cross-sections with the ordering of elements taken into account under the channelling condition. As shown in Fig. 2 for a core-shell Au-Pt nanorod, scattering cross-sections extracted from the multislice calculations agree reasonably well with the atomic lensing model predictions but are very different from those of the linear model where the signal is assumed to scale linearly with the number of atoms for each type. To deploy the atomic lensing model to experimental results, we can incorporate the experimentally measured EDX partial cross-section [4], which is called partial since it includes all the microscope-dependent factors during normalisation thus bypassing the difficult characterisation of the EDX detector. We can also make use of the linear dependence between the signal modes as a constraint for simultaneous ADF-EDX atom counting. This method allows us to explore the enormous ordering possibilities of heterogeneous materials with multiple elements.

References:

[1] J.M. LeBeau, S.D. Findlay, L.J. Allen, S. Stemmer, *Nano Letters* 10 (2010) p. 4405–4408.
[2] A. De Backer, K.H.W. van den Bos, W. Van den Broek, J. Sijbers, and S. Van Aert, *Ultramicroscopy* 171 (2016) p. 104-116.
[3] K.H.W. van den Bos, A. De Backer, G.T. Martinez, N. Winckelmans, S. Bals, P.D. Nellist, S. Van Aert, *Physical Review Letters* 116 (2016) p. 246101.
[4] A. Varambhia, L. Jones, A. London, D. Ozkaya, P.D. Nellist, & S. Lozano-Perez, *Micron* 113 (2018) p. 69-82.
[5] The authors acknowledge financial support from the Research Foundation Flanders (FWO, Belgium) through Project No. G.0502.18N and a post-doctoral grant to ADB. This project has received funding from the European Research Council (ERC) under the European Union's Horizon 2020 research and innovation programme (Grant Agreement No. 770887 PICOMETRICS and No. 823717 ESTEEM3.

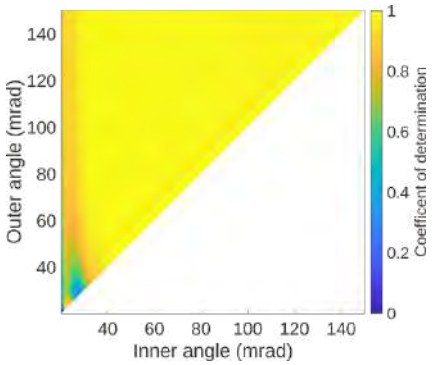

Figure 1. Scattering cross-sections of ADF (with different collection angles) against EDX with linear regression, where the coefficient of determination R^2 of EDX-ADF is a measure of linear dependence between different signal modes. The simulations were performed for a Au crystal in [001] direction with varying thickness (1-25 atoms), illuminated using 300 keV electrons with a 20 mrad condenser aperture and no lens aberrations.

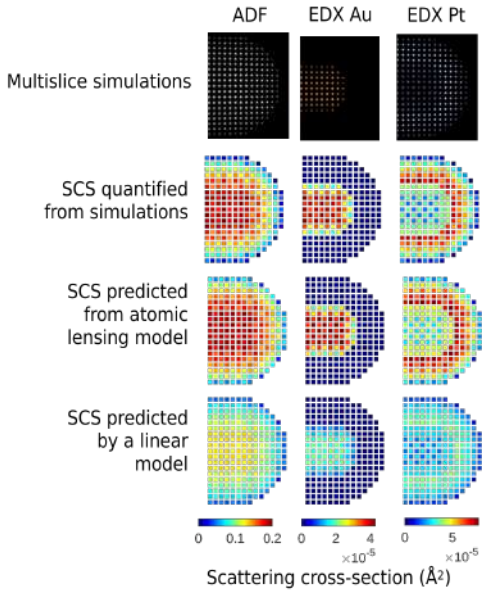

Figure 2. Comparing the simulated and predicted scattering cross-sections (SCS) of ADF and EDX for an Au-Pt core-shell nanorod.

Imaging Structural Defects and Associated Oxygen Positions in 3*d* Li-rich Metal Oxide

Weixin Song[1,2,3], John-J. Marie[1,2,3], Robert A. House[1,2,3], Peter G. Bruce[1,2,3], Peter D. Nellist[1,2,3]

1 Department of Materials, University of Oxford, Oxford, UK

2 The Faraday Institution, Didcot, UK

3 The Henry Royce Institute, Oxford, UK

Li-rich $Li_{1.2}Ni_{0.13}Mn_{0.54}Co_{0.13}O_2$ has delivered a high specific capacity over 250 mAh g^{-1} as a cathode material in Li-ion batteries compared with conventional layered metal oxides (<200 mAh g^{-1}). Such high capacity results from the redox reaction of the lattice O^{2-} ions and transition metals (TMs). Despite the boost in the capacities, $Li_{1.2}Ni_{0.13}Mn_{0.54}Co_{0.13}O_2$ still suffers from voltage hysteresis and degradation in the voltage and capacity over cycling [1]. Synthesis efforts aim to overcome these issues. The challenge is $Li_{1.2}Ni_{0.13}Mn_{0.54}Co_{0.13}O_2$ has rather inhomogeneous crystalline structures whose role in affecting the materials performance is unclear [2]. The as-prepared $Li_{1.2}Ni_{0.13}Mn_{0.54}Co_{0.13}O_2$ material contains a number of defects, such as stacking faults, and has raised debates on whether the material is a coherent mixture of *C2/m* Li_2MnO_3 and *R-3m* $LiTMO_2$ phase or a solid solution with the monoclinic phase [2]. The lack of understandings on the pristine structure of $Li_{1.2}Ni_{0.13}Mn_{0.54}Co_{0.13}O_2$ impedes the approach development for new materials.

In this work, we performed simultaneous annular dark field (ADF) imaging and electron ptychography on pristine $Li_{1.2}Ni_{0.13}Mn_{0.54}Co_{0.13}O_2$ prepared by sol-gel method. Figure 1a shows the ADF image projected along the pseudo [100] zone axis, which rather than showing only monoclinic [100] projection domains, shows three types of monoclinic domains projected along the [100], [110] and [1-10] zone axis, respectively. The domain variants are due to the faulted stacking of the TM layers in c direction. The TM layers composing the three types of domains have an in-plane rotation angle of 120 degree with respect to each other and the resulting stacking faults are referred to as rotation type. In the TM layers, Li^+/Ni^{2+} and Co^{3+}/Mn^{4+} cation ordering in a honeycomb pattern leads to the dumbbell contrast in ADF imaging that arising from the mixing Co/Mn atom columns [1]. The dumbbell contrast is not uniformly seen as shown in Figure 1b, where cation disordering contrast is seen in the transition regions (labelled with white dash) between the [110] and [1-10] projection domains. Such transition regions possibly result from the boundaries of the two types of domains or the in-plane cation disordering. Figure 1c displays several types of TM layers that lead to cation ordering (O), mixing ordering/disordering (O/D) and disordering (D) contrast in ADF imaging. In addition to the rotation-type stacking faults, Figure 1d shows another type resulting from out-of-plane TMs layer shift by a vector of c/2 in the c direction, namely shift type. Both types of stacking faults rely on the imaging of TMs layers whilst lack the understanding of oxygen stacking. To probe the oxygen lattice, we carried out focused-probe electron ptychography to reconstruct the phase image of the material and use the simultaneous aberration-corrected ADF image to point out TMs. Figures 2(a-c) show the simultaneous ADF and ptychographic image and their composite image, respectively, of a rotation-type stacking fault region and Figures 2(d-f) show that of a shift-type stacking fault region. Although TM layers possess a number of rotation-type stacking faults, the oxygen layers are seen in an O3-type stacking, coordinating with the TMs at the octahedral sites. Such TM-O coordination and the more covalent bonding of TM-O than Li-O lead to O layer mismatch in the shift-type stacking faults, indicated by the solid and dash circles in Figure 2f. The imaging on the TMs and O layer stacking shows different structure defects in $Li_{1.2}Ni_{0.13}Mn_{0.54}Co_{0.13}O_2$ that can affect the electrochemical performance [3].

References:

[1] RA House, GJ Rees, MA Pérez-Osorio, J-J Marie, E Boivin, AW Robertson, A Nag, M Garcia-Fernandez, K-J Zhou and PG Bruce, Nature Energy **5** (2020), p. 777.
[2] AK Shukla, QM Ramasse, C Ophus, DM Kepaptsoglou, FS Hage, C Gammer, C Bowling, PAH Gallegos and S Venkatachalam, Energy & Environmental Science **11** (2018), p. 830.
[3] The authors acknowledge use of characterization facilities within the David Cockayne Centre for Electron Microscopy, Department of Materials, University of Oxford and in particular the Faraday Institution (FIRG007, FIRG008), the EPSRC (EP/K040375/1 "South of England Analytical Electron Microscope") and additional instrument provision from the Henry Royce Institute (Grant reference EP/R010145/1).

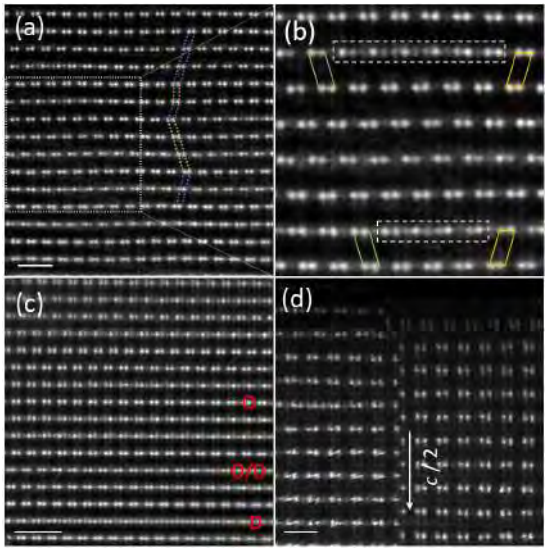

Figure 1 Stacking faults of $Li_{1.2}Ni_{0.13}Mn_{0.54}Co_{0.13}O_2$ from atomic resolution. (a) ADF image along pseudo [100]M zone axis in a rotation-type stacking fault region. The white rectangular region is magnified in (b). The red, green and orange tetragons indicate monoclinic domains projected along [100], [110] and [1-10] zone axis, respectively. (c) ADF image of various types of TMs layers showing cation ordering (O), mixed ordering/disordering (O/D) and disordering (D) contrast. (d) ADF image of shift-type stacking fault structure. Scale bar is 1 nm.

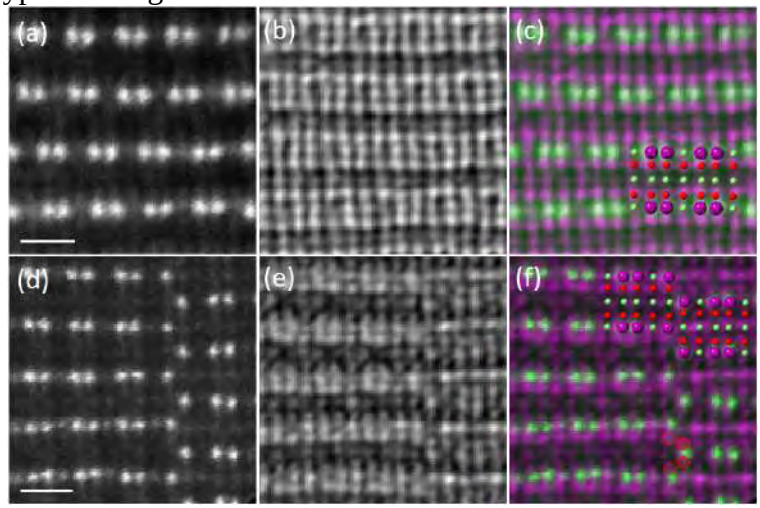

Figure 2 Imaging of layer stacking. (a-c) Rotation-type stacking faults. (d-f) Shift-type stacking faults. (a, d) ADF image. (b, e) Ptychographic image. (c, f) Composite image of the simultaneous ADF and ptychographic image. Superposed image in c and f is the monoclinic crystal models projected along [100] zone axis. Purple sphere is TM, green is Li and red is O. Scale bar is 0.5 nm.

Electron beam induced Brownmillerite – perovskite phase transition in $La_{0.6}Sr_{0.4}CoO_{3-\delta}$

Sergej Ražnjević[1,2], Matthäus Siebenhofer[3], Markus Kubicek[3], Zaoli Zhang[1,2]

1 Erich Schmid Institute of Material Science, Austrian Academy of Sciences, 8700, Austria

2 Montanuniversität Leoben, Franz-Jozef-Straße, 8700, Leoben, Austria

3 Institute of Chemical Technologies and Analytics

Perovskite structure is often described with a chemical formula ABO_3 where A is usually the bigger ion and B is the smaller one. In the perovskite structure, every B site is surrounded by an oxygen octahedral [1]. There are a large number of oxygen-deficient perovskites $A_mB_mO_{3m-\delta}$ that have a wide variety of oxygen vacancy ordering pattern [2]. Brownmillerite structure is chemically described as $A_2B_2O_5$ and here, unlike perovskites, oxygen atoms form alternating planes of octahedral and tetrahedral along the [100] direction [1].

Lanthanum Strontium Cobaltite has been heavily studied in the past decade because of its promising properties that can be used in solid oxide fuel cells, oxygen transport membranes and gas sensors [3]. In previous research, it has been shown that introducing the strain to the structure can lead to the Brownmillerite ordering [3,4]. The Brownmillerite phase has different properties from the, regular bulk, perovskite phase [1].

In this work we investigate how the electron beam influences the oxygen vacancy ordering in epitaxial Lanthanum Strontium Cobaltite thin films.

Using pulsed laser deposition (PLD) 40nm of epitaxial $La_{0.6}Sr_{0.4}CoO_{3-\delta}$ (LSCO) was grown on a (100) Yttrium stabilized Zirconia (YSZ) with a 10nm buffer layer of $Ce_{0.8}Gd_{0.2}O_{2-\delta}$ (GDC). An orientation relationship between the substrate and the buffer layer is $(010)_{YSZ}||(010)_{GDC}$ and $[010]_{YSZ}||[010]_{GDC}$ while LSCO layer has a 45° in-plane rotation with respect to the GDC, giving a relation of $(010)_{GDC}||(01\text{-}1)_{LSCO}$ and $[010]_{GDC}||[01\text{-}1]_{LSCO}$. TEM-sample was prepared using a Focused Ion Beam (FIB) cutting technique.

Atomic structure evolution under electron beam was systematically investigated using a JEOL 2100F microscope equipped with an image-side Cs-corrector and energy filtering system. The film was continuously illuminated for 8min with a beam current density of 64.8pA/cm2. Figure 1 shows HRTEM images of the thin film before and after electron beam illumination, together with corresponding FFT patterns. Before illumination, from the atomic structure image, darker stripe contrast (highlighted by a red arrows) in every other CoO plane are present, which indicates the presence of the Brownmillerite phase. This ordering trend in every other plane effectively doubles the cell parameters. During illumination, the difference in contrast between the planes gradually fades and, finally, disappears completely, as shown in figure 1(b). Doubling of the lattice parameter of the Brownmillerite structure is usually visible in the diffraction pattern as half-integer reflections. Therefore, the local fast Fourier transform (FFT) analysis was performed on the HRTEM images. An FFT pattern before illumination in which half-integer reflections are present (highlighted by a blue arrow) further confirms the existence of the Brownmillerite phase. After illumination, half-integer reflections disappear, indicating that the lattice doubling is no longer present, thus ensuring the transition to the perovskite phase. The analytical investigation was further carried out using electron energy-loss spectroscopy (EELS). Figure 2a show the oxygen K-edge before illumination where two

peaks with an energy difference of about 6 eV are distinguished. The first peak corresponds to the interactions of O 2p and La 5d orbitals, while the second peak is due to the interaction of O 2p and hybrid La/Sr 4sp orbital [5]. After illumination (Figure 2b), the peak with the higher energy (highlighted by a blue arrow) is not present anymore, thus indicating the change in the oxygen bounds in the film [6].

References:

[1] D. Gilbert et al. "Ionic tuning of cobaltites at the nanoscale", Adv. Mater. **26**, (2014), p. 2789–2793

[2] M. T. Anderson, J. T. Vaughey, and K. R. Poeppelmeier; "Structural Similarities among Oxygen-Deficient Perovskites", Chem. Mater. **5**, (1993)**,** p. 151-165

[3] S. Stemmer et al. "Oxygen Vacancy Ordering in Epitaxial $La_{0,5}Sr_{0,5}CoO_{3-\delta}$", J. Appl. Phys. **90**, (2001), p. 3319

[4] Y. Ivanov et al. "Strain-induced structure and oxygen transport interactions in epitaxial $La_{0,6}Sr_{0,4}CoO_{3-\delta}$", Communications Materials, **25**, (2020)

[5] X.Rui, R. Klie; "Atomic-resolution study of oxygen vacancy ordering in $La_{0,5}Sr_{0,5}CoO_{3-\delta}$ thin films on $SrTiO_3$ during in-situ cooling experiments", Appl. Phys. Lett. **114**, (2019), p. 233101

[6] The authors acknowledge the financial support from the Austrian Science Fund (FWF P31654-N37)

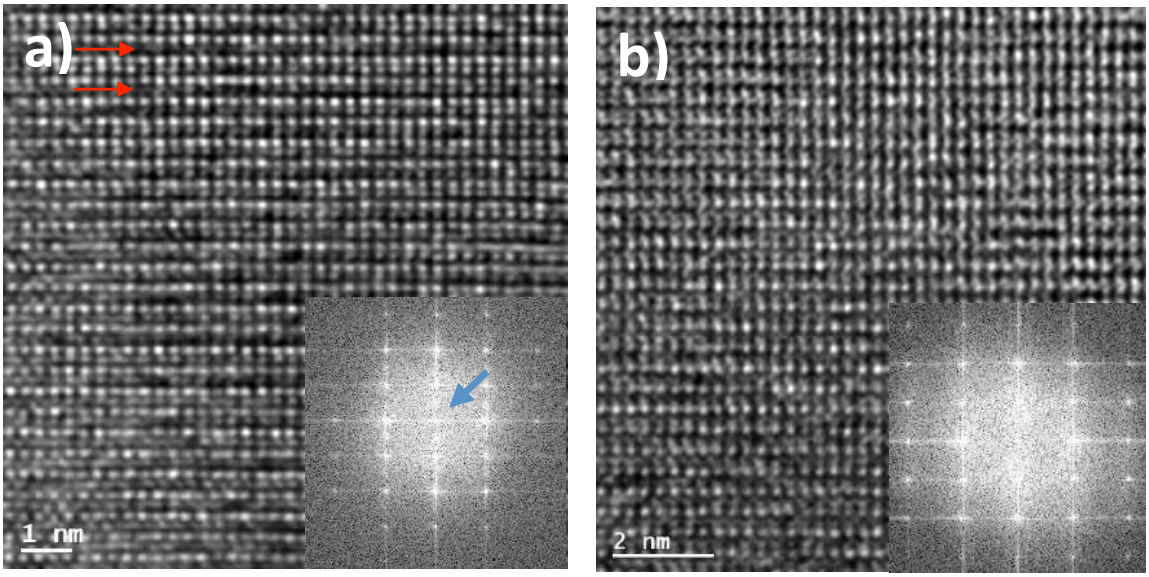

Figure 1. NL-Filtered HRTEM images along [011] zone axis, showing the evolution of LSCO film under electron beam illumination. The current density of the electron beam was 64.8pA/cm^2. The images were recorded before (a) and after 8min illumination (b). The inserts show corresponding FFT patterns. The blue arrow in (a) shows half-integer reflection.

In-Situ TEM Study of Flash Sintering in Oxide Materials

Fátima Zorro[1,2], Enrique Carbo-Argibay[2], and Paulo J. Ferreira[1,2,3]

1 Mechanical Engineering Department and IDMEC, Instituto Superior Técnico, Lisboa, Portugal.

2 INL - International Iberian Nanotechnology Laboratory, Braga, Portugal.

3 Materials Science and Engineering Program, University of Texas at Austin, Austin, TX, USA

As the demand for developing environmentally friendly and energy-efficient technologies increases, it is critical to devise processes to produce materials that match those requirements at lower costs.

One method which is widely used to process materials is conventional sintering. The global thermodynamic driving force for conventional sintering is a decrease in the total interfacial energy, causing adjacent particles to coarsen and densify. Locally, the kinetic driving force is the change in chemical potential between the regions with positive and negative curvature, leading to a flux of vacancies and atoms [1], [2].
Conventional sintering can be modified if an external driving force is applied to this process. In this context, the combination of electric field and temperature, denominated as flash-sintering (FS), has been attracting significant attention [3]. It has been used to obtain materials with outstanding functional properties, through much shorter processing times (from hours to seconds) and lower temperatures, thus becoming very appealing to the scientific and industrial communities [4]. In fact, to maximize energy savings, studies are now focused on room temperature (RT) FS, however, the mechanisms by which this process occurs are not yet well understood [5],[6]. Furthermore, most of the studies have been done in bulk specimens.

Among the candidate materials suitable for FS, this project focus on $LaSrCrO_3$ due to their semiconductor properties, thus prone to the FS process. More specifically, this work proposes to investigate thin lamellas of $LaSrCrO_3$ by in-situ transmission electron microscopy (TEM) to simulate in real-time the FS process. Under these conditions, the material is subjected to different electric fields and processing temperatures, including RT, inside the TEM, to fundamentally understand the kinetic and thermodynamic mechanisms that govern the flash sintering process.

To address the aforementioned issues, an experimental setup was developed for in-situ TEM analysis, including the sample preparation by focused ion beam (FIB) and a high precision method for positioning the lamella in the heating-biasing chip by the lift-out technique, being these stages the most critical of this in-situ study. Subsequently, the sample was subjected to an electric field and temperature, while multiple parameters were analyzed, with emphasis on the electric field, current density, electric power, and conductivity. In this fashion, we were unprecedently able to perform RT in-situ TEM flash sintering of $LaSrCrO_3$ to investigate the mechanisms driving the FS process, such as the local concentration of oxygen vacancies, heating of preferential sites, or nucleation of Frenkel pairs [7].

References:

[1] J. Hostaša, F. Picelli, S. Hříbalová, and V. Nečina, “Sintering aids, their role and behaviour in the production of transparent ceramics,” Open Ceram., vol. 7, May, 2021.
[2] G. S. Upadhyaya, “Future Directions in Sintering Research,” Sci. Sinter., vol. 43, no. 3–8, pp. 89–93, 2011.
[3] M. Yu et al., “Review of flash sintering: materials, mechanisms and modelling,” Adv. Appl. Ceram., vol. 116, no. 1, pp. 24–60, 2017.
[4] M. Biesuz et al., “Thermally-insulated flash sintering,” Scr. Mater., vol. 162, pp. 99–102, 2019.
[5] N. Yan et al., “Ethanol-Induced Flash Sintering of ZnO Ceramics at Room Temperature,” Materials (Basel)., vol. 15, no. 3, pp. 1–9, 2022.
[6] Y. Zhu et al., “Gas-discharge induced flash sintering of YSZ ceramics at room temperature,” J. Adv. Ceram., vol. 11, no. 4, pp. 603–614, 2022.
[7] Fátima Zorro acknowledges the financial support of “Fundação para a Ciência e Tecnologia” (FCT – Portugal), through the studentship 2021.05950.BD of the 2021 Call for Ph.D. Studentships.

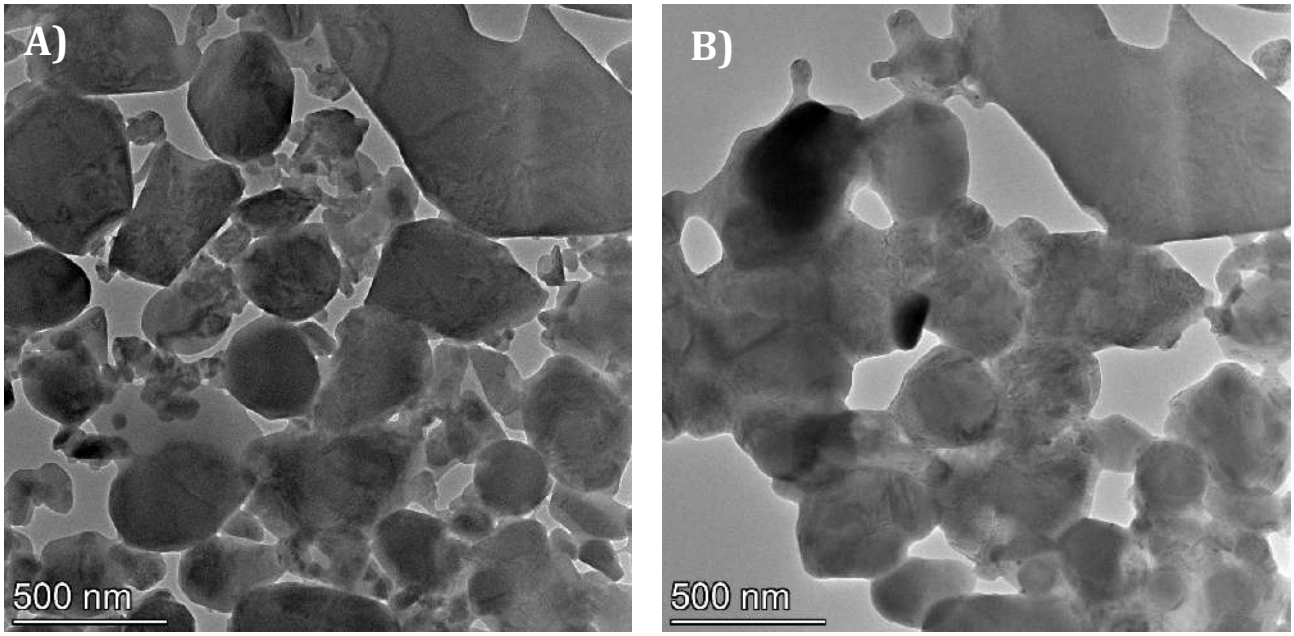

Figure 1. TEM image of a porous $LaSrCrO_3$ lamella on a heating/biasing MEMS chip: A) Before; B) After in-situ TEM flash sintering experiments at room temperature.

Direct insights into dry reforming of methane over Ni nanoparticles by *Operando* TEM

Milivoj Plodinec[1], Hannah C. Nerl[2], Thomas Lunkenbein[3], Robert Schlögl[3]

1 ScopeM, ETH-Zürich, Zürich, Switzerland

2 Humboldt University of Berlin, Berlin, Germany

3 Department of Inorganic Chemistry, Fritz Haber Institute, Berlin, Germany

Many studies have shown that catalysts are metastable and dynamic systems, where the nature of the active state depends on the applied chemical potential, associated "chemical dynamics" and the formation of transient active sites.[1,2] Therefore, active surfaces could be unstable at non-active conditions, leading to misinterpretation of inactive structures as active states in *ex situ* studies.[1] Recent progress in the development of *in situ* and *operando* techniques allow access to live information at high temporal and spatial resolution for the first time.[3-5] Operando transmission electron microscopy (TEM) allows to directly probe the active-state/-sites of catalysts under relevant reaction conditions and at high resolution. Up to date, the structure-function relationship remains unsolved in many catalytic reactions, including in the important industrial reaction - dry reforming of methane (DRM). This lack of fundamental understanding of DRM is hindering the choice and design of efficient catalyst material since an empirical approach to discovering new catalysts still prevails. Using *operando* TEM techniques presents a unique opportunity to gain fundamental insights into the DRM reaction to reveal what constitutes the active structure.

In this work, we used *operando* TEM to study DRM using nickel (Ni) catalyst nanoparticles (NPs). First, Ni NPs were deposited on the microelectromechanical systems (MEMS) chip using the magnetron sputtering method.

TEM imaging of the as-deposited Ni NPs showed the formation of a thin nickel-oxide (NiO) film (**Fig. 1 a,b**) due to the exposure to air during the assembly of the gas-cell TEM holder. Thus, to obtain metallic Ni NPs (which are required for DRM), *in situ* reduction inside the column of TEM was performed (**Fig. 1 c-e**). Next, the gas feed of methane (CH_4) and carbon dioxide (CO_2) was introduced at 700 ^oC to study structural and morphological changes of Ni NPs in DRM (**Fig. 2**). Several minutes after the introduction of gas feed, a significant decrease in the catalyst activity was observed due to the growth of graphitic layers over Ni NPs Graphitization of Ni NPs was confirmed by real-time SAED, which showed that structural changes of Ni NPs occurred in the first few minutes of DRM reaction (**Fig. 2a,b**). In addition, changes in the intensity of the diffraction reflections, including broadening and shifts of reflections could be assigned to the formation of different Ni carbide phases-Ni_xC_y (**Fig. 2c)**. Furthermore, high-resolution TEM imaging confirmed the formation of multi-layer graphitic growth on the surface of Ni NPs. Larger Ni NPs were found to be significantly more active for the growth of graphitic layers compared to smaller ones, thus leading to faster catalyst deactivation (**Fig. 2e**). Smaller NPs were found to suffer much less frequently from graphitic layers encapsulation and therefore suffered less deactivation. Furthermore, using this *operando* TEM approach, we were able to directly correlate the information on real-time structural changes of Ni NPs in DRM with the catalyst activity. Conversion of methane and carbon dioxide to hydrogen and carbon monoxide was detected and monitored throughout the *in situ* experiment. This leads us closer to a more mechanistic understanding of the reaction and ultimately our aim of rational design of better catalysts.

References:

[1] Schlögl, R., 2017. Catalysis 4.0. ChemCatChem **9(4)** (2017), p.533-541.
[2] Plodinec, M., et al., ACS Catalysis **10(5)** (2020), p.3183-3193.
[3] Kalz, K.F., et., ChemCatChem **9(1)** (2017), p.17-29.
[4] Bergmann, A. and Roldan Cuenya, B., ACS Catalysis, **9(11)** (2019) p.10020-10043.
[5]Chee S.W., et al., Journal of Physics: Condensed Matter, **33** 2021, p.15301 1-28.
[6] Plodinec, M., et al., Microscopy and Microanalysis 26 (2) (2020), p. 220-228.

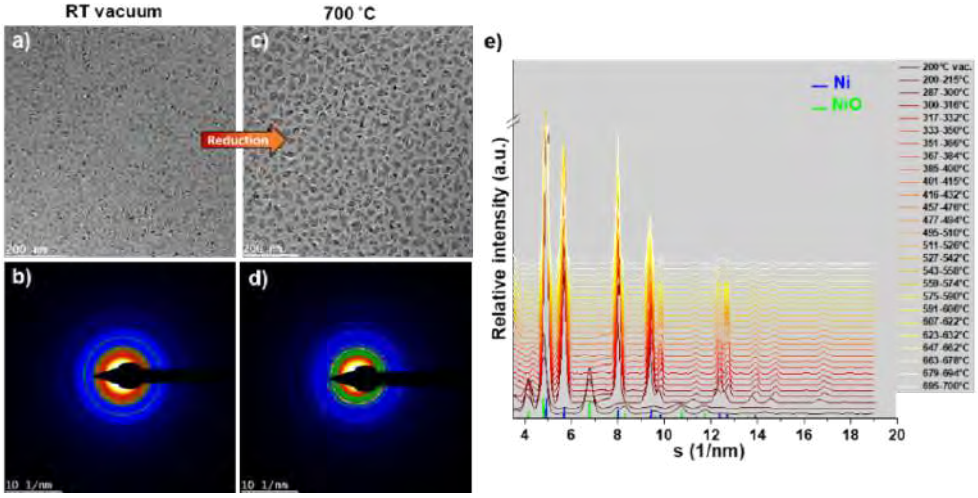

Figure 1. *In situ* reduction of as-prepared Ni NPs visualized by TEM. (a) TEM image of as-deposited Ni NPs imaged in vacuum depicts uniformly formed NiO thin film, which is also (b) confirmed by SAED analysis. (c) TEM image of reduced Ni NPs at 300 ºC, (d) with corresponding SAED pattern that confirms the presence of only metallic phase., and (f) evolution of averaged radial profiles extracted from SAED patterns acquired during temperature ramp from RT to 700 ºC. Reduction conditions: 20%H_2 in He, temperature ramp 5ºC/min from RT to 700 ºC.

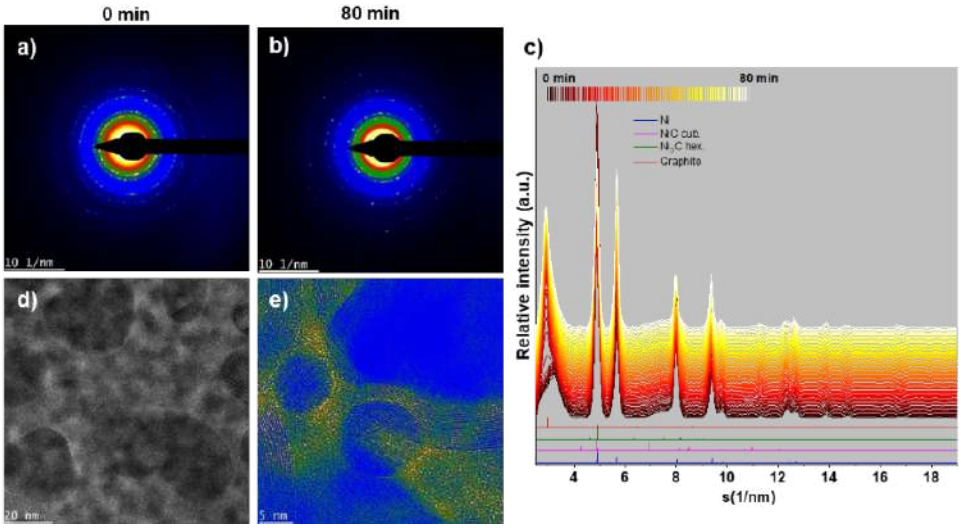

Figure 2. *Operando* TEM observation of structural changes on Ni NPs during the introduction of gas feed for DRM. Continuously acquired SAED patterns for: (a) 0 minutes (b) 80 minutes, accompanied with (c) corresponding averaged SAED radial profiles. HRTEM images of Ni NPs show; (d) clean metallic surface (active) at the beginning of the gas-feed introduction, and (e) fully encapsulated surface (non-active) with multi-graphitic layers after 80 min, (Gas feed in reaction conditions was: CH_4:CO_2=4:3. Grey square in Fig. f depicts catalyst deactivation.

Heterogeneous Electrochemical Dissolution of Au Nanoparticles Observed via In-situ Liquid TEM

Sorour Semsari Parapari[1], Miguel Bernal[2], Daniel Torres[2], Miran Čeh[1], Kristina Žužek[1], Jon Ustarroz[2,3], Sašo Šturm[1]

1 Jožef Stefan Institute, Department for Nanostructured Materials, Ljubljana, Slovenia.

2 ChemSIN – Chemistry of Surfaces, Interfaces and Nanomaterials, Université libre de Bruxelles (ULB), Campus de la Plaine, Brussels, Belgium.

3 Research Group Electrochemical and Surface Engineering (SURF), Vrije Universiteit Brussel, Brussels, Belgium.

Recently, the electrochemical deposition on low-energy substrates and the electrochemical stability of the bulk and nano-deposits have been the subject of numerous in-depth studies for better synthesis control of nanostructured electrocatalysts and their durability in electrochemical technologies. Electrodeposition and electrochemical dissolution studies of nanomaterials are conventionally investigated over large specimen areas. Typically, the electrochemical signals are measured over macro-scale (~cm^2) areas and then correlated with surface characterization obtained from much smaller regions in the range of few μm^2 or even nm^2, often resulting in discrepancies between the theory and the experimental observations. Despite their undoubted scientific value, most of these studies do not consider the effect of surface heterogeneity on the nucleation and dissolution of nanoparticles (NPs). The thermodynamics and kinetics of both NP nucleation and dissolution are affected by the specific surface interactions between NPs and substrate, which depend on the heterogeneous substrate's chemical, structural, and morphological properties [1]. Although some high-sensitivity electrochemical techniques allow recording electrochemical signals of the growth or dissolution of single NPs, nothing beats the direct visualization of growth and/or dissolution at high-spatial resolution.

Transmission electron microscopy (TEM) has been used for many decades to study atomic-scale interface problems in various fields of materials science. However, more recent in-situ TEM methods allow specialized TEM holders with liquid cells that can withhold the liquid in a confined environment, allowing the imaging and spectroscopy of samples in the liquid media. Combining the capabilities of liquid cell TEM holders with MEMS-based electrochemical chips with printed micro-size electrodes enables us to study dynamic phenomena during electrochemical reactions at high spatial and temporal resolution with the so-called in-situ Electrochemical Transmission Electron Microscopy (in-situ EC-TEM) [2]. In this work, the dynamic dissolution of gold nanoparticles on a glassy carbon substrate has been directly visualized by EC-TEM, and the results are correlated with a unique local electrochemical approach based on Scanning Electrochemical Cell Microscopy (SECCM). The combination of EC-TEM, SECCM, and macro-scale measurements provided a unique perspective on the interaction between the metal nuclei and the substrate.

The in-situ EC-TEM experiments were performed using a JEOL JEM 2100 TEM (JEOL, Tokyo, Japan), operated at a 200 kV accelerating voltage in the bright-field mode. Experimental images and videos were recorded using an Orius Model 832 SC1000 CCD camera at 20 frames per second and a theoretical pixel resolution of 0.5 nm. The standard illumination conditions were used for imaging the real-time experiments, which produced an electron dose rate of ≤ 100 e- nm^{-2} s^{-1} with controlled electron beam damage effects. The electrochemical measurements in the TEM were carried out using a Protochips Poseidon 500 liquid holder (Protochips Inc., Raleigh, NC, USA), which allows

observation of dynamic electrochemical processes in the liquid. The electrodeposition process of Au nanoparticles was conducted from a solution of 1 mM $HAuCl_4$ + 0.1 M NaCl in ultrapure deionized water. The electrochemical measurements were performed using a Gamry Reference 600 potentiostat (Gamry Instruments, PA, USA). Chronoamperometric experiments were conducted at a constant potential of E=0.4 V vs Pt and E=1.5 V vs Pt to electrochemically deposit and dissolve the gold NPs, respectively.

The in-situ observation of the dissolution kinetics has revealed that many Au NPs have been sporadically, that is, heterogeneously dissolved one by one during anodic polarization in the time span of more than 30s (Figure 1). Moreover, it was shown that Au NPs possess a core-shell structure, with the shells being more resistant to the dissolution process. The individual NP dissolution is a phenomenon distributed over time and, therefore, the most likely process responsible for the current spikes observed in our SECCM experiments. The unprecedented combination of EC-TEM and SECCM reveals previously untapped information from the electrochemical nucleation, growth, and dissolution of supported metal nanoparticles. This approach opens up new opportunities for the rational design of functional nanostructured materials electrodeposition and evaluating their durability under electrochemical polarization from the perspective of their resistance to electrochemical dissolution.

References:

[1] M. Bernal and J. Ustarroz, Current Opinion in Electrochemistry, (2021), 27, 100688.
[2] F. M. Ross, Science, (2015), 350.
[3] The authors acknowledge the support from the Fonds Wetenschappelijk Onderzoek in Vlaanderen (FWO, contract G0C3121N).

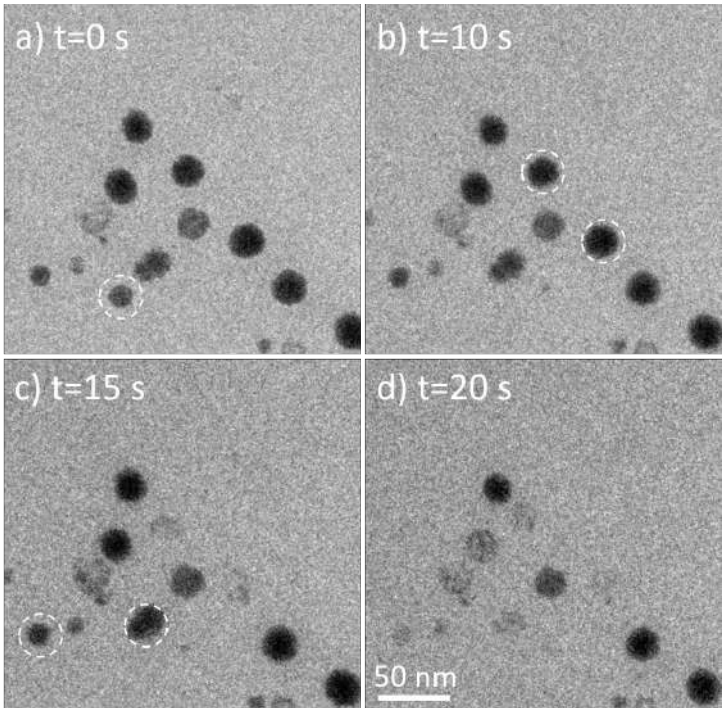

Figure 1. Bright-field TEM images of deposited Au NPs on the GC electrode were recorded in a time-resolved order during the anodic dissolution by potentiostatic hold, E = 1.5V vs. Pt, using the liquid EC-TEM setup. Dotted circles mark the dissolution of some of the particles during the potential hold.

Mesoporous Carbon Nanofibers and Spinel Oxide Nanocomposites for Energy Storage Applications

Daniel M. Mijailović[1], Vuk V. Radmilović[2], Uroš Č. Lačnjevac[3], Dušica B. Stojanović[2], Vladimir D. Jović[3], Velimir R. Radmilović[2,4] and Petar S. Uskoković[2]

1 University of Belgrade, Innovation Center, Faculty of Technology and Metallurgy, Karnegijeva 4, 11120, Belgrade, Serbia

2 University of Belgrade, Faculty of Technology and Metallurgy, Karnegijeva 4, 11120, Belgrade, Serbia

3 University of Belgrade, Institute for Multidisciplinary Research, Kneza Višeslava 1, 11030 Belgrade, Serbia

4 Serbian Academy of Sciences and Arts, Knez Mihailova 35, 11000 Belgrade, Serbia

In order to achieve the transition from energy systems that are based on fossil fuels to ones powered by clean and renewable energy on a global scale, it is mandatory to significantly improve the energy storage. Electrochemical energy storage devices with fast charging and long cycle lifetime will play very important role in this forthcoming energy revolution. Devices that fit these demands are supercapacitors, also knows as electrochemical capacitors, which can be fully charged within minutes, with almost unlimited cyclability. However, the main challenge of this technology is their low energy density, which varies from 5 to 8 Wh kg^{-1}, and 7 to 10 Wh L^{-1}. The performance of supercapacitors is determined by electrode materials which can drastically affect the capacitance and energy density in the appropriate voltage range and that is the main reason why high–rate materials are broadly explored [1,2].

Mesoporous materials based on carbon nanofibers and transition metal oxides have been produced by facile and advanced processing method. Scanning electron microscopy (SEM) analysis confirmed the formation of composite nanofibers with spinel nanocrystals deposited on the surface. The phase composition of cobalt/managenese spinel oxides, with an estimated diameter of about 13 to 60 nm, has been successfully controlled by varying the ratio of metal precursors in the electrospinning process. Scanning transmission electron microscopy (STEM) and energy dispersive X-ray spectroscopy (EDS) analysis of composite fibers cross-section revealed the distribution of chemical elements in the mesostructure. Interestingly, STEM–EDS analysis of cross-sections revealed the core-shell structure in which carbon occupies core space inside spinel rings.

Nanocomposites in alkaline electrolyte behave like materials with battery characteristics and have high values of capacity up to 68.5 mAh g^{-1}. By testing these novel self-standing composite electrodes in supercapacitor devices, high capacitance values as high as 384 F g^{-1} were obtained. Moreover, excellent stability was achieved with over 95% of all tested electrodes. The superior energy density of 11.5 Wh kg^{-1} at low potential sweep rates, and the superior power density of 2.6 kW kg^{-1} are comparable to commercially available supercapacitors, which has significant implications for the practical electrical energy storage.

References:

[1] H. Shao *et al.*, Chemical Society Reviews 49 (2020) p. 3005-3039.
[2] P. Simon, Y. Gogotsi, Nature Materials 19 (2020) p. 1151-11633.
[3] The authors acknowledge funding from the Ministry of Education, Science and Technological Development of the Republic of Serbia (Contract no. 451-03-9/2021-14/200135). V.R. Radmilović acknowledges support from the Serbian Academy of Sciences and Arts under project no. F-141.

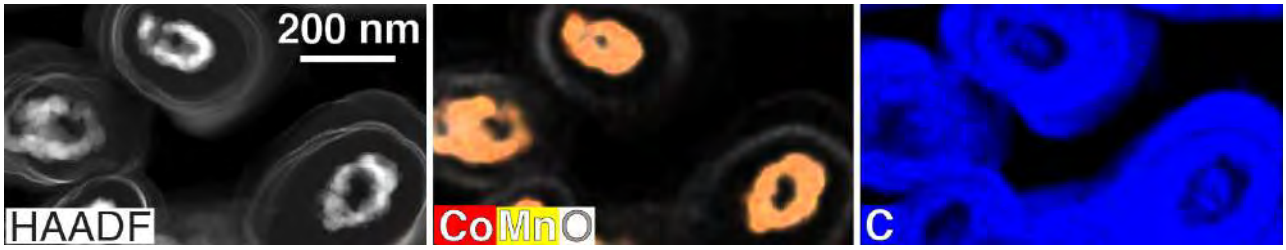

Figure 1. HAADF–STEM–EDS cross-section micrographs of composite nanofibers.

ADF/EDS/EELS Characterization of Spontaneous Cathode/Electrolyte Reaction In Air- and Beam-sensitive Solid-state Li-ion batteries

Ruomu Zhang[1], Alex Sheader[1], Weixin Song[1,2], Emanuela Liberti[1,3], Peter Bruce[1,2,4,5], Peter Nellist[1]

1 University of Oxford, Department of Materials, Oxford, United Kingdom

2 The Faraday Institution, Didcot, United Kingdom

3 Rosalind Franklin Institute, Harwell Campus, Fermi Avenue, Didcot, UK

4 University of Oxford, Department of Chemistry, Oxford, United Kingdom

5 The Henry Royce Institute, Oxford, United Kingdom

Solid-state Li-ion batteries (SSLIBs) have potential to revolutionise the electric-vehicle industry due to both their superior capacity and improved safety relative to conventional liquid cells. However, commercialisation of SSLIBs is at present hindered by the side reaction which occurs at the electrode-electrolyte interface. This reaction leads to voltage hysteresis and capacity fading, and subsequently to degraded battery performance [1].

Gaining insights into the origin of degradation and failure mechanisms at interface in SSLIBs requires the use of high spatial and energy resolution characterisation techniques such as scanning transmission electron microscopy (STEM). In this work, we applied annular dark field (ADF)/energy dispersive X-ray spectroscopy (EDS)/electron energy loss spectroscopy (EELS) to study the spontaneously formed interface between cathode material $LiNi_{0.6}Mn_{0.2}Co_{0.2}O$ (NMC622) and SSE Argyrodite Li_6PS_5Cl.

However, TEM studies of SSLIBs are complicated due to the extreme air- and electron-beam sensitivity of battery materials. We developed an anaerobic sample transfer protocol to prevent oxygen-related sample degradation. Beam damage on argyrodite was studied from the in-situ diffraction pattern revolution. Critical dose thresholds were calculated by monitoring the diffraction spots intensity decay with time (and therefore increasing electron dose), as shown in Figure 1(f).

By combining this anaerobic sample transfer and knowledge of critical electron dose limits, it was possible to study the argyrodite-NMC622 spontaneous redox side reaction at the interface in its near-native state. STEM EDS and ADF imaging allowed characterisation of chemical elemental distributions and particle morphology respectively. EELS mapping was also used to reveal the extent of side reaction by tracking the Ni L2,3 white line ratio on the NMC622/argyrodite interface. The EELS signal to noise ratio were enhanced from both sample preparation (wet ball-milling) and data acquisition (SmartAlign) [2]. Therefore, we are able to quantify Ni L2,3 white line ratio by performing model fitting (Fig. 2(c)) in Hyperspy on raw data from single pixel [3]. From the EELS fine structure analysis, we observed a trend of Ni reduction in NMC622 towards the interface with argyrodite due to the spontaneous redox reaction.

With the comprehensive analysis of the microstructure and chemistry of SSE/cathode interphase by using ADF/EDS/EELS in STEM, our work has exciting potential to guide future materials selection and interface design in SSLIBs by correlating the microstructure and composition with electrochemical performance [4].

References:

[1] J -M Tarascon, and M Armand, Materials for sustainable energy: a collection of peer-reviewed research and review articles from Nature Publishing Group (2011) p. 171.
[2] L Jones, *et al*, Advanced Structural and Chemical Imaging **1**(1) (2015), p. 1.
[3] FDL Peña, *et al*, Microscopy and Microanalysis **23**(S1) (2017) p. 214.
[4] The authors acknowledge use of characterization facilities within the David Cockayne Centre for Electron Microscopy, Department of Materials, University of Oxford and in particular the Faraday Institution (FIRG007, FIRG008), the EPSRC (EP/K040375/1 "South of England Analytical Electron Microscope") and additional instrument provision from the Henry Royce Institute (Grant reference EP/R010145/1).

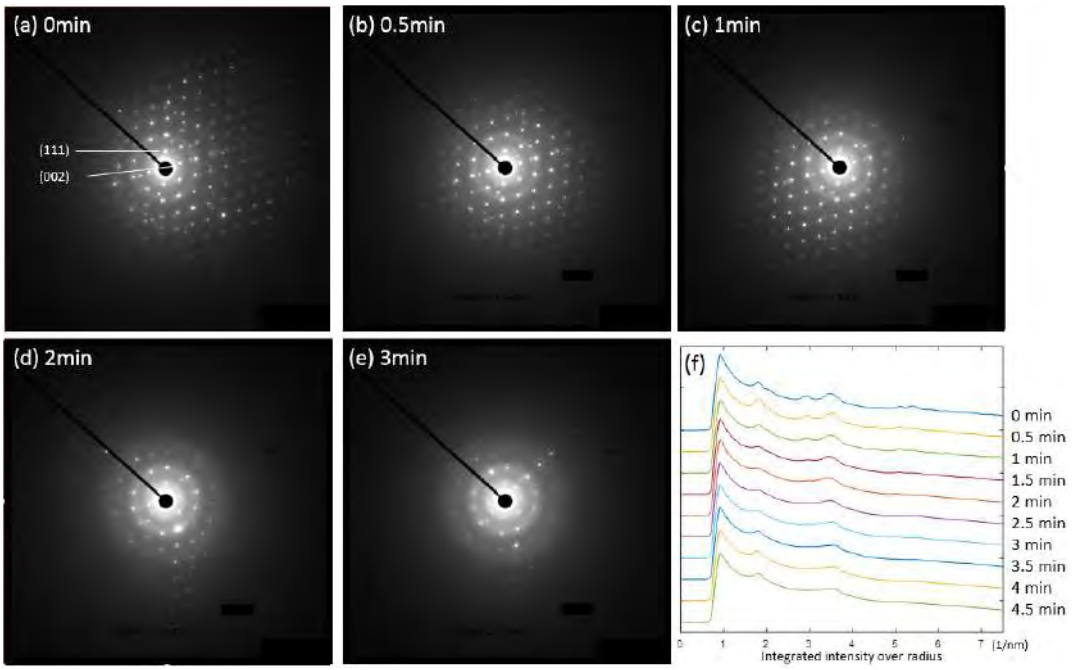

Figure 1. Diffraction pattern of argyrodite at 300kV at (a) t=0min, (b) t=0.5min, (c) t=1min, (d) t=2min, (e) t=3min; (f) integrated diffraction spots intensity over radius.

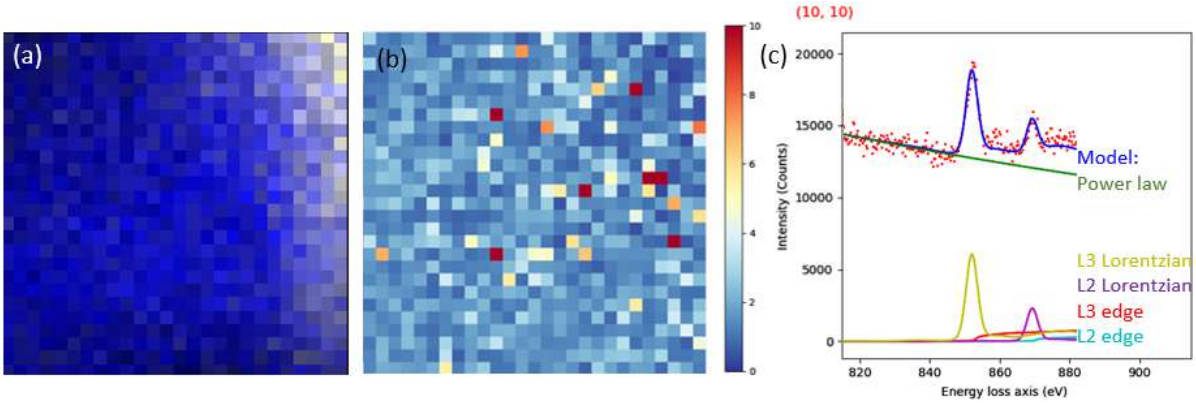

Figure 2. (a) EDS map of S (yellow) in LPSCl and Ni (blue) in NMC622, (b) Ni L2,3 white line ratio map, (c) Model fitting (dark blue) on raw data (red dots), model consists of 5 components.

Characterization of Coated Ni foam Electrodes for Industrial Hydrogen Production

Jelena Gojgić[1], Aleksandar Petričević[1], Thomas Rauscher[2], Christian Bernaecker[2], Mila Krstajić Pajić[1], and Vladimir Jović[3]

1 University of Belgrade, Faculty of Technology and Metallurgy, Karnegijeva 4, 11000 Belgrade, Serbia

2 Fraunhofer Institute for Manufacturing Technology and Advanced Materials IFAM, Branch Lab Dresden, Winterbergstraße 28, 01277 Dresden, Germany

3 University of Belgrade, Institute of Multidisciplnary Research, Kneza Viseslava 1, 11030 Belgrade, Serbia

Hydrogen is the most promising green energy carrier that can provide energy generation in small, portable devices, vehicles, as well as large scale power plants. Being produced from water splitting in a most pure form, it requires the use of renewable sources such as wind or sun, to complete the green energy cycle.

When it comes to alkaline water electrolysis, non-noble metals such as Ni are commonly used as hydrogen evolution catalysts, however their catalytic performance is enhanced by using 3D porous materials, with possible addition of a more active alloy as coating. Ni foams with open pores are produced commercially, and used in flow electrolyzers thanks to their structure.

For this research, Ni foams were produced by electrodeposition with the use of a polymer matrix, with tailored pore size [1], and used as substrates for a more efficient HER catalyst, Ni-Sn alloy. The coating was electrodeposited onto substrates, under different conditions, from a Pyrophosphate-Glycine bath [2] and the samples were characterized by Scanning Electron Microscopy (SEM) including Energy Dispersive X-ray Spectroscopy (EDS) from Jeol (JSM-IT800). Besides the characterization of structure, morphology and composition, the samples were investigated for HER by different electrochemical methods, including linear sweep voltammetry, chronopotentiometry and electrochemical impedance spectroscopy in an alkaline environment. The real surface area of Ni foam was estimated by electrochemical procedures and compared to the data obtained from BET isotherms and SEM investigation.

Thanks to the open pore structure of the foam, and appropriate electrodeposition methodology, the foam substrates were completely covered by the porous Ni-Sn coating, as confirmed by SEM top view (Fig. 1) and cross-section analysis. The coating composition is similar throughout the sample, and the coating thickness is greater at the edges of Ni struts, but no bare Ni surfaces were observed, before or after the electrochemical measurements. The electrodeposition of Ni-Sn was conducted with simultaneous hydrogen evolution, resulting in rough deposits that additionally increase the electrochemically active surface area of the foams.

As for the electrode performance for HER, the overpotentials at characteristic HER current densities (normalized per geometric electrode area) are very low, while the stability tests show no sign of peel of effect, or any significant decrease in activity over time. These electrodes are intended for single industrial hydrogen production after the scale up process.

References:

[1] P. S. Liu, G. F. Chen, Porous Materials: Processing and Applications Butterworth-Heinemann; 1. Edition (12. August 2014)
[2] U. Lacnjevac, B.M. Jovic, V.D.Jovic, “Electrodeposition of Ni, Sn and Ni–Sn Alloy Coatings from Pyrophosphate-Glycine Bath”, Journal of The Electrochemical Society **159** (2012) D310-D318
[3] This work was supported by the Federal Ministry of Education and Research – Germany, through the WBC2019 call – project NOVATRODES 01DS21010, and by the Ministry of Education, Science and Technological Development of the Republic of Serbia (Contract No.451-03-68/2022-14/200135).

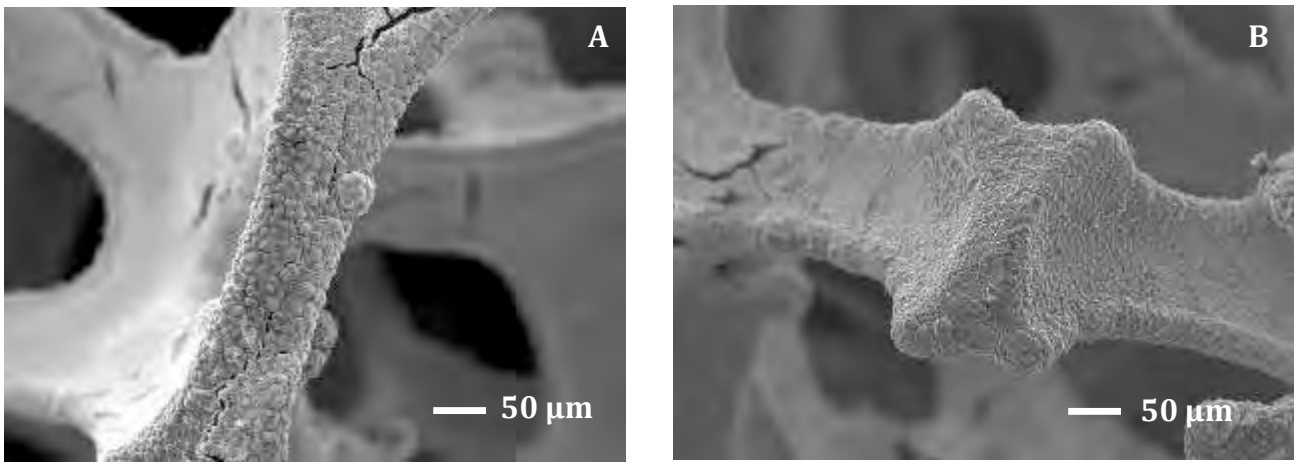

Figure 1. SEM top view micrograph of the coated Ni foam with pore size 1200 µm, Ni-Sn coating electrodeposited at - 1.25 V (A), and - 1.30 V (B), deposition potentials given versus Saturated Calomel Electrode.

Carbon Nanotubes Thin Films with Zn, Fe Oxides and Sulphides

Andjelika Bjelajac[1,2], Ileana Florea[1], Mihai Zamfir[1,3], Sandrine Tusseau-Nenez[4], Costel Sorin Cojocaru[1]

1 LPICM, CNRS, Ecole polytechnique, IP Paris, 91228 Palaiseau Cedex, France

2 Luxembourg Institute of Science and Technology (LIST), MRT, PPE, 28, avenue des Hauts-Fourneaux, L-4365 Esch-sur-Alzette, Luxembourg

3 National Institute for Laser, Plasma & Radiation Physics (INFLPR), Atomistilor Street, No. 409, Magurele, Ilfov RO-077125, Romania

4 PMC, CNRS, Ecole polytechnique, IP Paris, 91228 Palaiseau Cedex, France

Herein we explore the use of vertically aligned carbon nanotubes (VACNTs) thin films with Zn and Fe sulfides and oxides that can be used for ecological and energy-related applications such as photodegradation of organic pollutants from water [1], photocatalytic hydrogen evolution [2] and serving as anodes for Na and Li-ion batteries [3]. The motivation for choosing Fe and Zn oxides and sulphides comes from the fact that they are easy to fabricate, non-toxic, environmental friendly and low-cost. For the photocatalytic application the main factor is the absorption range of the catalyst since it affects its efficiency. The objective of producing a Zn/Fe based heterostructure was to benefit from the wider absorption range of Fe_2O_3, E_g = 2,1 eV, and FeS_2, E_g = 0.95 eV, whereas E_g (ZnO) = 3.37 eV, E_g (ZnS) = 3.60 eV [4]. What is more, FeS_2 has a high absorption coefficient ($\alpha > 6\times10^5$ cm^{-1} for $h\nu > 1.3$ eV), but a very short lifetime of photogenerated charge carriers (< 10 ps) and short hole diffusion length (~2-4 nm) [5]. Furthermore, in junction with Fe oxides and sulphides the photocorrosion of ZnS and instability in water of ZnO will be suppressed.

For the integration of such system in anodes for Na and Li-ion batteries, it is to note that ZnS exhibits better rate performance, and FeS possesses high specific capacity [3]. Therefore, nanostructured Fe/Zn sulfide composites could improve the electrochemical performance by the cooperative contribution of the advantages of ZnS and FeS. The buffering effect of individual sulfides and the desirable nanostructure can significantly reduce the mechanical stress from huge volume change during discharge-charge, and also improve the electrode/electrolyte contact and thus facilitate fast reaction kinetics.

The CNTs thin films are used as support of Zn/Fe oxides and sulphides since in that way the electron/hole (e-/h+) pair recombination is reduced. Further, the CNTs involvement increases the specific surface area and prevents the accumulation of the charge carriers within the catalyst inhibiting the photocorrosion reaction [6].

The CNTs were synthetized via a hot-filament chemical vapour deposition (HfCVD), using Fe catalyst film on top of Al_2O_3 buffer layer [7], Fig. 1. A pulsed-electrodeposition technique was then used for deposition of Zn. To obtain ZnO, ZnS and mix phase of ZnO/ZnS spread on CNTs, the oxidation, sulphurization and 2 steps subsequent annealing in oxygen and sulphur rich atmospheres were applied. High resolution transmission electron microscopy (HRTEM) followed by energy dispersive X-rays spectroscopy (EDS) done in scanning mode, provided the chemical mapping of the structures. X-ray diffraction (XRD) analyses proved the hexagonal phase of ZnO and ZnS, obtained after oxidation in H_2O and S vapour, respectively. However, in the case of the samples obtained by the 2 steps subsequent annealing, XRD showed mainly the presence of ZnO and a small detection of

ZnS. Additional analysis of EDS mapping showed the presence of S deposited along the nanotubes outer walls as well, probably as a consequence of ionic exchange with O trapped on the CNTs surface. The same approach was applied for Fe deposition, thermal treatments and characterization. The results showed that Fe_2O_3 can be partially or fully sulphurized by controlling the parameters of annealing in S vapour. This study proved that even a mix phase of Fe and Zn oxides and sulphides can be obtained with the proposed method (Fig. 2). [8]

References:

[1] S K Kansal, N Kaur, S Singh, Nanoscale Research Letters **4** (2009) p. 709
[2] G Wang *et al.*, Scietific Reports **5** (2015) p. 1
[3] D Xie *et al*, Inorganic Chemistry Communications **111 (**2020) p. 107635
[4] N A Molland *et al.*, Optical Materials Express. **5** (2015) p. 1613
[5] D Y Wang *et al.*, Advanced Materials **24** (2012) p. 3415
[6] H Y Phin, Y T Ong, J C Sin, Journal of Environmental Chemical Engineering **8** (2019) p. 103222
[7] K H Kim *et al.*, Thin Solid Films **575** (2015) p. 84

[8] This work received financial support from Campus France within the MOPGA (Make Our Planet Great Again) program. I.F. acknowledges financial support from the French state managed by the National Research Agency under the Investments for the Future program under the references ANR-10-EQPX-50 pole NanoMAX. All TEM analyses were performed at CIMEX (Centre Interdisciplinaire de Microscopie électronique de l'X) and XRD analyses at DIFFRAX (Diffraction des Rayons X à l'X), which are gratefully acknowledged.

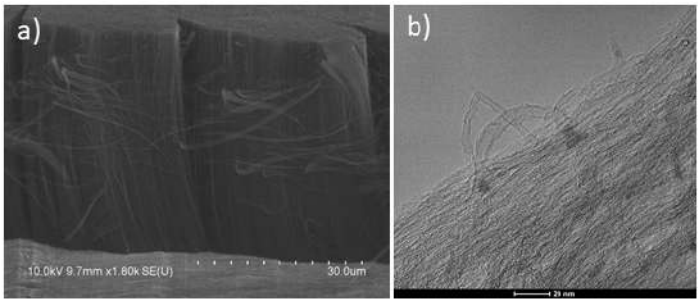

Figure 1. a) SEM and **b)** TEM micrograph of as-synthetized multi-wall CNTs (35 µm long with 4-5 walls and D_{in}= 4-6 nm)

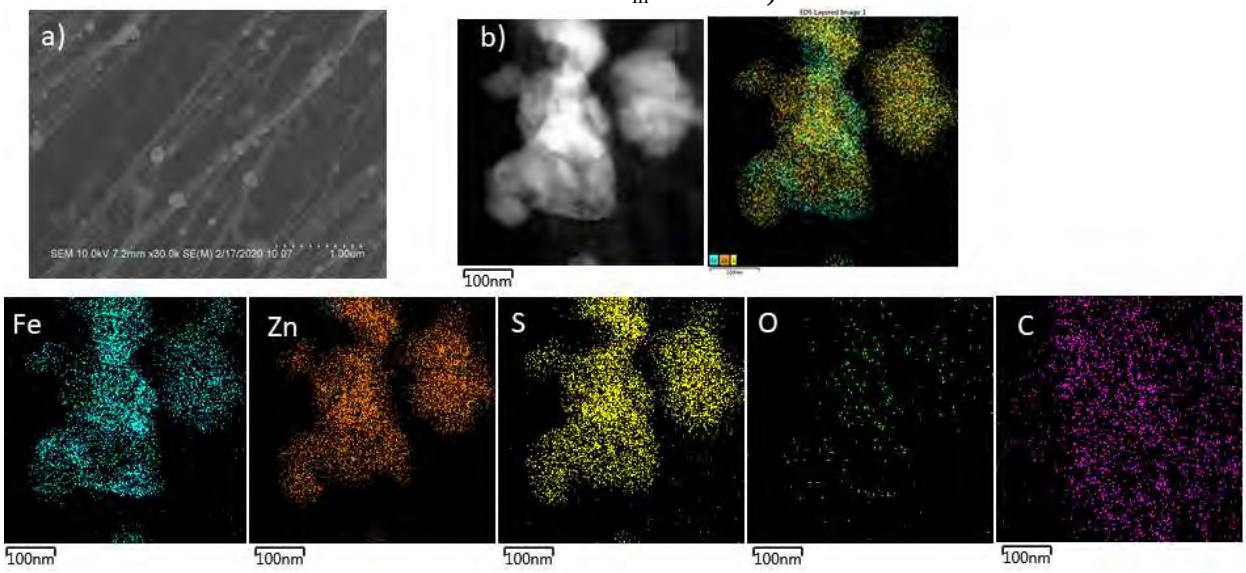

Figure 2. a) SEM micrograph and **b)** STEM/EDS results of Fe/Zn@O/S heterostructure on CNTs.

POSTER PRESENTATIONS

The Importance of Transmission Electron Microscopy for the Identification of Ultrastructural Changes in Non-Alcoholic Fatty Liver Disease

Tatjana Radosavljević[1], Milena Vesković[1], Milica Labudović-Borović[2], Jelena Jadžić[3], Dušan Mladenović[1], Danijela Vučević[1]

1 Institute of Pathophysiology, Faculty of Medicine, University of Belgrade, Belgrade, Serbia
2 Institute of Histology and Embriology, Faculty of Medicine, University of Belgrade, Belgrade, Serbia
3 Institute of Anatomy, Faculty of Medicine, University of Belgrade, Belgrade, Serbia

Nonalcoholic fatty liver disease (NAFLD) is the most common chronic liver disease, affecting up to 25% of people worldwide, and is referred to as a chronic disease of the 21st century [1,2]. The spectrum of NAFLD comprises steatosis, nonalcoholic steatohepatitis (NASH) which can progress to fibrosis, cirrhosis and hepatocellular carcinoma [1]. A methionine-choline-deficient (MCD) diet is widely used for the development of NAFLD/NASH in animal models [3,4,5].

The aim of this study was to detect ultrastructural changes in the mouse liver with MCD diet-induced NAFLD using electron microscopy. Male C57BL/6 mice were divided into two groups: Control group - fed with standard chow, and MCD group-fed with MCD diet, for 6 weeks. Ultrastructural changes in the liver tissue were studied using transmission electron microscopy. Semithin sections of liver tissue were cut from the blocks of embedded tissue, stained with toluidine blue and analyzed under the Olympus BX41 microscope (*Olympus* GmbH, *Hamburg*, Germany). All slides were photo documented with the an Olympus C5060-ADU wide zoom camera and the Olympus DP-soft Image Analyzer program (*Olympus* GmbH, *Hamburg*, Germany).

Electron microscopy has shown pronounced micro- and macrovesicular fatty changes in the MCD-induced NASH. Also, in animals treated with MCD diet, the ultrastructure of liver tissue revealed numerous stellate cells/myofibroblasts of the liver, as well as increased deposition of collagen fibers in the perisinusoidal spaces of the Disse. The liver cells were also affected by the MCD diet. The change was evident as apoptosis, vacuolization, and desquamation of endothelial cells. In addition to endothelial cells, apoptotic changes have been observed in hepatocytes and stellate liver cells. Rare autophagosomes in hepatocytes are evident in the MCD group. In contrast to the control group, the presence of megamitochondria in hepatocytes was pronounced in mice treated with the MCD diet. However, the number of mitochondria in the MCD group was significantly reduced.

Electron microscopy observation, ultrastructural modification of hepatocytes such as changes in the number of autophagosomes or changes in mitochondrial structure and nuclear chromatin may represent important early signs of altered hepatocellular function. Since the pathogenesis of NAFLD/NASH is still poorly understood, studying ultrastructural changes in liver tissue may help to further elucidate the pathophysiology, as well as a preventive and therapeutic strategy of NAFLD/NASH.

References:

[1] Metrakos P, Nilsson T. Non-alcoholic fatty liver disease--a chronic disease of the 21st century. J Biomed Res. 2018 Sep 29;32(5):327-335.
[2] Verhaegh P, Wisse E, de Munck T, Greve JW, et al. Electron microscopic observations in perfusion-fixed human non-alcoholic fatty liver disease biopsies. Pathology. 2021;53(2):220-228.

[3] Vesković M, Labudović-Borović M, Mladenović D...Radosavljević T. Effect of Betaine Supplementation on Liver Tissue and Ultrastructural Changes in Methionine-Choline-Deficient Diet-Induced NAFLD. Microsc Microanal. 2020;26(5):997-1006.
[4] This research was financially supported by the Ministry of Education, Science and Technological Development of the Republic of Serbia (Grant No. 175015).

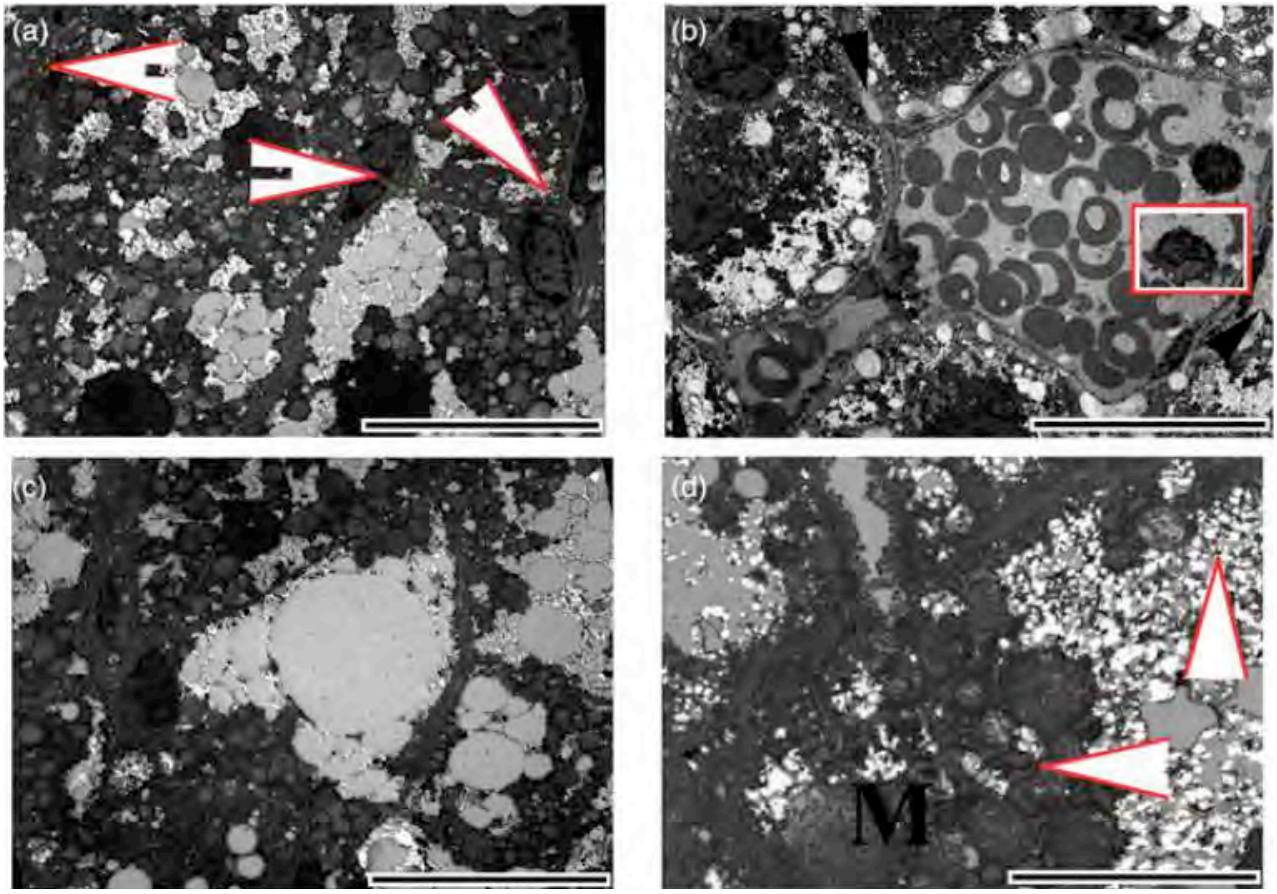

Figure 1. Liver tissue of animals treated with MCD (ultra-thin sections, uranyl acetate, lead citrate). (original magnification×1,800; bar = 20 μm) (a): extensive microvesicular fatty change; numerous hepatic stellate cells/myofibroblasts (white arrowheads); (b) fatty change; desquamation of endothelial cells (white rectangle); apoptotic and desquamated endothelial cells within the lumen of sinusoidal capillaries along with platelets and lymphocytes; collagen fibers in perisinusoidal spaces of Disse (black arrowheads); (c) microvesicular and macrovesicular fatty change; (d): (original magnification ×7,100; bar = 5 μm) rare megamitochondria compared to normal-sized mitochondria (white arrowheads).

Ultrastructural Analysis of Lymphocyte Nuclei in Type 2 Diabetes Mellitus

Tamara Martinovic[1], Darko Ciric[1], Katarina Lalic[2], Iva Rasulic[3], Danica Djuricic[3], Vladimir Bumbasirevic[1,4], Tamara Kravic-Stevovic[1]

1 Institute of Histology and Embryology, School of Medicine, University of Belgrade, Visegradska 26, Belgrade 11000, Serbia

2 Clinic for Endocrinology, Diabetes and Metabolic Disease, Clinical Center of Serbia, School of Medicine, University of Belgrade, Doktora Subotica 13, Belgrade, Serbia

3 Health Center "Savski Venac", Pasterova 1, Belgrade, Serbia

4 Serbian Academy of Sciences and Arts, Belgrade, Serbia

Diabetes is a very common endocrine-metabolic disorder [1]. The main hallmark in diabetes is high blood glucose levels due to the absolute or relative insulin deficiency [1]. To treat high blood glucose levels in type 2 diabetes an oral drug, metformin, is used [2]. Nuclear morphology irregularities in diabetes were first published in exfoliative cytology studies of oral mucosa cells [3, 4]. The aim of this study was to evaluate the ultrastructural features of peripheral blood lymphocyte nuclei in type 2 diabetes, and to investigate the effects of metformin therapy these features. Peripheral blood from type 2 diabetes patients and healthy volunteers was taken and isolation of mononuclear cells was done by density gradient centrifugation. After separation, cells were washed in PBS and fixed in 3% glutaraldehyde. After 24 h fixation cells were postfixed in 1% osmium tetroxide, dehydrated in graded alcohols and embedded in Epoxy medium. The characteristics of lymphocyte nuclei were determined in 60 cells per blood sample. Subnuclear structures, nucleoli and perichromatin granules, were counted in each nucleus. Lymphocytes of healthy individuals had rounded predominantly heterochromatic nuclei (Fig. 1a). Quite the opposite, vast majority of lymphocyte nuclei in type 2 diabetes patients had irregular nuclear contour and higher amount of euchromatin, nevertheless of the fact whether patients were newly diagnosed (Fig. 1b) or treated with metformin (Figs. 1c). We observed nuclei with deep indentations, convoluted nuclei and cerebriform-like nuclei in type 2 diabetes (Fig. 1c). The higher number of nucleoli per cell was found in newly diagnosed type 2 diabetes patients (0.44 ± 0.13, $p < 0.05$) and in metformin treated type 2 diabetes patients (0.57 ± 0.04, $p < 0.01$) compared to healthy individuals (0.27 ± 0.10) (Fig. 2a). We have found highly significant difference in the number of perichromatin granules between metformin treated diabetes patients and newly diagnosed patients (1.10 ± 0.15; 0.44 ± 0.18 respectively, $p < 0.01$), and metformin treated diabetes patients and healthy individuals (1.10 ± 0.15; 0.31 ± 0.14 respectively, $p < 0.01$) (Fig. 2b). No difference in the number of perichromatin granules was found between newly diagnosed diabetes patients and healthy individuals (Fig. 2b).Lymphocytes in type 2 diabetes ultrastructurally differ from lymphocytes in healthy individuals and these differences are more pronounced in metformin treated, longer duration diabetes group of patients. High levels of glucose in blood may induce ultrastructural changes in peripheral blood lymphocytes in type 2 diabetes.

References:

[1] World Health Organization, 2014. Global Status Report on Non-Communicable Diseases 2014. WHO Press, Geneva.
[2] Qaseem A *et al*, Ann Intern Med, **166** (2017), p. 279–290.
[3] Oz ZS et al, J Cytol, **31** (2014), p. 139–143.

[4] Hallikerimath S et al, Acta Cytol, **55** (2011), p. 197–202.
[5] The authors acknowledge funding from the Ministry of Education, Science, and Technological Development of the Republic of Serbia (Grants No. 41025, 175038, 175097, 175005) and SASA (grant No F-35).

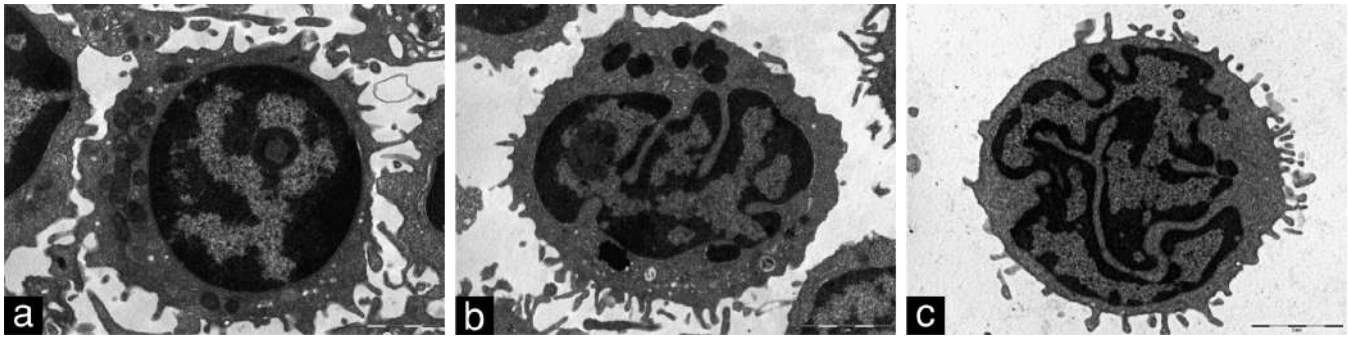

Figure 1. Shape of lymphocyte nuclei. Electron microscopic images of lymphocyte: nuclei are rounded and heterochromatic in healthy individuals (a), in newly diagnosed type 2 diabetes nuclei have irregular contour (b) and in metformin treated type 2 diabetes nuclei are cerebriform-like (c) (magnification 8900x; scale bar, 2 μm).

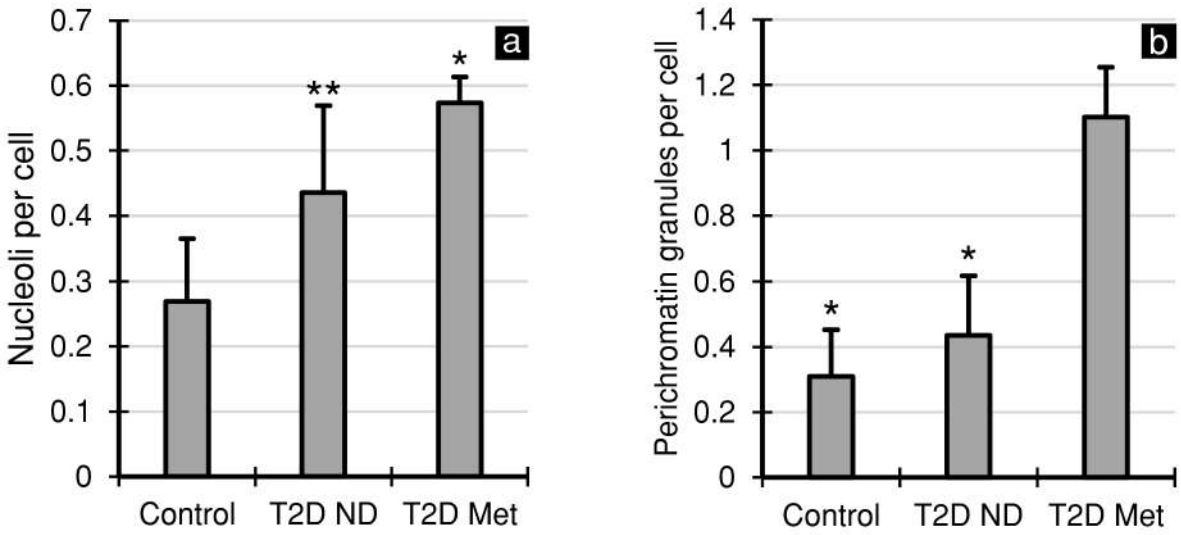

Figure 2. Comparison of number of nucleoli and perichromatin granules per cell section. Graph (a) showing number of nucleoli in lymphocyte nuclei per cell of healthy individuals, newly diagnosed type 2 diabetes (T2D ND, **$p < 0.05$) and metformin treated type 2 diabetes (T2D Met, *$p < 0.01$). Graph (b) showing number of perichromatin granules in lymphocyte nuclei per cell of healthy individuals, newly diagnosed type 2 diabetes (T2D ND) and metformin treated type 2 diabetes (T2D Met). *$p < 0.01$ between T2D Met and T2D ND, and between T2D Met and healthy individuals.

Euchromatin to heterochromatin ratio in the lymphocyte nuclei of patients with type 2 diabetes and hyperlipidemia

Tamara Kravic-Stevovic[1], Tamara Martinovic[1], Darko Ciric[1], Katarina Lalic[2], Iva Rasulic[2], Danica Djuricic[3], Vladimir Bumbasirevic[1,4]

1 Institute of Histology and Embryology, School of Medicine, University of Belgrade, Visegradska 26, Belgrade 11000, Serbia

2 Clinic for Endocrinology, Diabetes and Metabolic Disease, Clinical Center of Serbia, School of Medicine, University of Belgrade, Doktora Subotica 13, Belgrade, Serbia

3 Health Center "Savski Venac", Pasterova 1, Belgrade, Serbia

4 Serbian Academy of Sciences and Arts, Belgrade, Serbia

Diabetes mellitus is a major health problem worldwide [1]. Insulin deficiency or insulin resistance play a key role in the development of symptoms, clinical signs and complications of diabetes [2]. These disorders result in the development of chronic hyperglycemia [2]. Dyslipidemia is a quantitative disorder of LDL (Low Density Lipoprotein) cholesterol, triglycerides and HDL (High Density Lipoprotein) cholesterol [3]. Diabetes is an important factor in the pathogenesis of dyslipidemia, because these patients have an atherogenic combination of high LDL cholesterol, triglycerides and low HDL cholesterol, which is called diabetic dyslipidemia [3]. The aim of this study was to determine the euchromatin to heterochromatin ratio in the nuclei of lymphocytes in patients with type 2 diabetes and hyperlipidemia.

Lymphocytes were isolated from the peripheral blood of patients with type 2 diabetes and hyperlipidemia and healthy subjects. The cell pellet was fixed with glutaraldehyde and osmium tetroxide and washed with cacodylate buffer. The samples were contrasted with uranyl acetate and dehydrated with increasing concentrations of ethyl alcohol and propylene oxide, after which they were embedded into epoxy resins. The excised samples were then analyzed by electron microscopy. Using the ImageJ program the percentage of heterochromatin in the nucleus was analyzed on the acquired photomicrographs.

The analysis of photomicrographs showed that the percentage of heterochromatin in persons with type 2 diabetes and hyperlipidemia was 14.33% ± 0.42, the percentage of heterochromatin in healthy subjects was 19.95% ± 1.53 and that this difference was statistically highly significant ($p<0.001$).

It can be concluded that lymphocytes from patients with type 2 diabetes and hyperlipidemia have lower percentage of heterochromatin compared to healthy individuals. Difference detected in ultrastructural features of lymphocytes might imply that there is also difference in the activity of these cells.

References:

[1] Guthrie RA, Guthrie DW, Crit Care Nurs Q, **27** (2004), p. 113-125.
[2] Kerner W, Brückel J, Exp Clin Endocrinol Diabetes, **122** (2014), p. 384-386.
[3] Grundy SM et al, Circulation, **139** (2019), p. E1082–143.

[4] The authors acknowledge funding from the Ministry of Education, Science, and Technological Development of the Republic of Serbia (Grants No. 41025, 175038, 175097, 175005) and SASA (grant No F-35).

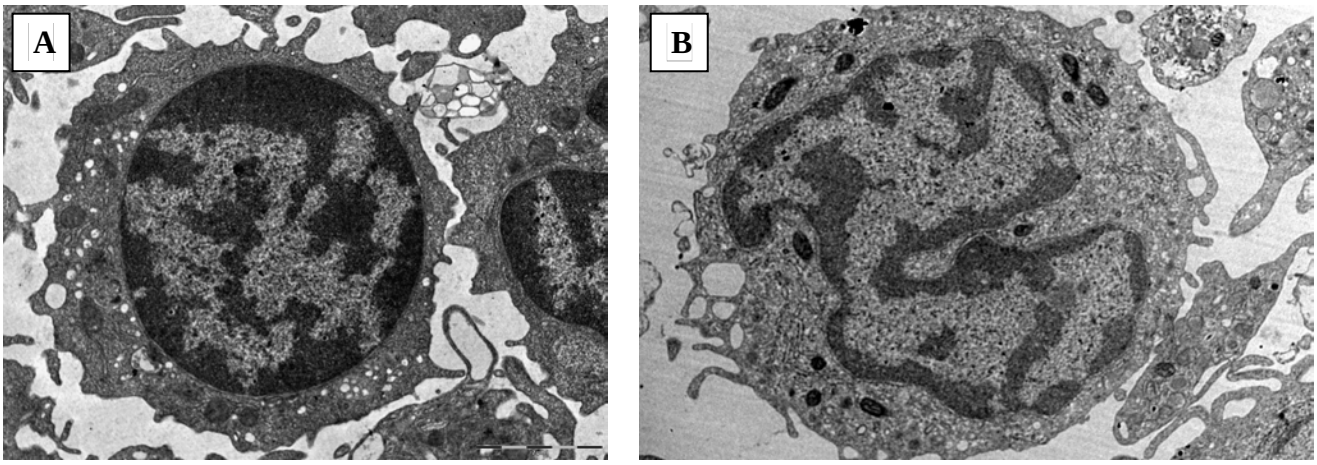

Figure 1. Chromatin distribution in lymphocyte nuclei. Nuclei are heterochromatic in healthy individuals (A). In patients with type 2 diabetes and hyperlipidemia nuclei have higher amount of euchromatin (B) (magnification 8900x; scale bar, 2 μm).

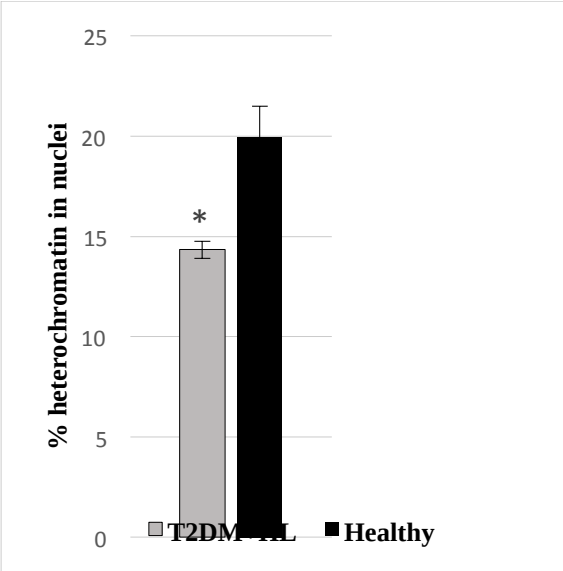

Figure 2. Graph showing percentage of heterochromatin in lymphocyte nuclei of healthy individuals (Healthy), patients with type 2 diabetes and hyperlipidemia (T2DM+HL) (b). *$p < 0.01$.

Ultrastructural Analysis of Skeletal Muscle Biopsy in the Diagnosis of MELAS Syndrome in Correlation to the Psychiatric Manifestations of the Disease

Maja Lačković[1,2], Maja Ivković[1,2], Vesna Lačković[2,3], Miloš Bajčetić[2,3], Milica Nestorović[2,4], Aleksandra Pavlović[5]

1 Psychiatry Clinic, University Clinical Center of Serbia, Belgrade, Serbia
2 Faculty of Medicine, University of Belgrade, Belgrade, Serbia
3 Institute of Histology and Embryology, Belgrade, Serbia
4 Institute for Human Genetics, Belgrade, Serbia
5 Faculty for Special Education and Rehabilitation, University of Belgrade, Belgrade, Serbia

MELAS (mitochondrial encephalopathy lactic acidosis and stroke-like episodes) syndrome is a rare inherited progressive neurodegenerative disorder caused by mitochondrial dysfunction and resulting in transient disturbances in energy production [1]. The pathogenetic basis of this condition are 29 point mutations in the mitochondrial DNA, leading to the disturbance in the respiratory chain protein synthesis and dysfunction of the oxidative phosphorylation and ATP production [2]. This process is mainly reflected in high-energy organs and tissues, such as the central nervous system.

We aimed to highlight neglected psychiatric manifestations of the MELAS and accentuate the role of the TEM in establishing the diagnosis. Our study included 9 patients hospitalized at the Neurology Clinic at the University Clinical Center of Serbia in whom clinical and neuroimaging findings indicated the MELAS syndrome, but a definitive diagnosis was obtained with TEM analysis of the skeletal muscle biopsy specimens. In addition, psychiatric evaluation was performed with the use of clinical interview, the Hamilton Depression Rating Scale (HAM-D), and the Hamilton Anxiety Rating Scale (HAM-A) [3].

For ultrastructural analysis samples of muscle biopsy were fixed in 3% glutaraldehyde and post-fixed in 1% osmium tetroxide overnight at +4^{o}C for 1 h, respectively. Both glutaraldehyde and osmium tetroxide were dissolved in cacodylate buffer (0.1 mol/l, pH=7.4). After dehydration in a linear ascending gradient of ethanol concentration, tissue samples were embedded in 4.8 ml of Epon, 1.7 ml of DDSA, and 0.2 ml BDMA. Semi-thin sections of muscle were stained with a mixture of 1% toluidine blue and 1% azure A in 1% aqueous solutions of borax and observed under light microscopy. Photomicrographs were taken using an Olympus BX41 microscope. All the slides were photo-documented by an Olympus C-5060 ADU wide zoom camera and the Olympus DP-soft Image Analyzer program. Ultra-thin sections were stained with uranyl acetate and lead citrate and examined with a transmission electron microscope (TEM) (Fei Morgagni 268D, Eindhoven, The Netherlands). The TEM was equipped with a MegaViewIII Soft Imaging System digital camera (Olympus Soft Imaging Solutions GmbH, Munster, Germany) [4]. Statistical analysis of the collected data included descriptive and inferential methods. The database was analyzed using the Software Package for Social Sciences for Windows v. 14.0 (SPSS Inc. Chicago, IL).

Diagnosis of MELAS was confirmed using TEM analysis of skeletal muscle biopsies of each patient. In all cases, significant alterations in the structural organization of skeletal muscle cells were detected. Sarcolemma was bulged and an increased number of subsarcolemmal mitochondria was noted with a disarranged cristae order (Fig.1). Accumulated mitochondria were of very irregular shape and large dimension, and included characteristic paracrystalline inclusions in the matrix which indicated MELAS diagnosis (Fig.2).

Ultrastructural analysis remains the gold standard for rare inherited neurodegenerative disorders although there are other diagnostic pathways for mitochondrial diseases [4,5]. Besides neurological manifestations, including cognitive decline, the use of HAM-D and HAM-A scales indicated a high frequency of depression and anxiety symptoms in our cohort [3,6]. Our research demonstrates the importance of screening the MELAS patients for psychiatric disorders, as these can occasionally be an initial presentation in this syndrome and potentially lead to misdiagnosis [5,6]. Pathogenesis of psychiatric manifestations of the MELAS syndrome, which greatly affect quality of life, is intriguing and comprises a role of damaged mitochondria in compromised circulation leading to hypoperfusion, generalized mitochondrial cytopathy, the role of impaired astrocyte-neuron communication, endothelial dysfunction, and an increased blood-brain barrier permeability [3-6].

References:

[1] S.G. Pavlakis *et al*, Ann Neurol 16 (1984), p. 481.
[2] I. Maurer, S. Zierz and H. Möller H, Schizophr Res 8 (2001), p. 125.
[3] M. Lačković, Master of Science thesis. Faculty of Medicine, University of Belgrade, 2010.
[4] V. Lackovic *et al*, Ultrastruct Pathol 36 (2012), p. 325.
[5] E. Watson, R Davis and C.M. Sue, J Transl Genet Genom 4 (2020), p. 188.
[6] M. Lačković *et al*, Engrami 37 (2015), p. 5.

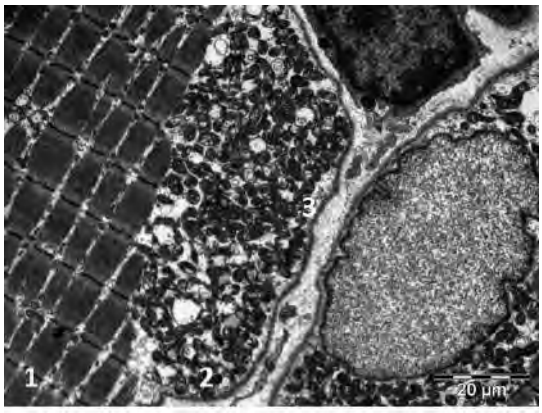

Figure 1. Subsarcolemmal accumulation of altered mitochondria (TEM): 1. Myofibrils, 2. Mitochondria, 3. Bulging sarcolemma.

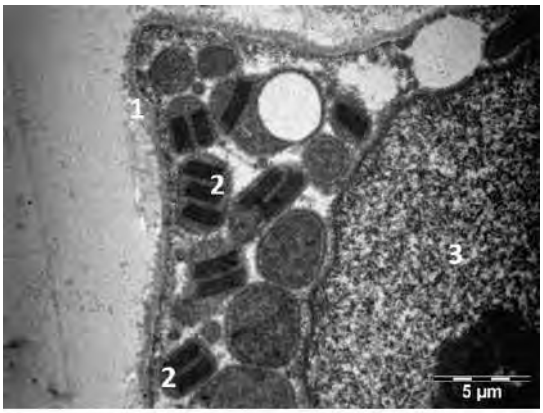

Figure 2. Paracrystalline inclusions in the mitochondrial matrix (TEM): 1. Sarcolemma, 2. Paracrystalline inclusions in mitochondria matrix, 3. Nucleus.

Cytotoxic and Genotoxic Effects of Polystyrene Nanoparticles and Microplastics *in vitro*

Marina Gazdic Jankovic[1], Sandra Nikolic[1], Marko Zivanovic[2], Nevena Milivojevic[2], Marina Miletic Kovacevic[3], Olivera Milosevic Djordjevic[1,4], Miodrag Stojkovic[5], Biljana Ljujic[1]

1 Department of Genetics, Faculty of Medical Sciences, University of Kragujevac, Kragujevac, Serbia.
2 Laboratory for Bioengineering, Institute of Information Technologies Kragujevac, University of Kragujevac, Kragujevac, Serbia.
3 Department of Histology and Embryology, University of Kragujevac, Faculty of Medical Sciences, Kragujevac, Serbia.
4 Department of Biology and Ecology, Faculty of Science, University of Kragujevac, Kragujevac, Serbia.
5 SPEBO Medical, Fertility Clinic Leskovac, Serbia.

There is growing evidence that the current use and disposal of plastics lead to significant pollution of the environment, already discussing plastic waste as the number one new global enemy [1]. One of the most commonly used plastics is polystyrene (PS). Daily contact with considerable amounts of PS micro-(MP)/nanoparticles (NP) in food, water, and air, may cause harmful effects on the living organisms, through mechanisms that are not fully understood.

The study aimed to evaluate the cytotoxic and genotoxic effects of PS-MP (size 200nm) and PS-NP (40nm) in cells isolated from C57BL/6 mice.

In order to estimate cellular uptake and retention of PS-MP/NP, mice bone marrow-derived mesenchymal stem cells have been exposed for 24 hours to PS-MPs (200nm). After treatment, the cells have been prepared for *transmission electron microscopy* (*TEM*) according to the TEM protocol. For assessing viability and metabolic activity of mice macrophages after PS-MP/NP treatment, we used 3-(4,5-dimethylthiazol-2-yl)2,5-diphenyl tetrazolium bromide (MTT) assay [2]. Genotoxicity of PS-MP/NP was evaluated by using the Comet test with the mice peripheral blood mononuclear cells [3].

TEM confirms cellular internalization of PS-MPs (200nm) and suggests that uptake is dominated by encapsulation within vesicles, indicative of endocytosis. The presented MTT *in vitro* data indicate increased toxicity of PS particles on mice macrophages after 24 and 72 h of exposure. PS particles of 200 nm and 40 nm showed increased cytotoxicity in a dose and time-depended manner. Higher concentration (4.7 µl/ml) had a greater effect than the lower concentration (0.47 µl/ml) which showed a statistically significant ($p < 0.05$) decrease in viability after 24 h and 72 h. Both environmentally relevant concentrations of PS particles (0.47 and 4.7 µl/ml) significantly increased the genetic damage index (GDI) in mice cells after 24 h exposure, in dose dependent-manner, in comparison with negative control. Whereas control cells appeared to be largely spherical, cells exposed to PS particles (40nm and 200nm) exhibited cell trailing or tail formation, indicating DNA damage, which increased with the concentration of polystyrene items.

Our results clearly demonstrate that PS-MP/NP penetrate, accumulate and induce functional changes in mammalian cells. These findings strongly motivate future research to mitigate the deleterious effects of nanosized plastic particles on human health.

References:

[1] Bojic S, *et al*. Platform to study intracellular polystyrene nanoplastic pollution and clinical outcomes. Stem Cells. 2020; 38:1321-1325.
[2] Petrovic A, *et al*.. Experimental and quantum chemical study small o, Cyrillicn the DNA/protein binding and the biological activity of a rhodium(iii) complex with 1,2,4-triazole as an inert ligand. Dalton Trans. 2020; 49:9070–9085.
[3] Nikolic S, *et al*. Orally administered fluorescent nanosized polystyrene particles affect cell viability, hormonal and inflammatory profile, and behavior in treated mice. Environ Pollut. 2022;305:119206.

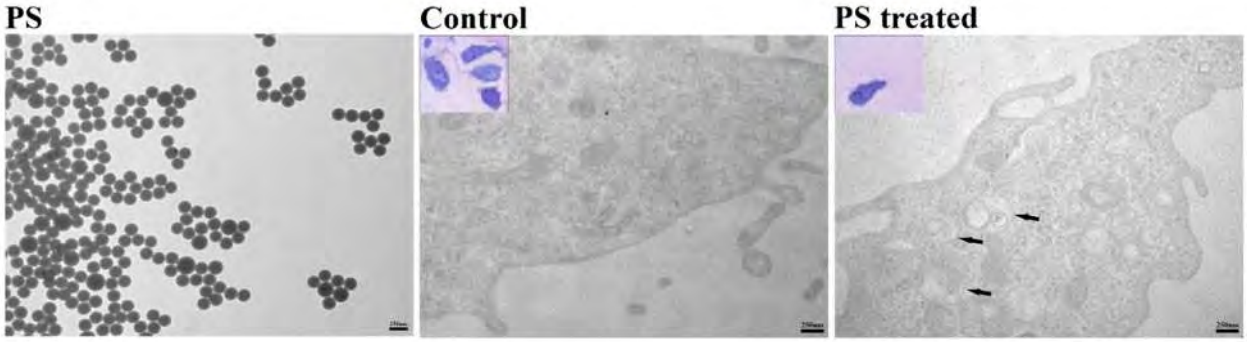

Figure 1. T*ransmission electron microscopy* analysis of mesenchymal stem cells treated with polystyrene particles (200nm in diameter). Polystyrene items were internalized by MSCs and found in endocytic structures of the treated cells. *Scale bars* = 250 nm.

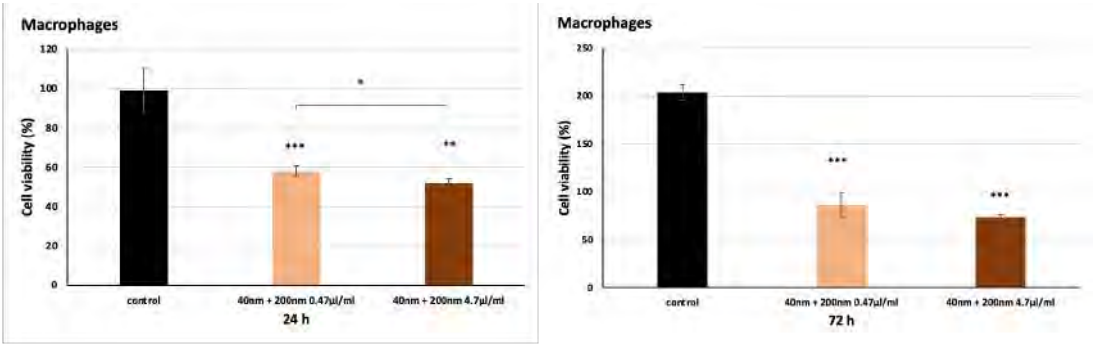

Figure 2. The effect of PS-MP/NP on mice macrophages growth. The cells were treated with polystyrene items (40nm+200nm) in a concentration 0.47 and 4.7 µl/ml. The antiproliferative effect was measured by MTT assay after 24 and 72 h exposure. All values are mean ± standard error, n=3, **p < 0.05*, ***p<0.01*, ****p<0.001* as compared with control.

Treatments	No. of analyzed cells	Distribution of cell classes 0-4					GDI (mean ± SD)
		0	1	2	3	4	
Negative control	300	83.67	14.33	2.00	/	/	0.13 ± 0.02
Positive control H_2O_2 (10 µg/mL)	300	2.33	35.33	38.00	10.00	14.33	1.99 ± 0.10
Positive control MMC (0.5 µg/mL)	300	2.33	26.00	34.33	18.67	18.67	2.25 ± 0.04
0.47 µg/mL nanoparticles	300	55.33	35.00	11.00	2.33	0.33	0.65 ± 0.12*
4.7 µg/mL nanoparticles	300	/	12.33	43.00	18.33	26.33	2.59 ± 0.31***

Table 1. Genetic damage index (GDI) in lymphocytes of mice after treatment with polystyrene particles.

Morphology of Waterborne Polyurethanes Based on Poly(dimethylsiloxane)

Ivan S. Stefanović[1], Jasna V. Džunuzović[1,2], Enis S. Džunuzović[3], Andrea Basagni[4] and Carla Marega[4]

1 Institute of Chemistry, Technology and Metallurgy, Center of Chemistry, University of Belgrade, Belgrade, Serbia

2 Institute of Chemistry, Technology and Metallurgy, Center of Excellence in Environmental Chemistry and Engineering, University of Belgrade, Belgrade, Serbia

3 Faculty of Technology and Metallurgy, University of Belgrade, Belgrade, Serbia

4 Department of Chemical Sciences, University of Padova, Padova, Italy

Waterborne polyurethanes (WBPUs) represent a class of polyurethanes (PUs), in which water is used as the dispersion medium, instead hazardous organic solvents. In this manner, the emission of volatile organic compounds is decreased, leading to the environmental preservation. Poly(dimethylsiloxane) (PDMS) has a lot of useful features, such as low glass transition temperature, T_g, low surface energy, excellent biocompatibility, high thermal and oxidative stability, which is why PDMS is often used in WBPU formulations. Siloxane-modified WBPUs exhibit the properties of both, PDMS and PUs. WBPUs based on PDMS have good surface properties, such as excellent hydrophobicity, chemical resistance and low surface energy. Because of these useful features, WBPUs based on PDMS can be used as coatings, adhesives, paints, etc [1].

In this work, a series of WBPUs was synthesized *via* one-step polymerization method, without a chain extension step, using acetone and water as solvents and stannous octoate as a catalyst. The prepared WBPUs are based on *α,ω*-dihydroxypropyl poly(dimethylsiloxane) (PDMS, M_n = 725 g/mol), isophorone diisocyanate (IPDI), 2,2-bis-(hydroxymethyl)propionic acid (DMPA) and triethylamine (TEA). Three samples with different molar ratio between DMPA and PDMS (from 0.2 to 0.5) and constant –NCO/–OH molar ratio of 1.7, were synthesized [2]. WBPU samples were labeled as WBPU-0.2, WBPU-0.35, and WBPU-0.5, where the numbers represent the DMPA/PDMS molar ratio. Surface morphology was examined by SEM and AFM analyses. SEM analysis was performed on the XL30 scanning electron microscope, on the surface of the samples, at a magnification of 3k ×, previously gold coated with 5 nm thickness. For determination of the surface composition of the prepared WBPUs, SEM-EDS measurements were also conducted. AFM analysis was carried out on an Agilent 5500 SPM microscope, under ambient conditions, with tapping mode. The scan area of the WBPUs surface was 1 × 1 μm^2.

The surface morphology and surface element composition of WBPUs was analyzed by SEM and SEM-EDS analyses, respectively. According to the obtained micrographs presented in Figure 1, it can be seen that all samples have very smooth and homogenous surfaces, without some major relief irregularities. Besides that, SEM-EDS measurements show the presence of all expected elements, and also a large quantity of Si atoms (> 20 wt.%) on the surface that originates from PDMS. These results arise as a consequence of the low surface energy of PDMS, which is why it tends to migrate and cover the surfaces of the prepared WBPUs [3]. In order to examine the surface topography of WBPUs, AFM analysis was performed. In Figure 2, 3D height and 2D phase AFM images of the surface of WBPUs are presented. On the obtained 3D height AFM figures, it can be observed that surface of WBPUs becomes rougher with increasing DMPA content. Furthermore, brighter microdomains, originating from PDMS, are also visible on the surface of prepared WBPUs. 2D

phase AFM images provided more information, and revealed the presence of microphase separated morphology in these WBPUs, caused by the termodynamic incompatibility of the applied reagents. Microphase separated morphology is more pronounced in WBPUs with higher PDMS content [4].

A series of novel WBPUs based on PDMS, IPDI, DMPA and TEA was successfully prepared. SEM and AFM analysis confirmed positive surface properties, such as smooth and homogenous surface, enriched with a large amount of PDMS, and the existence of microphase separated morphology, which is responsible for good features and wide application area of the prepared WBPUs [5].

References:

[1] G Zhen, L Yunjun, Prog. Org. Coat. **76** (2013), 1522-1526.
[2] I Stefanović *et al*, Prog. Org. Coat. **161** (2021), 106474.
[3] F Yu, X Xu, N Lin, XY Liu, RSC Adv. **5** (2015), 72544-72552.
[4] E Yilgör, I Yilgör, Prog. Polym. Sci. **39** (2014) 1165-1195.
[5] This work was financially supported by the Ministry of Education, Science and Technological Development of the Republic of Serbia (Grant No. 451-03-68/2022-14/200026).

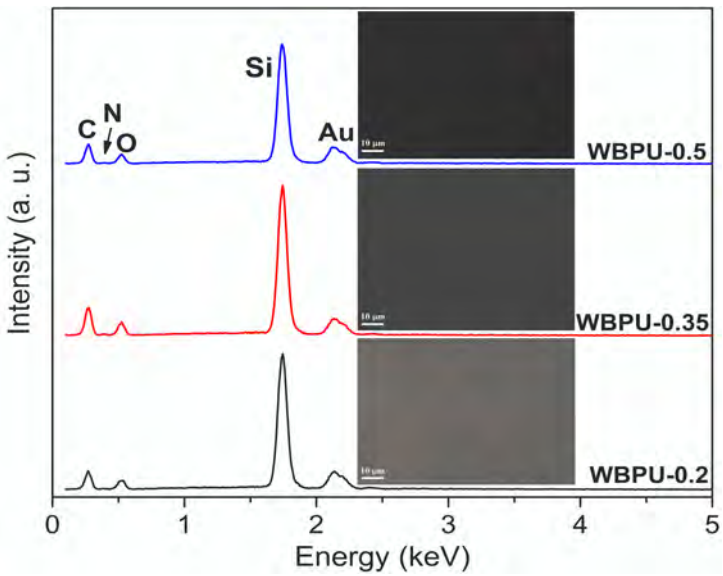

Figure 1. SEM micrographs and SEM-EDS curves of the WBPUs, magnification ×3k.

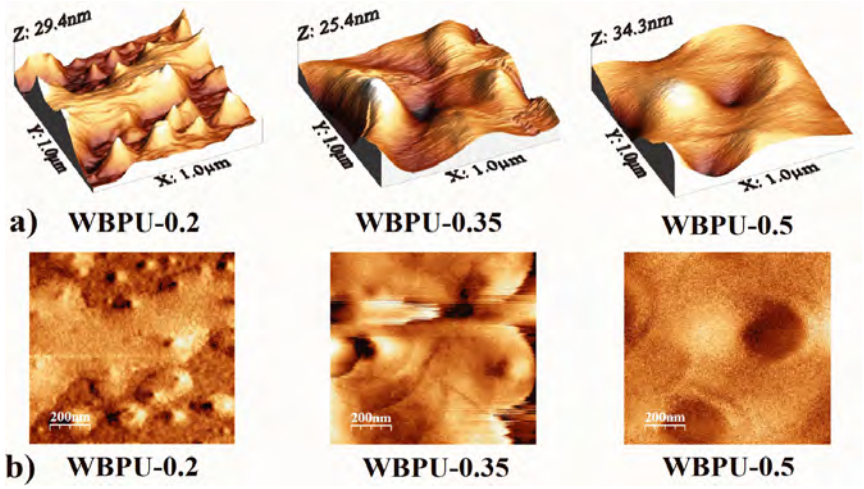

Figure 2. a) 3D height and b) 2D phase AFM images of the surface of WBPUs, scan area 1×1 μm^2.

The effect of poly(dimethylsiloxane) segment content on the morphology of polyurethane composite materials

Marija V. Pergal[1], Igor Kodranov[2], Dana Vasiljević-Radović[1], Milos Steinhart[3], Gordana Gojgić-Cijović[1], Dragan Manojlović[2], and Milena Špírková [3]

1 Institute of Chemistry, Technology and Metallurgy, University of Belgrade, Department of Microelectronic Technologies, Belgrade, Serbia

2 Faculty of Chemistry, University of Belgrade, Belgrade, Serbia

3 Institute of Macromolecular Chemistry AS CR, v.v.i. (IMC), Prague, Czech Republic

Polyurethane (PU) is an extraordinarily versatile polymeric material and has been widely used in industrial and biomedical applications [1,2]. To meet the demands of any particular application, the properties of PU can be modified in two possible ways: changing PU microstructures or adding nanofillers within polymer matrix. Polyurethane/clay nanocomposites have been intensively investigated in the last decades as promising nano-engineered materials with achieved a significantly improved performances (thermal, mechanical, barrier and anticorrosion) compared to pristine ones [3]. The clays or layered silicate are good candidates for the preparation of PU nanostructured materials due to their availability, low cost, high ion exchange capacity, high aspect ratio and well-developed intercalation chemistry. Depending on preparation methods, dispersion, and degree of the delamination of clay particles within a polymer matrix, hybrids are obtained with structures ranging from intercalated to exfoliated [3]. The difference in the micro-phase morphology of these two types of polymer/clay nanocomposites is a reason for the differences in their physical properties. Many literatures report that *in situ* polymerization gives PU nanocomposites with the improved properties [3].

Therefore in this study, *in situ* polymerization procedure in solvent mixture was used for the preparation of thermosetting PU nanocomposites (PUNCs) with different content of soft segment (from 30 to 60 wt%), and with the addition of organomodified montmorillonite clay (Cloisite 30B®) as the nanofiller, in an amount of 0.5 wt.%. The PUNCs were based on poly(dimethylsiloxane) macrodiol (PDMS) that represents soft segment and 4,4′-diphenylmethane diisocyanate (MDI) and hyperbranched polyester (BH-30) which were selected as the hard segment. The PUNCs are marked so that the last two numbers in title indicate wt.% of soft segment in materials. Namely, the main objective of this study is to analyze the effect of the soft segment content on the morphology of the prepared PU nanocomposite films using atomic force microscopy (AFM), scanning electron microscopy (SEM), and small- and near wide-angle X-Ray scattering (SWAXS) analyses. SEM images of the fractured surfaces were obtained on JEOL JSM-6610LV. AFM analysis was carried out by atomic force microscope (Dimension Icon, Bruker, USA). SWAXS measurements of the PUNCs were performed using SAXS instrument (originally Molecular Metrology, USA, recently considerably upgraded by SAXSLAB, now Xenocs).

The surface topographies and heterogeneity of relief of the prepared PUNCs were investigated by AFM (Fig 1). The nanocomposite with 60 wt% of soft segments (PUNC-60) has smoot surface and homogeneous phase relief, while topographies of other samples display oval like formations (or spherical harder ‘nanoparticles’). Bigger and more spherical formations were observed in PUNC-40 than in nanocomposite PUNC-30. All materials were characterized by lighter (harder) and darker (softer) areas originating mainly from the micro-phase separation of the soft and hard PU segments.

SEM micrographs of fractured surfaces of the PUNCs (Fig. 2) show the presence of brighter parts („points“) in the investigated samples, which originate from the addition of clay nanoparticles. It was observed oval formations composed of hard domains in PUNCs, but they were slightly bigger in PUNC with higher soft segment content than in nanocomposite PUNC-30, which is in agreement with AFM.

Based on SWAXS results, the strong and significant Cloisite 30B peak at 3.48 nm^{-1} was not visible in any of the prepared materials, apparently due to its negligible concentration or the presence of organoclay exfoliated structure in the PUNC matrix [4].

References:

[1] J. Zhang et al, Prog. Org. Coat. **75** (2012), 579-583.
[2] M. Špírková et al, Polymers. 12 (2020), 1-18.
[3] M.V. Pergal et al, Ind. Eng. Chem. Res. 56 (2017), 4970-4983.
[4] This work was financially supported by the Ministry of Education, Science and Technological Development of the Republic of Serbia (Grant No: 451-03-68/2022-14/200026) and by the Czech Science Foundation (Grant Agency of the Czech Republic, Project No. No: 18-03932S).

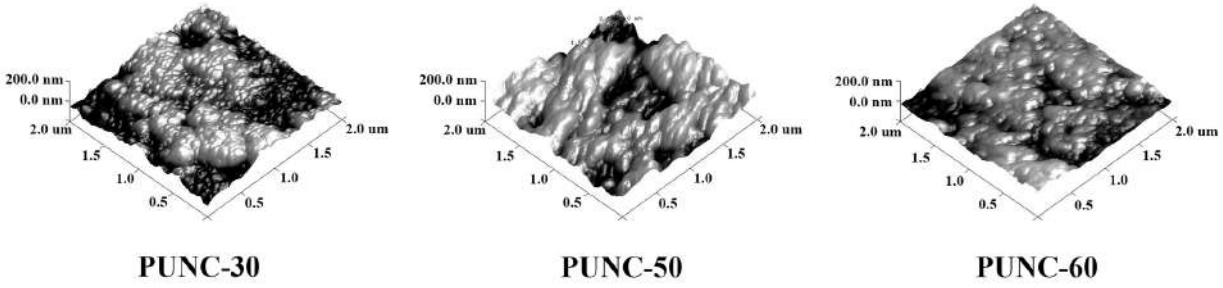

Figure 1. 3D AFM images of selected PUNC films.

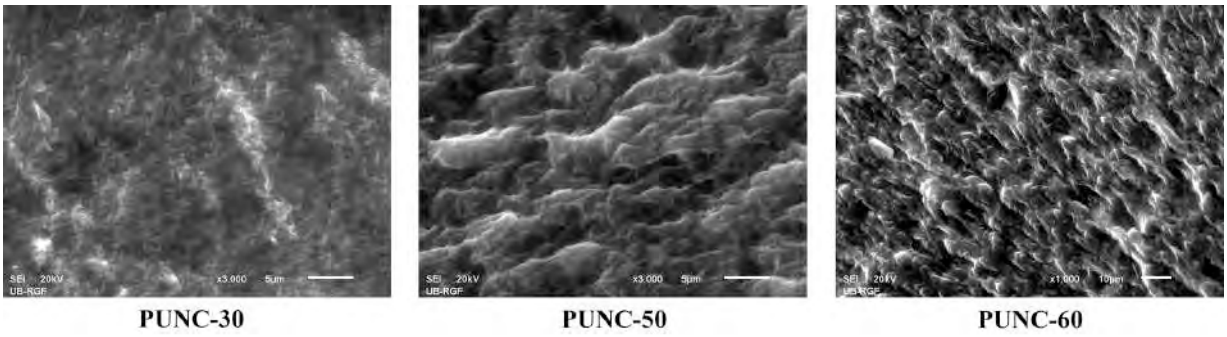

Figure 2. SEM micrographs of selected PUNC films.

Establishing of 3D Scaffolds Based on Human Adipose Tissue Extracellular Matrix for *in vitro* Breast Cancer Research

Drenka Trivanović[1], Ivana Drvenica[2], Djordje Veljović[3], Branko Bugarski[3], Diana Bugarski[1] and Aleksandra Jauković[1]

1 Group for Hematology and Stem Cells, Institute for Medical Research, National Institute of Republic of Serbia, University of Belgrade, Serbia

2 Group for Immunology, Institute for Medical Research, National Institute of Republic of Serbia, University of Belgrade, Serbia

3 Faculty of Technology and Metallurgy, University of Belgrade, Belgrade, Serbia

Increasing evidence suggests that noncellular components of the cancer ecosystem, particularly interstitial extracellular matrix (ECM) and its stiffness and remodeling, play a key role in the progression of breast cancer. Understanding of the underlying mechanisms of tumorigenic ECM remodeling is crucial for developing therapeutic treatments. Creation of three-dimensional (3D) models appeared to be more reliable approaches to investigate and predict tumor cell invasion and drug response than conventional 2D substrates. In recent years, investigations have focused on the implementation of decellularized adipose tissue (hAdECM) as scaffold materials for fat, cartilage, or bone tissue regeneration as well as disease modelling [1,2]. Here, we explored potential of hAdECM as *in vitro* 3D scaffold for human breast cancer cell lines under static conditions.

Human adipose tissue extracellular matrices were obtained from adipose tissues of oncology patients. Native decellularized and delipidized hAdECM were estimated for its appearance, mechanical features, protein content and support of adipose tissue stromal cell growth [3]. Stress-strain curves were obtained by measuring samples (30 mm × 2 mm × 0.1 mm, length × width × thickness) at pulled rate of 10 mm/min using AG-Xplus Universal Testing Machine (Shimadzu, Japan) equipped with 100 N load cell. hAdECM structure and morphology was analyzed by scanning electron microscopy (SEM) using FE-SEM, a TESCAN MIRA 3 XMU (Tescan, Czech Republic), operated at 20 keV, after a deposition of gold thin layer on the dried and fixed samples as described in our protocol [4]. Cytocompatibility of hAdECM was tested by *in vitro* adhesion and viability of breast cancer cell lines MCF-7 and MDA-MB231 cells which were cultured on native hAdECM fragments for 7 days under static conditions.

Nonlinear stress-strain behavior observed in tensile testing of native hAdECM and its initial modulus are comparable to the values obtained for the intact adipose tissue, as previously reported [5]. DNA and lipid stainings, followed by the SEM microscopy of hAdECM confirmed successful decellularization of adipose tissue. Comparing to the intact adipose tissue, we observed that hAdECM fibers predominantly formed by different types of collagen, maintained the architecture and orderliness after decellularization. SEM imaging confirmed the absence of mature adipocytes in hAdECM. In addition, our results showed that hAdECM can provide a permissible 3D environment and biomechanics for hosting of both breast cancer cell lines, where MCF-7 and MDA-MB231 closely associated with hAdECM fibers. Our additional experiments, applying hAdECM-coated surfaces, demonstrated that the presence of hAdECM significantly affects the antiproliferative effect of doxorubicin and promoted the epithelial to mesenchymal transition of both breast cancer cell lines.

Our results suggest that native hAdECM can be used as a permissive 3D microenvironment for

breast cancer cells. These findings will help and advance further investigations of key tumorigenic ECM components in breast cancer and the fabrication of hAdECM-based scaffolds for regenerative strategies and drug screening [6].

References:

[1] AL Wishart *et al*, Science Advances **6(43)** (2020), p. eabc3175.
[2] LW Dunne *et al*, Biomaterials **35(18)** (2014), p. 4940.
[3] Trivanović *et al*, Artificial Cells, Nanomedicine, and Biotechnology **46(sup3)** (2018), p. S370.
[4] Kostić *et al*, Colloids and Surfaces B: Biointerfaces **122** (2014), p. 250
[5] Alkhouli *et al*, American Journal of Physiology Endocrinology and Metabolism **305(12)** (2013), p. E1427.

[6] The authors acknowledge funding from the Ministry of Education, Science and Technological Development of Republic of Serbia (contract number 451-03-68/2022-14/200015 with Institute for Medical Research University of Belgrade, National Institute of Republic of Serbia).

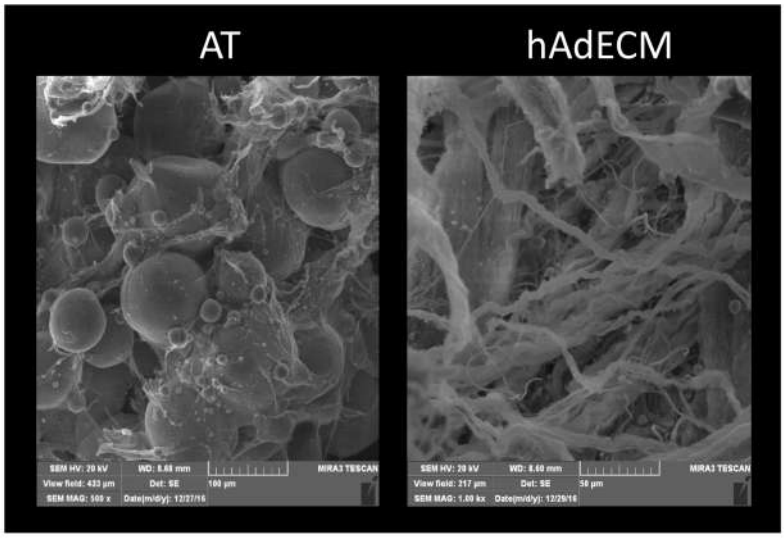

Figure 1. Validation of decellularization and delipidization of adipose tissue. SEM micrographs of native adipose tissue before (AT) and hAdECM.

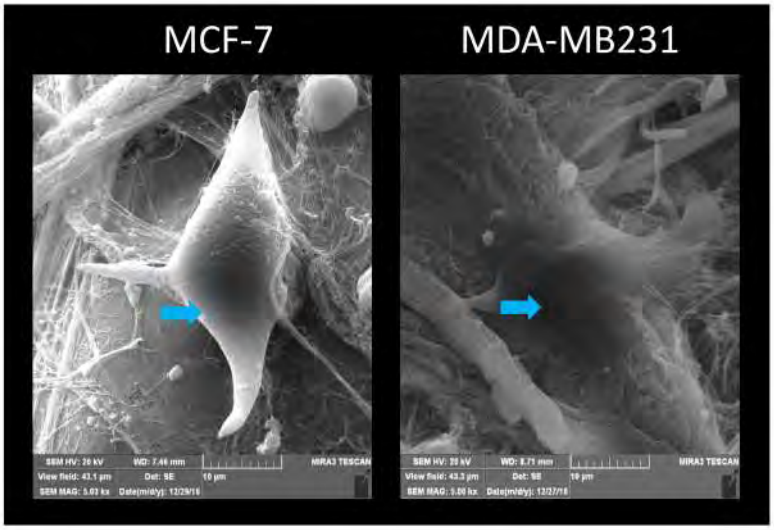

Figure 2. Scanning electron microscopy of breast cancer cells (MCF-7 and MDA-MB-231) cultured on native hAdECM for 7 days. Blue arrows indicate tumor cells.

Application of Scanning Electron Microscopy in the Analysis of Tissue Response to Implanted Collagen-based Biomaterials

Sanja Stojanović[1,2], Milena Radenković[2] and Stevo Najman[1,2]

1 Department of Biology and Human Genetics, Faculty of Medicine, University of Niš, Niš, Serbia

2 Department for Cell and Tissue Engineering, Scientific Research Center for Biomedicine, Faculty of Medicine, University of Niš, Niš, Serbia

Collagen-based biomaterials have a wide application in regeneration of both soft and hard tissues [1]. Collagen that is used for the development of collagen-based biomaterials may be of different origin and type, but also very popular nowadays is its chemical modification to obtain better mechanical and biological properties and final outcome [2]. Very often, different biologically active molecules with certain activities are added to biomaterials, to achieve better and faster healing process, tissue regeneration and reparation [2]. Before any potential clinical application, it is necessary to examine those newly developed biomaterials in preclinical studies using different *in vitro* cell and *in vivo* animal models [3]. Subcutaneous implantation model in mice or rats is the most frequently used animal model *in vivo* to study general tissue response to biomaterials intended for use in regenerative medicine. Biomaterials' biocompatibility, tissue reaction to implanted biomaterials and changes of biomaterials in biological systems *in vivo*, are mostly examined by using histological methods of analysis [4].

Our aim in this study was to present how scanning electron microscopy (SEM) can be used to assess tissue response to implanted collagen-based biomaterials and changes in biomaterials in the *in vivo* system.

We have analyzed two different collagen membranes of the same origin, both derived from porcine dermis, with and without the addition of hyaluronic acid. Hyaluronic acid is glycosaminoglycan with anti-inflammatory properties and has been increasingly added to biomaterials for both hard and soft tissue regeneration to modulate tissue response and lower the initial inflammatory reaction that usually occurs after implantation. To analyze general tissue response to these two collagen membranes, examined membranes were subcutaneously implanted into mice. Membranes with surrounding tissue were explanted 10 and 30 days after implantation, fixed in glutaraldehyde, processed according to already established protocols and analyzed by SEM (JEOL, JSM 5300).

Results are shown in Figures 1 and 2. In Figure 1, the appearance of the collagen membrane before implantation (a), explanted 10 days (b) and 30 days after implantation is shown, while in Figure 2, the appearance of the collagen membrane with hyaluronic acid before implantation (a), explanted 10 days (b) and 30 days after implantation is shown. The results indicate that there are differences in the number of cells and type of the cells located on the surface of membranes as well as their interaction and integration into the membranes, which were related to the membrane type and examined time point. Also, there were differences in the amount of collagen fibers and their organization related to the type of examined collagen membrane and examined time point.

According to the results obtained in our study, we can conclude that SEM can be used as a method to study and assess the biocompatibility and tissue response to implanted collagen-based biomaterials.

References:

[1] Lindner C, *et al*. Membranes. 2022; 12(4):378.
[2] Radenković M, *et al*. Membranes. 2021; 11(9):712.
[3] Jung O, *et al*. In Vivo September 2020, 34 (5) 2287-2295
[4] Ottenbacher N, *et al*. Dentistry Journal. 2021; 9(11):127.
[5] The authors acknowledge funding from the Ministry of Education, Science and Technological Development of Republic of Serbia for financial support (Grants No: III 41017, 451-03-68/2020-14/200113, 451-03-9/2021-14/200113 and 451-03-68/2022-14/200113).

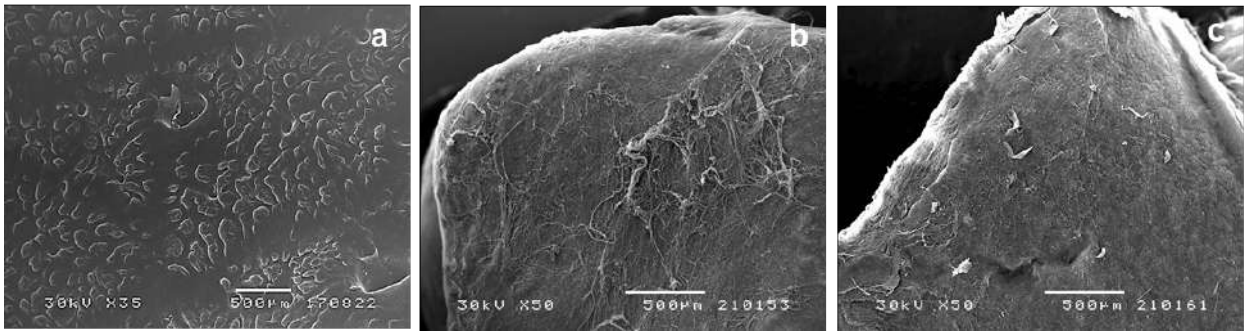

Figure 1. Scanning electron microscopy micrographs of collagen membrane: (a) prior to implantation; (b) explanted 10 days after implantation; (c) explanted 30 days after implantation.

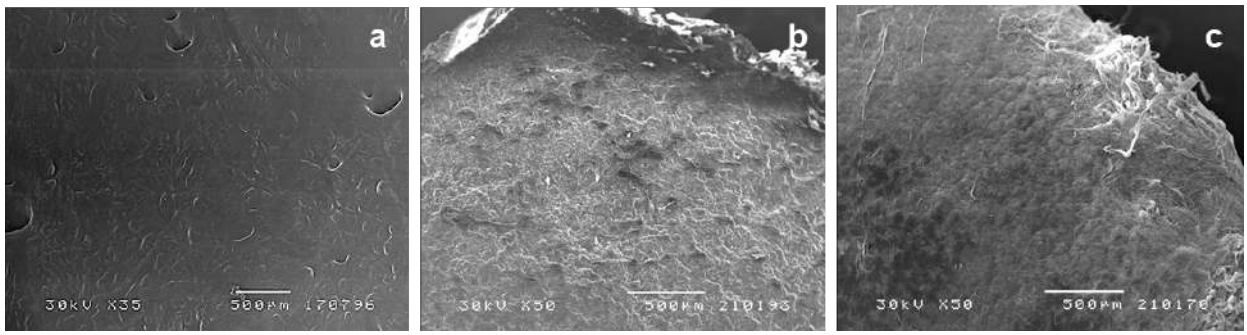

Figure 2. Scanning electron microscopy micrographs of collagen membrane with hyaluronic acid: (a) prior to implantation; (b) explanted 10 days after implantation; (c) explanted 30 days after implantation.

Influence of Post-Synthesis Treatments on the Properties of Brushite/Monetite Powders

Željko Radovanović[1], Lidija Radovanović[1], Aleksandar Kremenović[2], Đorđe Janaćković[3] and Rada Petrović[3]

1 Innovation Center of Faculty of Technology and Metallurgy, Karnegijeva 4, 11120 Belgrade, Serbia

2 University of Belgrade, Faculty of Mining and Geology, Đušina 7, Belgrade 11000, Serbia

3 University of Belgrade, Faculty of Technology and Metallurgy, Karnegijeva 4, 11120 Belgrade, Serbia

Dicalcium phosphate (DP) materials, of which brushite and monetite were the most known, have been intensively studied for several decades because of excellent resorptive and osteoconductive properties that can satisfy the requirements needed for various medical applications, such as bone cements, coatings of metallic implants and bone grafts [1,2]. Brushite and monetite are the di-hydrated ($CaHPO_4 \cdot 2H_2O$) and anhydrous ($CaHPO_4$) forms of DPs, respectively, which showed much better resorption due to higher solubility in comparison to the hydroxyapatite (HAp) and tricalcium phosphate (TCP) [2].

In this study, the effect of different post-synthesis treatments on composition and morphology of four brushite/monetite powders, were analyzed. All the powders have been prepared by modified precipitation method described previously [3] with molar ratio of starting reagents $(NH_4)_2HPO_4$ and $Ca(NO_3)_2 \cdot 4H_2O$ being 7:10. After filtering, powder I was obtained by drying the precipitate at 105 °C for 4 h, while powder II was obtained by precipitate freezing at –10 °C for 72 h, followed by drying at room temperature for 72 h. By drying the precipitate at 110 °C for 24 h and 105 °C for 3 h, powders III and IV were obtained, respectively. X-ray powder diffraction (XRPD) revealed that all the powders are two-phase systems consisting of brushite and monetite: 98.8 mas.% brushite and 1.2 mas.% of monetite in I, 97.7 mas.% brushite and 2.3 mas.% of monetite in II, 66.7 mas.% brushite and 33.3 mas.% of monetite in III and 45.9 mas.% brushite and 54.1 mas.% of monetite in IV. Field Emission Scanning Electron Microscopy (FESEM, Figure 1) showed that particles of prepared materials form the agglomerates in the form of triangular plates. In addition, materials were analyzed for their spectral, thermal and textural properties.

References:

[1] F Tamimi, Z Sheikh and Jake Barralet, Acta Biomaterialia **8** (2012), p. 474.
[2] E Boanini *et al*, Journal of Functional Biomaterials **13** (2022), p. 65.
[3] I Mayer *et al*, European Journal of Inorganic Chemistry (2003), p. 1445.
[4] The authors acknowledge funding from the Ministry of Education, Science and Technological Development of the Republic of Serbia (Contract No. 451-03-68/2022-14/200287 and Contract No. 451-03-68/2022-14/200135).

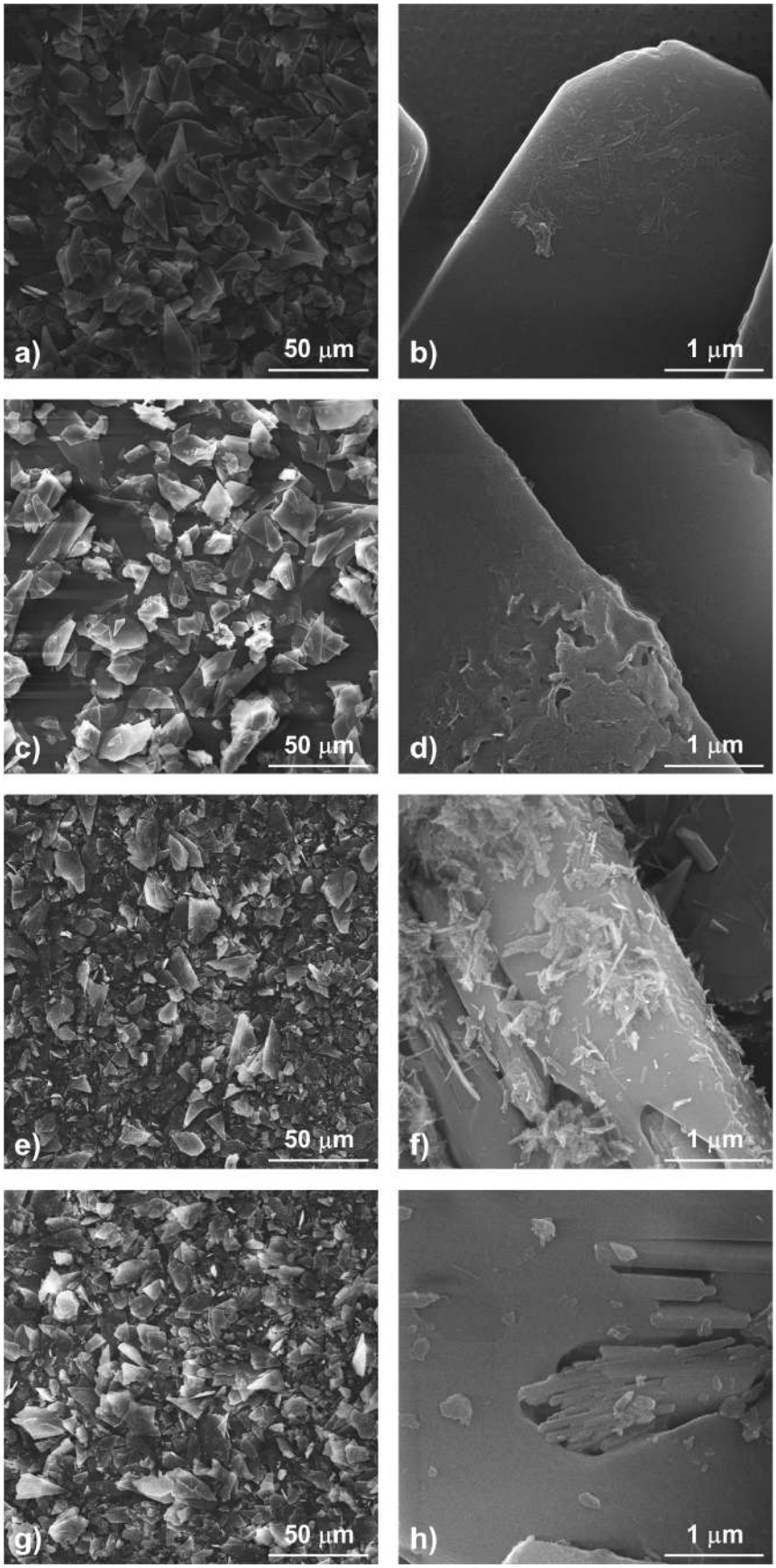

Figure 1. FESEM micrographs of powders: I (a, b), II (c, d), III (e, f) and IV (g, h).

Hydroxyapatite Reinforced Poly(methacrylic acid)/Gelatin Interpenetrating Network Hydrogels for Drug Delivery Applications

Vukasin Ugrinovic[1], Vesna Panic[1], Milica Milutinovic[2], Bojan Bozic[3], Rada Petrovic[4], Djordje Janackovic[4] and Djordje Veljovic[4]

1 Innovation Center of Faculty of Technology and Metallurgy, University of Belgrade, Belgrade, Serbia

2 Department of Biochemical Engineering and Biotechnology, Faculty of Technology and Metallurgy, University of Belgrade, Belgrade, Serbia

3 Institute of Physiology and Biochemistry „Ivan Đaja“, University of Belgrade, Belgrade, Serbia

4 Department of Inorganic Chemical Technology, Faculty of Technology and Metallurgy, University of Belgrade, Belgrade, Serbia

Hydrogels are three-dimensional hydrophilic polymer networks capable to retain large amounts of water or biological fluids. Due to their highly hydrated, porous, permeable structure with the possibility to accommodate living cells, drugs, or bioactive factors and deliver them in a controllable manner, hydrogels are promising materials for biomedical applications [1]. Different synthetic and natural polymers have been investigated as hydrogels for biomedical purposes. Among them, gelatin, a denatured form of collagen, has been widely applied in biomedicine due to its low price, biocompatibility, and biodegradability. In addition, it contains Arg-Gly-Asp (RGD)-like sequences that promote cell adhesion, proliferation, migration, and differentiation [2]. However, the soft nature of gelatin-based hydrogels, as well as rapid dissolution under physiological conditions, makes them unsuitable for *in vivo* biomedical applications. This often requires the implementation of toxic crosslinkers such as glutaraldehyde, carbodiimides, or epoxy compounds that can compromise the biocompatibility of the hydrogels [3]. Over the last decade, remarkable progress in the mechanical properties of hydrogels has been achieved by developing interpenetrating network hydrogels (IPN) based on different types of strengthening mechanisms [4,5]. By combining gelatin with synthetic polymers it is possible to obtain interpenetrating networks (IPN) which retain the biocompatibility of gelatin but are characterized by markedly improved structural and mechanical properties compared to pure gelatin [6]. The incorporation of different nano-fillers such as nano-cellulose, carbon nanotubes, or calcium phosphate ceramics, could additionally improve the functionality of these materials [7,8].

In this work, we synthesized composite hydrogels based on IPN of poly (methacrylic acid) (PMAA), gelatin and nanostructured hydroxyapatite (HA), for potential biomedical applications. Different amounts of hydroxyapatite (HA) were incorporated to increase the mechanical properties of composites. Composites were characterized by SEM, mechanical testing, and swelling behavior. The ability for controlled drug release was investigated in simulated body fluid at 37 °C, with two different types of drugs. SEM micrographs revealed a highly porous structure of the hydrogels with embedded nano-structured particles of HA (Figure 1). The increase in HA amount led to proportional improvement of mechanical properties, as well as lower swelling rate and porosity, which also affected the drug release kinetics. *In vitro* release experiments indicated that physicochemical properties of the drug significantly affected drug release kinetics, due to interactions with the hydrogels matrix. *In vitro* antimicrobial testing demonstrated bactericidal and fungicidal activity of the drug-loaded hydrogels against *E. Coli*, *S. Aureus* and *C. Albicans* [9].

References:

[1] AS Hoffman, "Hydrogels for biomedical applications." Advanced drug delivery reviews, **vol. 64** (2012), pp. 18-23.
[2] A Georgopoulou, *et al.* "Chitosan/gelatin scaffolds support bone regeneration." Journal of Materials Science: Materials in Medicine, **vol. 29** (2018), pp. 1-13.
[3] H Sung, *et al.* "Evaluation of gelatin hydrogel crosslinked with various crosslinking agents as bioadhesives: in vitro study." Journal of Biomedical Materials Research, **vol. 46** (1999), pp. 520-530.
[4] Q Chen, *et al*. "Fracture of the physically cross-linked first network in hybrid double network hydrogels." Macromolecules, **vol. 47** (2014), pp. 2140-2148.
[5] X Chang, *et al*. "Dual Crosslink Physical Hydrogels with High Toughness Based on Synergistic Hydrogen Bonding and Hydrophobic Interactions." Macromolecular rapid communications **vol. 39** (2018), pp. 1700806.
[6] V Ugrinovic *et al*. "Strong and tough, pH sensible, interpenetrating network hydrogels based on gelatin and poly (methacrylic acid)." Polymer Engineering & Science **vol. 62** (2022), pp. 622-636.
[7] L Zheng, *et al*. "Evaluation of novel in situ synthesized nano-hydroxyapatite/collagen/alginate hydrogels for osteochondral tissue engineering." Biomedical Materials **vol. 9** (2014), pp. 065004.
[8] Z Li, *et al*. "Nano-hydroxyapatite/polyacrylamide composite hydrogels with high mechanical strengths and cell adhesion properties." Colloids and Surfaces B: Biointerfaces **vol. 123** (2014), pp. 959-964.
[9] The authors acknowledge the financial support of the Ministry of Education, Science and Technological Development of the Republic of Serbia (Contracts No. 451-03-68/2022-14/200287 and 451-03-68/2022-14/200135).

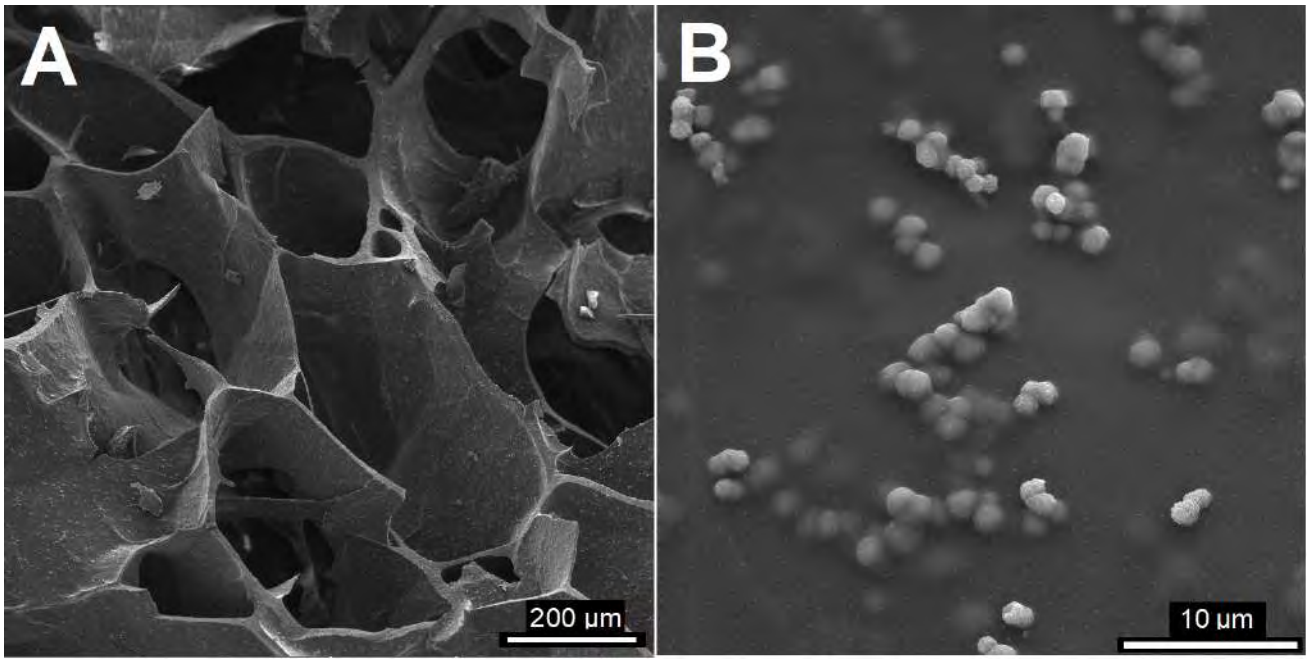

Figure 1. Cross-section micrographs of freeze-dried PMAG/HA10 composite hydrogels under different magnifications (A) 200x magnification and (B) 5000x magnification.

Hydroxyapatite-based Bioceramic Dental Inserts as Dentin Substitutes

Tamara Matić[1], Maja L. Zebić[2], Vesna Miletić[3], Rada Petrović[4], Djordje Janaćković[4], Djordje Veljović[4]

1 Innovation Center of the Faculty of Technology and Metallurgy Ltd, Belgrade, Serbia

2 University of Belgrade, School of Dental Medicine, Belgrade, Serbia

3 The University of Sydney, Faculty of Medicine and Health, Sydney Dental School, Surry Hills NSW, Australia

4 University of Belgrade, Faculty of Technology and Metallurgy, Belgrade, Serbia

Tooth caries presents one of the most common diseases worldwide, and its treatment involves removal of the decayed tooth structure, and the cavity restoration using restorative dental materials. Resin based composites (RBCs) are the most commonly used restorative material in practice owing to their great aesthetic appearance allowing the clinicians to adapt the nuance of the restoration to the patient's tooth color. However, the RBCs harden by the polymerization of monomers that leads to the polymerization shrinkage of the restoration, leaving the micro-gaps at the teeth-restorations interface which allows the secondary caries formation.

In order to overcome this problem inorganic dental inserts based on feldspar, glass, porcelain etc. were introduced as cavity megafillers [1]. Nevertheless, these materials were very distinct from the human dentin tissue, leading to inadequate properties. Recently, the bioactive, biomimetic materials gained more attention for application in biomedicine. The goal of this study was to develop a dentin substitute based on hydroxyapatite, the main inorganic component of the bones and teeth, processed in the form of dense compacts with satisfactory mechanical properties, in order to mimic the removed dentin tissue. The dental inserts are intended to be placed in the central area of the removed dentin, while a thin layer of RBCs would be used as a top coat in the area of enamel for great aesthetic, wear and sealing purposes [2]. Therefore, a great bonding ability of the dental inserts with commercially available restorative materials needs to be achieved as well.

Hydroxyapatite nanosized powders doped with 5 mol. % magnesium and binary doped with 3 mol. % magnesium and 3 mol. % strontium ions were synthesized hydrothermally at 150 °C, pressed into compacts by applying cold isostatic pressing and sintered at 1200 °C for 2 h in order to obtain bioceramic dental inserts. Microstructure, average pore and grain size, phase composition and mechanical properties of the obtained dental inserts were determined. The bonding ability of the inserts with commercially available dental composites, adhesives and cements applied by *total-etch* and *self-etch* clinical protocols were tested by the shear bond strength test. The *total-etch* protocol implied acidic surface pre-treatment of the inserts with 37 % phosphoric acid. A Field Emission Scanning electron microscope (FE-SEM Tescan Mira 3 XMU) was engaged to determine the particles morphology, inserts' microstructure, as well as the intimate bonding of the dental inserts with the restorative materials, applied by the *self-etch* and *total-etch* protocols. A cross-section of a molar restored by the proposed protocol involving a hydroxyapatite-based dental insert was also examined by using the FE-SEM.

The results showed that dopants have a significant effect on the microstructure and phase composition of the hydroxyapatite-based dental inserts, distinct solubility and mechanical properties. Smaller average grain and pore size, as well as greater hardness by Vickers were obtained in the case

of magnesium doped hydroxyapatite. The bonding strength values of both dental insert types with the Filtek Z_250 dental composite applied by Single Bond Universal adhesive system by both *self-etch* and *total-etch* protocols were in the range of the bonding strength values previously reported for human dentin [3].

In conclusion, the obtained hydroxyapatite-based dental inserts present dentin substitutes that are chemically and structurally similar to the mineral component of the human dentin, with adequate mechanical properties, as well as great bonding ability to restorative materials commonly used in dental practice, which makes them promising materials for application in restorative dentistry.

References:

[1] M. Federlin, B. Thonemann, and G. Schmalz, "Inserts – megafillers in composite restorations: a literature review," Clinical Oral Investigations, **vol. 4** (2000), pp. 1–8.
[2] M. Lezaja et al., "Bond strength of restorative materials to hydroxyapatite inserts and dimensional changes of insert-containing restorations during polymerization," Dental Materials, **vol. 31** (2015), pp. 171–181.
[3] L. Bracher and M. Özcan, "Adhesion of resin composite to enamel and dentin: a methodological assessment," Journal of Adhesion Science and Technology, **vol. 32** (2018), pp. 258–271.
[4] The authors wish to acknowledge funding from the the Ministry of Education, Science and Technological Development of the Republic of Serbia (Contract No. 451-03-68/2022-14/200135, 451-03-68/2022-14/200287, and 451-03-9/2021-14/200129).

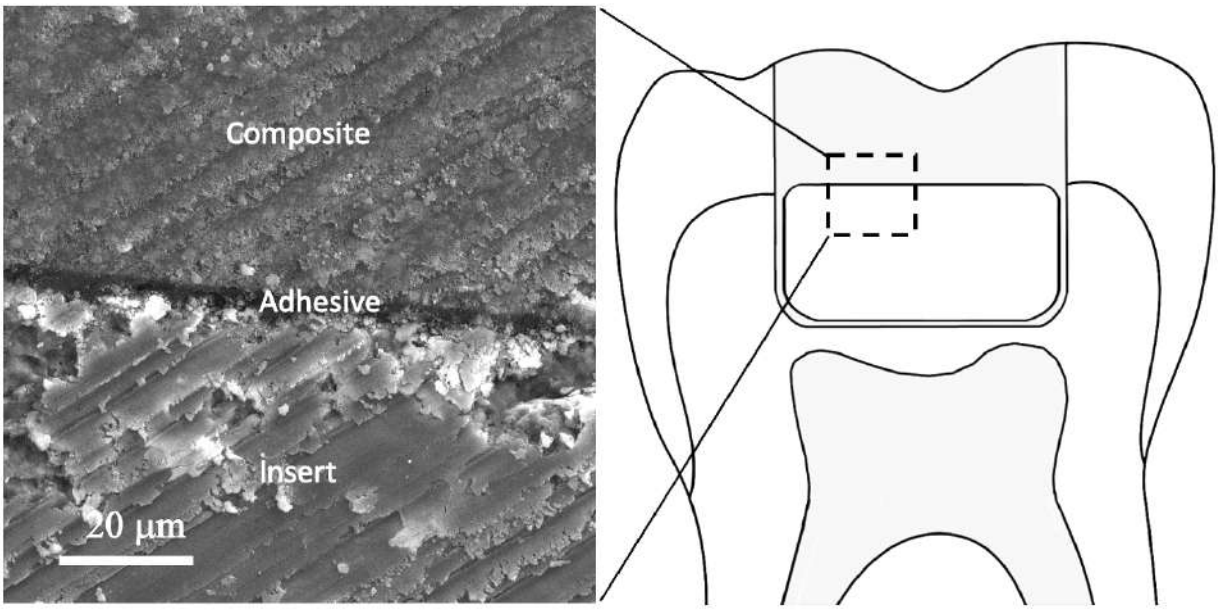

Figure 1. Schematic representation of cross-section of a molar restored by the newly proposed protocol involving hydroxyapatite-based dental insert, and FE-SEM micrograph of the composite-adhesive-insert interface. The dental insert based on hydroxyapatite doped with magnesium is bonded with Filtek Z_250 dental composite by Single Bond Universal adhesive applied by *total-etch* protocol.

Synthesis and Characterization of ZnO Deposited on Hydroxyapatite for Dental Application

Marija Stevanović[1], Marija Milivojević[1], Rada Petrović[2], Đorđe Veljović[2], Suzana Dimitrijević[2], Đorđe Janaćković[2]

1 Innovation Center of the Faculty of Technology and Metallurgy Ltd, Belgrade, Serbia

2 University of Belgrade, Faculty of Technology and Metallurgy, Belgrade, Serbia

Hydroxyapatite (HAp) is the main mineral component of natural teeth. The bioactivity and biocompatibility of its synthetic analog make it a suitable material for different applications in restorative and preventive dentistry [1]. In order to prevent contamination, it has been proposed to use antimicrobial agents such as antibiotics, biocide metal ions, and metal oxides such as ZnO, MgO, and CaO. There are at least two problems when it comes to antibiotics. The first one is the development of resistant microorganisms, and the second one is that adsorbed antibiotics are quickly washed out by body fluids, so they can not prevent post-treatment infections long-term. Dental caries and periodontal disease are the most prevalent oral diseases for which no perfectly regenerative solutions are available yet. The main reason for endodontic failure is the persistence of bacteria inside the root canal system, such as the *Enterococcus faecalis*, which represents the most resistant species [2]. The use of ZnO to optimize the fight against microbial resistance has been receiving increased attention due to the non-specific activity of this inorganic antimicrobial agent against both gram-positive and gram-negative bacteria [3].

Due to the excellent antimicrobial properties of ZnO and biocompatibility of HAp, the combination of ZnO deposited on hydroxyapatite particles seems to be a promising material for dental application. The goal of our work was to obtain antibacterial biomaterial by creating a hybrid material consisting of ZnO and HAp, optimizing the ZnO content, and investigating its potential advantages in dental application.

The HAp was synthesized hydrothermally, and further modified with Zn-acetate as a precursor by the sonochemical method [4]. The obtained powders HAp, and HAp/ZnO were characterized using scanning electron microscopy (SEM), energy-dispersive X-ray spectroscopy (EDX), and X-ray diffraction (XRD) techniques. The antimicrobial activity of the powders was evaluated against *Enterococcus faecalis*.

The results of EDX analysis confirmed the presence of the Zn in HAp/ZnO powders, whereas the XRD analysis suggested the presence of the ZnO phase in obtained HAp/ZnO powders. The SEM analysis showed different morphology between the HAp and the HAp sonochemically modified with ZnO as showen in Figure 1. The ZnO crystallite can be observed at the surface of the HAp particles. The size of the ZnO particles depends on the concentration of the Zn-acetate precursor. The antimicrobial test showed a remarkable antimicrobial effect against one of the main dental pathogens, which makes the HAp/ZnO biocomposite a promising material for application in dental therapy [5].

References:

[1] S V Dorozhkin, J Dent Res **1** (2019), p. 024.
[2] I Prada *et al*, Med Oral Patol Oral Cir Bucal **24** (2019), p. 364.
[3] F Heidari *et al*, Int J Appl Ceram Technol **17** (2020), p. 2752.

[4] A Gedanken, Ultrason Sonochem **11** (2004), p. 47.
[5] The authors wish to acknowledge the financial support for this research from the Ministry of Education, Science and Technological Development, Republic of Serbia through the project Contract No. 451-03-68/2022-14/200287, and 451-03-68/2022-14/200135.

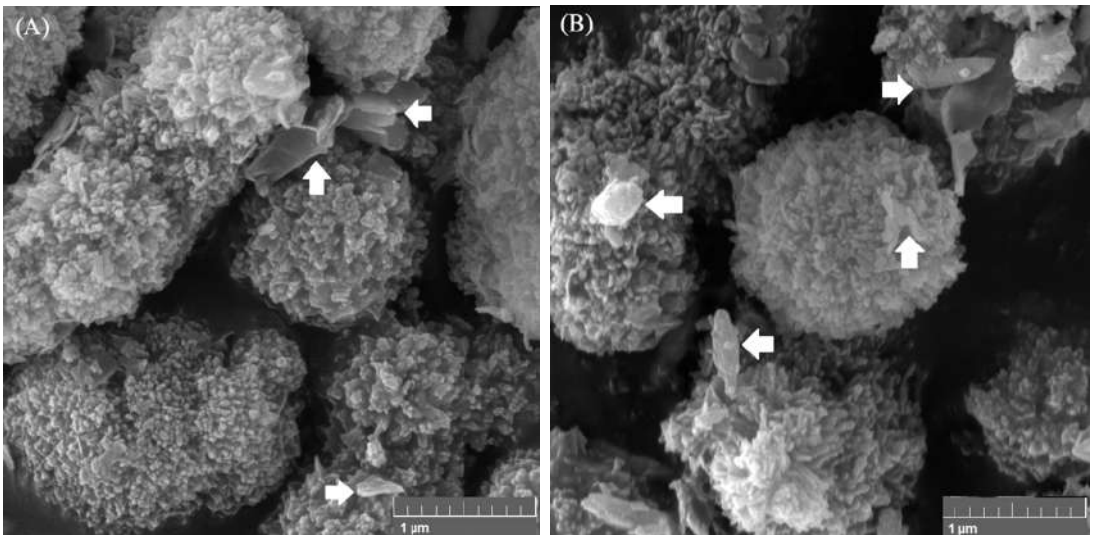

Figure 1. SEM micrographs of the (A) HAp/ZnO 0.3g, and (B) HAp/ZnO 0.6g powders.

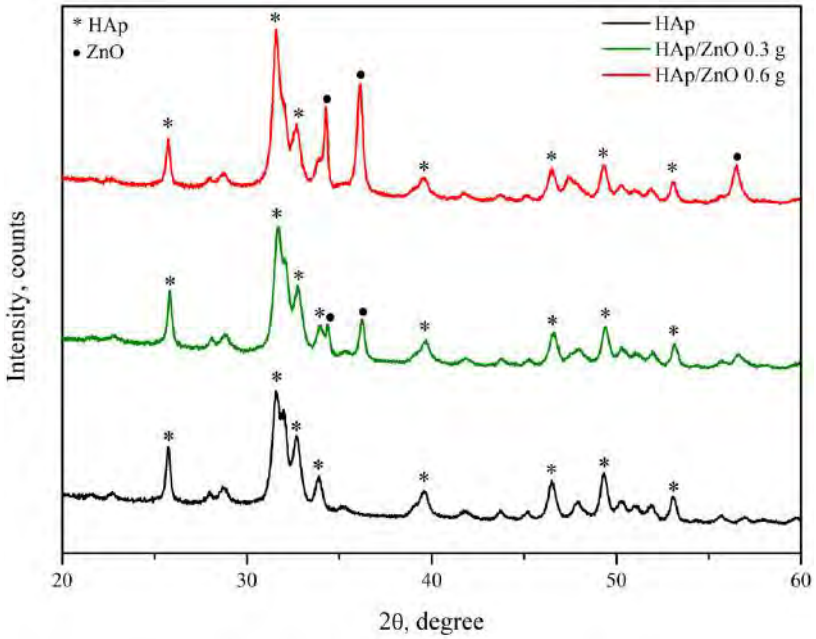

Figure 2. X-ray diffraction patterns of HAp powder, and HAp powders with different amount of Zn-acetate as a precursor.

TEM Study on the Nanostructure Change of Primary Dental Enamel Subjected to Mechanical and Chemical Surface Modifications

Viktória K. Kis[1], Attila Sulyok[1], Máté Hegedűs[2], Noémi Rózsa[3] and Zsolt Kovács[2]

1 Centre for Energy Research, Konkoly-Thege Miklós u. 29-33, H-1121 Budapest, Hungary

2 Department of Materials Physics, Eötvös Loránd University, Pázmány P. st. 1/a, H-1117 Budapest, Hungary

3 Department for Pedodontics and Orthodontics, Semmelweis University, H-1088 Budapest, Szentkirályi u. 47, Budapest, Hungary

Dental enamel is a hard tissue built up from hierarchically organized tightly spaced hydroxyapatite nanocrystallines. This special biological material exhibits crack resistance and fracture toughness while it withstands large compression and shear forces during grinding and biting in chemically reactive environment.

Chemical surface modification, i.e., Mg ion exchange experiments, using $MgCl_2$ solution applied on the outer surface of sound primary molars. Nanoindentation tests were performed on the cross-section and on both treated and untreated enamel surface to map mechanical properties. Surface magnesium incorporation increased enamel strength according to nanohardness change of up to 20%. Based on high resolution transmission electron microscopy (TEM) of the Mg-exchanged dental enamel, a poorly ordered surface layer of approximately 10–15 nanometer thickness was identified. For quantification of the compositional change of dental enamel surface X-ray photo electron spectroscopy (XPS) was applied. This surface sensitive method provides compositional information on the uppermost few nanometers thick layer of the sample from the measured area which spans 3 and 5 mm laterally. XPS spectra were recorded after repeated Ar ion sputtering stages to reveal the in-depth distribution of components. Based on XPS measurements, the ion exchanged layer is strongly enriched in Mg and has non-apatitic composition. Below the surface layer, the Mg content increased only moderately (up to ~3 at%) and the apatite crystal structure of enamel was preserved [1].

Arrangement of nanocrystals was studied in the deformation zone affected by stresses field of nanoindentation imprint using TEM. The cross-section of an imprint was prepared by focused ion beam milling for TEM investigations. High resolution imaging and Fast Fourier Transforms (FFT) made from 15x15 nm areas near the surface layer revealed structural changes as function of distance from enamel surface. Strong fragmentation and loss of texture was observed in this mechanically modified surface layer in both the ion exchanged and untreated dental enamel [2].

References:

[1] VK Kis, A Sulyok, M Hegedűs, I Kovács, N Rózsa and Z Kovács, Acta Biomaterialia **120** (2021), p. 104.

[2] Financial support was provided by the National Research, Development and Innovation Fund Office, Hungary, grant number K-125000. Electron microscopy and FIB facility at Centre for Energy Research was granted by the European Structural and Investment Funds, grant no.s VEKOP-2.3.3-15-2016-00002 and VEKOP-2.3.2-16-2016-00011, respectively.

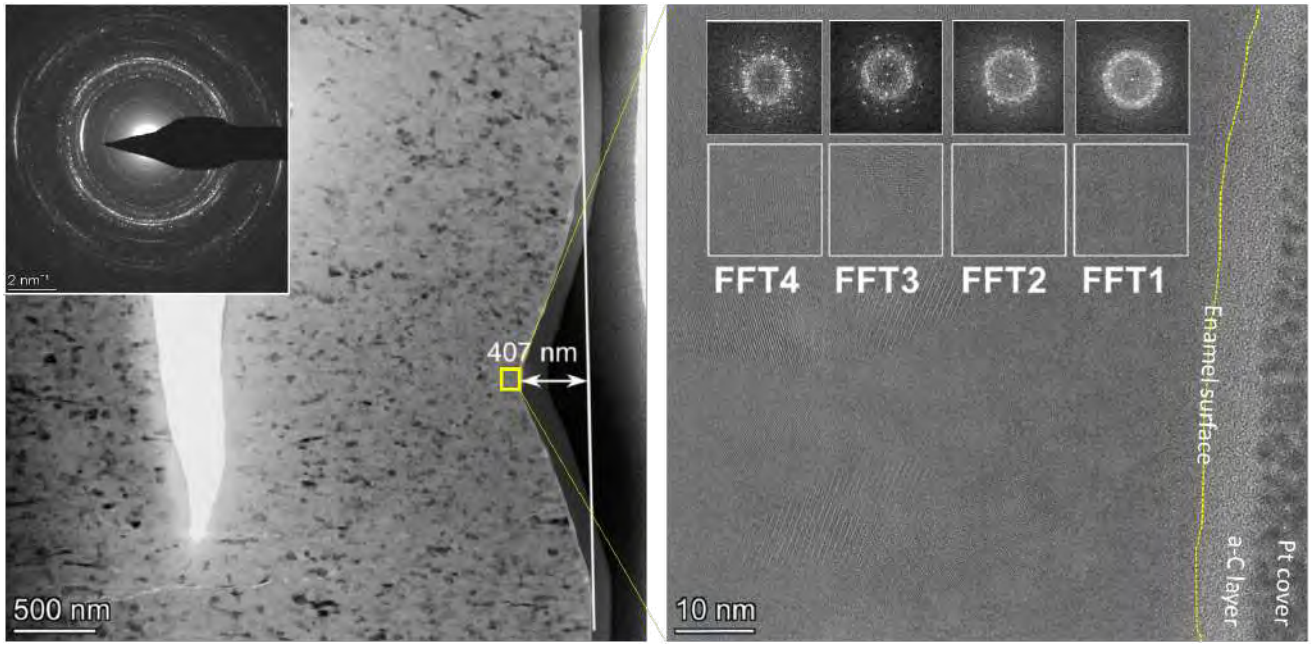

Figure 1: (left) Transmission electron microscopy image of the cross section of a nanoindentation imprint in primary dental enamel together with its selected area electron diffraction pattern. (right) High resolution transmission electron microscopy image of the area indicated with yellow box on the left low-resolution image. Fast Fourier transforms made from 15x15 nm areas allow to follow structural change as function of distance from enamel surface.

Synthesis of Silica Fibers from Natural Asbestos by Acid Leaching Procedure

Branko Matović[1], Jelena Maletaškić[1], Nadežda Radmilović[1], Nina Daneu[2], Biljana Babić[1], Jelena Ercić[1], Milovan Stoiljković[1]

1 Vinča Institute of Nuclear Sciences, National Institute of Republic of Serbia, University of Belgrade, Belgrade, Serbia

2 Department for Nanostructured Materials, Jozef Stefan Institute, Ljubljana, Slovenia

Nanofibrous silica with a high surface area was produced from chrysotile by the acid-leaching method. Natural mineral chrysotile asbestos from Stragari, Korlace in Serbia was used as the starting material. The fibers were modified by chemical treatment with 1M HCl and the mineral dissolution was monitored by transmission electron microscopy, X-ray powder diffraction, inductively coupled plasma spectrometry and low-temperature nitrogen adsorption techniques in order to highlight the effects of the leaching process. The results showed that the applied concentration of acid solution and processing time of 4 h were sufficient to effectively remove the magnesium hydroxide layer and transform the crystal structure of the hazardous starting chrysotile to porous SiO_2 nanofibers. According to the IUPAC classification the isotherms are of type IV and have a hysteresis loop associated with mesoporous materials. In all samples the shape of the hysteresis loop is type H4 which indicates narrow, slit pores. The relatively high adsorption of nitrogen at a low relative pressure indicates the presence of a significant number of micropores in the samples. With prolonged acid leaching, the specific surface area, SBET, calculated by BET equation, was increased from 147 up to 435 $m^2 g^{-1}$, with micropores representing a significant part of the specific surface.

The XRD pattern of the starting material displays only reflections characteristic for crystalline chrysotile [1]. XRD patterns of the acid-leached samples with higher HCl concentrations of 1M and 2M reveal only a slightly higher degree of structural decomposition. For example, in the sample treated with 2 M HCl for 4h, the trace of the (002) peak is no longer observed. However, according to the XRD analyses, it appears that the HCl concentration is less important for the structural decomposition of the chrysotile than the treatment time. The lowest HCl concentration of 0.5 M was sufficient for the amorphization of the initially crystalline chrysotile fibers and the process was not significantly accelerated for higher concentrations of HCl.

FT-IR spectra of the samples that were leached for 4 h at all acid concentration and IR bands were recorded at 425, 570, 790, 965 and 1060 cm^{-1}. The IR bands at 3390 cm^{-1} and 1645 cm^{-1} are due, respectively, to the stretching and bending vibrations of H_2O molecules absorbed by the material. Band intensity gradually decreased with leaching process. This hydroxyl band at 3390 cm^{-1} according to some authors [2] is bonded to trivalent cations (Al^{3+} or Fe^{3+}) in the octahedral layer. On the other hand, the decreasing of band intensity can be related to the dehydroxylation process and indicates that a little water remained in the samples [3]. The characteristic asymmetric stretching vibrations of Si-O-Si bonds are shown by the IR band at 1060 cm^{-1} whilst their symmetric stretching vibrations are shown by the band at 790cm^{-1}. This can be attributed to amorphous silica and can be direct result of leaching [4]. The IR band at 965 cm^{-1} can be assigned to Si-OH stretching vibrations and the IR bands at 570 and 425 cm^{-1} are due to O-Si-O bending vibrations.

The TEM images [5] showed that the inner diameter of the nanotubes is about 8 nm (mesopores) which means that micropores are present in the walls of nanotubes (Fig. 1).

References:

[1] R. T Downs. M. Hall-Wallace, American Mineralogist, **88** (2003), p.:247-250.
[2] J. Lu, M. Liong J. I. Zink, *et. al,* Small **3** (2007), p.1341–1346.
[3] C. Jiang, Y. Zhang, O. Wang O, *et. al*, (2013) Journal of Applied Polymer Science, **129** (2013), p. 2959-2965.
[4] L. Wang, A. Lu, C. Wang *et. al*, Journal of Colloid Interface and Science (2006) **295**, p:436–439.
[5] K. Yada. Acta Crystallographica Section A **27** (1971), p.:659-664.
[6] This project was financially supported by the Ministry of Education and Science of Serbia (Project no. III 45012) This work has been enabled through the Slovenian-Serbian bilateral collaboration under the project No. BI-RS/12-13-019: Minerals as precursors for advanced technologies.

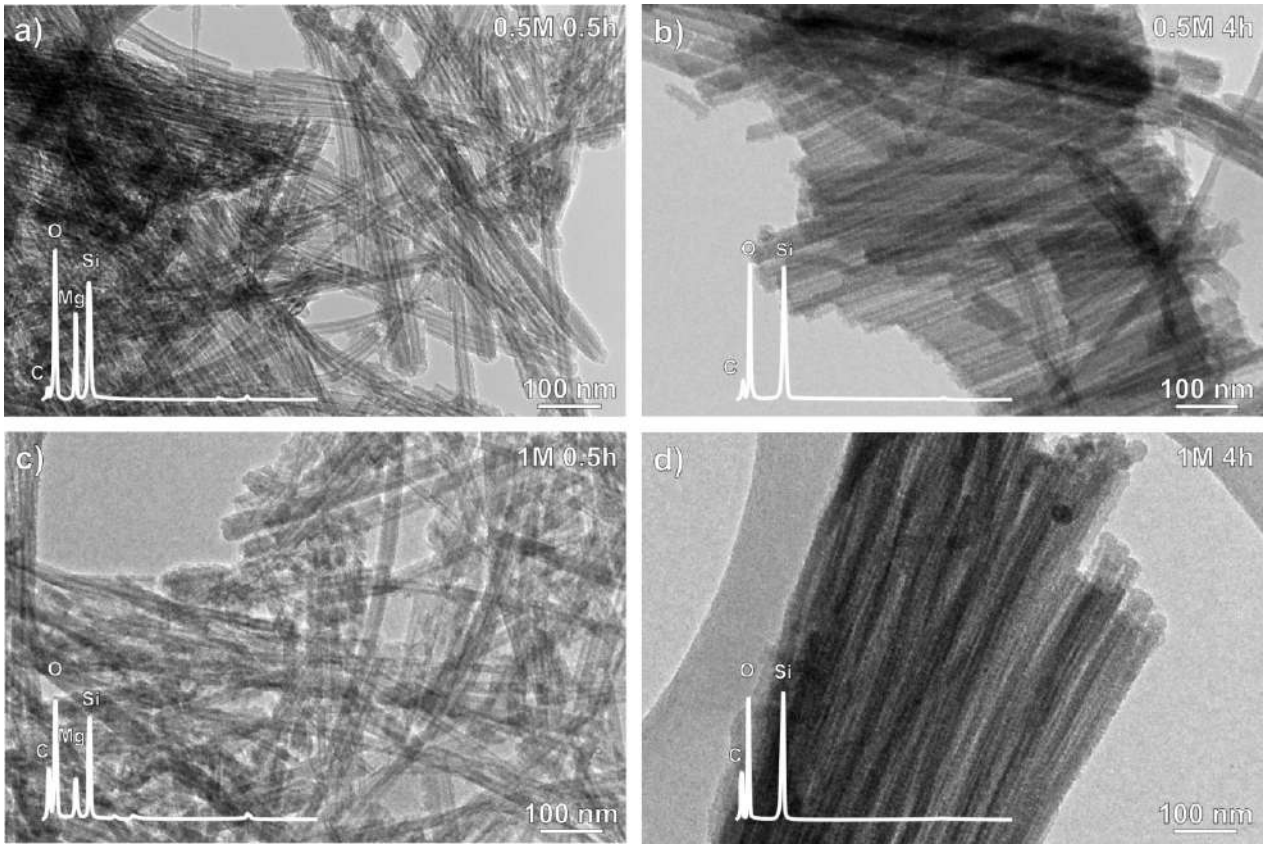

Figure 1. TEM/EDS image of chrysotile samples treated with HCl. a, c) Samples treated for 0.5 h with 0.5 M and 1 M HCl is presented with the single fibers with the presence of Mg. b, d) Samples treated for 4 h with the HCl of different molarity (0.5 and 1 M) show presence of SiO_2 attached fibers.

Effect of concentration pigment particles on microstructure of the metal matrix copper composite coatings

Ivana Mladenović[1], Nebojša D. Nikolić[1], Jelena Lamovec[2], Dana Vasiljević Radović[1] and Vesna Radojević[3]

1 University of Belgrade, Institute of Chemistry, Technology and Metallurgy, Njegoševa 12, Belgrade, Serbia

2 University of Criminal Investigation and Police Studies,Cara Dušana 196, Belgrade, Serbia

3 Faculty of Technology and Metallurgy, University of Belgrade, Karnegijeva 4, Belgrade, Serbia

Copper electrodeposits are widely used for many engineering applications due to their physical, electrical and mechanical properties such as eco-friendly synthesis, corrosion resistance, excellent electrical and thermal conductivity, good chemical selectivity and mechanical features [1,2]. However the need for functional and decorative coatings motivates this research to explore possibilities of future develop the electrochemically synthesis of copper with incorporating pigments particles to produce copper matrix reinforced coatings with different surface appearance (color and brightness) or better mechanical properties [3]. This research focuses on the synthesis and characterization of composite coatings via electrochemical route with co-deposition pigments. For that reason, the effect of adding yellow green phosphorescent pigment on microstructural evaluation of the Cu/pigment composite systems has been investigated.

The copper coatings produced from the basic sulfate electrolyte without or with different content of phosphorescent pigment particles were characterized by Scanning Electron Microscope (SEM) and Atomic Force Microscope (AFM). Thin metal matrix composite coatings were prepared by galvanostatic electrodeposition technique with the assistance of magnetic stirring of electrolyte (DC/MS regime) on the brass substrate. The basic sulfate electrolyte consisted of: 240 g L^{-1} $CuSO_4 \cdot 5 H_2O$ in 60 g L^{-1} H_2SO_4. The particles of phosphorescent pigment (Sennelier Paint Pigment Phosphoyellow green, France) were added into the basic sulfate electrolyte. Five different particle concentrations were used: 0.25; 0.5; 1; 1.5 and 3 g particles in 100 ml basic electrolyte.

The morphology of the deposited copper coatings without and with pigment particles and cross-section analysis are given at Figure 1. Top surface and cross-section SEM images confirmed the co-deposition of pigment particles within the metal copper matrix throughout the entire coating thickness. It was also confirmed that the presence of particles in the sulfate electrolyte drastically changes the topography of the obtained coatings, via a change in micro roughness. The topographic analysis and micro roughness of coatings (according to an average absolute roughness parameter, R_a) were given at Figure 2. Roughness is evidently reduced to some critical concentration of pigment particles in the electrolyte (up to 1 g), and then increases due to a formation of agglomerates at higher concentrations of the particles. Therefore, the critical particle concentration in the electrolyte should be taken into account [4].

References:
[1] A O Konakov *et al*, Surfaces and Interfaces, In Press, (2022), p. 102054.
[2] E Delbos *et al*, Microelectron. Eng.**87** (2010), p. 514.
[3] N K Shrestha and T Saji, J. Jpn. Soc. Colour Mater.**73** (2000), p. 227.
[4] The authors acknowledge funding from the Ministry of Education, Science and Technological Development of Serbia (Grants No. 451-03-68/2022-14/200026 and 451-03-68/2022-14/200135).

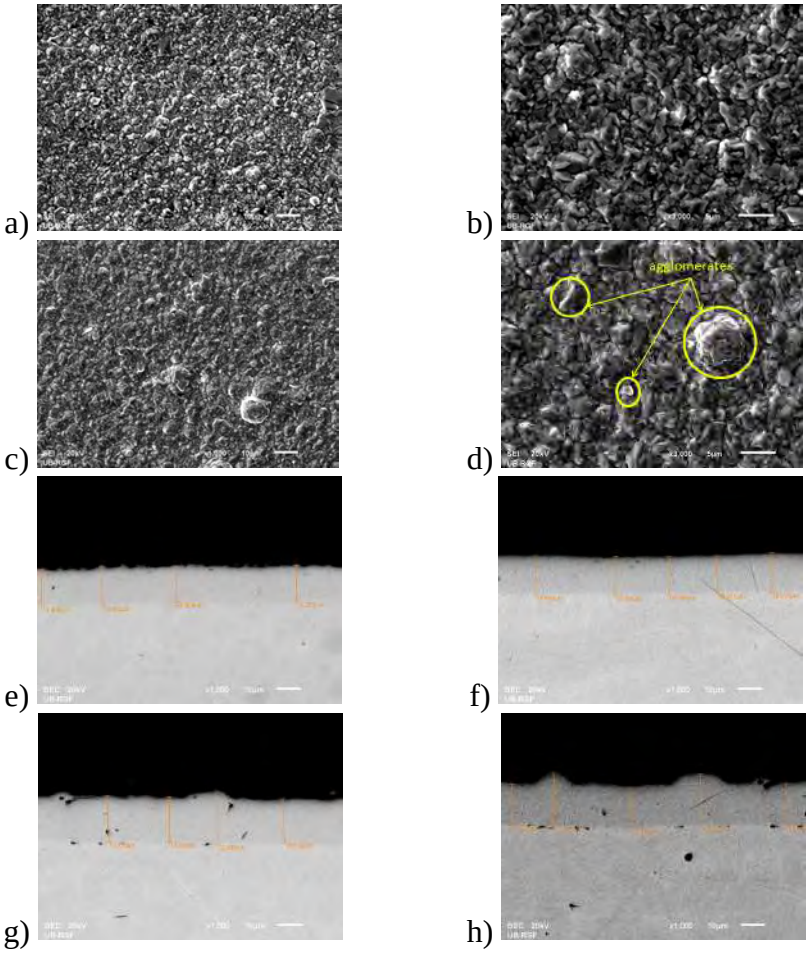

Figure 1. SEM micrographs on top side of Cu coatings: a) and b) without pigment particles, ×1000 (a) and ×3000 (b); c) and d) with 0.25 g pigment particles, ×1000 (c) and ×3000 (d). Cross-section views: e) Cu+0.25 g, f) Cu+1 g, g) Cu+1.5 g and h) Cu+3 g of pigment particles, ×1000. The particles are added to 100 mL the basic sulfate electrolyte.

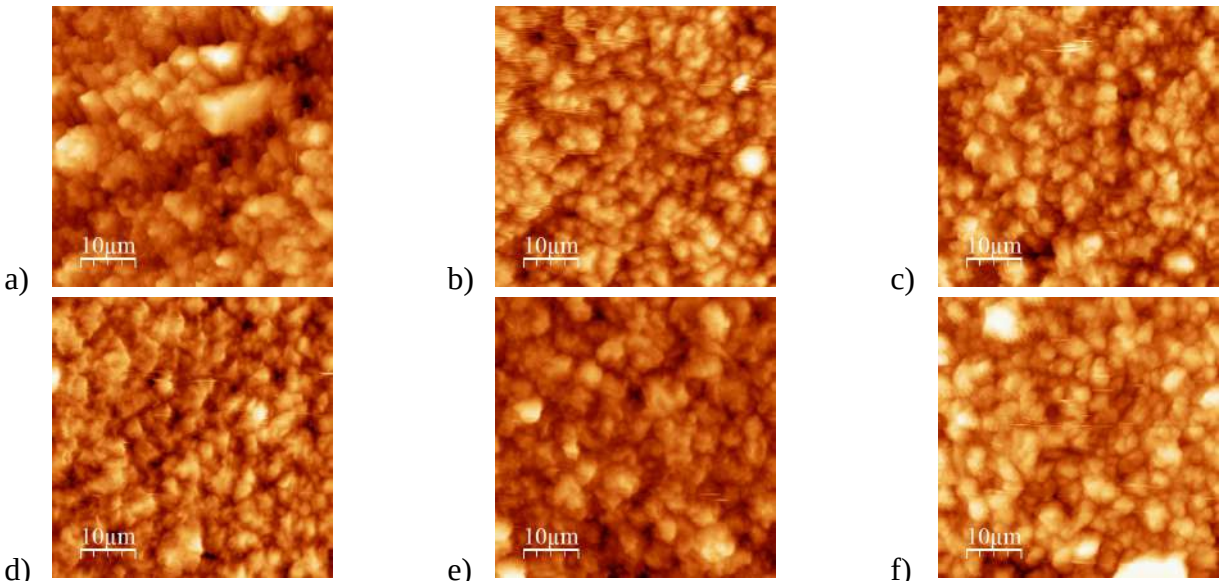

Figure 2. AFM analysis on top side of Cu coatings with included roughness values: a) without pigment particles (R_a = 280.8 nm), b) Cu+0.25 g (R_a = 246.1 nm), c) Cu+0.5 g (R_a = 221.7 nm), d) Cu+1.0 g (R_a = 213.6 nm), e) Cu+1.5 g (R_a = 230.3 nm) and f) Cu+3 g (R_a = 251.4 nm) of pigment particles. The particles are added to 100 mL the basic sulfate electrolyte.

The Microstructure Evolution of AA6026 Al-Mg-Si alloy during Homogenization

Tamara Radetić and Miljana Popović

University of Belgrade, Faculty of Technology and Metallurgy, Belgrade, Serbia

Wrought Al-Mg-Si alloys (6xxx series) are widely used in the construction and transportation industries as well as for electric parts due to the excellent combination of properties such as strength-to-weight ratio, formability, machinability, corrosion resistance, and weldability [1]. In order to improve the extrudability and final properties of the material, the homogenization treatment of as-cast alloys is necessary before further processing. The selection of homogenization parameters depends very much on the as-cast microstructure and the chemistry of the alloy. In addition to the main alloying elements, Mg and Si, the alloys usually contain minor alloying elements and impurities such as Mn, Cr, Cu, Zn, and Fe. In this study, we investigated the effects of homogenization temperature on phase transitions, dissolution, and precipitation reactions in AA6026 alloy.

One of the key requirements for a successful homogenization treatment is the transformation of the Fe-bearing microconstituents with acicular morphology into a stable cubic α-$Al_{15}(Fe,Mn)_3Si_2$ phase with a more benevolent globular morphology [2]. Although there is a number of iron-rich metastable phases [3], it is generally accepted that the as-cast microstructure of wrought Al-Mg-Si alloys mainly consists of a mixture β-Al_5FeSi and stable α-$Al_{15}(Fe,Mn)_3Si_2$ phase. The distinction between phases in a routine characterization is based on morphological characteristics, Fe(Mn)/Si ratio, and lack of manganese in the β-phase. However, in our study, SEM/EDS characterization of over 300 needle-shaped phases, morphology typical of β-Al_5FeSi, showed Fe(Mn)/Si spanning in a range of 0.5-2, and all particles contained Mn in the amount that could not be attributed to the matrix. Elemental mapping in TEM confirmed the presence of manganese in acicular microconstituents (Figure 1) whereas selected area diffraction characterization showed that the acicular microconstituents tend to have the tetragonal crystal structure of the δ-Al_4FeSi_2 phase. This phase, with acicular needle-like morphology, while frequently observed in cast Al-Mg-Si alloys with higher Mg and Si content, has not been reported in wrought Al-Mg-Si alloys. Diffraction also showed that the part of the microconstituents has the cubic crystal structure of the stable α-$Al_{15}(Fe,Mn)_3Si_2$ phase.

Homogenization treatment leads to transformation of acicular microconstituents into globular form, while the extent the transformation increases with homogenization temperature. In addition, precipitation of dispersoids took place during the homogenization treatment. Low-temperature homogenization treatment (480°C) gives rise to precipitation of cubic α-$Al_{15}(Mn, Fe)_3Si_2$ dispersoids and the formation of dispersoid free zones in the vicinity of grain boundaries (Figure 2a). Beside the Mn(Cr),Fe-bearing dispersoids, the second set of particles was observed in the microstructure after high temperature homogenization (550°C). The lath-shaped particles with a longer axis parallel to the $<100>_{Al}$ direction occupied both grain interiors and otherwise dispersoid-free zones (Figure 2b). Despite low Cu content in the studied alloy, the lath-shaped particles appear to be Q'/Q phase [4]. SAD patterns showed characteristic extra reflections near the {110} positions and EDS maps revealed the presence of Cu [5] that is consistent with $Al_{3-5}Cu_{1-2}Mg_{5-9}Si_{4-7}$ stoichiometry of Q-type phases [4]. The temperature range and kinetics of Q-phase precipitation in Al-Mg-Si alloys are not well studied, but the results of STEM imaging and elemental mapping [5] showed that the lath-like particles in grain interior were frequently enclosed or attached to a-Al(Mn,Fe)Si dispersoids indicating that Mn(Cr,Fe)-bearing dispersoids act as nucleation sites for precipitation of the Q-phase.

References:

[1] T. Sheppard in “Extrusion of Aluminium Alloys”, (Kluwer Academic Publishers, Dordrecht/Boston/London) 1999.
[2] N. C. W. Kuijpers et al., Mater. Sci. Eng. A 394 (2005), p. 9.
[3] J. Yu, PhD thesis (Technischen Universität Berlin, Berlin) 2016.
[4] D .J. Chakrabarti, D. E. Laughlin, Prog. Mater. Sci. 49 (2004), p. 389.
[5] T. Radetic et al., J. Alloy. Compd. 902 (2022), 163719
[6] This work was supported by Ministry of Education, Science and Technological Development of the Republic of Serbia under contract No. 451-03-68/2022-14/200135.

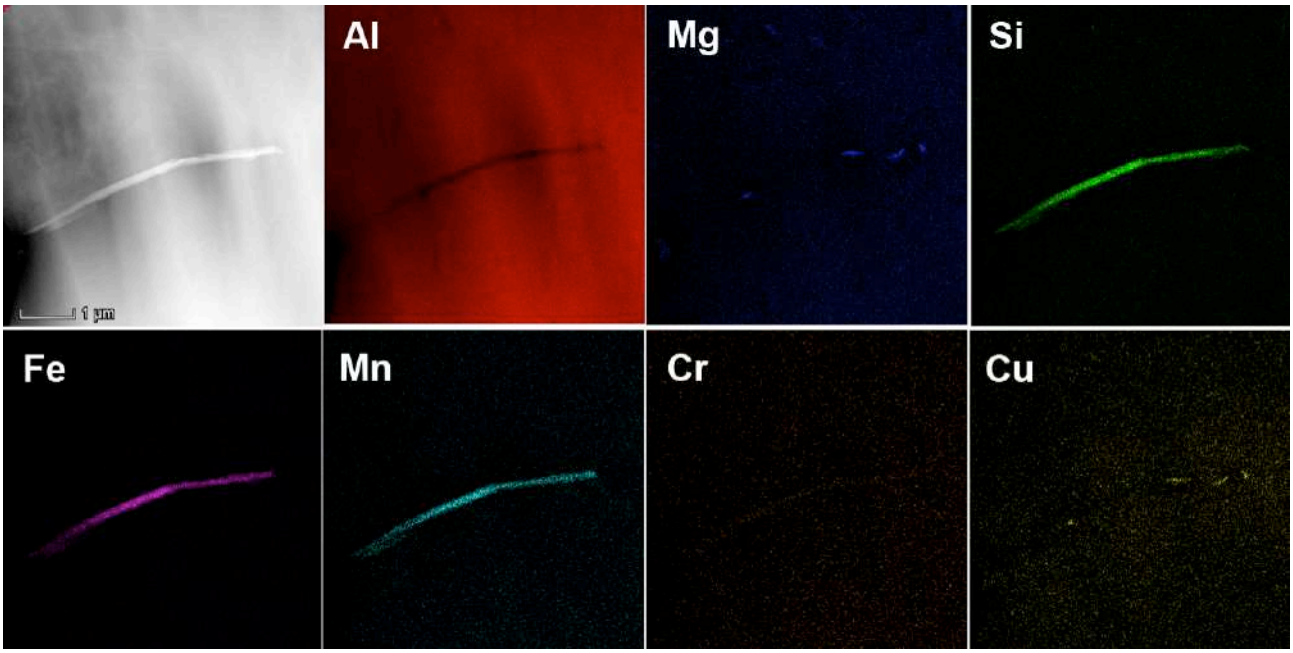

Figure 1. STEM image and EDS elemental maps of the needle-like microconstituent in as-cast state.

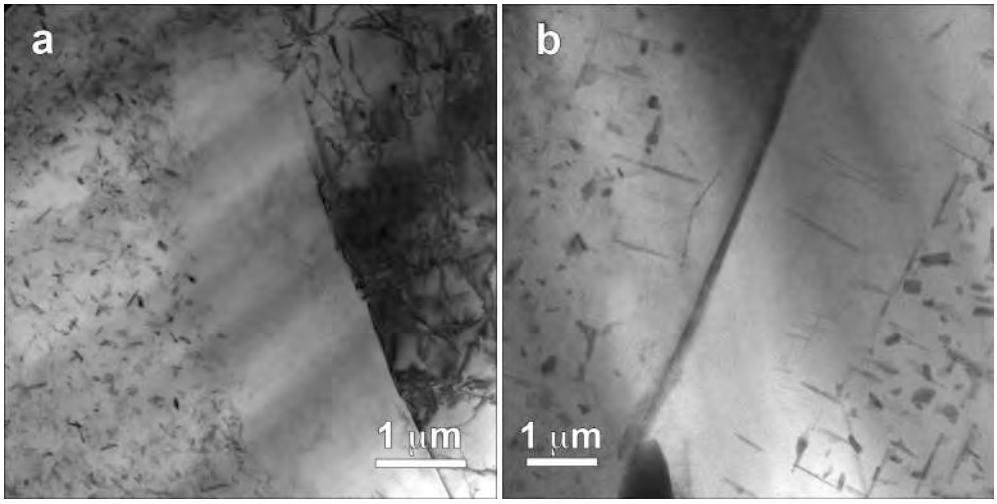

Figure 2. Bright field TEM micrographs of grain boundary regions after homogenization at (a) 480°C/12h and (b) 550°C/6h.

Microstructural study of hematite formation during extraction of valuable metals from Jarosite PbAg sludge

Nataša Gajić[1], Željko Kamberović [2], Marija Korać[2], Milisav Ranitović[1], Vaso Manojlović[2]

1 Innovation Center of the Faculty of Technology and Metallurgy in Belgrade Ltd, University of Belgrade, Karnegijeva 4, 11120 Belgrade, Serbia.

2 Faculty of Technology and Metallurgy, University of Belgrade, Karnegijeva 4, 11120 Belgrade, Serbia.

Jarosite is generated as hazardous waste during hydrometallurgical production of zinc. Jarosite-type compounds ($NH_4Fe_3(SO_4)_2(OH)_6$) in addition to iron, contain a high concentration of valuables (Zn, Cu, and In) and toxic (Pb, Cd, and Cr) elements which are now disposed at landfills. The examination process for his treatment involved the roasting followed by the water leaching process for the extraction of valuable metals. Through the process of its roasting, iron is transformed into insoluble hematite, valuable metals into water-soluble sulfates, while anglesite remains water-insoluble.

The goal of this study was to characterize the chemical and microstructural properties of products generated during the roasting process of Jarosite PbAg sludge to extract valuable metals.

Changes in the chemical and microstructure were analyzed using different analytical methods, including X-ray fluorescence (XRF), X-ray diffraction (XRD), scanning electron microscopy (SEM) equipped with energy dispersive spectrometry (EDS), and thermogravimetric–differential thermogravimetric–differential scanning calorimetry (TG-DTG-DSC) analysis.

The thermogravimetric curve (TGA) shows three segments, which indicate that the degradation of jarosite occurs in three steps. In the range of 520-750 °C (DTG maximum at 625 °C), sulfates and sulfites decompose straightforwardly and proceed by the evolution of SO_3 (SO_2+O_2); hematite is formed from mikasait. Two minima (420.1 and 625.9 °C) are observed on the DSC curve, which indicates that the process of jarosite decomposition is endothermic (Figure 1).

From images of SEM, it was determined that both the non-treated jarosite in the form of small crystals collected in groups, and anglesite occurring in the form of tabular and prismatic rhombohedral shapes (Figure 2a) remained morphologically and structurally unchanged by roasting at 550°C (Figure 2b). However, after its roasting at 730°C hexagonal hematite grains are dominated zonally distributed (Figure 2c).

The results obtained by SEM analysis are supported by X-ray diffraction results showed in addition to anglesite, hematite and zincosite the presence of mikasait and jarosite, in the sample roasted at 550°C (Figure 3b), opposite to the sample roasted at higher temperatures without the presence of these two phases. This proves that the complete transformation of jarosite PbAg sludge is not possible at lower temperatures than 730°C (Figure 3a).

According to the all obtained results, it was found that insoluble hematite and anglesite, and water-soluble sulfates from Jarosite PbAg sludge can be obtained by roasting at 730°C, followed by a leaching process. Such a processing route leads to the successful extraction of valuable metals.

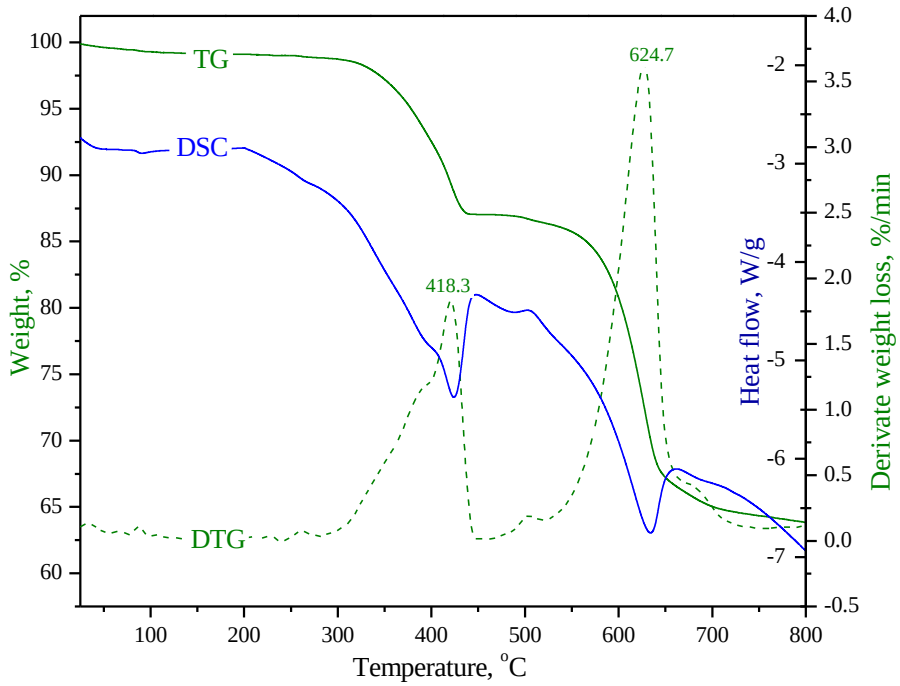

Figure 1. TG-DSC-DTG curves of Jarosite PbAg sludge decomposition.

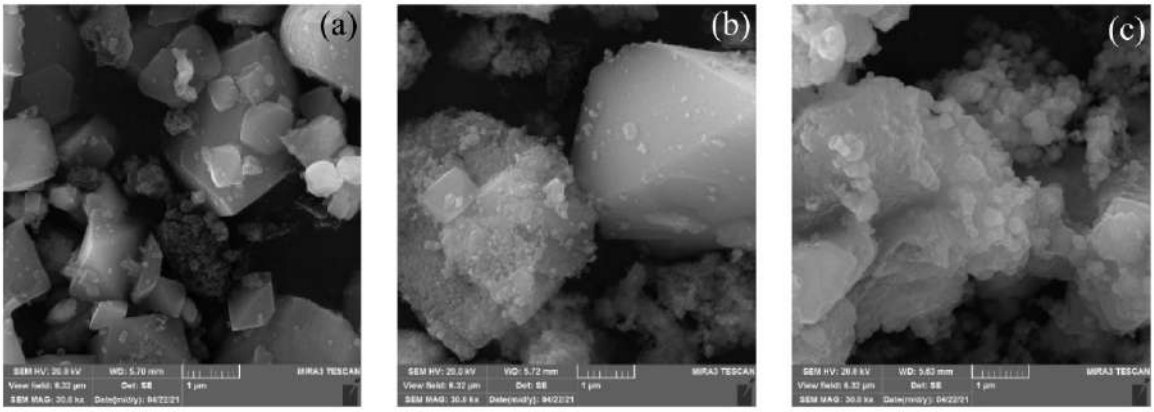

Figure 2. SEM images of the (a) non-treated Jarosite PbAg sludge, roasted sample at (b) 550°C and (c) 730°C.

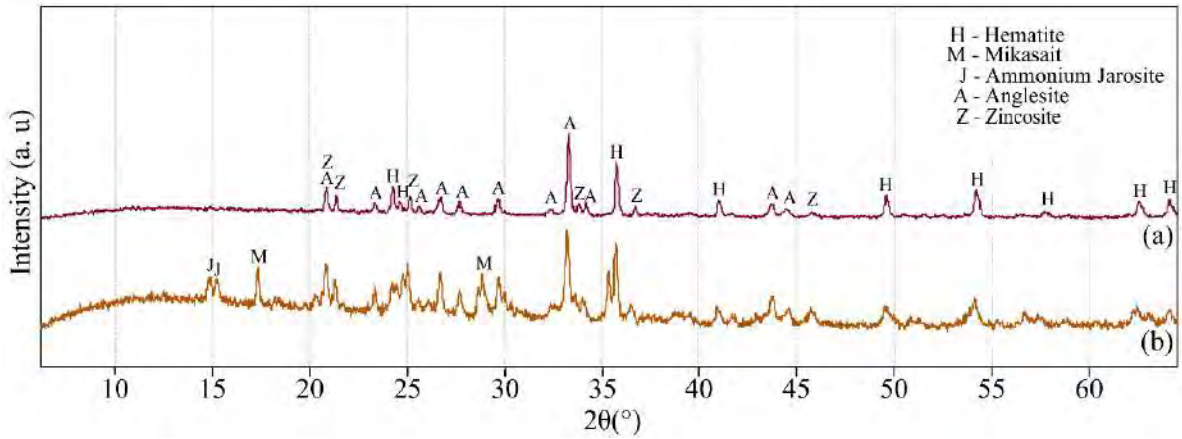

Figure 3. XRD patterns of the roasted samples at different temperatures: (a) 730°C and (b) 550°C.

Detecting the Changes on Fibers' Surfaces after Different Chemical Treatments using Scanning Electron Microscopy

Aleksandra Ivanovska[1], Mirjana Kostić[2]

1 University of Belgrade, Innovation Center of the Faculty of Technology and Metallurgy, Department for Textile Engineering, Belgrade, Serbia.

2 University of Belgrade, Faculty of Technology and Metallurgy, Department for Textile Engineering, Belgrade, Serbia.

In the last decade, jute fibers are within the scope of a wide variety of investigations thanks to their possibility for functionalization by using different chemical treatments. Among them, alkali and oxidative treatments represent the most direct, simplest, economical, and efficient methods for fibers' functionalization and therefore for improving their quality [1]. Namely, alkali treatments using sodium hydroxide lead to selective hemicellulose removal, increased the content of cellulose exposed on the fiber surface, and decreased the crystallinity index, while oxidation using sodium chlorite is used to selectively remove lignin that is accompanied by conversion of fiber carbonyl to carboxyl groups. After both chemical treatments, scanning electron microscopy (SEM) was employed to confirm the removal of the non-cellulosic components and to evaluate the changes in jute fiber surface morphology.

As can be seen from Figure 1a, the surface of multicellular raw jute fiber is uneven and rough and covered with fats, waxes, and pectin. It has to be noted that elementary fibers within the raw jute fiber cannot be seen since they are joined together into bundles by the hemicelluloses and lignin. By observing the SEM photographs of the fibers after hemicellulose or lignin removal, some changes in the fiber surface morphology can be spotted. More precisely, after the alkali treatments under different experimental conditions (sodium hydroxide concentration and/or treatment duration), the fibers' surfaces are relatively clean and smooth (Figures 1b and c) indicating the removal of the hemicelluloses and other non-cellulosic components located on the fibers' surfaces. As a consequence, new free spaces in the fiber structure were created, which is followed by pronounced elementary fibers' liberation, as is evident in Figures 1b and c [2]. In the case of the most severe alkali treatment (17% NaOH for 45 min, Figure 1d), the multi-cellular fiber structure is clearly visible as well as some of the elementary fibers stick out away from the fiber bundles [3]. The changes in the fiber surface morphology are also evident after the oxidative treatments using 0.7% sodium chlorite. Significant lignin removal and elementary liberation were observed after the oxidation for 90 min, Figure 1d.

The applied alkali and oxidative treatments are an appropriate starting point for obtaining multifunctional fibers. For example, to improve the jute fibers' dielectric properties, *in situ* synthesis of Cu-based nanoparticles (NPs) could be performed on the alkali and oxidatively modified fibers' surfaces [4]. Besides different characterization methods, SEM is usually used to confirm the presence of NPs on fibers' surfaces. A few smaller agglomerates of Cu-based NPs were observed across the surface of alkali treated fiber, while smaller irregularly shaped and larger agglomerates of Cu-based NPs (along with a low amount of fiber impurities) were distributed over the oxidatively treated fibers surface, Figure 2 [5].

References:

[1] A Ivanovska *et al*, Cellulose **26** (2019), p. 5133.
[2] A Ivanovska *et al*, Industrial Crops and Products **140** (2019), p. 111632.
[3] A Ivanovska *et al*, Industrial Crops and Products **171** (2021), p. 113913.
[4] A Ivanovska *et al*, Industrial Crops and Products **180** (2022), p. 114792.
[5] The authors acknowledge funding from the Ministry of Education, Science and Technological Development of the Republic of Serbia (Contract No. 451-03-68/2022-14/200287 and 451-03-68/2022-14/200135).

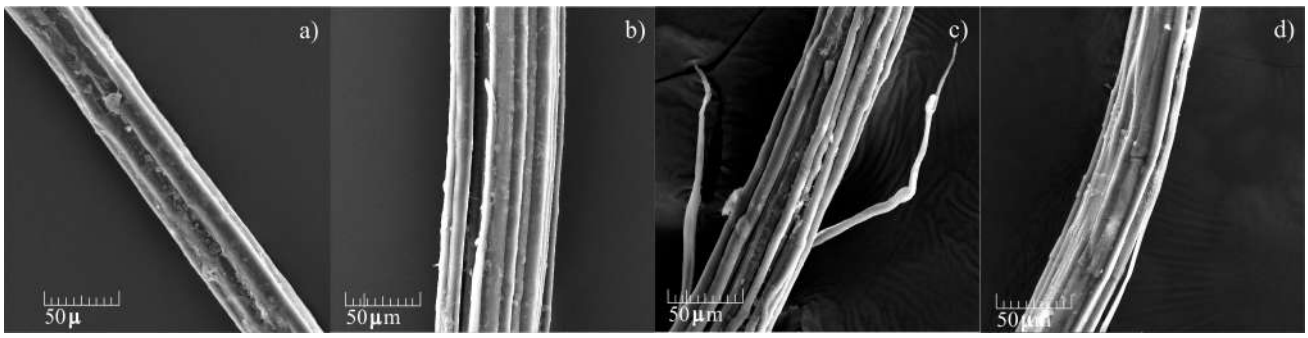

Figure 1. SEM photographs of: a) raw jute fiber, and fibers treated with: b) 5% NaOH for 10 min, c) 17.5% NaOH for 45 min, and e) 0.7% $NaClO_2$ for 90 min.

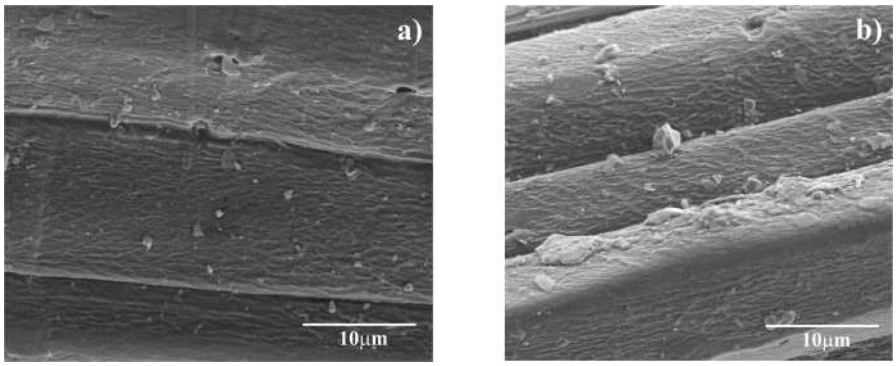

Figure 2. SEM photographs of fibers treated with: a) 17.5% NaOH for 30 min, and b) 0.7% $NaClO_2$ and coated with Cu-based NPs.

Gain the maximum throughput with artifact-free surfaces for sample characterization by using high current plasma FIB-SEM

Martin Suchanek

TESCAN ORSAY HOLDING, a.s.

The standard procedure for preparing cross sections using the FIB-SEM technique is to use high currents to remove material quickly, then reduce the FIB current to obtain better beam profile and consequently, a better quality for the final surface. Reducing the maximum current used for final polishing of the section surface, however, results in a longer preparation process. For small cross sections with sizes in the tens of μm, this current reduction method is acceptable. However, as the size of the cross-sectional area to be polished increases, the analysis time increases substantially; therefore, this method is not suitable for preparing cross sections with sizes in the hundreds of μm. To overcome this limitation for large cross sections, plasma FIB was introduced to deliver higher beam currents than those achievable with conventional Ga FIB-SEMs.

Plasma FIB-SEM provides several advantages for sample characterization. First, its high current ion beam is capable of high material sputtering rates which enables efficient preparation of large trenches or cross sections. Plasma FIB also can be used for polishing large surface areas, thereby enhancing sample features and providing more detailed contextual information about structure and composition about the sample. This can help to reveal material distribution, obtain better statistical information, and link the microscale to the nanoscale sample characterization.

Several technologies have been introduced that improve the implementation of high current plasma FIB for large scale materials characterization. In this webinar, we will walk through the typical plasma FIB cross-sectioning workflow and discuss high current polishing methods. We will present TESCAN's TRUE X-Sectioning TESCAN Rocking Stage, which were developed to suppress artifacts and improve the final cross section surface quality when using high beam currents for final polishing. Finally, we will show how plasma FIB-SEM speeds not only cross section preparation, but also enables a greater understanding of your materials by improving 3D FIB-SEM tomography analyses.

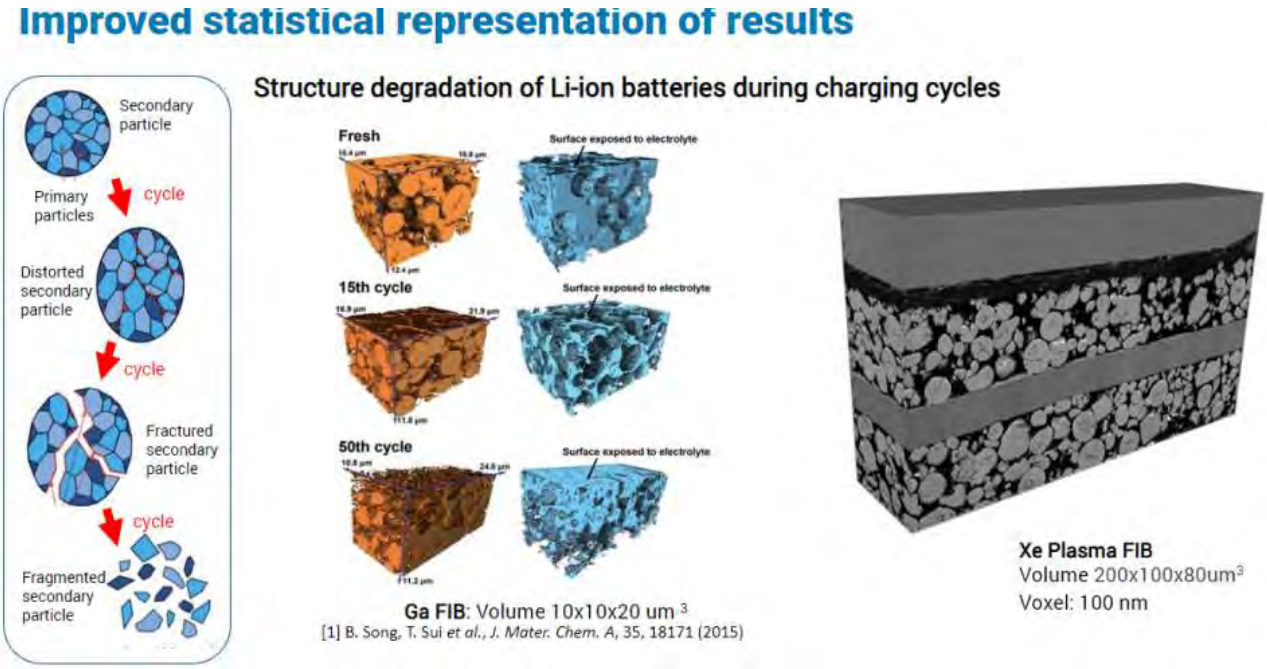

Figure 1. Structure degradation of Li-ion batteries during charging cycles.

Mesoporous Carbon Nanofibers and Spinel Oxide Nanocomposites for Energy Storage Applications

Daniel M. Mijailović[1], Vuk V. Radmilović[2], Uroš Č. Lačnjevac[3], Dušica B. Stojanović[2], Vladimir D. Jović[3], Velimir R. Radmilović[2,4] and Petar S. Uskoković[2]

1 University of Belgrade, Innovation Center, Faculty of Technology and Metallurgy, Karnegijeva 4, 11120, Belgrade, Serbia

2 University of Belgrade, Faculty of Technology and Metallurgy, Karnegijeva 4, 11120, Belgrade, Serbia

3 University of Belgrade, Institute for Multidisciplinary Research, Kneza Višeslava 1, 11030 Belgrade, Serbia

4 Serbian Academy of Sciences and Arts, Knez Mihailova 35, 11000 Belgrade, Serbia

In order to achieve the transition from energy systems that are based on fossil fuels to ones powered by clean and renewable energy on a global scale, it is mandatory to significantly improve the energy storage. Electrochemical energy storage devices with fast charging and long cycle lifetime will play very important role in this forthcoming energy revolution. Devices that fit these demands are supercapacitors, also knows as electrochemical capacitors, which can be fully charged within minutes, with almost unlimited cyclability. However, the main challenge of this technology is their low energy density, which varies from 5 to 8 Wh kg^{-1}, and 7 to 10 Wh L^{-1}. The performance of supercapacitors is determined by electrode materials which can drastically affect the capacitance and energy density in the appropriate voltage range and that is the main reason why high–rate materials are broadly explored [1,2].

Mesoporous materials based on carbon nanofibers and transition metal oxides have been produced by facile and advanced processing method. Scanning electron microscopy (SEM) analysis confirmed the formation of composite nanofibers with spinel nanocrystals deposited on the surface. The phase composition of cobalt/managenese spinel oxides, with an estimated diameter of about 13 to 60 nm, has been successfully controlled by varying the ratio of metal precursors in the electrospinning process. Scanning transmission electron microscopy (STEM) and energy dispersive X-ray spectroscopy (EDS) analysis of composite fibers cross-section revealed the distribution of chemical elements in the mesostructure. Interestingly, STEM–EDS analysis of cross-sections revealed the core-shell structure in which carbon occupies core space inside spinel rings.

Nanocomposites in alkaline electrolyte behave like materials with battery characteristics and have high values of capacity up to 68.5 mAh g^{-1}. By testing these novel self-standing composite electrodes in supercapacitor devices, high capacitance values as high as 384 F g^{-1} were obtained. Moreover, excellent stability was achieved with over 95% of all tested electrodes. The superior energy density of 11.5 Wh kg^{-1} at low potential sweep rates, and the superior power density of 2.6 kW kg^{-1} are comparable to commercially available supercapacitors, which has significant implications for the practical electrical energy storage.

References:

[1] H. Shao *et al.*, Chemical Society Reviews 49 (2020) p. 3005-3039.
[2] P. Simon, Y. Gogotsi, Nature Materials 19 (2020) p. 1151-11633.
[3] The authors acknowledge funding from the Ministry of Education, Science and Technological Development of the Republic of Serbia (Contract no. 451-03-9/2021-14/200135). V. R. Radmilović acknowledges support from the Serbian Academy of Sciences and Arts under project no. F-141.

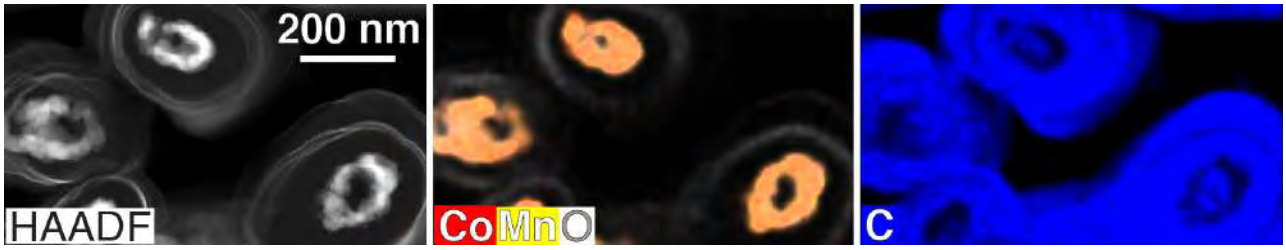

Figure 1. HAADF–STEM–EDS cross-section micrographs of composite nanofibers.

Nickel manganite-carbonized alginate composite for use as energy storage electrodes

Milena Dojcinovic[1], Zorka Vasiljevic[1], Nenad Tadic[2], Matjaz Spreitzer[3], Lazar Rakocevic[4], Maria Vesna Nikolic[1]

1 University of Belgrade, Institute for Multidisciplinary Research, Department for Materials Science, Belgrade, Serbia

2 University of Belgrade, Faculty of Physics, Belgrade, Serbia

3 Jozef Stefan Institute, Ljubljana, Slovenia

4 University of Belgrade, Institute of Nuclear Sciences Vinca, Belgrade, Serbia

High fossil fuel consumption has a negative impact on the environment as it causes pollution and greenhouse effect that is one of the main reasons for global warming. This negative phenomenon adds to rising socioeconomic differences and the limited quantity of fossil fuels available for energy production and they all together cause technology and science to develop other energy production and storage solutions. One of the perspectives is electrical energy production and storage in fuel cells, batteries and supercapacitors. Batteries and supercapacitors store energy via ion intercalation/insertion, redox or capacitive electrochemical processes [1]. Nickel-manganite is a versatile material used in many technology applications. One of the established uses is as a supercapacitor electrode. The advantage of this type of material is the earth abundance of required metals, compared to noble metals, and simplicity of the synthesis methods, along with high redox activity. Metal-oxide battery materials are usually combined with activated carbon to enhance the specific surface area and add to energy storage capacity via surface charge accumulation [1], [2]. Activated carbon is usually made by pyrolytic carbonization of carbon-rich organic compounds such as sodium alginate and subsequent chemical activation.

In the current work, nickel manganite was synthesized via sol-gel combustion synthesis method with glycine as fuel and nitrate ions as oxidizers. Post-combustion amorphous powder was calcined at temperatures between 300 and 800 °C. Powders were structurally characterized via X-ray diffraction crystallography (XRD) and Fourier transform infrared spectroscopy (FTIR). Their morphology was examined with SEM, FESEM and TEM microscopy. Chemical analysis was conducted with X-ray photoelectron spectroscopy (XPS). Results revealed that the samples sintered at 400 and 800 °C are pure cubic spinel nickel manganite with the space group $Fd\bar{3}m$ and partially inverse structure, while materials calcined at the temperatures between 500 and 700 °C consist of perovskite $NiMnO_3$, cubic spinel $NiMn_2O_4$ combined with manganese oxide – Mn_2O_3. FESEM and TEM microscopy revealed nanocrystalline structure with a high agglomeration degree. Selected area electron diffraction (SAED) confirmed XRD analysis. To obtain activated carbon, sodium alginate was carbonized in nitrogen atmosphere. Nickel manganite-carbonized sodium alginate composite was made by carbonizing lyophilized nickel manganite-alginate hydrogel. Obtained materials, including synthesized nickel manganite, carbonized sodium alginate and nickel manganite-carbonized sodium alginate were characterized via FESEM and TEM microscopy, XRD analysis, XPS, and FTIR spectroscopy. Obtained materials were tested as energy storage electrodes in a three electrode cell setup in 6 M KOH aqueous solution as electrolyte. Methods embedded in electrochemical characterization were cyclic voltammetry (CV), electric impedance spectroscopy (EIS) and constant current chronopotentiometry at different current densities to obtain galvanostatic charge-discharge (GCD) curves. Results show considerable charge storage activity, which can be ascribed to oxido-

reduction reactions of manganese ions and charge accumulation on the surface of the activated carbon.

References:

[1] J Liu *et al.*, Advanced Science **5** (2018) p. 1700322.
[2] L Qie *et al.*, Energy & Environmental Science **6** (2013) p. 2497.
[3] The authors acknowledge funding from the Ministry of Education, Science and Technological Development of the Republic of Serbia, contract number 45103-68/2022-14/200053.

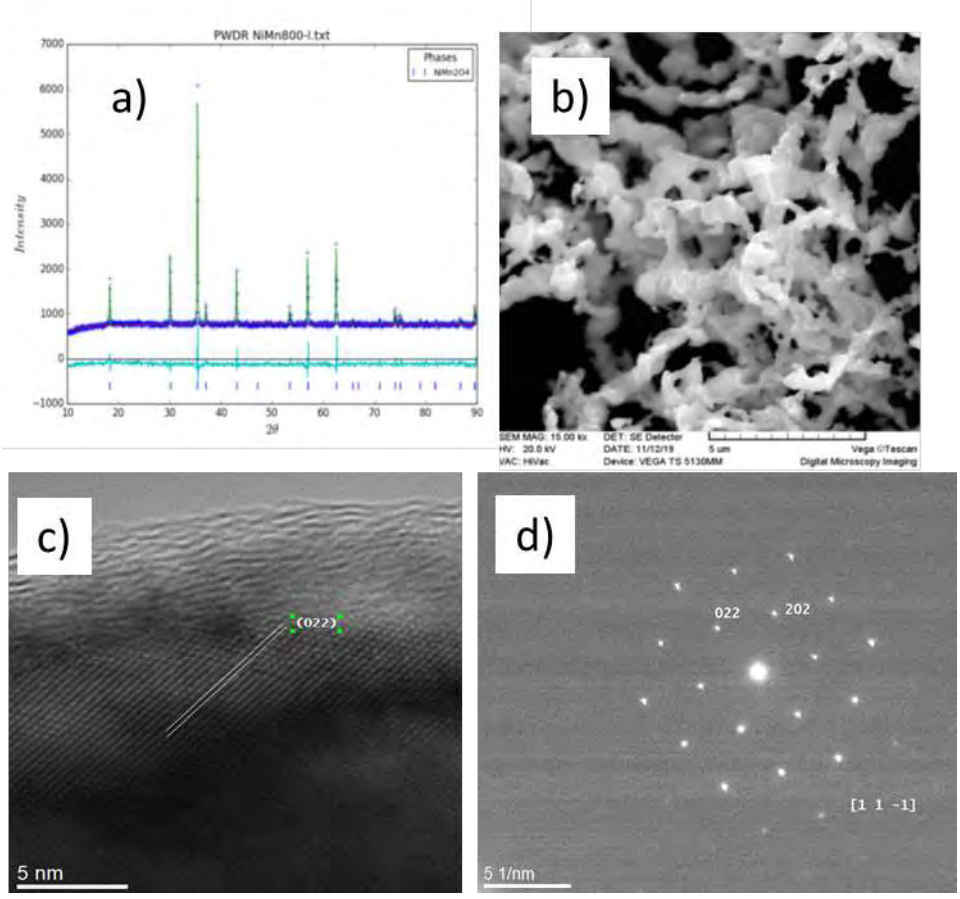

Figure 1. a) XRD pattern, b) SEM micrograph, c) TEM micrograph, d) SAED pattern of $NiMn_2O_4$ calcined at 800 °C.

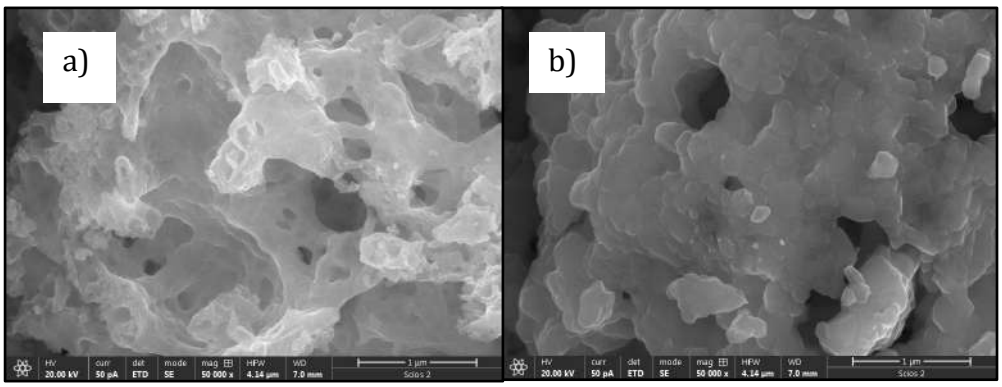

Figure 2. FESEM micrographs of $NiMn_2O_4$ a) calcined at 400 ºC b) calcined at 800 ºC.

Sodium-pillared vanadium oxide decorated with carbon particles as electrode material for more sustainable energy storage of the future

Milica Vujković[1], Tamara Petrović[1], Dušan Mladenović[1], Miloš Milović[2], Danica Bajuk-Bogdanović[1], Biljana Šljukić-Paunković[1], Slavko Mentus[1,3]

1 University of Belgrade-Faculty of Physical Chemistry, Studentski trg 12-14, Belgrade and Serbia.

2 Institute of Technical Sciences of Serbian Academy of Sciences and Arts, Knez Mihajlova 35/IV, 11000 Belgrade, Serbia.

3 Serbian Academy of Sciences and Arts, Knez Mihajlova 35, Belgrade, Serbia.

An increased utilization of intermittent renewable energy (wind, solar…) requires the expansion of energy storage/conversion systems to a large scale, which can be integrated with renewable source devices into electrical grid. The state-of-the-art Li-ion batteries present the good choice in terms of energy and power density. However, their massive applications are strongly limited by restricted lithium resources and safety issues. In that context, the research on different alternative battery systems, relying on Earth abundant elements such as Na, Ca, Mg, Al, etc, have been launched, where advanced materials play the central role as electrodes in their operation [1,2].

Due to adaptable interlayer distance and multivalent stage of vanadium, layered vanadium oxides are interesting electrode materials for multivalent-ion charge storage devices. Herein, the multiphase Na-pillared vanadium oxide was hydrothermally synthesized in the form of the composite with carbon (SVM/C) to serve as a platform for understanding mono/multivalent ion chemistry and to be examined as an electrode for different aqueous rechargeable batteries. The carbon (Vulcan XC72) presence in the precursor solution during the synthesis of targeted $Na_2V_6O_{16}$, was found to change the reaction path, leading to a phase mixture $Na_2V_6O_{16}/NaV_6O_{15}$ (SVM/C) instead of the expected single $Na_2V_6O_{16}$ phase. Both Scanning electron microscopy (SEM) and Transmission Electron microscopy (TEM) revealed nanowire nanosphere arrays of SVM/C (Fig1). Some of nanowires are stacked into larger parallel bundles, 2-3 μm in diameter (Fig.1, left), while the spherical-shape particles (≈ 100 nm in diameter) are grouped into smaller or larger clusters, with the tendency to form chains (Fig.1, right). The amount of carbon in the composite, determined by thermogravimetric and differential thermal analysis (TG/DTA), was found to be ≈ 8 wt.%.

The applicability of the synthesized composite as electrode material was first checked in Li-ion aqueous battery. As anode of SVM/C//$LiNO_3$//$LiFe_{0.95}V_{0.05}PO_4$/C full cell, multiphase SVM/C composite shows better performance than those for reported NaV_6O_{15} and $Na_2V_6O_{16}$ anodes in the form of either Li or Na rechargeable aqueous batteries. Furthermore, the high insertion capability of the synthesized multiphase oxide was shown not only in Li but also in Mg-, Al- and Ca-containing aqueous electrolytes. The main novelty we found here is that Ca redox processes of sodium vanadate in an aqueous solution are more stable than Li and Mg redox processes. Significantly higher Ca^{2+} vs. Li^+ capacity retention (87 vs. 45 wt%) is shown during prolonged potentiodynamic cycling and that was explained by coinserted water/hydroxyl groups. Hydroxyl groups introduced by coinsertion, as evidenced by Fourier-transform infrared spectroscopy (FTIR), may take over the charge fraction and make vanadium ions less strained, thus producing better cyclic stability. Their redox process during charging/discharging of vanadium oxide is proposed. The influence of different parameters (pH, the type of anion and electrolyte concentration) to the stability of Ca redox processes is examined. The synthesized SVM/C is combined with the carbon anode to get the aqueous multivalent hybrid cell, whose performance will be presented.

With these results, we would like to put in motion the interest for Ca interfacial reactions of vanadate structures, in the aqueous-based electrolytes, as new directions towards development of a new generation of more sustainable energy storage devices.

References:

[1] C. Masquelier, L. Croguennec, Chemical Reviews, 113, (2013), p. 6552.
[2] A. Gezović, M. J. Vujković, M. Milović, V. Grudić, R. Dominko, S. Mentus, Energy Storage Materials, 37 (2021), p. 243.
[3] This research is supported by the Science Fund of the Republic of Serbia, PROMIS, #6062667, HISUPERBAT.

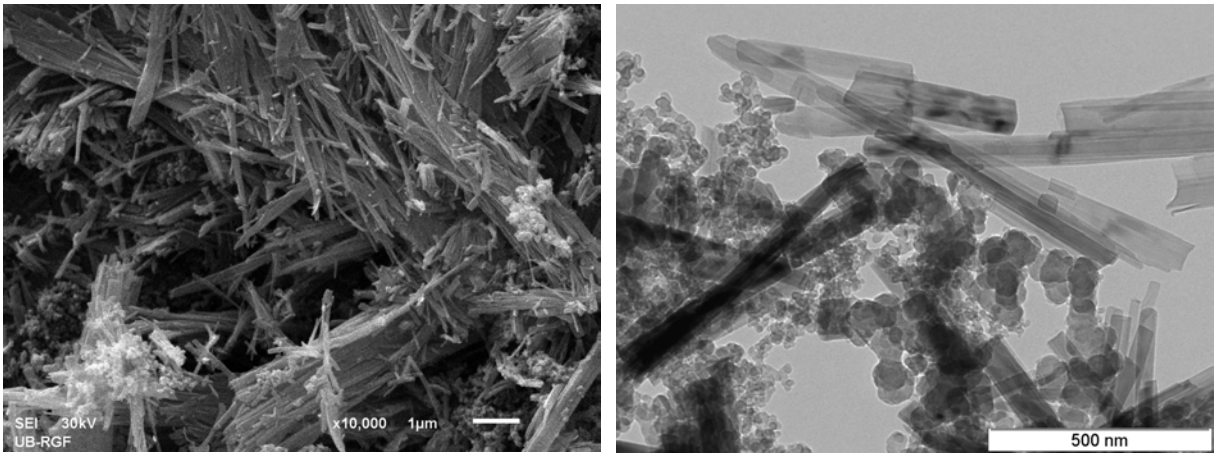

Figure 1. SEM (left) and TEM (right) micrographs of SVM/C.

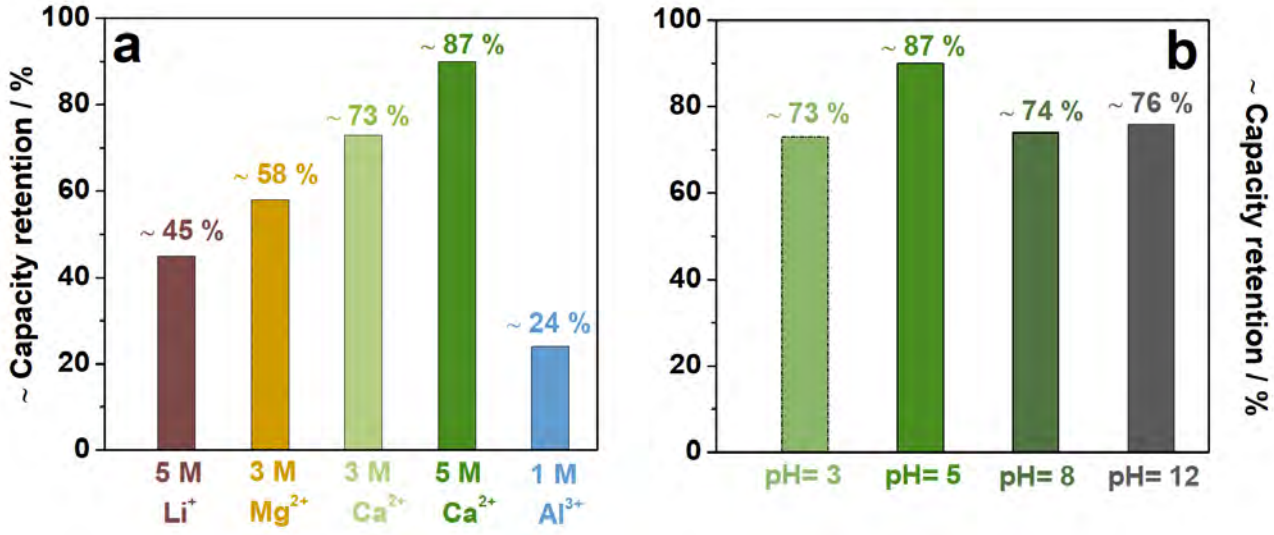

Figure 2. The capacity retention of SVM/C after 20 cycles in a) different M-containing aqueous electrolytes (M=Li, Mg, Ca and Al) and b) pH-different Ca-containing electrolytes.

Sol-gel Synthesis of $MgMn_2O_4$ and $MgCr_{0.15}Mn_{1.85}O_4$

Nikolina Jokić[1], Dragana Jugović[2], Srečo Škapin[3], Ivana Stojković Simatović[4]

1 Institute Mol, Nikole Tesle 15, Stara Pazova, Serbia

2 SASA Institute of Technical Sciences, Kneza Mihaila 35/IV, Belgrade, Serbia

3 Institute Jožef Stefan, Jamova cesta 39, Ljubljana, Slovenia

4 Faculty of Physical Chemistry, Studentski trg 12 Belgrade, Serbia

Electrochemical energy storage systems, primarily lithium-ion batteries, have experienced a huge expansion in the last couple of decades, but as they are very expensive to manufacture a lot of effort is being put into finding a more affordable replacement. For this purpose, multivalent cation compounds whose crystal structure is similar to the crystal structures of lithium compounds used in lithium-ion batteries are often studied. Magnesium cation is particularly interesting due to its high availability, significantly lower cost and high theoretical capacity. [1]

In this work, the glycine-nitrate method (GNM) was applied for the synthesis of cathode material $MgMn_2O_4$ after which its electrochemical properties were studied. As it is known that the addition of chromium ions to the lithium form of this compound increases the stability of capacity during cycling [2,3], the glycine-nitrate method was also used to synthesize $MgCr_{0.15}Mn_{1.85}O_4$. One part of the synthesized $MgCr_{0.15}Mn_{1.85}O_4$ was annealed at 700 ^oC, and the other part at 800 ^oC, and all three of the obtained materials were tested in parallel.

Structural analysis of the materials was performed by X-ray diffraction and morphology was determined by scanning electron microscopy (FESEM). To study the electrochemical behavior of the materials the following methods were used: cyclic voltammetry and galvanostatic cycling.

XRD spectrum of synthesized $MgMn_2O_4$ showed all reflections characteristic for $MgMn_2O_4$, which confirmed that this synthesis method yielded the desired product. $MgMn_2O_4$ annealed at 700 ^oC showed crystal structure and high values of discharge capacity. Its maximum discharge capacity was 97.5 mAh/g at current density of 100 mA/g, but ten cycles later the capacity was 67.5 mAh/g which is a decrease of 30%. XRD analysis of $MgCr_{0.15}Mn_{1.85}O_4$ confirmed that two phases are present in the samples - tetragonal, which is characteristic of $MgMn_2O_4$, and cubic, which is characteristic of $MgCr_2O_4$. $MgCr_{0.15}Mn_{1.85}O_4$ annealed at 700 ^oC wasn't electrochemically active, unlike $MgCr_{0.15}Mn_{1.85}O_4$ annealed at 800 ^oC, which is why only the material annealed at 800 ^oC was studied further. In comparison to $MgMn_2O_4$, $MgCr_{0.15}Mn_{1.85}O_4$ annealed at 800 ^oC shows lower capacities due to lower content of manganese ions, but it also shows significantly higher stability of capacities during cycling. Its maximum discharge capacity was 69.5 mAh/g at current density of 200 mA/g, and ten cycles later the capacity was 64,8 mAh/g which is a decrease of 7%, Fig. 1. From this it can be concluded that the cation doping had the desired, expected effect of stabilizing the discharge capacity.

From the data on the morphology of the material, it was concluded that the material is formed by agglomerates in the form of a three-dimensional network, and that the material annealed at 700 ^oC has larger and more adherent particles due to which it has a smaller active surface which makes the flow of ions through the structure difficult. As a result, this material has poor electrochemical properties. In comparison, the material annealed at 800 ^oC has less cohesive particles that form

agglomerates of smaller average size. This allows for easier passage of ions during intercalation and deintercalation, which explains this material's better electrochemical behavior, Fig 2.

References:

[1] Priyono, S., Ginting, N. R., Humaidi, S., Subhan, A., & Prihandoko, B. Synthesis of lithium mangan dioxide ($LiMn_2O_4$) for lithium-ion battery cathode from various lithium sources. Journal of Physics: Conference Series, 2018

[2] M. Rao, V. Basaveswara Rao, T Satyanarayana, Spectroscopic and electrochemical investigations on $LiCr_xMn_{2-x}O_4$ cathodes for rechargeable battery application, Materials Research Express, 2019

[3] Cvjeticanin, N., Stojkovic, I., Mitric, M., & Mentus, S. (2007). Cyclic voltammetry of $LiCr_{0.15}Mn_{1.85}O_4$ in an aqueous $LiNO_3$ solution. Journal of Power Sources, 174(2), 1117–1120

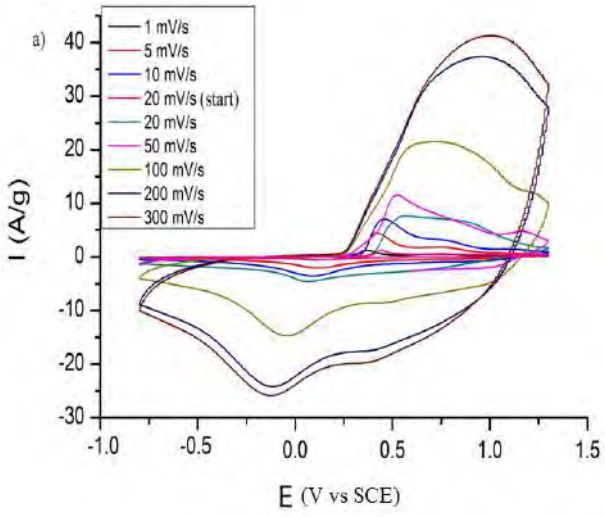

Figure 1. Cyclovoltamograms of the 10th cycles at different polarization rates for $MgCr_{0.15}Mn_{1.85}O_4$ annealed at 800 °C.

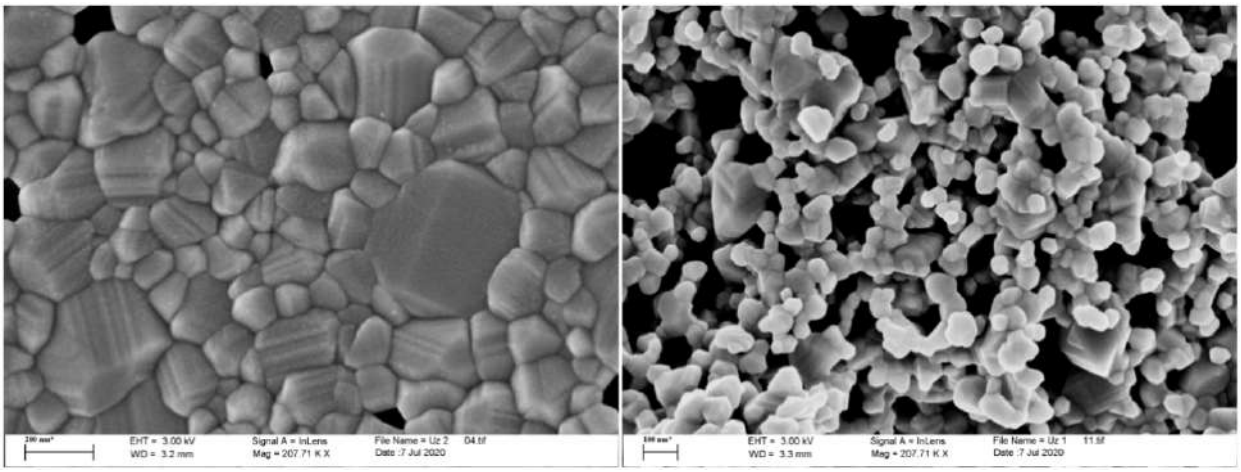

Figure 2. Comparative view of FESEM micrographs of $MgCr_{0.15}Mn_{1.85}O_4$ annealed at 700 °C (left) and at 800 °C (right).

Characterizing Graphene Supported PtAu and PdAu Nanoparticles with SEM, TEM and XPS for use as Catalysts for Hydrogen Evolution Reaction

Lazar Rakočević[1], Irina Srejić[1], Aleksandar Maksić[1], Vladimir Rajić[1], Mirjana Novaković[1], Svetlana Štrbac[2]

1 INS Vinča, Department of Atomic Physics, University of Belgrade, Mike Alasa 12-14, 11001 Belgrade, Serbia

2 Institute of Chemistry, Technology and Metallurgy, Department of Electrochemistry, University of Belgrade, Njegoševa 12, 11000 Belgrade, Serbia

Reducing fossil fuel consumption and switching to green renewable sources of energy is necessary for a sustainable future. One of the key emerging technologies are fuel cells using elemental hydrogen as fuel. Although hydrogen is plentiful it needs to be first converted to H_2. One of the ways for obtaining H_2 gas is hydrogen evolution reaction (HER) which needs an efficient and cost-effective catalysts. Platinum group metals (PGM) are currently the most extensively exploited catalysts for the studies of HER. Although such catalysts are expensive and scarce they are still widely used, but for practical use, novel designs aim to limit the amount of PGM. Therefore, the synthesis of cost-effective catalysts goes in the direction of their minimum consumption by using bimetallic nanoparticles supported by a conductive and cheap material [1]. Carbon-based materials are widely used as support owing to their electrical conductivity, cheapness, abudance and inertness [2]. Most recently, the use of graphene as a support has gained particular attention due to its contribution to electrocatalytic activity through the interaction between the support and bimetallic nanoparticles [3].

In this work, PtAu and PdAu nanoparticles on graphene support are synthesized and characterized using SEM, TEM and XPS. Goal is to create a catalysts with low amount of Au, Pt and Pd, deposited in sub-monolayer nanoclusters on the surface of graphene. The graphene was synthesized using electrochemical exfoliation of graphite, and spread using a drop of suspension over the glassy carbon (GC) support. PtAu and PdAu nanoparticles were obtained by a spontaneous deposition of Au on the graphene/GC, followed by a subsequent spontaneous deposition of Pt and Pd on top of it. TEM micrographs were obtained for graphene showing individual sheets of different thickness and that individual graphene sheets consist of less than 10 layers. SEM analysis of graphene/GC, and graphene supported Au, PtAu and PdAu nanoparticles show that the edges of the graphene sheets are active sites for deposition of Au, Pt, and Pd nanoparticles. Additionally Pt and Pd nanoparticles that are non uniform in size are deposited on top and at the edges of already present uniform Au nanoparticles. All particles range in size from 10 nm to 120 nm. XPS analysis indicates that based on chemical bonds obtained form high resolution C 1s spectra that graphene is partially reduced graphene oxide. XPS also shows that percentages of Au, Pt and Pd are approximately 1 %, while percentage of Au slightly drops with addition of Pt and Pd confirming that they are deposited on top of Au.

These catalysts were tested electrochemicaly for HER and they show electrocatalytical activity comparable to, or even slightly better than pure Pt depending on the conditions.

References:

[1] Hou, J *et all*., Platinum-group-metal catalysts for proton exchange membrane fuel cells: From catalyst design to electrode structure optimization. *Energy Chem.* **2020**, *2*, 100023.
[2] Zheng, J. *et all*.,. Universal dependence of hydrogen oxidation and evolution reaction activity of platinum-group metals on pH and hydrogen binding energy. *Sci. Adv.* **2016**, *2*, e1501602.
[3]Martín,A. *et all*., The cutting–edge interaction between chemistry and electrochemistry. *Trends Analyt. Chem.* **2014**, *56*, 13–26.

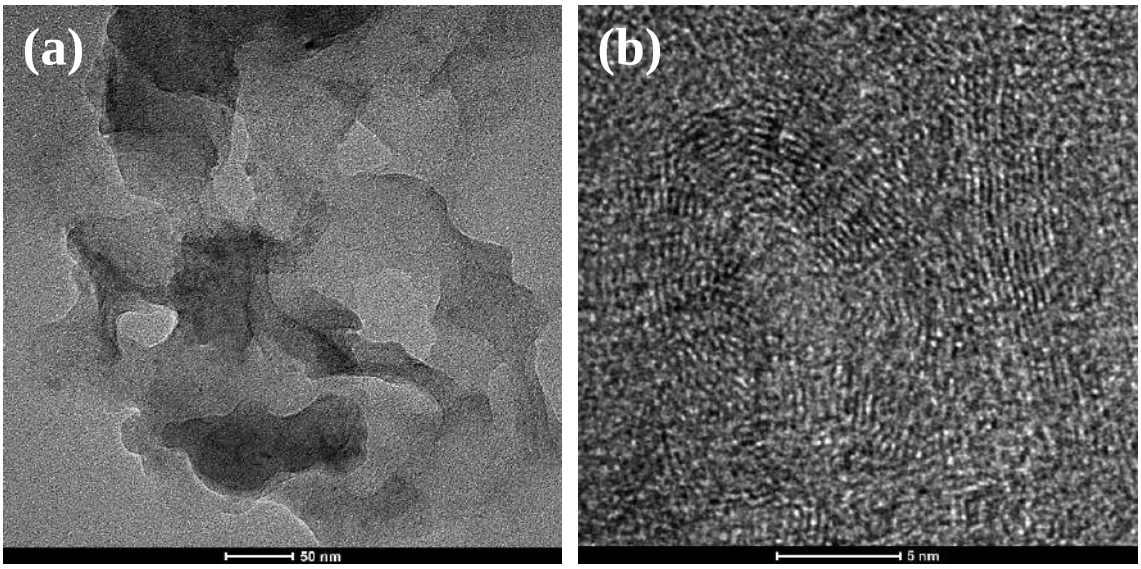

Figure 1. TEM micrographs showing: a) graphene sheets with different thickness (scale bar = 50 nm; b) that individual graphene sheets (scale bar = 5 nm) consist of less than 10 layers.

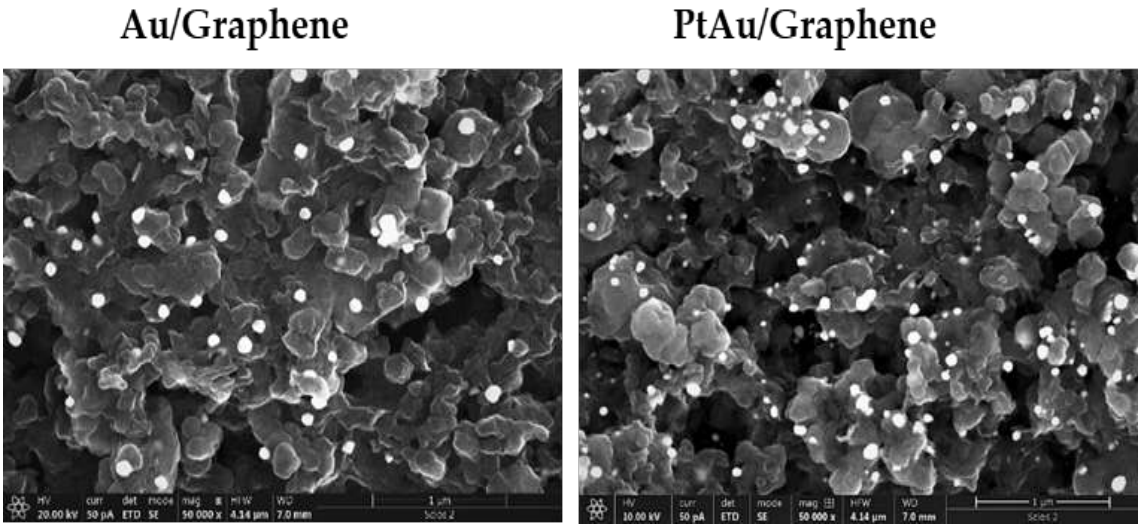

Figure 2. SEM micrographs showing Au and PtAu nanoparticles supported by graphene at 50 000x magnification (scale bar = 1μm).

Electrodeposited Platinum Group Metals Catalysts on Max Phases Based Support for Hydrogen Energy Related Applications

Nevenka R. Elezovic[1], Uros Lacnjevac[1], Mila Krstajic Pajic[2], Piotr Zabinski[3], Vladimir Jovic[1]

1 University of Belgrade Institute for Multidisciplinary Research, Kneza Višeslava 1, 11030 Belgrade, Serbia

2 University of Belgrade Faculty of Technology and Metallurgy, Karnegijeva 4, 11000 Belgrade Serbia

3 AGH University of Science and Technology, Faculty of Non-Ferrous Metals, Al. Mickiewicza 30, 30-059 Krakow, Poland

The hydrogen evolution reaction (HER) and hydogen oxidation reaction (HOR) were studied in sulfuric acid at electrodeosited thin layers of Ru, Pd, Ir and Pt at Ti_2AlC and $(Nb\text{-}Ti)_2AlC$ supports. Thin layers of Ru were electrodeposited by cyclic voltammetry (CV), samples of Pd were electrodeposited by pulse technique (PT) and chronopotentiometry (CP), while ultra-thin and sub-monolayers of Ir were electrodeposited by CV (v = 5 mV s-1) and controlled potential coulometry (CPC). The HER and HOR was investigated by electrochemical impedance spectroscopy (EIS) and polarization measurements.

Physical - chemical characterization of the catalysts was performed by the following techniques application: Scanning Electron Microscopy (SEM), Atomic Force Microscopy (AFM), and Transmission Electron Microscopy (TEM). Thus, the surface of all samples was characterized by scanning electron microscopy (SEM), while the thickness of electrodeposited Ru layers was determined by atomic force microscopy (AFM) [1]. The presence of holes and cracks was detected at the surface of Ru and Ir samples, while certain samples of Pd were characterized by the presence of isolated hemispherical 3D centers [2] Typical AFM image of electrodeposited Pd layer is presented in Fig. 1.

All samples showed high catalytic activity for the HER. Tafel slopes of about -60 mV dec^{-1} were observed in the high cathodic current density range at Ru polarization curves, as well as at the Pd layer mainly composed of isolated hemispherical 3D Pd centers and dendrites, while for the thicker Pd electrodeposit with the theoretical thickness of 1000 nm Tafel slope of -224 mV dec^{-1} was detected. All Ir samples showed very small Tafel slope of about 16 mV dec^{-1} up to about -0.1 A cm^{-2}, with only 6 monolayers of electrodeposited Ir being enough to show high catalytic activity for the HER. Mass activities at the overpotentials of 25 mV, 50 mV and 100 mV for certain samples were obtained from the current density divided by noble metal loadings. It appeared that the highest mass activity was obtained for Ir-6ML sample []3]. Comparing overpotentials at j = -0.01 A cm^{-2} and j = -0.10 A cm^{-2} for all samples it was shown that the lowest values were obtained for Ir samples.

For platinum based catalyst Scanning Electron Microscopy combined with Energy Dispersive Spectroscopy Mapping Analysis (SEM-EDS mapping) characterization was performed, while for cross section analysis TEM investigations were performed via Focused Ion Beam (FIB) technique using a Quanta 3D 200i FIB/SEM dual beam microscope. A typical cross section of Pt deposited layer is presented in Fig. 2

The short survey of state of the art Pd, Ru and Ir catalysts for HER was presented and discussed, as well. The authors are indebted for financial support, as it was stated below [4].

References:

[1] BM Jović *et al*, Journal of Electroanalytical Chemistry **766** (2016), p. 78.
[2] BM Jović *et al*, Electrochemica Acta **224** (2017), p. 571.
[3] N Elezović *et al*, Journal of Electroanalytical Chemistry **878** (2020), p. 14575.
[4] This work was financially supported by the Ministry of Education, Science and Technological Development of the Republic of Serbia (Contract No. 451-03-68/2022-14/200053 and Contract No.451-03-68/2022-14/200135). The authors would like to thank Prof. M. Barsoum, Drexel University Department of Material Science & Engineering 3141, Chestnut Street Philadelphia, PA 19104 USA, for Max phases preparation.

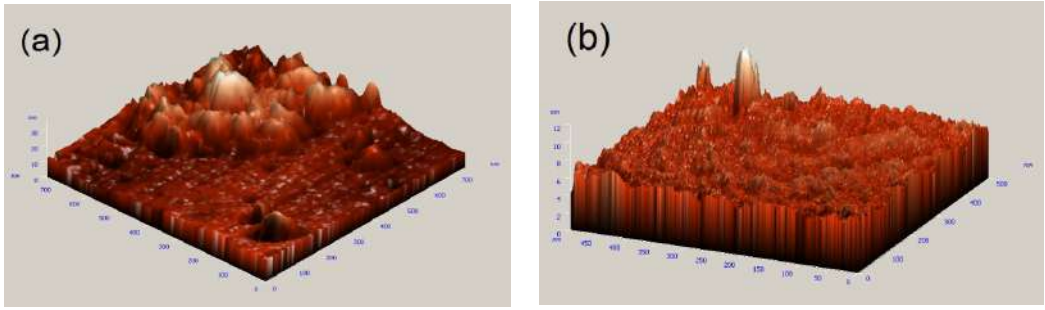

Figure 1. Typical AFM's of the less densely packed Pd layer (a) agglomerate with several 3D centers - nanoparticles; (b) isolated 3D center – isolated nanoparticle [2].

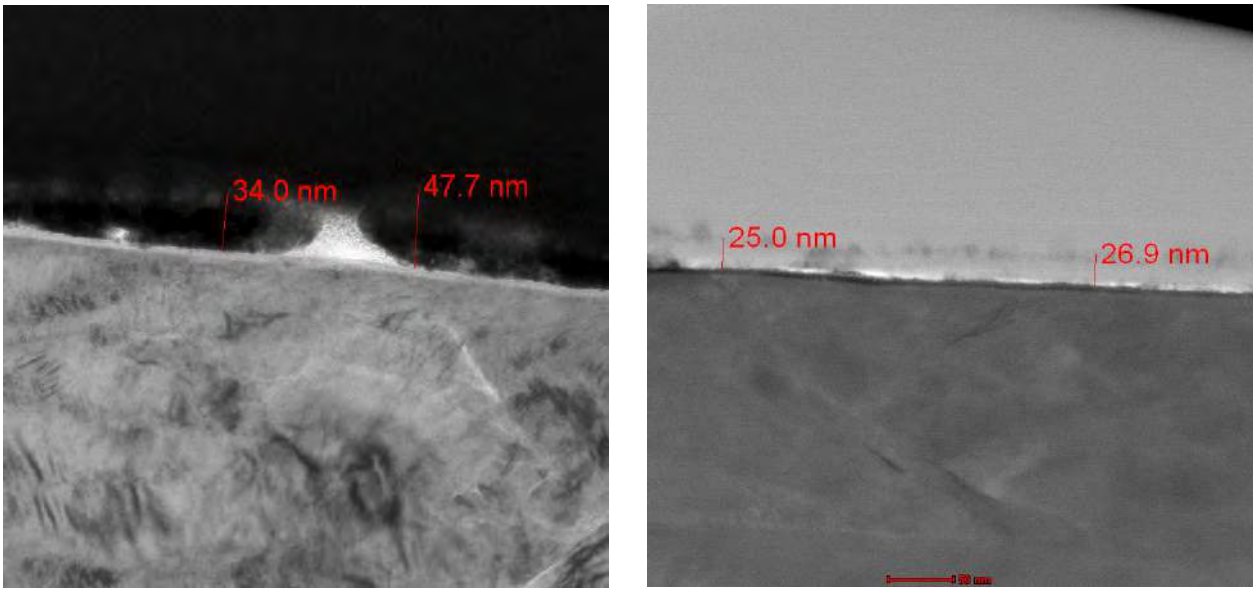

Figure 2. Typical Pt based catalyst cross section results obtained by TEM investigations prepared via focused ion beam (FIB): BF an HAADF image respectively.

Characterization of Coated Ni foam Electrodes for Industrial Hydrogen Production

Jelena Gojgić[1], Aleksandar Petričević[1], Thomas Rauscher[2], Christian Bernaecker[2], Mila Krstajić Pajić[1], and Vladimir Jović[3]

1 University of Belgrade, Faculty of Technology and Metallurgy, Karnegijeva 4, 11000 Belgrade, Serbia

2 Fraunhofer Institute for Manufacturing Technology and Advanced Materials IFAM, Branch Lab Dresden, Winterbergstraße 28, 01277 Dresden, Germany

3 University of Belgrade, Institute of Multidisciplnary Research, Kneza Viseslava 1, 11030 Belgrade, Serbia.

Hydrogen is the most promising green energy carrier that can provide energy generation in small, portable devices, vehicles, as well as large scale power plants. Being produced from water splitting in a most pure form, it requires the use of renewable sources such as wind or sun, to complete the green energy cycle.

When it comes to alkaline water electrolysis, non-noble metals such as Ni are commonly used as hydrogen evolution catalysts, however their catalytic performance is enhanced by using 3D porous materials, with possible addition of a more active alloy as coating. Ni foams with open pores are produced commercially, and used in flow electrolyzers thanks to their structure.

For this research, Ni foams were produced by electrodeposition with the use of a polymer matrix, with tailored pore size [1], and used as substrates for a more efficient HER catalyst, Ni-Sn alloy. The coating was electrodeposited onto substrates, under different conditions, from a Pyrophosphate-Glycine bath [2] and the samples were characterized by Scanning Electron Microscopy (SEM) including Energy Dispersive X-ray Spectroscopy (EDS) from Jeol (JSM-IT800). Besides the characterization of structure, morphology and composition, the samples were investigated for HER by different electrochemical methods, including linear sweep voltammetry, chronopotentiometry and electrochemical impedance spectroscopy in an alkaline environment. The real surface area of Ni foam was estimated by electrochemical procedures and compared to the data obtained from BET isotherms and SEM investigation.

Thanks to the open pore structure of the foam, and appropriate electrodeposition methodology, the foam substrates were completely covered by the porous Ni-Sn coating, as confirmed by SEM top view (Fig. 1) and cross-section analysis. The coating composition is similar throughout the sample, and the coating thickness is greater at the edges of Ni struts, but no bare Ni surfaces were observed, before or after the electrochemical measurements. The electrodeposition of Ni-Sn was conducted with simultaneous hydrogen evolution, resulting in rough deposits that additionally increase the electrochemically active surface area of the foams.

As for the electrode performance for HER, the overpotentials at characteristic HER current densities (normalized per geometric electrode area) are very low, while the stability tests show no sign of peel of effect, or any significant decrease in activity over time. These electrodes are intended for single industrial hydrogen production after the scale up process.

References:

[1] P. S. Liu, G. F. Chen, Porous Materials: Processing and Applications Butterworth-Heinemann; 1. Edition (12. August 2014)
[2] U. Lacnjevac, B.M. Jovic, V.D.Jovic, "Electrodeposition of Ni, Sn and Ni–Sn Alloy Coatings from Pyrophosphate-Glycine Bath", Journal of The Electrochemical Society **159** (2012) D310-D318
[3] This work was supported by the Federal Ministry of Education and Research – Germany, through the WBC2019 call – project NOVATRODES 01DS21010, and by the Ministry of Education, Science and Technological Development of the Republic of Serbia (Contract No.451-03-68/2022-14/200135).

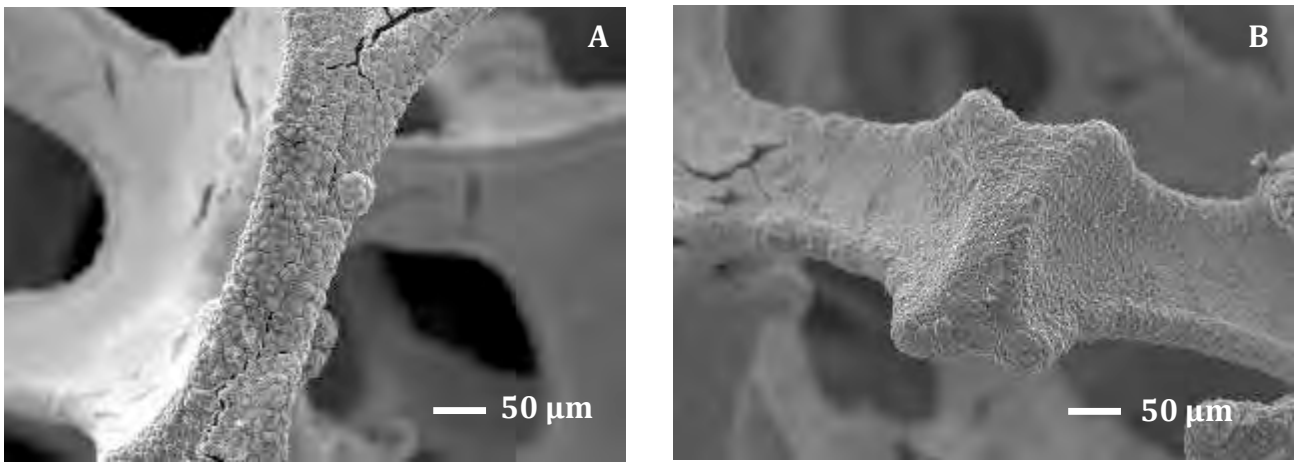

Figure 1. SEM top view micrograph of the coated Ni foam with pore size 1200 µm, Ni-Sn coating electrodeposited at - 1.25 V (A), and - 1.30 V (B), deposition potentials given versus Saturated Calomel Electrode.

Cu_{upd}@Pd/C and Pd-Cu/C Nanocatalysts for Electrochemical Ethanol Oxidation in Alkaline Solution

Maja D. Obradović[1], Jelena R. Rogan[2], Uroš Č. Lačnjevac[3], Aleksandra Gavrilović-Wohlmuther[4], Vuk V. Radmilović[2], Velimir R. Radmilović[2,5], Snežana Lj. Gojković[2]

1 University of Belgrade, Institute of Chemistry, Technology and Metallurgy, Belgrade, Serbia.
2 University of Belgrade, Faculty of Technology and Metallurgy, Belgrade, Serbia.
3 University of Belgrade, Institute for Multidisciplinary Research, Belgrade, Serbia.
4 Schoeller-Bleckmann Nitec GmbH, Ternitz, Austria.
5 Serbian Academy of Sciences and Arts, Belgrade, Serbia.

Easy storage and handling, high energy density, wide availability, and low toxicity are the features of ethanol that make direct ethanol fuel cells the most promising among all alternative power sources [1,2]. Unfortunately, the ethanol oxidation reaction (EOR), taking place at the anode, is slow and incomplete even on the best available catalysts known to date. Pure Pt and Pd are not capable of catalyzing the oxidation of ethanol through a total oxidation pathway [2]. However, Pt and Pd are necessary catalyst constituents in providing efficient adsorption of ethanol, which is the first reaction step in ethanol oxidation. The activity of Pd and Pt for alcohol oxidation can be enhanced by adding a co-catalytic element, mainly oxophilic metal (either d- or p-metals), or compounds such as oxides [3]. Therefore, the Pd nanoparticles supported on carbon black (Pd/C) and decorated by Cu sub-monolayers by underpotential deposition (Cu_{upd}@Pd/C), as well as alloyed Pd-Cu nanoparticles (Pd-Cu/C) were investigated for the EOR in an alkaline solution.

Nanocatalysts Pd/C and Pd-Cu/C were synthesized by a borohydride reduction method [4] and characterized by thermogravimetric analysis (TGA), X-ray diffraction (XRD) and transmission electron microscopy (TEM). Total metal loadings of the Pd/C and Pd-Cu/C catalysts, determined by TGA measurements, were 8.0 mass% and 15.0 mass%, respectively. The average atomic ratio between Pd and Cu in the Pd-Cu/C catalyst was calculated to be 0.83:0.17 by energy dispersive X-ray spectroscopy (EDS). Taking into account the total metal loading, the Pd-Cu/C catalyst contained 12.4 mass% of Pd. The XRD patterns of the Pd/C and Pd-Cu/C powders are displayed in Fig. 1a) and 1b). The overall peak positions corresponding to Pd diffraction planes are shifted toward higher angles in the presence of Cu atoms, indicating alloyed structure of the Pd-Cu catalyst. The XRD analysis did not reveal the presence of pure copper metal or oxide phases in Pd-Cu/C. TEM characterization of the Pd/C and Pd-Cu/C powders indicated nanosized structure with mean diameters of 3.7 nm and 2.5 nm, respectively (Fig. 1c, d, e, f and g).

In addition, the Pd/C catalyst was decorated by Cu_{upd} in an acid solution with various surface coverages (up to 0.5). The catalysts were electrochemically characterized by cyclic voltammetry (CV) and CO_{ads} stripping in acid and alkaline solutions. A decreased hydrogen adsorption/desorption charge in CVs and increased currents in the potential region of hydroxide adsorption/desorption (Fig. 2a-d) indicate the presence of metallic Cu on the bimetallic catalyst surface. The electrochemically active surface area (ECSA) was estimated from the charge under the CO desorption peak in the alkaline solution and used for determining specific and mass activity for the EOR. As shown in Fig. 2a-d, the onsets of CO desorption on the Cu_{upd} decorated and alloyed surfaces are negatively shifted compared the pure Pd surface. This indicates that Cu atoms provide oxygen-containing species at adjacent Pd sites at a lower potential than that achieved on pure metals.

The activity of the Pd/C, Cu_{upd}@Pd/C and Pd-Cu/C nanocatalysts for EOR was investigated in 0.1 M NaOH under potentiodynamic (Fig. 2e) and potentiostatic conditions (Fig. 2f). The Pd/C with a Cu_{upd}

coverage of 0.30 and Pd-Cu/C exhibited lower onset potentials and up to a 2.5-fold increase in EOR activity with respect to Pd/C (calculated per Pd ECSA). However, with a further increase in coverage, the positive effect of Cu_{upd} disappeared, and the activity even decreased. Although the EOR currents are higher on Cu_{upd}@Pd/C than Pd-Cu/C nanoparticles in potentiodynamic measurement (Fig. 2e), the potentiostatic curves show that the highest EOR currents are observed on the Pd-Cu alloy nanoparticles (Fig. 2e). This is indicative of their higher stability compared to the Cu_{upd}-modified nanoparticles.

References:

[1] E. Antolini, Journal of Power Sources 170 (2007) p. 1.
[2] N.S. Marinkovic, M. Li, R.R. Adzic, Topics in Current Chemistry 377 (2019) p. 11.
[3] L. Ma, D. Chu, R. Chen, International Journal of Hydrogen Energy 37 (2012) p. 11185.
[4] M.D. Obradović, J.R. Rogan, U.Č. Lačnjevac, A. Gavrilović-Wohlmuther, V.V. Radmilović, V.R. Radmilović, S.Lj. Gojković, Applied Catalysis B: Environmental 189 (2016) p. 110.

[5] The authors acknowledge funding from the Science Fund of the Republic of Serbia (the grant No 7739802), the Ministry of Education, Science and Technological Development of the Republic of Serbia (Contracts No. 451-03-68/2022-14/200135 and 451-03-68/2022-14/200026) as well as the Serbian Academy of Sciences and Arts (Contract No. F141).

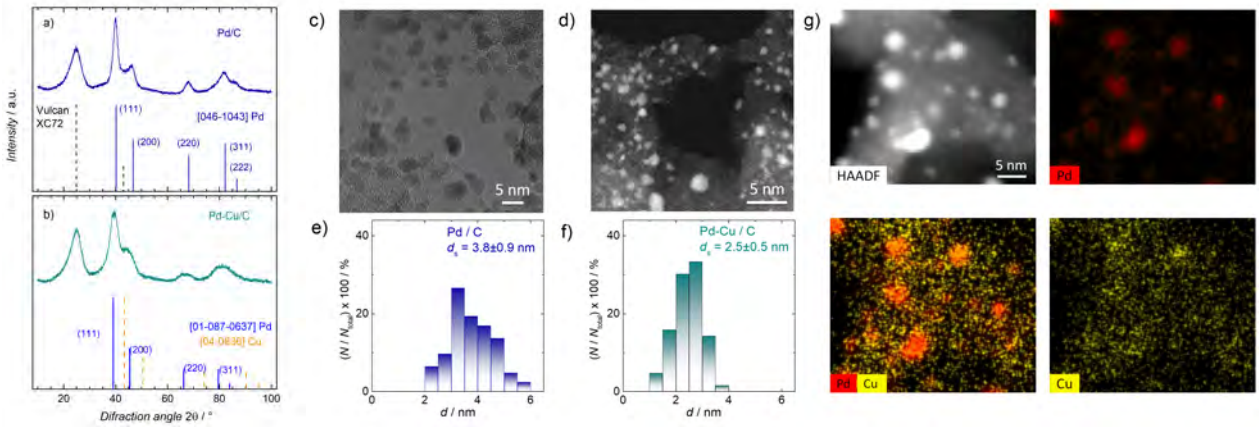

Figure 1. XRD patterns of a) Pd/C and b) Pd-Cu/C; TEM images and corresponding particle size distribution of Pd (c and e) and Pd-Cu nanoparticles (d and f); g) EDS elemental mapping showing Pd (red) and Cu (yellow) distribution in Pd-Cu/C sample.

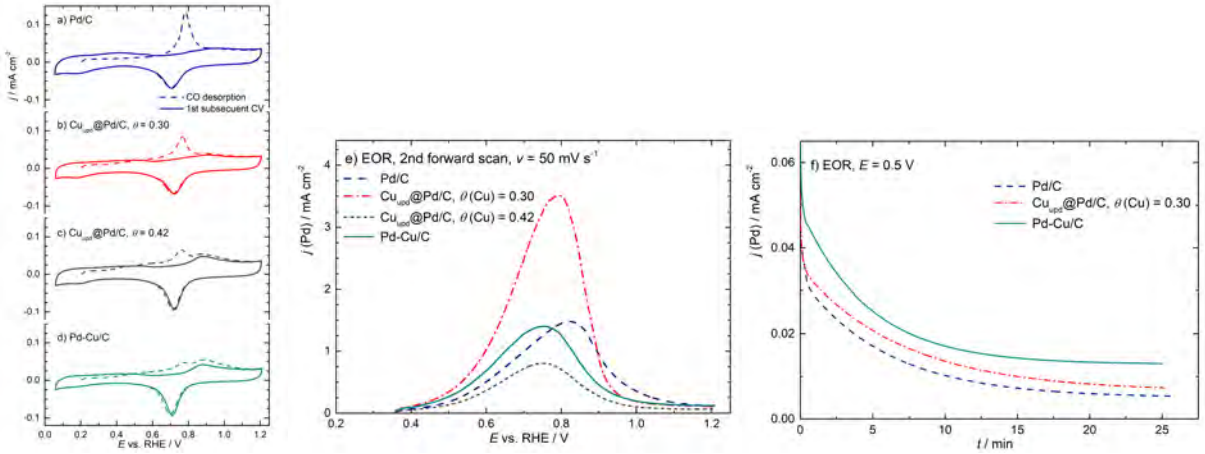

Figure 2. Stripping voltammograms of CO_{ads} (dashed lines) and the first subsequent voltammograms (solid lines) of a) Pd/C; b) Cu_{upd}@Pd/C, θ (Cu) = 0.30; c) Cu_{upd}@Pd/C, θ (Cu) = 0.42 and d) Pd-Cu/C in 0.1 M NaOH at the scan rate of 20 mV s^{-1}; e) Potentiodynamic polarization curves and f) chronoamperometric curves for the EOR in 0.1 M NaOH + 0.5 M ethanol solution.

Development of the Low-cost Carbon-based Mid-IR Transparent Electrode

Sara Joksović[1], Jovana Stanojev[1], Branimir Bajac[1], Vladimir V. Srdić[2]

1 BioSense Institute, University of Novi Sad, Novi Sad, Serbia

2 Faculty of Tecnology Novi Sad, University of Novi Sad, Novi Sad, Serbia

In recent decades, development of the transparent electrodes in the form of a thin film has played important role in the field of optoelectronic devices. Indium tin oxide (ITO) is a well-known optic material with low resistivity, but when it comes to the fabrication of ITO thin films, the exploitation of ITO and usage in the infrared (IR) range, there are some limitation [1–3]. Carbon-based transparent electrodes have gained a considerable attention as a replacement for the ITO, due to their exeptional electrical, mechanical and optical properties [4,5]. In this work, we have fabricated multi-walled and single-walled carbon nanotubes (MWCNTs and SWCNTs) thin films with the possible application in the uncooled mid-IR detectors.

Today, we have a wide spectra of different methods for obtaining the high quality thin films. The aim of this paper is to produce mid-IR transparent electrode based on MWCNTs and SWCNTs by easy and low-cost technique. Layer by layer (LbL) deposition is recognized as a simple technique, suitable for the alternating deposition of polyethyeneimine (PEI) and carboxyl functionalized single-walled or multi-walled carbon nanotubes (MWCNTs-COOH and SWCNTs-COOH) in monolayers. Polyethyeneimine was used as a positively charged layer and carboxylic functionalized nanotubes were used as a negatively charged layer in order to achieve electrostatic bond. In the first step, soda lime glasses were cleaned and 1% water based solutions of PEI and polyacrylic acid (PAA) were deposited on the surface as an adhesive layers. After that, substrates were soaked in the 1% PEI solution for 10 minutes and then in the CNT dispersion for 60 minutes with the washing step in between, in order to remove excess material. Prepared samples were composed of 1, 2, 3, 4 or 5 bilayers (PEI+CNT) and after each bilayer samples were dried at 120 ^{o}C for 10 minutes.

Raman spectroscopy was used in order to examine structure of a prepared thin films. Electrical properties were investigated by Hall device and sheet resistance multimeter. Morphology and microstructure of the surface and film cross section were examined with the scanning electron microscope (SEM) and transmission electron microscope (TEM) [6].

References:
[1] Jovana Stanojev et al, Ceramics International **46** (2020), p. 11340.
[2] Tingting Wang et al, Crystals **11** (2021), p. 1.
[3] Xuan Wang et al, Angewandte Chemie - International Edition **47** (2008), p. 2990.
[4] David S. Hecht, Liangbing Hu and Glen Irvin, Advanced Materials **23** (2011), p. 1482.
[5] Qing Cao and John A. Rogers, Advanced Materials **21** (2009), p. 29.
[6] The authors thank Nanocenter at Department of Complex Matter, Jozef Stefan Institute, Ljubljana, Slovenia, for performed HRSEM and TEM analysis.

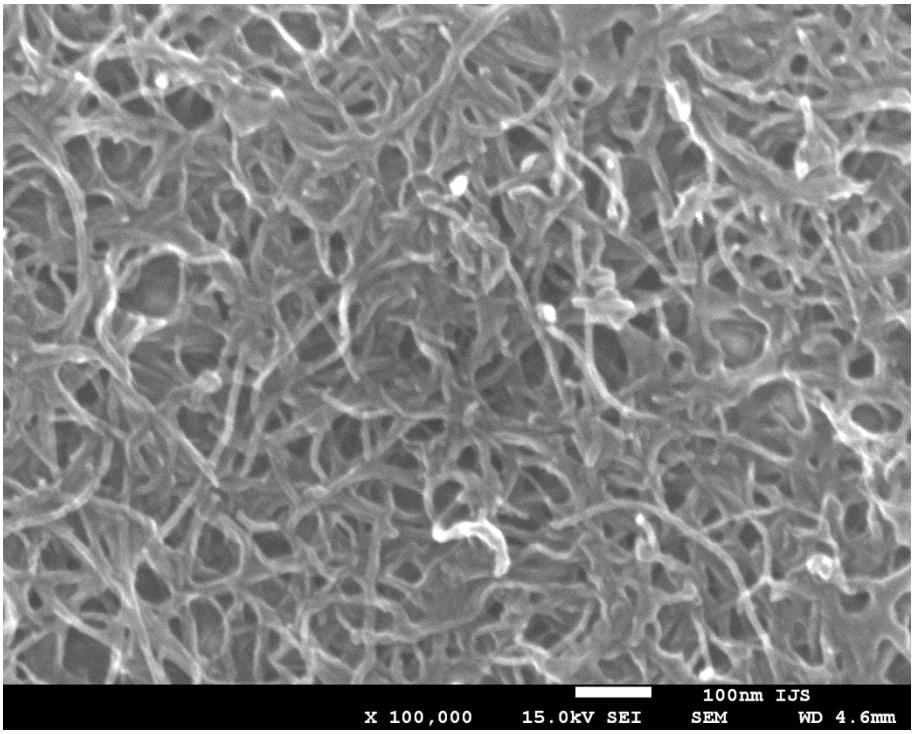

Figure 1. SEM image of surface of PEI-MWCNT consisted of 4 bilayers.

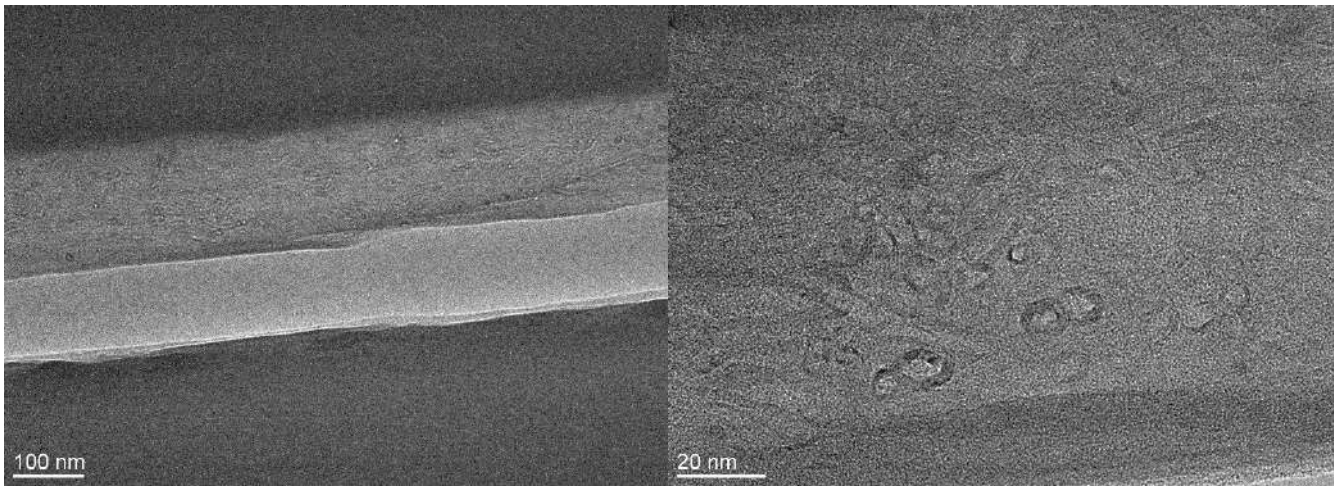

a) b)

Figure 2. TEM image of: a) cross section of PEI-MWCNT deposited on a glass substrate composed of 4 bilayers and b) multi-walled carbon nanotubes in PEI matrix.

Thin Film Polyaniline/Silver Nanowires Nanocomposites for Optoelectronic Applications

Jovan Lukic, Vuk V. Radmilovic

Faculty of Technology and Metallurgy, University of Belgrade, Belgrade, Serbia

The broad application of optoelectronic devices has influenced intense R&D to follow in its wake. As one of the building block materials in these devices, transparent electrodes (TE) represent an area of growing interest, owing to the fact that it is possible to drastically improve the performance of optoelectronic devices by improving properties of TE [1], such as transsmiting light, transffering and collecting charge carriers and providing a distributed electrical field. So far the most succesfully applied TE is indium tin oxide (ITO) with it's high transmitance and low sheet resistance [2]. Altough ITO has many favourable properties, there are certain drawbacks that limit it's application, such as demanding processing methods, brittleness, high price and inability to transmitt in the UV part of the spectra [3]. Mainly due to its high brittleness and the increasing width of application, researchers have proposed suitable replacements.

Silver nanowires (AgNW) having high transmittance, low sheet resistance, excellent flexibility, simple processing methods coupled with the option of wet chemical synthesis have been analysed as a suitable candidate [4]. However, liabilites such as low adhesion, low chemical stability and high surface roughness still have to be addressed. The aim of this work was to overcome these setbacks by developing polymer/AgNW nanocomposites [5], where the polymer matrix should maintain the essential TE properties all the while improving mechanical properties, stability, adhesion and surface roughness.

In this work TE thin films based on the nanocomposite of AgNW and polymer polyaniline (PANI) were processed via spincoating during which various wt% of polymer dispersions were coated on a layer of AgNWs, after which the nanocomposite was doped with orto-phosphorous acid to transform the polymer from its non-conductive emeraldine base (EB) to its conductive state – emeraldine salt (ES). PANI/AgNWs nanocomposites have shown promising optoelectronic properties, where the best ratio of optical transparency and sheet resistance was obtainted with the composition of AgNW suspension 1:1 and PANI 0.5 wt%. The values of 84.6% and 35 Ω/□ achieved for transparency and sheet resistance respectfully, could be considered adequate for TE performance.

References:

[1] Cui, N., Song, Y., Tan, CH. et al. npj Flex Electron **5,** (2021) p. 1.
[2] Zhang, R. & Engholm, M. et al. Nanomaterials **8**, (2018) p. 2.
[3] Ghosh, D. S. in "Ultrathin Metal Transparent Electrodes for the Optoelectronics Industry", (Springer International Publishing, Switzerland 2013), p. 4
[4] Wang Z., Han Y., Yan L. et al. Advanced Functional Materials **31**, (2020) p. 1.
[5] R. Karimi-Chaleshtori, A. H. Nassajpour-Esfahani, M. R. Saeri et al. Materials Today **21**, (2021), p.2.

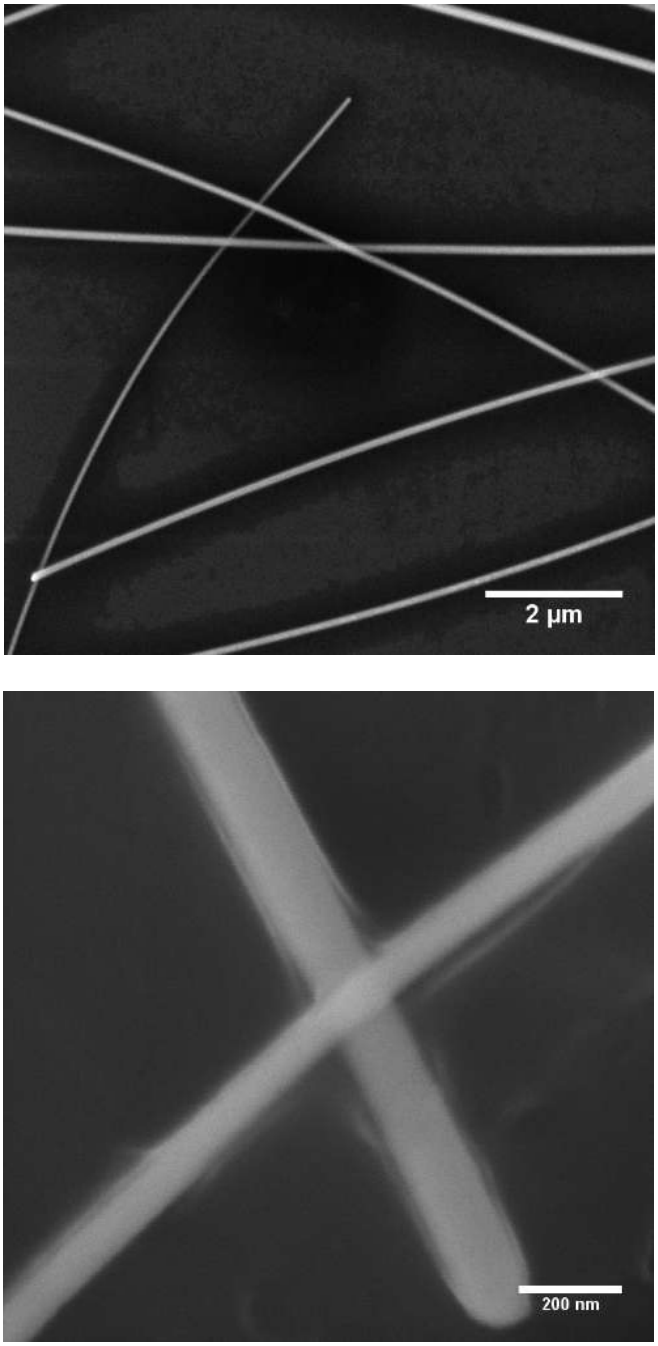

Figure 1. Morphology of the PANI/AgNW nanocomposite structures; top) the polymer fills the empty space between the nanowires, bottom) the polymer coats the nanowires.

Improving the contact surface between TiO_2 nanotubes and $MAPbBr_3$ to make perovskite solar cells

Milica Stefanović[1], Ivana Lukić[2], Jelena Vujančević[3], Rada Petrović[2] and Đorđe Janaćković[2]

1 Innovation Center of Faculty of Technology and Metallurgy, Ltd, Belgrade, Serbia

2 University of Belgrade, Faculty of Technology and Metallurgy, Belgrade, Serbia

3 Institute of Technical Sciences of SASA, 11000, Belgrade, Serbia

The organo-inorganic perovskites are extraordinary materials that have recently revolutionized the field of photovoltaics due to their low-cost fabrication and high optical absorption. In a short period, they reached great efficiency. Many parameters which affect the quality of perovskite films can be optimized, so the efficiency of these devices can be further improved [1]. In perovskite solar cells, the perovskite layer is an active layer that absorbs the visible part of the spectrum, resulting in the formation of the electron-hole pair. To decrease the recombination of charge carriers, the construction of solar cells requires the existence of two additional layers in order to separate the holes and electrons. TiO_2 could be used as an electron transport layer because its conduction band (CB) lies under the CB of perovskite [2]. In that way, electrons diffuse from CB of perovskite to CB of TiO_2. For these experiments, TiO_2 nanotubular structure provides a one-dimensional transmission channel for the charge carriers, which resulting in faster carrier transport. Perovskite methylammonium lead bromide ($MAPbBr_3$) was coupled with TiO_2 nanotube arrays which were synthesized by anodization of Ti foil and annealed at 450 °C [3]. The most used methods for deposition of perovskite materials on mesoporous and planar TiO_2 are: one-step deposition, two-step sequential deposition, and vapor-assisted solution processing. Disadvantage of these methods is a small contact area between TiO_2 and perovskite [4,5]. The aim of this research was to increase the contact surface of the perovskite and TiO_2 nanotubes by filling the nanotubes with the perovskite material in order to improve electron transport. Due to that, two different methods were used for deposition of $MAPbBr_3$ crystals onto TiO_2 nanotubes: high vacuum assisted with nitrogen gas and application of the supercritical CO_2 as a cosolvent. The procedure of deposition of perovskite in a high vacuum system included degassation of the sample under a high vacuum for 3 h at 200 °C, cooling down the sample, and putting a solution of $MAPbBr_3$ in dimethylformamide (DMF) onto the sample, and then treating with inert gas (N_2), which enabled the filling of the nanotubes with perovskite material to some extent [6]. Deposition of solution perovskite on TiO_2 nanotubes assisted by supercritical carbon dioxide was done at 200 bar and 35 °C for 1 h. The supercritical fluid, CO_2 had a role of a cosolvent which would help the filling nanotubes with perovskite material. XRD analysis of synthesized perovskite confirms coincidence with literature data [6]. Morphological characterization of samples after deposition of perovskite was carried out by FESEM. It was observed that the filling of nanotubes is better when deposition of perovskite was assisted by supercritical CO_2. The measurement of the *I-V* characteristic under visible light shows that the value of current for this sample is also higher, so it could be concluded that a better contact between perovskite and TiO_2 nanotubes was achieved in this case. Perovskite photodiodes that were made in this study will be the basis for future solar cell construction.

References:

[1] Q. Chen *et al*, Nano Today **10** (2015), pp 355.
[2] N. Marinova, S. Valero, J.L. Delgado, Journal of Colloid and Interface Science **488** (2017), pp. 373.

[3] E. Marchezini *et al*, Materials Research Express **7** (2020), pp. 025017.
[4] U. Mehmood *et al*, Renewable and Sustainable Energy Reviews **78** (2017), pp. 1.
[5] J. Vujančević *et al*, Ceramics International **45** (2019), pp.10013.
[6] M. Stefanović *et al*, Tehnika **77** (2022), pp. 15.
[7] The authors acknowledge funding from the Ministry of Education, Science and Technological Development of the Republic of Serbia Contact No. 451-03-68/2022-14/200287, 451-03-68/2022-14/200135 and 451-03-68/2022-14/200175.

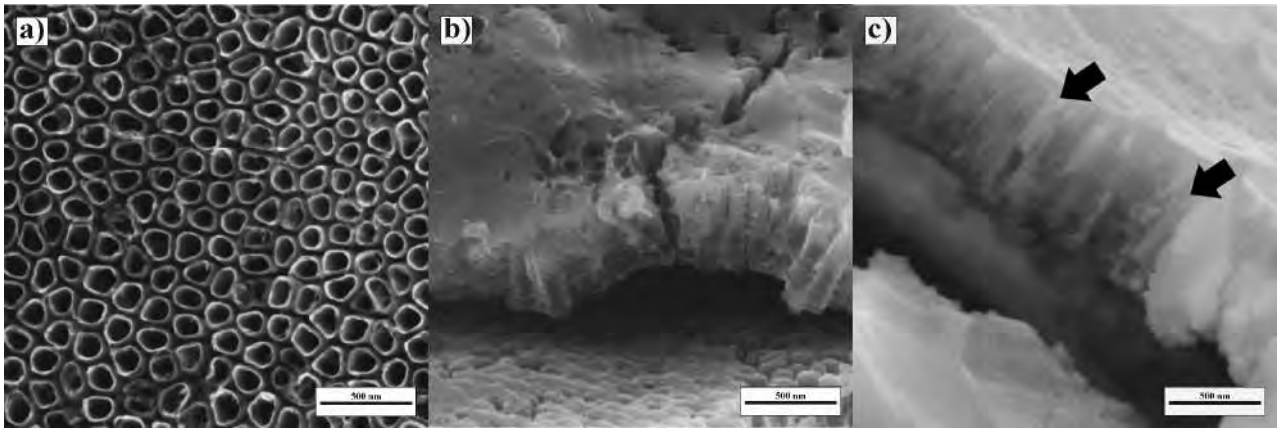

Figure 1. FESEM micrographs of a) pristine TiO_2 nanotube arrays, and TiO_2 nanotube arrays with $MAPbBr_3$ perovskite deposited b) in a high vacuum and inert gas [6] and c) assisted by supercritical CO_2 (the black arrow shows that the TiO_2 nanotubes are more filled with perovskite compared to the sample under b).

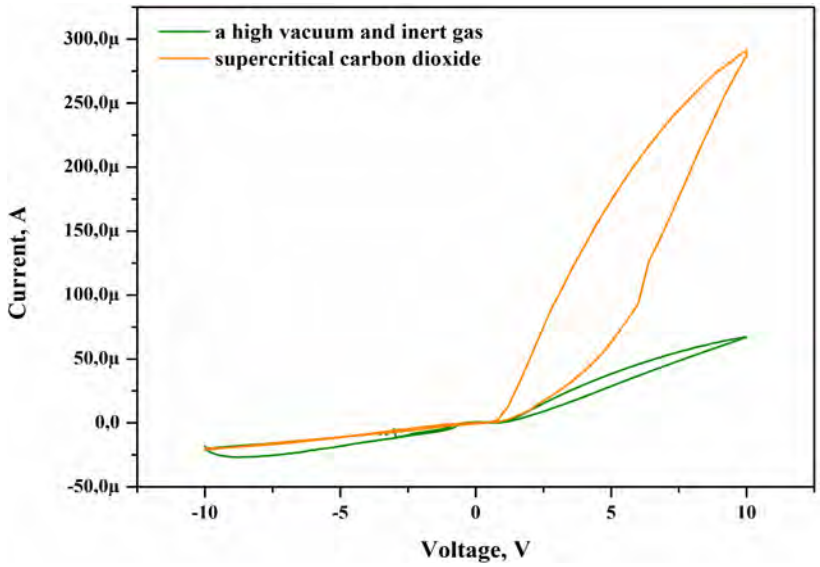

Figure 2. *I-V* characteristics of TiO_2 nanotubes-$MAPbBr_3$ perovskite photodiodes after preconditioning (poling at 10 V for 30 s) with external bias voltage under visible light. Hysteresis curves were obtained for both samples, but the value of current was higher for the sample which was done with supercritical CO_2. It supposes that one of the reasons is a larger contact surface between TiO_2 nanotubes and $MAPbBr_3$ perovskite.

Synthesis of Up-converting β-$NaYF_4$:Yb/Er Nanoparticles by Low-temperature Sonochemical Method

Ivana Dinić[1], Marina Vuković[2], Paula Jardim[3] and Lidija Mančić[1]

1 Institute of Technical Sciences of SASA, Belgrade, Serbia

2 Innovative Centre, Faculty of Chemistry, University of Belgrade, Serbia

3 Department of Metallurgical and Materials Engineering, Federal University of Rio de Janeiro, Rio de Janeiro, Brazil

Up-converting nanoparticles (UCNPs) have unique optical properties to convert NIR to VIS light, and therefore are widely used in optoelectronics, forensic, medicine, etc. [1,2]. During the last decade interest in obtaining of the pure hexagonal (β) $NaYF_4$:Yb/Er phase through some environmental friendly method which could be easily scaled-up is permanently present in scientific community. Different synthesis methods, like co-precipitation, thermal decomposition, hydro- and solvo-thermal methods were usually reported like promising ones, but obtaining of the highly efficient (β) phase is usually coupled with harsh processing conditions [3]. This phase is characterized by a higher degree of crystal asymmetry and multisite dopant accommodation which ensures better luminescence response than of cubic (α) phase. To prevent nucleation of kinetically stable α phase, we applied for the first time ultrasound treatment (20 kHz, Vibra Cell VCX750 Sonic) to the simple mixture of the rare earth nitrates and NaF in different solvents (ethanol and water) for 30, 60, 90 and 120 min.

The x-ray powder diffraction analysis implied that monophase samples are obtained only after 120 min of sonication: while α phase is stabilized when ethanol was used as a solvent, crystallization of β-$NaYF_4$:Yb/Er mesocrystalline particles is observed when water was used as a liquid medium. The structural refinement of β phase demonstrated that introduction of dopants with smaller ionic radii (Y^{3+}:101.9 pm;Yb^{3+}:98.5 pm; Er^{3+}:100 pm) leads to a decrease in cell volume from 108.59 $Å^3$ to 107.61 $Å^3$. Scanning transmission electron microscopy (STEM) revealed that synthesized particles are mesocrystalline. Typical spindle-like morphology of particles is presented at Fig.1. High-resolution transmission electron microscopy (HRTEM) image and corresponding selected area electron diffraction (SAED) pattern implied that mesocrystals could be indexed as the zone axis [-111] with a preferential growth direction perpendicular to (1–12) planes, Figs.1a,b. HRTEM presented at Fig.1d implicates that these are assembles of smaller crystallites which size is of about 10nm.

Homogeneous distribution of dopants in host matrix is additionally confirmed by STEM/EDS mapping (not presented). As a result, good up-conversion emission is observed. Visible spectral response with CIE color coordinates (0.29 0.60) is assigned to the f–f electronic transitions of the Er^{3+} ion: $^2H_{11/2}$,$^4S_{3/2}\rightarrow {}^4I_{15/2}$ and $^4F_{9/2}\rightarrow {}^4I_{15/2}$ which are consequence of successful energy transfer from Yb^{3+}. Measuring of the up-conversion intensity in the function of pumping power (λ_{ex}=980nm), as well as presenting of obtained results in log-log diagram gives straight line with constant *n* value which corresponds to the number of the excitation photons absorbed per emitted photon. Slope values of 1.25 ($^4S_{3/2}\rightarrow {}^4I_{15/2}$) and 1.32 ($^4F_{9/2}\rightarrow {}^4I_{15/2}$) obtained confirm that both, green and red emissions are established by two-photon processes [4].

References:

[1] F Auzel, Chem. Rev. 104 (2004) p.139
[2] J Xie et al, Nanotechnology 31 (2020) 505605
[3] C Chen, C Li, Z Shi, Adv. Sci. 3 (2016)1600029
[4] The research was financially supported by the Ministry of Education, Science and Technological Development of Republic of Serbia through agreements related to the realization and financing of scientific research work at the Institute of Technical Sciences of SASA and Innovative Centre Faculty of Chemistry Belgrade in 2022, contract numbers: 451-03-68/2022-14/ 200175 and 451-03-68/2022-14/200288, respectively.

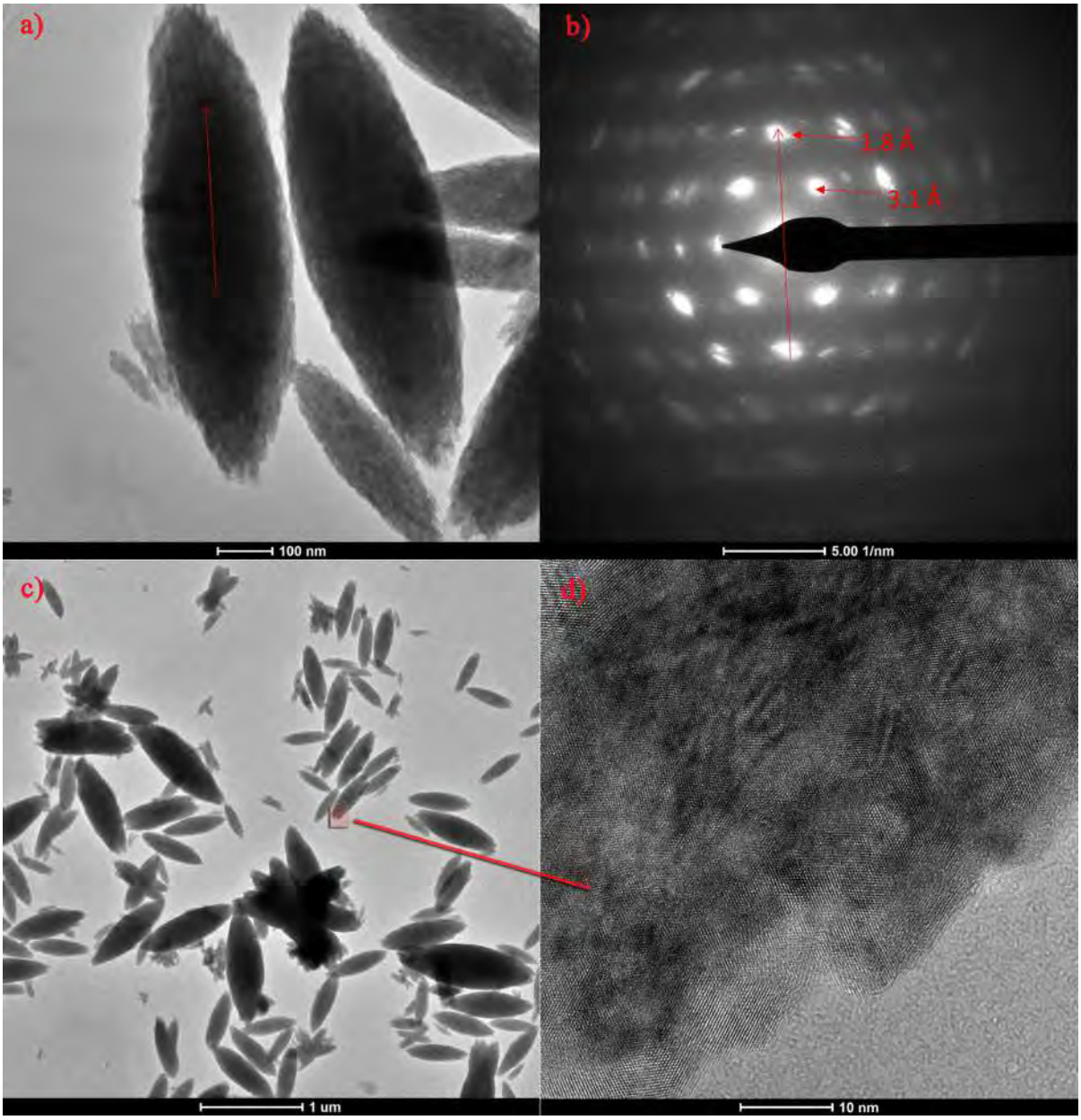

Figure 1. a) High-resolution transmission electron microscopy and b) selected area electron diffraction of (β) $NaYF_4$:Yb/Er mesocrystal; Scanning transmission electron microscopy c) and mesocrystal substructure d).

Scanning and Transmission Electron Microscopy Investigation of $SrGd_2O_4$: Yb,Tm Up-conversion Luminescent Material

Tijana Stamenković[1], Ivana Dinić[2], Marina Vuković[2], Vladimir Rajić[1], Nadežda Radmilović[1], Lidija Mančić[2], Vesna Lojpur[1]

1 Vinča Institute of Nuclear Sciences, National Institute of the Republic of Serbia, University of Belgrade, Belgrade, Serbia.

2 Institute of Technical Science of SASA, Belgrade, Serbia.

In recent decades, inorganic luminescent materials have gathered significant attention due to their great potential for various applications [1-4]. The rare-earth (RE)-based UC luminescent materials are particularly interesting for their exceptional optical, electronic, and magnetic properties. These materials have distinct intra-4f electronic transitions and existence of plenty long-living electronic excited states at different energies, all of which makes electron promotion to high-energy states possible [5, 6].

RE-based UC luminescent materials are composed of a host material (matrix), a sensitizer (absorbs the IC radiation), and an activator (provides emission in the visible and UV part of the spectrum) [7]. So far, the best results have been gained by co-doping the matrix using Yb^{3+} as sensitizer and Er^{3+}, Ho^{3+}, Tm^{3+}, etc. as activators [8-10]. As for the hosts, rare-earth oxides (ARE_2O_4; A = Ca, Sr, Ba and RE = trivalent rare-earth ions) have great perspective for producing highly efficient luminescent materials. To the best of our knowledge, $SrGd_2O_4$ has been poorly investigated so far, although it has an enormous potential for variety of applications since it is environmentally friendly, has high thermal stability and good chemical durability [11]. In this work, we will present new UC luminescent material composed of $SrGd_2O_4$ (host) doped with Yb^{3+} (sensitizer) and Tm^{3+} (activator).

Control of particle morphology has attracted a great deal of attention from researchers, so efforts for finding appropriate synthesis method are still very current issue. The morphology of the obtained particles is mostly influenced by the synthesis methods used for preparing the material. Luminescent properties mainly interested for us, are in very close connection with the morphology. Here, samples were synthesized using glycine-assisted combustion method, with constant concentration of Tm^{3+} (1 at%) and different concentration of Yb^{3+} (2, 4, 6 at%). All samples were heated in the furnace at 500 °C for 1.5h and then thermally treated for 2.5 h at 1000 °C. X-ray diffraction (XRD) was used to see phase crystallinity and purity, and revealed that all peaks are assigned to the pure orthorhombic lattice of $SrGd_2O_4$ with space group *Pnma* (JCPDS Card No.:01-072-6387). Luminescent properties were investigated after recording UC luminescence spectra at room temperature under 980 nm excitation for all samples. The spectra revealed strong blue emission bands which originates from Tm^{3+} ions $^1D_2 \rightarrow {}^3F_4$ and $^1G_4 \rightarrow {}^3H_6$ and weak red emission $^1G_4 \rightarrow {}^3F_4$ transitions. Morphology and structure were thoroughly studied by field emission scanning electron microscopy (FE-SEM) and transmission electron microscopy (TEM), whilst energy dispersive spectroscopy (EDS) was used to provide additional information about constituting elements and their distribution. FE-SEM analysis revealed irregular spherical-like morphology with all samples, and particle size of around 100 nm. TEM examination showed nanostructures organized as a group of agglomerated nanoparticles. EDS verified uniform distribution of all composing elements through every sample [12].

References:

[1] A Kitai in “Luminescent Materials and Applications”, ed. A Kitai, (Wiley & Sons, New York).
[2] A Silversmith, W Lenth and R Macfarlane, Applied Physics Letters **51** (1987), p. 1977.
[3] P Shuai *et al*, RSC Advances **10** (2020), p. 1658.
[4] R Khrishnan *et al*, Journal of Alloys and Compounds **878** (2021), p. 160386.
[5] V Lojpur, P Ahrenkiel and M Dramicanin, Nanoscale Research Letters **8** (2013), p. 131.
[6] A Shyichuk *et al*, Journal of Luminescence **170** (2016), p. 560.
[7] X Wang *et al*, Matererials Chemistry and Physics **99** (2006), p. 370.
[8] M Quintanilla *et al*, Applied Physics Express **4**(2) (2011), p. 022601.
[9] V Lojpur *et al*, Ceramics International **39** (2013), p. 1129.
[10] N Ishiwada, T Ueda and T Yokomori, Journal of Biological Chemistry **26** (2011), p. 381.
[11] J Zhang *et al*, Journal of American Ceramic Society **95** (2012), p. 243.
[12] The research was funded by the Ministry of Education, Science and Technological Development of the Republic of Serbia on the research program grant No. 0402211, Vinča Institute of Nuclear Sciences, National Institute of the Republic of Serbia, University of Belgrade, Serbia.

Different Up-conversion Oxides Co-doped with Er^{3+}/Yb^{3+} Synthesized at High Temperatures

Nadežda Radmilović[1], Tijana Stamenković[1], Vesna Lojpur[1], Ivana Dinić[2], Lidija Mančić[2]

1 Vinča Institute of Nuclear Sciences, National Institute of the Republic of Serbia, University of Belgrade, Department for atomic physics, Belgrade, Serbia.

2 Institute of Technical Science of SASA, Knez-Mihailova 35/4, Belgrade, Serbia

The process where long-wavelength excitation radiation is converted into shorter wavelength output radiation is known as photon upconversion (UC). Research of up conversion materials is mainly focused on chloride, bromide, fluoride and oxide compounds doped with Pr^{3+}, Nd^{3+}, Dy^{3+}, Ho^{3+}, Er^{3+} and Yb^{3+} as activators [1]. Activators are incorporated in the form of rear earth elements (REE) at a proper position in the host lattice. The unique emission mechanism of REE is associated with the incompletely filled 4f shell which enables large numbers of sharp intra-4f electronic transitions and the existence of abundant, long-living electronic excited states. Oxides possess relatively low phonon energy, high thermal stability and admirable intrinsic luminescence properties compared to chlorides and fluorides as host crystal lattice [2,3]. Various host latticed and dopant metal ions have been implemented for obtaining new UC compounds and in our work we studied Ln_2MoO_6 (Ln=Y,Gd) and $Sr_2Gd_2O_4$ doped with various concentrations of Yb^{3+} at constant Er^{3+} concentration. Synthesized powders were examined by X-ray diffraction (XRD), scanning electron microscopy (SEM), transmission electron microscopy (TEM) and luminescence emission and excitation spectroscopy.

XRD analyses showed that $SrGd_2O_4$ single phase is obtained at 1100 °C, Gd_2MoO_6 phase starts to form at 750 °C and the pure phase is obtained at 900 °C, while Y_2MoO_6 was obtained at the lowest temperature of 600 °C. TEM analyses gave insight into particle size - powders obtained at lowest temperatures (Y_2MoO_6) have the smallest particle size in the range of ~10 nm (Figure 1a), while $SrGd_2O_4$ exhibited grain sizes in 150-200 nm range (Figure 1b). The EDS mapping confirmed presence of Yb^{3+}, uniformly distributed in host lattice. Photoluminescence spectra of $SrGd_2O_4$ showed emission peaks that can be assigned to the trivalent Er^{3+} f-f electronic transitions in the following way: two green emission bands at 523 and 551 nm while the red emission band at 661 nm. Continual intensification of UC with the increase of Yb^{3+} content indicates that the $SrGd_2O_4$ host matrix easily accommodates high dopant concentration without quenching. Photoluminescence properties showed that co-doped Y_2MoO_6 has double emitting luminescence with green emission band at 546 and 560 nm ($^2H_{11/2}$, $^4S_{3/2} \rightarrow {}^4I_{15/2}$) and red emission band at 655 nm ($^4F_{9/2} \rightarrow {}^4I_{15/2}$); Gd_2MoO_6 showed double emitting luminescence with two green emission bands at 525 and 546 nm as well as a red emission band at 657 nm. The green UC emission intensity increased gradually with the increment of Yb^{3+} ion concentration. In comparison, the optimal doping concentration for the red UC emission was found to be 2.5 at %, which was much higher than that of the green UC emission. While the change of Yb^{3+} ion concentration does not influence the band position, it led to the change of the emission intensity. Increase of Yb^{3+} concentration in the host lattice leads to change of the green to red ratio, showing the ability for fine-tuning of the color output. Therefore, these materials can be used in lasers and devices for optical communications because of the infrared-to-visible light conversion.

References:

[1] W Yang *et al*, Nanotechnology **25** (2014), p. 482001.
[2] P Du, X Huang and J S Yu, Inorganic Chemistry Frontiers **12** (2017), p. 1987.
[3] X Huang *et al*, Chemical Society Reviews **42 (**2013), p. 173.
[4] The authors acknowledge funding from the the Ministry of Education, Science and Technological Development of the Republic of Serbia, under contract No. 451-03-68/2022-14/200017.

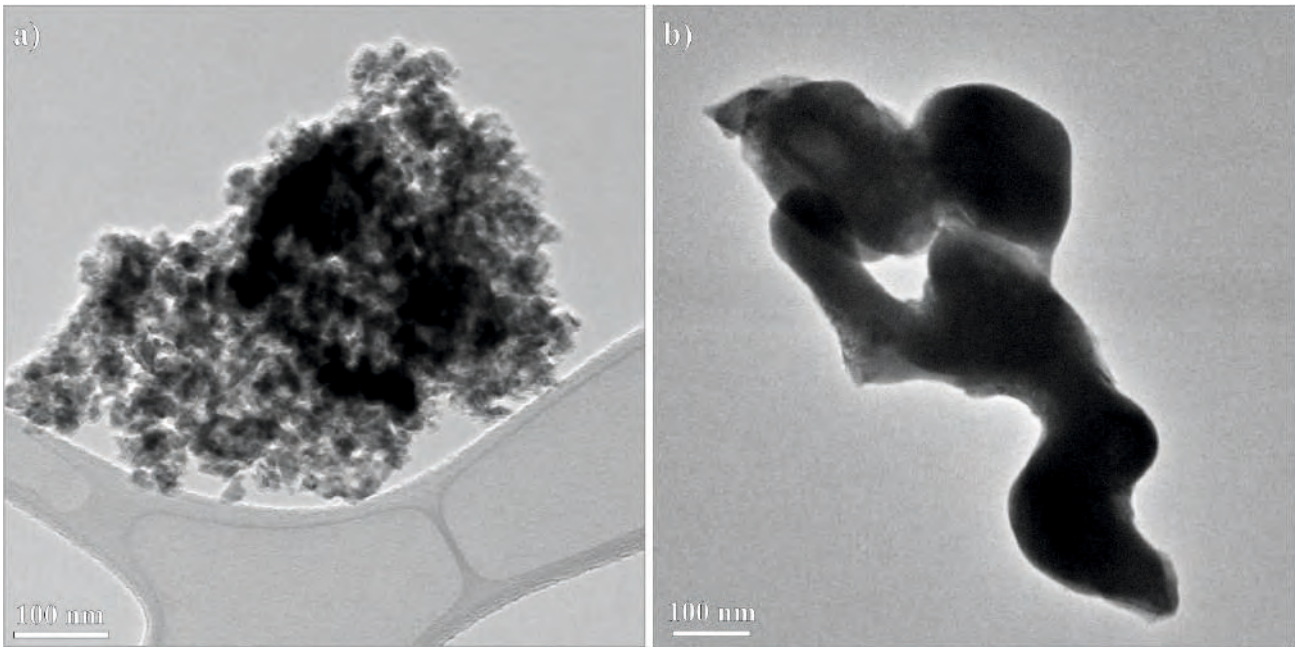

Figure 1. TEM images at low magnification of two up-convirsion oxides: a) Y_2MoO_6 obtained at 600 °C showed agglomerated nanoparticles with single particles of the ~10 nm; b) $SrGd_2O_4$ obtained at 1100 °C, grains are in the 150-200 nm range.

Carbon quantum dots-assisted CdS/TiO_2 heterojunction for photocatalytic reduction of hexavalent chromium under visible light

Jana Petrović[1], Slavica Lazarević[1], Nemanja Barać[2], Vukašin Ugrinović[2], Đorđe Janaćković[1] and Rada Petrović[1]

1 University of Belgrade, Faculty of Technology and Metallurgy, Belgrade, Serbia

2 Innovation Center of Faculty of Technology and Metallurgy, Ltd, Belgrade, Serbia

In the field of photocatalysis, various semiconductor materials have been widely used, precisely because of their electronic structure, which allows them to operate under the different types of irradiations. Titanium dioxide, TiO_2, is the most widely used photocatalyst due to its biological and chemical inertness, non-toxicity, availability and affordability. Nevertheless, the inefficient utilization of visible light and high recombination rate of electrons and holes, limit its practical application. Two types of modifications have been used to improve certain properties of TiO_2 and take the advantages of the good ones: changing the phase structure, crystallinity, or morphology and combining with various ions, noble metals, semiconductors or other materials by doping, deposition, or sensitization [1,2]. In this work, sol-gel synthesized TiO_2 [3] was modified by depositing carbon quantum dots (CQD) and/or cadmium sulfide, CdS, in order to form heterojunctions and so-called "Z" scheme [4]. CQDs were deposited by decomposition of citric acid in hydrothermal conditions (sample CQD-TiO_2), and CdS by thermal decomposition of thiourea in the presence of cadmium acetate (samples CQD-TiO_2 and CQD-TiO_2-CdS).

FESEM showed that TiO_2 is formed from relatively spherical particles of different sizes, which are composed of spherical nanoparticles, whose sizes are < 50 nm (Fig. 1a). It was not possible to clearly distinguish CQD particles in the sample CQD-TiO_2 by FESEM, but the beige color of the sample indicated the presence of CQD. FESEM and EDS analyzes of the samples CQD-TiO_2 and CQD-TiO_2-CdS confirmed the presence of randomly dispersed CdS nanoparticles on the surface of TiO_2 (Fig. 1b). Diffusion reflection spectroscopy (DRS) showed that the deposition of CQD slightly increased the light absorption limit of TiO_2, but also led to additional absorption in the visible part of the spectrum (Fig. 2). CdS is considered responsible for shifting the absorption limit of TiO_2-CdS and CQD -TiO_2-CdS up to ~530 nm (Fig. 2).

The obtained photocatalysts were used for photocatalytic reduction of Cr(VI) under simulated visible irradiation, at pH = 3. As it was expected, pure TiO_2 was inactive due to the wide band gap. The photocatalytic activity of CQD-TiO_2 was improved compared to pure TiO_2, thanks to CQD that expand the range of light absorption. While studying the photocatalytic activity of TiO_2-CdS, the concentration of Cr(VI) decreased during equilibration in the dark. The presence of Cd^{2+} in the solution, determined by atomic absorption spectroscopy, indicated CdS corrosion due to low pH values, so it is possible for S^{2-} ions to reduce Cr(VI). When comparing the overall performance of the samples with CdS, CQD -TiO_2-CdS had a much smaller decrease in Cr(VI) concentration during equilibration in the dark and better photocatalytic efficiency compared to TiO_2-CdS, which can be attributed to the presence of carbon nanoparticles and probably the formation of "Z" scheme, which provides significantly higher efficiency of photocatalysts than heterojunction type II, which is formed in TiO_2-CdS. The CQD-TiO_2 and CQD-TiO_2-CdS photocatalysts represent a good basis for further research with the aim of removing harmful Cr(VI) from waste streams.

References:

[1] M. Humayun, F. Raziq, A. Khan, W. Luo, Green Chemistry Letters and Reviews, 11 (2018), pp. 86–102.
[2] Y. Li, Z. Liu, Y. Wu, J. Chen, J. Zhao, F. Jin, P. Na, Applied Catalysis B: Environmental, 224 (2018), pp. 508–517
[3] R. Petrović, N. Tanasković, V. Djokić, Ž. Radovanović, I. Janković-Častvan, I. Stamenković, Dj. Janaćković, Powder Technology, 219 (2012), pp. 239-243
[4] H. Yin, Y. Cao, T. Fan, B. Qiu, M. Zhang, J. Yao, P. Li, X. Liu, S. Chen, Journal of Alloys and Compounds, 824 (2020), pp. 153915
[4] The authors acknowledge funding from the Ministry of Education, Science and Technological Development of the Republic of Serbia through the project E!13305 INSOLT-CHR and contracts No. 451-03-68/2022-14/200287, and 451-03-68/2022-14/200135.

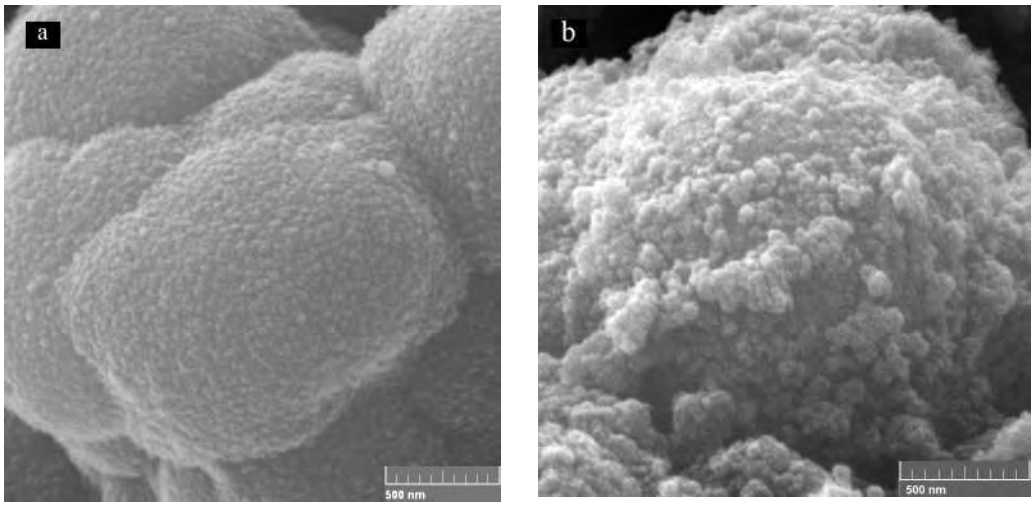

Figure 1. FESEM micrographs of a) TiO_2 and b) CQD -TiO_2-CdS.

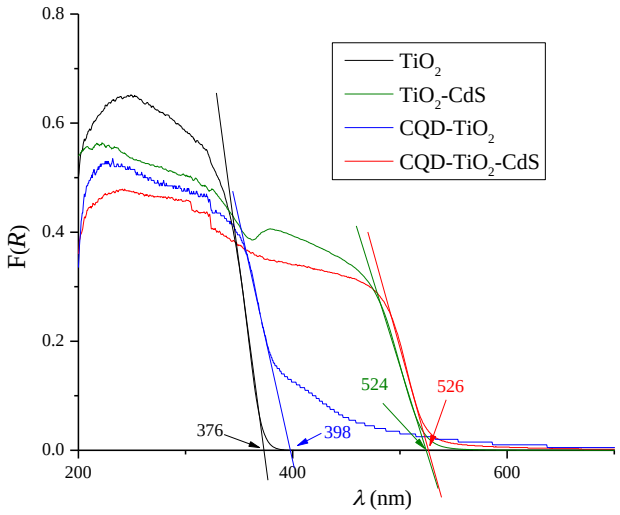

Figure 2. DRS spectra of TiO_2, CQD-TiO_2, TiO_2-CdS and CQD-TiO_2-CdS with marked absorption limits.

Structural Properties of $CaCu_3Ti_3RuO_{12}$

Smilja Marković[1], Ljiljana Veselinović[1], Lidija Mančić[1] and Paula M. Jardim[2]

1 Institute of Technical Sciences of SASA, Belgrade, Serbia.

2 Department of Metallurgical and Materials Engineering, Federal University of Rio de Janeiro, Rio de Janeiro, Brazil.

Due to a very large dielectric permittivity ($\geq 10^5$), thermal stability over a wide temperature range (from 100 to 400 K) and frequency independence in the frequency range of 1 kHz–1 MHz, calcium coper titanate ($CaCu_3Ti_4O_{12}$, CCTO) ceramics have been recognized as promising materials for applications in microelectronics industry and microwave devices [1–5]. Although a high permittivity value of CCTO-based materials allows fabrication of capacitors with improved capacitive performance for portable electronics devices, the nature of ceramics-metal electrode interface can deteriorate dielectric properties. Actually, significant differences in the crystal structure and electrical properties of the $CaCu_3Ti_4O_{12}$ as a dielectric material and a metallic electrode, can cause an energy barrier and the occurrence of stress on the ceramic-electrode interface which reduce the dielectric permittivity. Therefore, to avoid occurrence of an energy barrier and stress on the ceramic-electrode interface it is necessary to use dielectric ceramic and electrode with similar both crystal structure and unit cell parameters. The reduction of the stress on the ceramic-electrode interface can be achieved by using commercially available materials as an interlayer having lattice parameters match with both dielectric and electrode. It was noticed that incorporation of Ru^{4+} ions into the CCTO crystal structure significantly increases conductivity of these materials. It has been shown that $CaCu_3Ru_4O_{12}$ (CCRO) material is isostructural with $CaCu_3Ti_4O_{12}$ material, it has cubic $Im\bar{3}$ space group and shows metallic character [6]. Thys, since CCTO and CCRO have the same crystal structure and similar unit cell parameters, with CCRO layer as an interface between ceramic and electrode it can be possible to overcome problem of an energy barrier on the ceramic-electrode interface.

The aim of our work was to optimize Ti^{4+}/Ru^{4+} ratio in the $CaCu_3Ti_{4-x}Ru_xO_{12}$ crystal structure in order to obtain inexpensive, commercially acceptable, materials with the desired characteristics. Here we presented results of structural analysis of $CaCu_3Ti_3RuO_{12}$ ceramics, synthesized by the semi-wet precipitation method. The detailed structural analysis was done by the Rietveld refinement of X-ray powder diffraction data. The structural investigations were confirmed using TEM, HRTEM and ADF/STEM analysis including EDXS elemental mapping. The results of detailed crystal structure analysis show that regardless of the substitution of the Ti^{4+} ions by Ru^{4+} ions in the *B* crystallographic position, the crystal structure remains cubic with $Im\bar{3}$ space group. A slight increase of the unit cell parameters, cell volume and interatomic distances indicate that the larger radius ions (ruthenium) are incorporated in the $CaCu_3Ti_{4-x}Ru_xO_{12}$ crystal structure. The TEM, HRTEM and FFT analysis were performed as an additional confirmation of X-ray structural analysis. Fig. 1a shows TEM micrograph of $CaCu_3Ti_3RuO_{12}$ powder. The HRTEM image (Fig. 1b) and corresponding fast Fourier transformation (FFT) confirmed the cubic crystal symmetry with $Im\bar{3}$ space group. Fig. 1c, shows two sets of crystallographic planes (400) and (220) with *d*-values of 1.8 and 2.6 Å, respectively which is in agreement with literature data for cubic $CaCu_3Ti_4O_{12}$ (JCPDS 75-2188). High-angle annular dark-field STEM, and corresponding energy-dispersive X-ray spectrum analysis, presented in Fig. 2 confirm the presence of ruthenium in the structure of $CaCu_3Ti_3RuO_{12}$.

References:

[1] K. Pal *et al*, Physical Chemistry Chemical Physics **22** (2020), p. 3499.
[2] R. Kumar *et al*, Crystal Growth and Design **15** (2015), p. 1374.
[3] N. A. Zhuk *et al*, Solid State Ionics **364** (2021), p. 115633.
[4] P. Thongbai *et al*, Journal of Applied Physics **112** (2012), p. 114115.
[5] S. Marković *et al*, Processing and Properties of Advanced Ceramics and Composites V: Ceramic Transactions (2013) p. 337.
[6] T. T. Tran *et al*, Physical Review B: Condensed Matter **73** (2006), p. 93105.

Acknowledgments: This study was financially supported by the Ministry of Education, Science and Technological Development of Republic of Serbia, through the agreement related to the realization and funding of scientific research work at the Institute of Technical Sciences of SASA in 2022, Contract number: 451-03-68/2022-14/200175.

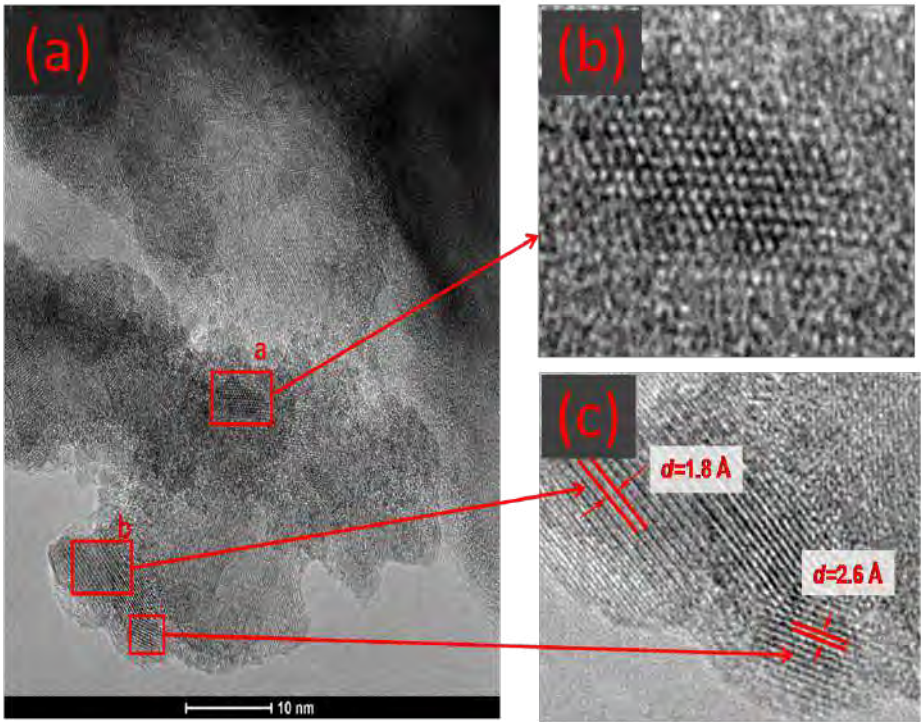

Figure 1. TEM micrograph (a), HRTEM (b) and FFT analysis (c) of $CaCu_3Ti_3RuO_{12}$ powder.

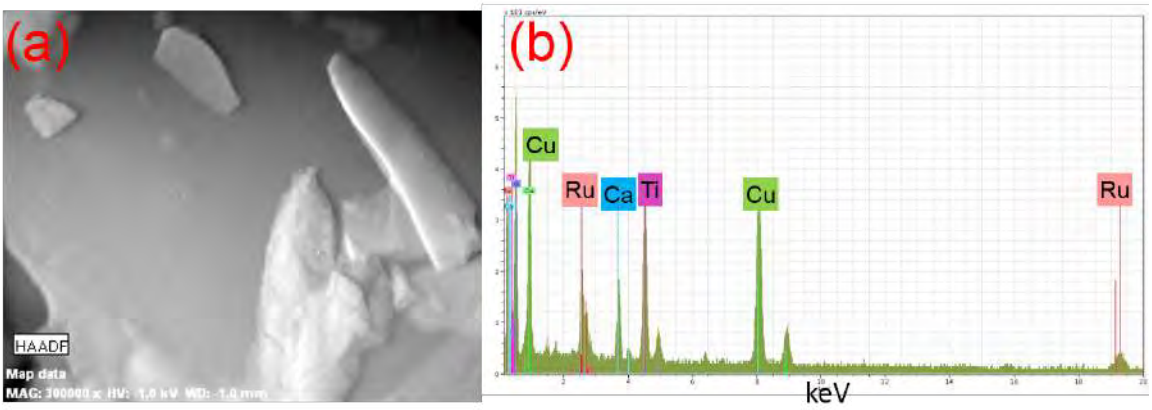

Figure 2. High-angle annular dark-field STEM (a), and corresponding energy-dispersive X-ray spectrum (b) of $CaCu_3Ti_3RuO_{12}$ powder.

Multilayer and Epitaxial Multiferroic Thin Films Prepared by Solution Deposition Technique

Danica Piper[1], Jelena Vukmirović[1], Branimir Bajac[2], Sara Joksović[2], Miloš Bokorov[3], Andrea Nesterović[1], Ivan Stijepović[1], Marija Milanović[1], Elvira Toth[4], Željka Cvejić[4], Vladimir V. Srdić[1]

1 Faculty of Technology, Department of Materials Engineering, University of Novi Sad, Serbia

2 BioSense Institute, University of Novi Sad, Serbia

3 Faculty of Sciences, Department of Biology and Ecology, University of Novi Sad, Serbia

4 Faculty of Sciences, Department of Physics, University of Novi Sad, Serbia

Multiferroic materials simultaneously show ferroelectric and ferromagnetic properties. The attractiveness of these materials lays in magnetoelectric coupling effect which makes them desirable in different fields of applications. As the magnetoelectric effect in single-phase systems does not meet the needs of nowadays technologies, multiphase structures have been imposed as a solution. Among them there is great interest in materials in the form of thin films whose functionality differs from bulk materials due to the presence of strain in the structure caused by the interaction of film and substrate layers.

Perovskite structure materials are most often used as the ferroelectric phase, while ferrite-based spinels or perovskite materials, such as some manganites, are used as a ferromagnetic phase. By controlling the strain at the interface, it is possible to directly couple ferroelectric and ferromagnetic orders and produce strong magnetoelectric coupling [1]. Nanostructure form of these materials is very desirable since it satisfies needs of novel microelectronic devices. In addition, some multiferroic systems are very sensitive to external stimuli such as magnetic and electric field or light, and special interest is caused by possibility of manipulation of magnetic order by ultrashort laser pulses. This phenomenon opens new field of application in spintronic and data storage devices [2].

The aim of this work was obtaining multiferroic multilayered thin films. In the first part of this research the focus was on preparation of multilayered structure based on $NiFe_2O_4$ as a ferromagnetic layer and $BaTiO_3$ as a ferroelectric layer. Both layers were prepared by sol-gel method and deposited on commercial Si substrate by spin coating. The precursor solution for the deposition of $BaTiO_3$ phase was prepared by mixing of $BaCO_3$ dissolved in glacial acetic acid with tetrabutyl-orthotitanate ($Ti(OC_4H_9)_4$. Ferrite phase was deposited from a clear, brownish precursor solution, prepared by dissolving stoichiometric amounts of $Fe(NO)_3 \times 9H_2O$ and $Ni(NO)_3 \times 6H_2O$. Structural analysis was performed by XRD, AFM, SEM and HRTEM and gave information about the phase composition, thickness of layers and grain structure (Fig. 1). Measurements of electric and magnetic properties were also performed.

In the second part of this research, the aim was obtaining epitaxial multiferroic bilayered films. Epitaxial ferromagnetic layer, $LaMnO_3$ or $(La,Sr)MnO_3$, was prepared by polymer-assisted deposition (PAD) technique on single crystal $SrTiO_3$ (001) substrates using aqueous solution of corresponding cations stabilized with PEI and EDTA. The second ferroelectric layer, $BaTiO_3$ or $(Ba,Sr)TiO_3$, was prepared by chemical solution deposition technique, using $BaCO_3$, $Sr(C_2H_4O_2)_2$ and Ti-alcoxide as a precursors.

Structural characterization of thin films was done by XRD, AFM and HRTEM which confirmed

phase composition and epitaxial growth (Fig. 2). Electrical and magnetic measurements were also performed.

References:

[1] W Eerenstein, N. D. Mathur, J. F. Scott, Nature **442** (2006), p.17.
[2] S Majumdar, S van Dijken, J. Phys. D: Appl. Phys. **47** (2014), p.15.

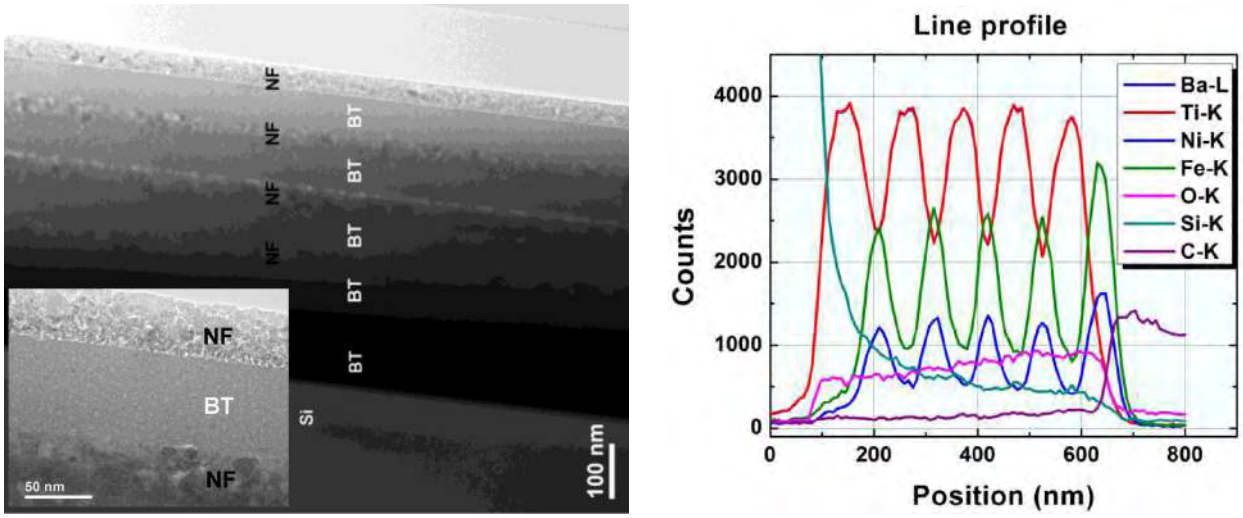

Figure 1. TEM image of multilayer BaTiO3/$NiFe_2O_4$ thin film thermal treated at 500 °C.

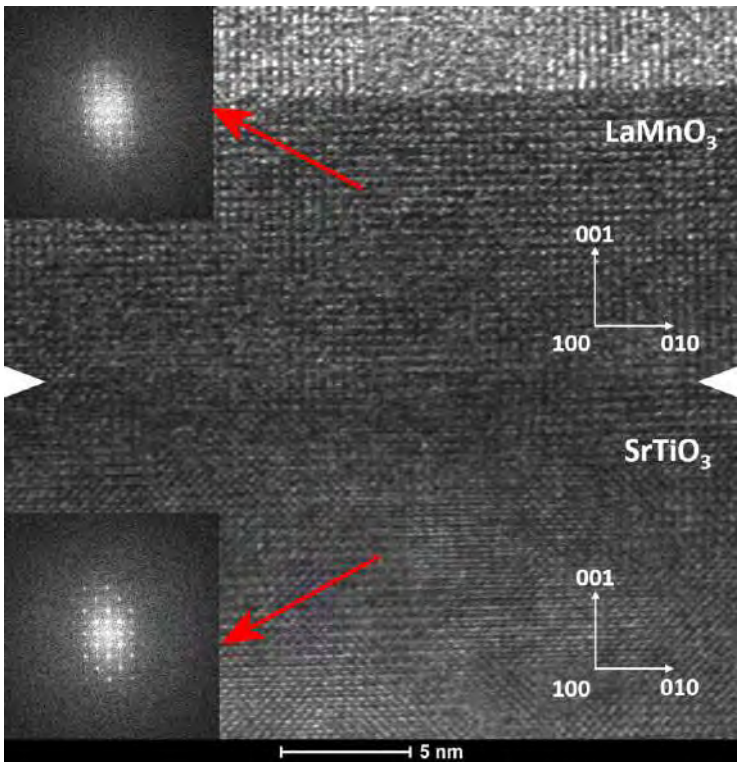

Figure 2. TEM image of epitaxial $LaMnO_3$ thin film on single-crystal $SrTiO_3$ substrate.

Nanodomain Structure and Charged Domain Walls in Single Crystal $BiFeO_3$

Wanbing Ge[1], Quentin Ramasse[2], Richard Beanland[1], Marin Alexe[1], Ana Sanchez[1]

1 Department of Physics, University of Warwick, Coventry CV4 7AL, United Kingdom

2 SuperSTEM Laboratory, SciTech Daresbury, Keckwick Lane, Warrington WA4 4AD, United Kingdom

Ferroelectric materials are characterized by the existence of reversable spontaneous polarization (Ps) without external electric field[1]. To minimize total system energy, local ferroelectric domains with aligned Ps are usually generated inside the material when transiting into ferroelectric phase, and are separated by domain walls where Ps adapts its orientation and/or magnitude within several atomic lengths. Their accessible manipulation to be reproducibly written, erased, and moved has enabled domain walls to play an active role in future electronic devices[2]. Among them, the so-called charged domain wall has drawn special attention because its discontinuity of Ps' normal component across the wall will significantly increase the system energy and need to be compensated either by accumulating portable bound charges at this ultrathin interface, or by introducing charged local phase[3]. Either case would result in novel electrical properties that have not been observed in the bulk, such as enhanced conductivity. But due to its less favourable energy configuration, charged domain walls, especially those strongly charged 180° walls, are rarely found and their properties less studied in literature so far.

Here we report our study of domain distribution[4] and structure analysis in multiferroic perovskite $BiFeO_3$ single crystal[5,6] by various electron microscopy methods, with an emphasis on atomic resolution scanning transmission electron microscopy (STEM). The crystal has a very regular domain pattern where sawtooth domain walls are sandwiched by stripe domain walls, as conformed by diffraction contrast TEM and PFM (Fig.1). For $BiFeO_3$, main contribution of Ps comes from the shift of Bi atoms away from their surrounding Oxygen octahedra, and Ps value is conventionally quantified by calculating the shift of Fe atoms relative to their nearest Bi unit cell. With the help of atomic resolution STEM, we can record the position information of Fe and Bi atoms within nanodomain areas under bright/dark field imaging and then map domain distribution. By examining specimens made from different orientations such as psedocubic (100), (001), (110) and (1-10) and treating them as projections of the same structure viewed from different directions, it is possible for us to reconstruct the domain distribution in a three-dimensional way that explains our observations.

As a result, we have identified two types of 180° domain walls in this sample, with the stripe domain walls being head-to-head and sawtooth walls being tail-to-tail (Fig.2). Our three-dimensional model shows that the stripe walls intersect with $[111]_{pc}$ Ps at about 70°, while the sawtooth walls have an intersection angle less than 10°, so the former are more strongly charged.

To understand the mechanisms behind those highly charged domain walls, we also tried to take annular bright field (ABF) images where the light O atoms can be seen, making it possible to study the behaviour of Oxygen octahedra at the domain walls. What is more, high resolution EELS analysis has been conducted at the domain walls, which gives additional information about how the chemical status changes within these areas.

In this work, we report the observation and analysis of regular nano-domain pattern in single crystal $BiFeO_3$. Two types of 180° domain walls have been found in this crystal, with one being head-to-head walls and the other tail-to-tail walls. Structural and chemical changes are studied to explain the

mechanism behind those charged domain walls.

References:

[1] J Scott, Applications of Modern Ferroelectrics. Science 2007, 315 (5814), 954–959.
[2] J Seidel *et al*, Conduction at Domain Walls in Oxide Multiferroics. Nature Mater 2009, 8 (3), 229–234.
[3] I MacLaren *et al*, The atomic structure and chemistry of Fe-rich steps on antiphase boundaries in Ti- doped Bi0.9Nd0.15FeO3. APL Materials 2, 066106 (2014).
[4] J Peters *et al*, Polarization Curling and Flux Closures in Multiferroic Tunnel Junctions. Nat Commun 2016, 7 (1), 13484.
[5] A Berger *et al*, Regular Nanodomain Vertex Arrays in BiFeO3 Single Crystals. Phys. Rev. B 2012, 85 (6), 064104.
[6] CL Jia *et al*, Nanodomains and Nanometer-Scale Disorder in Multiferroic Bismuth Ferrite Single Crystals. Acta Materialia 2015, 82, 356–368.

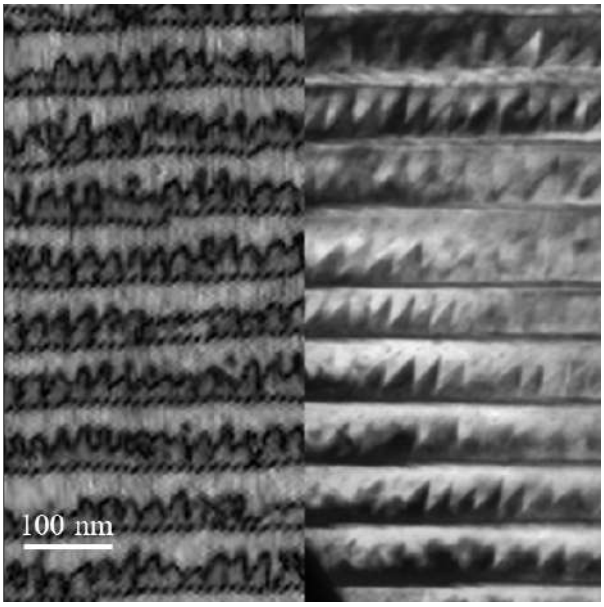

Figure 1. Domain patterns observed by PFM (left) and diffraction contrast TEM (right). Stripe and sawtooth nanodomains can be found in both cases.

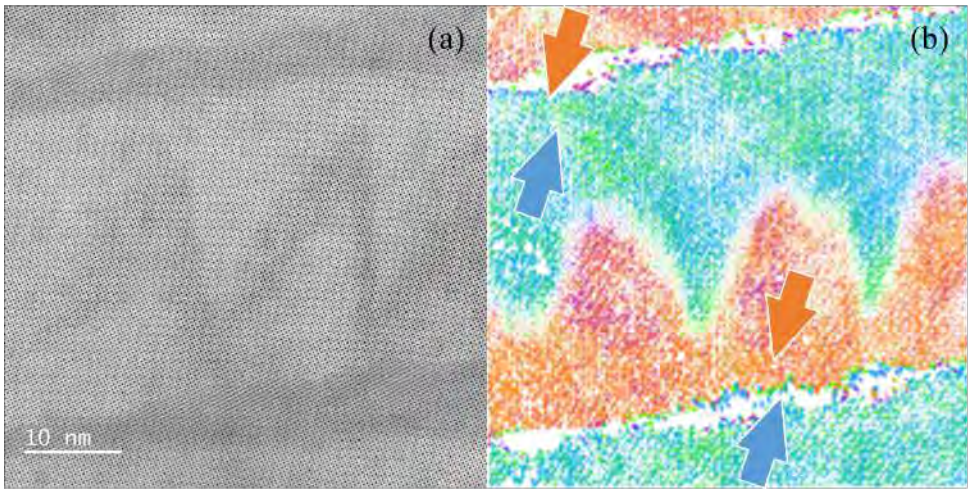

Figure 2. (a) Atomic resolution STEM-BF image of a nanodomain area in $(001)_{pc}$ sample; (b) Ps map of image (a) with arrows indicating Ps direction.

Cobalt Ferrite Nanospheres for Removal of Cr^{6+} Ions from Waste Water

Sonja Jovanović, Željko Mravik, Jelena Rmuš, Marija Grujičić, Marko Jelić, Milica Pejčić, Zoran Jovanović

Laboratory of Physics, Vinča Institute of Nuclear Sciences – National Institute of the Republic of Serbia, University of Belgrade, Belgrade, Serbia

Water is the most important resource sustaining life on the Earth. However, the growth of the industry and rapid increase of human population leads to an increase in water pollution caused by heavy metals [1,2]. Thus, providing a clean water is of essential importance. One of the toxic elements whose presence in nature is caused both by natural sources, such as volcanic activity, mineral weathering and erosion, forest fires, and by anthropogenic activities, including electroplating, metal finishing, leather tanning, dye and textile industries is chromium (Cr) [3,4]. According to the World Health Organization the maximum level of chromium in drinking water is 0.05 mg/L [5]. Among the conventional techniques for the removal of heavy metals, such as chemical precipitation, ion exchange, membrane separation, reverse osmosis, electrochemical treatment, etc [6], adsorption is recognized as a simple, effective and economical method for the removal of metal ions from wastewater. Among other methods, the use of nanosized magnetic materials as adsorbents has recently attracted significant interest due to their high surface area and optimal magnetic properties, which lead to high adsorption efficiency, high removal rate of contaminants, and easy and rapid separation of adsorbent from solution via magnetic field [7]. The aim of this study was to prepare magnetic, cobalt ferrite, nanospheres (CFO NS) by solvothermal method under different synthesis conditions and to explore their use as adsorbents for the removal of Cr^{6+} ions from aqueous solution.

Cobalt ferrite nanospheres (CFO NS) were prepared via one-step, template free solvothermal method. In a typical synthesis, 2.4 mmol of $FeCl_3 \cdot 6H_2O$ was dissolved in 30 ml of ethylene glycol. After that, 1.2 mmol of $CoCl_2 \cdot 6H_2O$ was poured into the above solution under vigorous stirring until it dissolved. Finally, ethanolamine (EA, 1.5 ml or 3.0 ml) was added to the solution and kept under vigorous stirring for 1 h at room temperature, after which the autoclave was closed and placed into an oven at 200 °C for different synthesis time. Then, obtained particles were washed with deionized water and ethanol. Finally, they were re-dispersed in ethanol, transferred to the watch glass, and left to dry in the air overnight. The synthesized materials were characterized by X-ray powder diffraction (XRD), scanning electron microscopy (SEM), transmission electron microscopy (TEM) and vibrating sample magnetometry (VSM). Scanning transmission electron microscopy (STEM EDXS) analysis was used for elemental mapping of CFO NS after adsorption of Cr^{6+} ions [8].

The XRD results confirmed the cubic spinel structure of CFO NS while the SEM revealed sphere-like morphology with diameters of the CFO NS in the range of 100–300 nm (**Figure 1a,b**). TEM images showed that each NS is composed of smaller CFO nanoparticles with size around 7–8 nm (**Figure 1c,d**). The magnetic measurements revealed ferromagnetic character of CFO nanospheres with the maximum saturation magnetization and coercivity of 75 emu/g and 677 Oe, respectively. The synthetized CFO NS were tested as an adsorption material for removal of Cr^{6+} ions from aqueous solution. The elemental mapping illustrates the homogeneous distribution of cobalt (Co), iron (Fe) and oxygen (O) ions, as well as Cr^{6+} ions adsorbed on the surface of CFO NS (**Figure 2**). The obtained removal efficiency is in the range from 38 to 88%. The results suggest that the adsorption capacity of CFO NS strongly depends on conditions of the solvothermal synthesis [8].

References:
[1] M Fujita *et al*, Chemosphere 95 (2014), p. 628.
[2] G Akinci *et al*, Environ. Sci.-Proc. Imp. 15 (2013), p. 2252.
[3] S Sander *et al*, Electroanal. 15 (2003), p. 1513.
[4] L.-X Yang *et al*, J. Nanomater. 2013 (2013), p. 5.
[5] World Health Organization, Guidelines for Drinking Water Quality, WHO Press, Geneva, Switzerland (2011), p. 564.
[6] F. Fu and Q. Wang, J. Environ. Manage. 92 (2011), p. 407.
[7] AR Vazquez-Olmos *et al*, J. Nanomater. 2016 (2016), p. 9.
[8] S Jovanović *et al*, J. Nanosci. Nanotechnol. 19 (2019), p. 1–8.

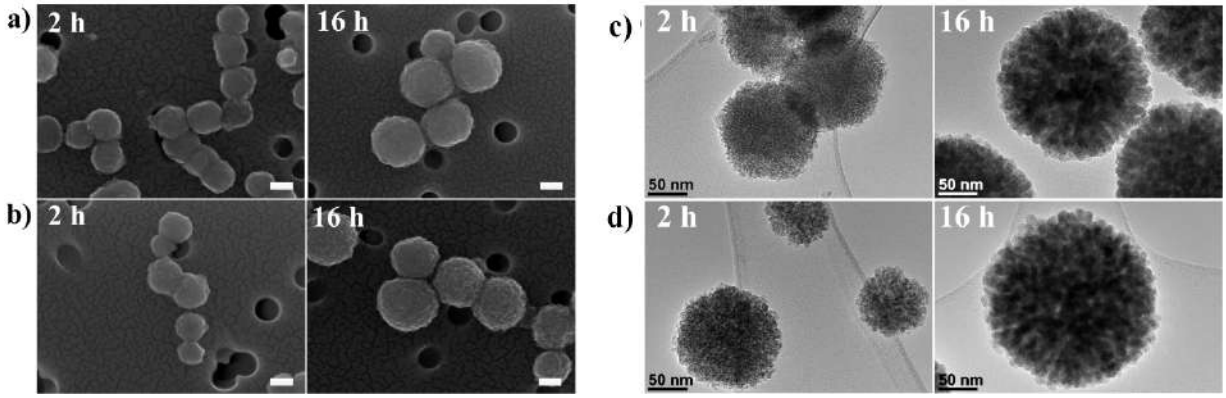

Figure 1. SEM (a,b) and TEM (c,d) micrographs of CFO NS prepared with 1.5 ml (a,c) and 3.0 ml (b,d) EA at T = 200 °C for 2 h and 16 h. Scale bar is 100 nm.

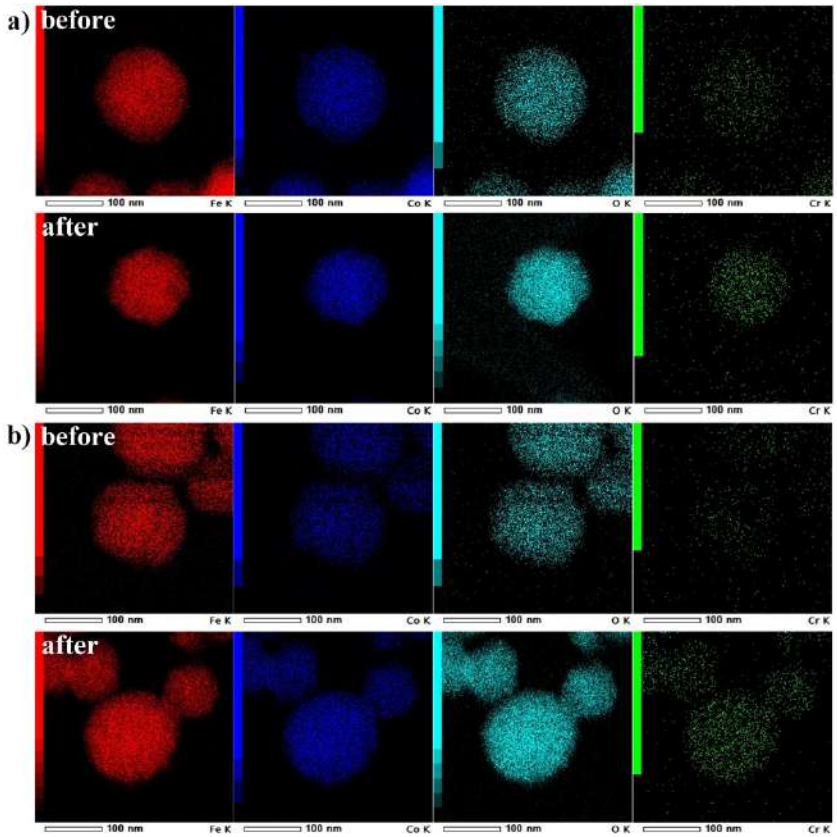

Figure 2. STEM EDXS mapping of the CFO NS prepared with (a) 1.5 ml EA and (b) 3.0 ml EA for 2 h after Cr^{6+} adsorption.

Influence of Plasmon-excitation Electrons on Ptychography Phase Imaging

Zhiyuan Ding[1], Angus I. Kirkland[1,2,3], and Peter D. Nellist[1]

1 Department of Materials, University of Oxford, Oxford, OX1 3PH, UK

2 Electron Physical Sciences Imaging Centre, Diamond Light Source Ltd., Harwell Science and Innovation Campus, Didcot OX11 0DE, UK.

3 The Rosalind Franklin Institute, Harwell Campus, Didcot OX11 0FA, UK.

Electron ptychography is a phase retrieval method in transmission electron microscopes (TEM) in which the phase of exit wavefunction is reconstructed from electron diffraction patterns[1]. It is used for a wide range of specimens for atomic-scale imaging, including sensitive battery materials[2] and biological structures[3]. As a method of coherent imaging, contrast of electron ptychography is based on coherence of electron beam. However, inelastic scattering that happens in the interaction between beam and specimen introduces an energy distribution of the exit beam. With increased thickness of the sample, the proportion of inelastic scattered electrons (most of which are plasmon-excited electrons) increases. In this work, we investigate the influence of inelastic electrons, especially plasmon-excited electrons on ptychographic reconstruction.

To explore the influence of inelastic scattered electrons, in an aberration-corrected TEM at 200kV, 4D-STEM datasets with and without energy filter were recorded at different defocus conditions on a sample of gold nanoparticles and carbon film. The convergence angle of the electron beam is 22 mrad. Then ptychography reconstructions were carried out on recorded 4D-STEM datasets using the ePIE algorithm[4].

The reconstruction results shows that phase contrast images for atomic-scale resolution are stable whether or not the inelastic scattered electrons are filtered. This result is in line with the prediction based on characteristic scattering angle for inelastic scattering. For this experiment, the characteristic scatter angle of plasmon-exited electrons (energy loss: 20 eV) is 0.005 mrad. However, the pixel size of 4D-STEM detector used in the experiment is 0.25 mrad, which is far bigger than the characteristic scatter angle. This means that statistically, most electrons will still be detected by the same pixel whether or not they are inelastic scattered along with the image-forming elastic scattering. Therefore, the normalized intensity distribution of recorded diffraction patterns with or without energy filter are almost the same.

However, if a smaller pixel size is used, i.e. a larger camera length, for a beam with a smaller convergence angle, the situation is different. For example, if a convergence angle of 1~2 mrad is used for large field-of-view ptychographic imaging3, the pixel size on detector may be comparable to characteristic scatter angle under a similar experimental condition. In this situation, the influence of inelastic scattered electrons on electron ptychography should not be ignored.

References:

[1] P. Nellist, B. McCallum, and J. M. Rodenburg, *Nature*, vol. 374, no. 6523 (1995), pp. 630-632.
[2] J. G. Lozano *et al.*, *Nano letters*, vol. 18, no. 11 (2018), pp. 6850-6855.
[3] L. Zhou *et al.*, *Nature communications*, vol. 11, no. 1 (2020), pp. 1-9,.
[4] A. M. Maiden and J. M. Rodenburg, *Ultramicroscopy*, vol. 109, no. 10 (2009), pp. 1256-1262.

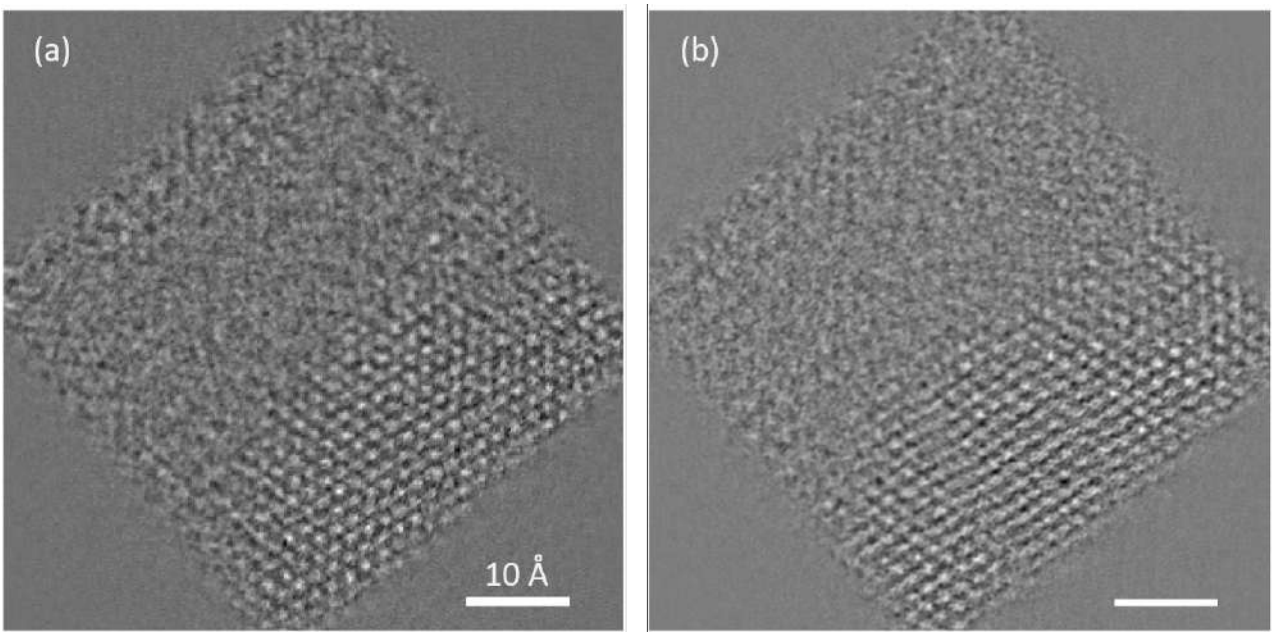

Figure 1. Ptychographic phase reconstructions (a) without energy filter, i.e. elastic and inelastic scattered electrons are both recorded, and (b) with energy filter, i.e. only elastic scattered electrons are recorded. Defocus value is -14 nm.

Atomic Scale Observations and Analysis of the Island Grain Shrinkage in <110> Au Thin Films

Tamara Radetić[1] and Ulrich Dahmen[2]

1 University of Belgrade, Faculty of Technology and Metallurgy, Belgrade, Serbia

2 Molecular Foundry - NCEM, LBNL, Berkeley, USA

The mobility of grain boundaries has a crucial influence on the stability and microstructure evolution of nano-crystalline and ultrafine-grained metallic materials. Recent advances in TEM instrumentation with the extended range of spatial and temporal resolution enabled observations of atomistic mechanisms of migration of the singular interfaces by glide, step motion and cooperative shuffles [1-5]. In this paper, we report on atomic mechanisms and dynamics of grain boundary migration during shrinkage of small island grains in 90° <110> bicrystals of Au thin films under the influence of capillary forces.

The results of in-situ conventional and atomic resolution electron microscopy showed that the rate of grain shrinkage does not obey parabolic kinetics but is irregular, characterized by bursts of rapid, localized motion alternating with long periods of stagnation [5]. The grain rotation, expected for shear/migration coupling, was not observed even at the smallest grain sizes (Figure 1), similar to the results of study on shrinking island grains in Al [6]. It was found the nucleation and propagation of steps on grain boundary facets controls dynamics of the boundary migration.

The structural detail and temporal detail, provided by in-situ atomic resolution electron microscopy, enabled direct observation and characterization of steps structure, topology, frequency as well as such events as their nucleation and propagation. A pronounced anisotropy enforces pure tilt character for all boundaries in Au <110> bicrystal thin films. Statistical measurements of the grain shape evolving during shrinkage indicate a strong preference for three types of facets: A-facet $(\sqrt{211})_{\mu}$ / $(\sqrt{211})_{\lambda}$; B-facet $(111)_{\mu}$ / $(211)_{\lambda}$; C-facet $(100)_{\mu}$ / $(011)_{\lambda}$. The mobility of the facets strongly depends on their crystallography and structure.

TV rate recordings showed that the most prominent, and shrinkage rate-controlling are C-facets. Many C-facets appear to be vicinal, i.e. their traces deviate from $(100)_{\mu}$ / $(011)_{\lambda}$, due to the step-like defects. Those defects, known as disconnections, have dislocation content in addition to the step component due to the incommensurate character of the boundaries [7]. Measurements showed that the step mobility depends on step height *m|n* (*In this work, n|m denotes the numbers of {100} and {011} at the step in adjacent grains*). The steps of even|odd parity have height mobility and tend to fluctuate along the C-facet (Figure 2). In the absence of step-like defects, the C-facets remain flat and stationary.

Most facets connected to C-facets are B- type and show 9R dissociation [3]. They may also appear vicinal due to the presence of steps whose hight can be correlated to the geometry of the 9R structure. The migration of B-facets appears to be more regular, shortening the encroached C-facet as they move inward. When encroached C-type facet reaches critical width, it advances perpendicularly to itself in discrete increments of 5|7 or 4|6. Those jumps, which involve cooperative motion of numerous atoms, are swift, occurring within a single frame at TV rate (0.03s). More detailed insight, enabled by employing Gatan K2-IS camera with recording rate of 2.5μs per frame, showed the jump proceeds by nucleation and progression of buried step [8] in the plane perpendicular to the film surface.

References:

[1] U. Dahmen et al., Philos. T. R. Soc. A 367 (2009), p. 3795.
[2] K. Merkle, L. Thompson, F. Phillipp, Interface Sci. 12 (2004), p. 277.
[3] D. L. Medlin, S. M. Foiles, D. Cohen, Acta Mater 49 (2001), p. 3689.
[4] M. L. Bowers et al., Phys. Rev. Lett. 116 (2016), 106102.
[5] T. Radetic et al., Acta Materialia 60 (2012), p. 7051.
[6] F. Mompiou et al., Acta Materialia 60 (2012), p. 2209.
[7] F. Lançon, Europhys. Lett. 57 (2002), p. 74.
[8] A. Gautam et al., Microsc. Microanal. 19 (S2) (2013), p. 596.
[9] This work at the Molecular Foundry – NCEM, LBNL, was supported by the Office of Science, Office of Basic Energy Sciences, of the U.S. DOE under Contract No. DE-AC02-05CH11231.

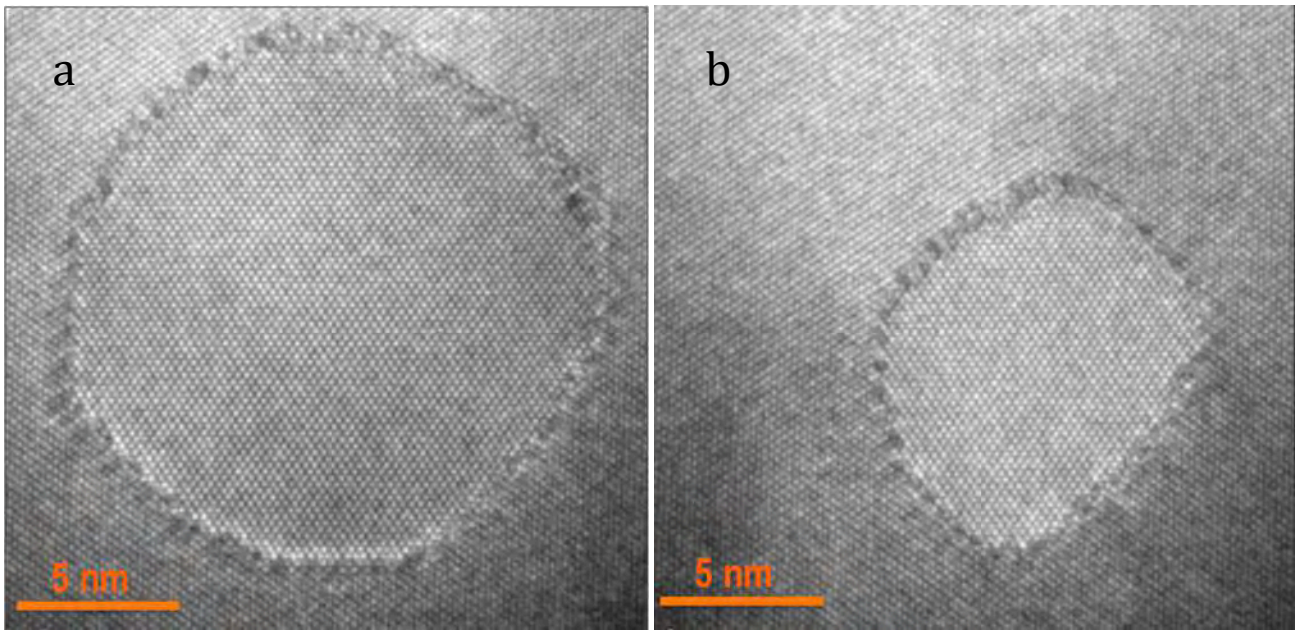

Figure 1. HREM images showing shrinking of the island grain: (a) grain 60 s before contraction; (b) same grain 33 ms before the collapse. No grain rotation was observed.

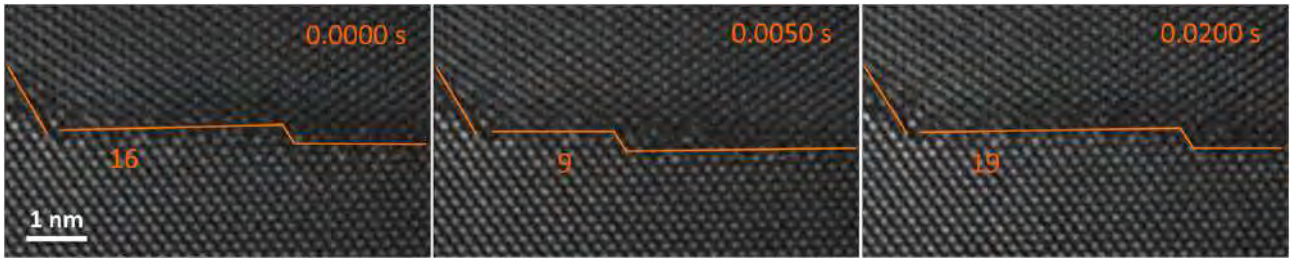

Figure 2. Sequence of images showing fluctuation of the step recorded with K2 camera at 217°C.

AUTHOR INDEX

Abdellaoui, Lamya		59
Achinuq, Barat		25
Ahmadian, Ali		55
Ahrens, Lara		65
Akinwande, Deji		105
Albu, Mihaela		53
Alexe, Marin		203
Arbiol. Jordi	arbiol@icrea.cat	49
Assender, Hazel E.		63
Babić, Biljana		157
Bajac, Branomir	branimir.bajac@tf.uns.ac.rs	185, 201
Bajčetić, Miloš		135
Bajuk-Bogdanović, Danica		173
Barać, Nemanja	nbarac@tmf.bg.ac.rs	197
Basagni, Andrea		139
Basak, Shibabrata		65
Beanland, Richard		203
Beckers, Maximilian		61
Beckett, Alison		83
Belić, Domagoj	dbelic@fizika.unios.hr	83
Bernaecker, Christian		123/181
Bernal, Miguel		117
Bjelajac, Andjelika	abjelajac@tmf.bg.ac.rs	125
Bokorov, Miloš		201
Bosch, Eric G.T.		75
Bozic, Bojan	bbozic@bio.bg.ac.rs	149
Bruce, Peter G.		63, 109, 121
Brust, Mathias		83
Bugarski, Branko	branko@tmf.bg.ac.rs	143
Bugarski, Diana		143
Bugnet, Matthieu		27
Bumbasirevic, Vladimir B.		81, 131, 133
Calderon, Sebastian		105
Carbo-Argibay, Enrique		113
Carlsson, Anna		61, 75
Chen, Hui		47
Ciric, Darko	darko.ciric@med.bg.ac.rs	81, 131, 133
Clark, William		51
Clausen, Alexandar		39
Cojocaru-Mirédin, Oana		59
Cojocaru, Costel S.		125
Couzinié, Jean-Philippe		51
Cvejić, Željka	zeljka.cvejic@df.uns.ac.rs	201
Czigany, Zsolt	czigany.zsolt@ek-cer.hu	99
Ćosović, Aleksandar	a.cosovic@itnms.ac.rs	95
Ćosović, Vladan	vlada@tmf.bg.ac.rs	95
Čeh, Miran	miran.ceh@ijs.si	117

Dachraoui, Wild		37
Dahmen, Ulrich	udahmen@lbl.gov	209
Daneu, Nina	nina.daneu@ijs.si	157
De Backer, Annick		107
de Haas, Felix		61
de Raveschoot, Victor W.P.		35
Dehm, Gerhard	dehm@mpie.de	55
Dimitrijević, Suzana	suzana@tmf.bg.ac.rs	153
Ding, Zhiyuan	zhiyuan.ding@materials.ox.ac.uk	207
Dinić, Ivana	ivana.dinic@itn.sanu.ac.rs	191, 193, 195
Djokić, Veljko R.	vdjokic@tmf.bg.ac.rs	89
Djuricic, Danica		131, 133
Dojcinovic, Milena	milena.dojcinovic@imsi.rs	171
Drvenica, Ivana	ivana.drvenica@imi.bg.ac.rs	143
Dunin-Borkowski, Rafal E.	r.dunin-borkowski@fz-juelich.de	39, 43
Džunuzović, Enis S.		137
Džunuzović, Jasna V.	jdzunuzovic@ihtm.bg.ac.rs	137
Elezović, Nevenka R.	elezovic@imsi.bg.ac.rs	179
Erčić, Jelena		157
Erni, Rolf	Rolf.Erni@empa.ch	37
Ersen, Ovidiu	ovidiu.ersen@ipcms.unistra.fr	89
Ferreira, Paulo J.	ferreira@mail.utexas.edu , paulo.ferreira.at@inl.int	67, 105, 113
Ferreira, Rafael V.	rafael.ferreira@inl.int	105
Fink, Rainer H.		69
Fisslthaler, Evelin	evelin.fisslthaler@felmi-zfe.at	53
Florea, Ileana		125
Foord, David		75
Fragueiro, Oihane		83
Fraser, Hamish L.	fraser.3@osu.edu	51
Freitag, Bert		75
Friedrich, Thomas		103
Gadre, Chaitanya		29
Gajić, Nataša	ngajic@tmf.bg.ac.rs	163
Galindo, Pedro		25
Gault, Baptiste		59
Gavrilović-Wohlmuther, Aleksandra	aleksandra.gavrilovic@cest.at	183
Gazdic Jankovic, Marina	marinagazdic87@gmail.com	137
Ge, Wanbing	wanbing.ge@warwick.ac.uk	203
Ghasemi, Arsham		25
Glass, Hugh		23
Glišić, Sandra		95
Gojgić-Cvijović, Gordana		141
Gojgić, Jelena		123/181
Gojković, Snežana Lj.	sgojkovic@tmf.bg.ac.rs	183
Golić, Igor	igor.golic@bio.bg.ac.rs	85
Gorman, Brian		33
Grogger, Werner	werner.grogger@felmi-zfe.at	53
Grujičić, Marija		205

Haberfehlner, Georg		53
Hage, Fredrik		27
Hao, Botao		63
Harreiß, Christina	christina.harreiss@fau.de	69
Hebert, Cecile	cecile.hebert@epfl.ch	47
Hegedűs, Máté		155
Henninen, Trond		37
Herz, Laura M.		63
Hesjedal, Thorsten	Thorsten.Hesjedal@physics.ox.ac.uk	25
House, Robert A.		109
Huang, Chen		45
Humphreys, Colin	c.humphreys@qmul.ac.uk	23
Ikram, Awais		43
Ivanovska, Aleksandra	aivanovska@tmf.bg.ac.rs	165
Ivković, Maja		135
Jadžić, Jelena		129
Janaćković, Djordje	nht@tmf.bg.ac.rs	79/151, 89, 147, 149, 153, 189, 197
Janković-Častvan, Ivona	icastvan@tmf.bg.ac.rs	93
Jardim, Paula		199
Jauković, Aleksandra		143
Jelača, Sanja		85
Jelić, Marko		205
Jensen, Jake		51
Jiang, Lin		75
Johnson, Manuel		69
Johnson, Michael B.		63
Jokić, Nikolina	jokicnikolinaffh@gmail.com	175
Joksović, Sara	sara.joksovic@biosense.rs	185, 201
Jovanović, Sonja	tamara.kravic-stevovic@med.bg.ac.rs	205
Jovanović, Zoran	zjovanovic@vin.bg.ac.rs	205
Jović, Vladimir D.	vladajovic@imsi.bg.ac.rs	119/169, 123/181, 179
Jugović, Dragana	dragana.jugovic@itn.sanu.ac.rs	175
Jung, Chanwon		59
Kadirvel, Kamalnath		51
Kaiser, Christoph		71
Kamberović, Željko	kamber@tmf.bg.ac.rs	163
Keller, Debora		37
Kelly, Thomas	thomas.kelly@steaminstruments.com	33
Kepaptsoglou, Demie		25, 27
Kersting, Benedikt		39
Khavnekar, Sagar		71
Kirkland, Angus I.	angus.kirkland@materials.ox.ac.uk	45, 207
Kis, Viktoria K.	kis.viktoria@ek-cer.hu	99, 101, 155
Kittel, Agnes	kittel.agnes@koki.hu	73
Kloenne, Zachary		51
Klumpe, Sven		71
Kobe, Spomenka		43

Kodranov, Igor		141
Kohei, Hamaya		25
Komelj, Matej	matej.komelj@ijs.si	43
Korać, Marija	marijakorac@tmf.bg.ac.rs	163
Koruga, Djuro		85
Kostić, Mirjana	kostic@tmf.bg.ac.rs	165
Kothleitner, Gerald	gerald.kothleitner@felmi-zfe.at	53
Kovacs, Andras		43
Kovacs, Zsolt	kovacs.zsolt@ttk.elte.hu	99, 101, 155
Krajnović, Tamara		85
Kravic-Stevovic, Tamara	tamara.kravic-stevovic@med.bg.ac.rs	81, 131, 133
Kremenović, Aleksandar		147
Krisper, Robert		53
Krstajić Pajić, Mila	mpajic@tmf.bg.ac.rs	123/181, 179
Kubicek, Markus		111
Labudović-Borović Milica		129
Lačković, Maja		135
Lačković, Vesna		135
Lačnjevac, Uroš Č.	uros.lacnjevac@imsi.bg.ac.rs	119/169, 179, 183
Lalic, Katarina		131, 133
Lammer, Judith	judith.lammer@felmi-zfe.at	53
Lamovec, Jelena		159
Lari, Leonardo		25
Lazarević, Slavica		197
Lazarov, Vlado	vlado.lazarov@york.ac.uk	25
Lazić, Ivan	ivan.lazic@thermofisher.com	61, 75
Leidl, Max L.		61
Li, Lian		25
Liberti, Emanuela		121
Liebscher, Christian H.		55
Lin, Alex		41
Ljujic, Biljana		137
Lobato, Ivan		107
Lojpur, Vesna		193, 195
Longo, Paolo		75
Lović, Jelena D.	jelena.lovic@ihtm.bg.ac.rs	91
Lukić, Ivana		189
Lukić, Jovan	jovlukic@tmf.bg.ac.rs	187
Lunkenbein, Thomas	lunkenbein@fhi-berlin.mpg.de	115
Luo, Hui		63
Luo, Ting		59
Madsen, Steven		35
Maksić, Aleksandar		177
Maksimović-Ivanić, Danijela		85
Maksimović, Vesna M.	vesnam@vin.bg.ac.rs	91
Maletaškić, Jelena		157
Mančić, Lidija	lidija.mancic@itn.sanu.ac.rs	193, 195
Mann, Daniel		75
Manojlović, Dragan		141
Manojlovic, Vaso	v.manojlovic@tmf.bg.ac.rs	163
Marčeta-Kaninski, Milica		87

Marega, Carla		137
Marie, John-J.		109
Marinković, Aleksandar D.	marinko@tmf.bg.ac.rs	89
Markoli, Boštjan	bostjan.markoli@ntf.uni-lj.si	43
Marković, Smilja	smilja.markovic@itn.sanu.ac.rs	93
Marks, Laurence	laurence.marks@gmail.com	41
Martinovic, Tamara	tamara.martinovic@med.bg.ac.rs	81, 131, 133
Matić, Tamara	tmatic@tmf.bg.ac.rs	173
Matović, Branko	mato@vin.bg.ac.rs	157
Maunders, Christian		75
Mayer, Joachim	mayer@gfe.rwth-aachen.de	65
Meffert, Matthias		97
Meingast, Arno		61, 75
Mentus, Slavko	slavko@ffh.bg.ac.rs	173
Migunov, Vadim		39
Mijailović, Daniel M.	dmijailovic@tmf.bg.ac.rs	119/169
Mijatović, Sanja		85
Milanović, Marija		201
Miletic Kovacevic, Marina		137
Miletić, Vesna		137
Milivojević, Marija	mmilivojevic@tmf.bg.ac.rs	153
Milivojevic, Nevena		137
Milosevic Djordjevic, Olivera		137
Milovanović, Dubravka		87
Milović, Miloš	milos.milovic@itn.sanu.ac.rs	173
Milutinovic, Milica		149
Mitrić, Miodrag	mmitric@vin.bg.ac.rs	89
Mizzi, Christopher	chris.mizzi@u.northwestern.edu	41
Mladenović, Dušan		173
Mladenović, Ivana	ivana@nanosys.ihtm.bg.ac.rs	159
Mravik, Željko	mravik@vin.bg.ac.rs	205
Müller-Caspary, Knut		61
Najman, Stevo		145
Nedelkovski, Zlatko		25
Nellist, Peter D.	peter.nellist@materials.ox.ac.uk	63, 107, 109, 121, 207
Nerl, Hannah C.	hannah.nerl@@physik.hu-berlin.de	115
Nesterović, Andrea		201
Nestorović, Milica		135
Nikolić, Irena	irena@ucg.ac.me	93
Nikolic, Maria V.		171
Nikolić, Nebojša D.	nnikolic@ihtm.bg.ac.rs	91, 159
Nikolic, Sandra		137
Nikolić, Vladimir		87
Novaković, Mirjana	mnovakov@vinca.rs	177
O' Leary, Colum M.		63
Obradović, Maja D.	maja.obradovic@ihtm.bg.ac.rs	183
Olson, Karl		41
Olsson, Eva	eva.olsson@chalmers.se	57
Ophus, Colin	clophus@lbl.gov	69, 89
Orlović, Aleksandar	orlovic@tmf.bg.ac.rs	95

Ozsoy-Keskinbora, Cigdem		75
Pan, Xiaoqing	xiaoqing.pan@uci.edu	29
Panic, Vesna		149
Parapari, Sorour S.	sorour.semsari.parapari@ijs.si	43, 117
Pavlović, Aleksandra	aleksandra3003@yahoo.com	135
Pechnikova, Evgeniya V.		61
Pejčić, Milica		205
Pergal, Marija V.	marija.pergal@ihtm.bg.ac.rs	141
Petricevic, Aleksandar		123/181
Petricevic, Sasa		81
Petrović, Jana	janapetrovic52@gmail.com	173
Petrović, Rada	radaab@tmf.bg.ac.rs	79/151, 89, 147, 149, 153, 189, 197
Petrović, Tamara		
Piazza, Luca		97
Piper, Danica	dana.piper24@gmail.com	201
Plitzko, Jürgen M.	plitzko@biochem.mpg.de	71
Plodinec, Milivoj	mplodinec@ethz.ch	115
Podlogar, Mateja		43
Podmiljsak, Benjamin		43
Popović, Miljana	miljana@tmf.bg.ac.rs	161
Porcu, Mauro		75
Radenković, Milena		145
Radetić, Tamara	tradetic@tmf.bg.ac.rs	161, 209
Radmilović, Nadežda	nadezdas@vinca.rs	157, 193, 195
Radmilović, Velimir R.	vrradmilovic@tmf.bg.ac.rs	89,93,119/169, 183
Radmilović, Vuk V.	vukradmilovic@tmf.bg.ac.rs	93,119/169, 183, 187
Radojević, Vesna	vesnar@tmf.bg.ac.rs	159
Radosavljević, Tatjana	tatjana.radosavljevic@med.bg.ac.rs	129
Radovanović, Lidija	lradovanovic@tmf.bg.ac.rs	147
Radovanović, Željko	zradovanovic@tmf.bg.ac.rs	147
Raghavendrarao, Jayanth		105
Rajić, Vladimir	vladimir.rajic@vinca.rs	177, 193
Rakocevic, Lazar	lazar.rakocevic@vin.bg.ac.rs	171, 177
Ramasse, Quentin	qmramasse@superstem.org	27, 203
Ranitović, Milisav		163
Rasulic, Iva		131, 133
Rauscher, Thomas		123/181
Ražnjević, Sergej	Sergej.Raznjevic@oeaw.ac.at	111
Ribeiro, Ricardo M.		105
Rigort, Alexander		71
Rmuš, Jelena		205
Rogan, Jelena R.	rogan@tmf.bg.ac.rs	183
Romaner, Lorenz		55
Rothmann, Mathias U.	mathias.rothmann@physics.ox.ac.uk	63
Rózsa, Noémi		155
Ruzaeva, Karina		39
Sachse, Carsten	c.sachse@fz-juelich.de	61
Salah, Dina		83

Salinga, Martin	martin.salinga@uni-muenster.de	39
Sanchez, Ana		203
Scheiber, Daniel		55
Scheu, Christina	scheu@mpie.de	59
Schioetz, Oda	schioetz@biochem.mpg.de	71
Schlögl, Robert	robert.schloegl@cec.mpg.de	115
Sentürk, Duygy G.	duygugizem.senturk@uantwerpen.be	103
Sheader, Alex		121
Siebenhofer, Matthäus	m.siebenhofer@tugraz.at	111
Sinclair, Robert	bobsinc@stanford.edu	35
Song, Weixin	weixin.song@materials.ox.ac.uk	63, 109, 121
Spiecker, Erdmann	erdmann.spiecker@fau.de	69
Spreitzer, Matjaz	matjaz.spreitzer@ijs.si	171
Srdić, Vladimir V.	srdicvv@uns.ac.rs	185, 201
Srejić, Irina		177
Stamenković, Tijana	tijanas@vinca.rs	193, 195
Stanojev, Jovana		185
Stefanović, Ivan S.	ivan.stefanovic@ihtm.bg.ac.rs	137
Stefanović, Milica	mstefanovic@tmf.bg.ac.rs	189
Steinhart, Milos		141
Stevanović, Marija	marija.stevanovic@tmf.bg.ac.rs	153
Stijepović, Ivan	mstijepovic@tmf.bg.ac.rs	201
Stoiljković, Milovan		157
Stojanović , Sanja	sanja.genetika.nis@gmail.com	145
Stojanović, Dušica B.	duca@tmf.bg.ac.rs	119/169
Stojković Simatović, Ivana	ivana@ffh.bg.ac.rs	175
Stojkovic, Miodrag		137
Stroppa, Daniel	daniel.stroppa@dectris.com	97
Suchanek, Martin	martin.suchanek@tescan.com	167
Suenaga, Kazu	suenaga-kazu@sanken.osaka-u.ac.jp	31
Sulyok, Attila		155
Šaponjić, Zoran	zsaponjic@iofh.bg.ac.rs	87
Škapin, Srečo	sreco.skapin@ijs.si	175
Šljukić-Paunković, Biljana	biljka@ffh.bg.ac.rs	173
Špirkova, Milena		141
Štrbac, Svetlana	svetlana.strbac@ihtm.bg.ac.rs	177
Šturm, Sašo	saso.sturm@ijs.si	43, 117
Tadic, Nenad		171
Talijan, Nadežda		95
Taneja, Deepyanti		105
Teurtrie, Adrien		47
Tomše, Tomaž		43
Torres, Daniel		117
Toth, Elvira	elvira.djurdjic@df.uns.ac.rs	201
Trivanović, Drenka		143
Tusseau-Nenez, Sandrine	sandrine.tusseau-nenez@polytechnique.edu	125
Ugrinovic, Vukasin	vugrinovic@tmf.bg.ac.rs	149
Uskoković, Petar S.	puskokovic@tmf.bg.ac.rs	119/169
Ustarroz, Jon		117

Valencia-Naranjo, Helen		65
Van Aert, Sandra	sandra.vanaert@uantwerpen.be	103, 107
Van Cappellen, Eric	eric.van.cappellen@thermofisher.com	75
Vasiljević-Radović, Dana	dana@nanosys.ihtm.bg.ac.rs	141, 159
Vasiljevic, Zorka		
Veljović, Djordje	djveljovic@tmf.bg.ac.rs	73, 143, 79/151, 153
Veselinović, Ljiljana	ljiljana.veselinovic@itn.sanu.ac.rs	93
Vesković, Milena		129
Villoro, Ruben B.	r.bueno@mpie.de	59
Viswanatha, Gobal		51
Volk, Martin		83
Vranješ, Mila		87
Vu, Xuan		39
Vučević, Danijela		129
Vujančević, Jelena	jelena.vujancevic@itn.sanu.ac.rs	189
Vujković, Milica	milica.vujkovic@ffh.bg.ac.rs	173
Vukmirović, Jelena		201
Vuković, Marina		193
Walfort, Sebastian	swalfort@uni-muenster.de	39
Wang, Yunzhi		51
Weber, Dieter		39
Weinert, Mike		25
Weng, Szhichao		23
Wirix, Maarten		61, 75
Wu, Mingjian	mingjian.wu@fau.de	69
Xuan, Xu		43
Yan, Xingxu		29
Yu, Yuan		59
Zabinski, Piotr	zabinski@agh.edu.pl	179
Zaefferer, Stefan		59
Zafeiratos, Spyridon	spiros.zafeiratos@unistra.fr	89
Zak, Tomaš		95
Zamfir, Mihai		125
Zebić, Maja L.		79/151
Zeng, Yitian		35
Zhang Ruomu	ruomu.zhang@materials.ox.ac.uk	121
Zhang, Siyouan		59
Zhang, Zaoli		111
Zhang, Zezhong	zezhong.zhang@unatwerpen.be	107
Zhou, Langyan		105
Zhou, Xuyang		55
Zivanovic, Marko		137
Zorro, Fatima	fatima.zorro@inl.int	113
Žagar Soderžnik, Kristina	kristina.zagar@ijs.si	43
Živković, Predrag	peca@tmf.bg.ac.rs	91
Žužek, Kristina	Tina.Zuzek@ijs.si	43, 117

ACKNOWLEDGEMENTS

DIAMOND SPONSOR

ThermoFisher SCIENTIFIC

GOLD SPONSORS

Innovation Center of the Faculty of Technology and Metallurgy, University of Belgrade

ICTM

NanoMEGAS

NanoMEGAS
Advanced Tools for electron diffraction

SILVER SPONSORS

Mikrolux/Tescan

Mikrolux TESCAN
PERFORMANCE IN NANOSPACE

ELMINA2022 Conference acknowledges Institute for Materials Testing, Dectris AG and Analysis Ltd. for their support.

MEDIA SUPPORT:

European Microscopy Society (EMS)

Federation of European Materials Societies (FEMS)

Imaging & Microscopy Journal

CIP – Каталогизација у публикацији
Народна библиотека Србије, Београд

66.017/.018(048)
544.2(048)
621.385.833.2(048)

INTERNATIONAL Conference on Electron Microscopy of Nanostructures ELMINA (2 ; 2022 ; Beograd)
Program ; & Book of Abstracts / Second International Conference ELMINA [Electron Microscopy of Nanostructures] 2022, Belgrade, Serbia, August 22nd-26th, 2022 ; organized by Serbian Academy of Sciences and Arts and University of Belgrade, Faculty of Technology and Metallurgy ; [editors Velimir R. Radmilović and Vuk V. Radmilović]. - Belgrade : SASA, 2022 (Belgrade : SASA). - 223 str. : ilustr. ; 30 cm

Na nasl. str.: European Microscopy Society and Federation of European Materials Societies. - Tiraž 55. - Bibliografija uz svaki apstrakt. - Registar.

ISBN 978-86-7025-943-0

а) Наука о материјалима -- Апстракти б) Нанотехнологија -- Апстракти в) Електронска микроскопија -- Апстракти

COBISS.SR-ID 72022025